Full-wave numerical simulation of T-waves and of moving acoustic sources

Alexis Bottero

AIX-MARSEILLE UNIVERSITÉ CNRS,
CENTRALE MARSEILLE
ED 353 SCIENCES POUR L'INGÉNIEUR
MÉCANIQUE, PHYSIQUE, MICRO ET NANOÉLECTRONIQUE

LABORATOIRE DE MÉCANIQUE ET D'ACOUSTIQUE / UMR 7031 AMU-CNRS-ECM

Thèse de Doctorat

Spécialité : Acoustique

Présentée par : Alexis BOTTERO

Simulation numérique en forme d'onde complète d'ondes T et de sources acoustiques en mouvement

Full-wave numerical simulation of T-waves and of moving acoustic sources

Soutenue le jeudi 13 septembre 2018 à 14h30 devant le jury composé de :

Catherine de Groot-Hedlin	Directrice de Recherche, University of California at San Diego, USA	Rapporteur
Christophe Bailly	Professeur des Universités, École Centrale de Lyon	Rapporteur
Oleg A. Godin	Professeur des Universités, Naval Postgraduate School, Monterey, USA	Examinateur
Claude Guennou	Maître de Conférences, Université de Bretagne Occidentale	Examinatrice
Joseph Moysan	Professeur des Universités, Université d'Aix-Marseille, LMA	Examinateur
Pierre Franck Piserchia	Ingénieur CEA, Docteur ès Sciences, DAM Bruyères-le-Châtel	Invité
Dimitri Komatitsch	Directeur de Recherche CNRS, LMA Marseille	Directeur de thèse
Paul Cristini	Chargé de Recherche CNRS HDR, LMA Marseille	Co-directeur de thèse

Alexis BOTTERO
Laboratoire de Mécanique et d'Acoustique UMR 7031 AMU-CNRS-ECM
4 impasse Nikola Tesla
13453 Marseille cedex 13, France
Email: bottero@lma.cnrs-mrs.fr et alexis.bottero@gmail.com

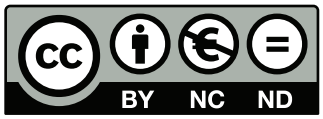

À mon grand père.

Abstract

This thesis combines observations, simulations and development of high-performance numerical tools in the field of underwater acoustics, and in particular for the study of T-waves.

The term T-waves is generally associated with acoustic waves generated by seismic events that subsequently travel horizontally in the ocean at the speed of sound. After a thematic review of the literature on T-waves we analyzed real data recorded in Sicily and Calabria following earthquakes occurring near the West coast of Greece. In order to model the phenomenon, we developed an axisymmetric spectral-element solver (2.5-D) in the time domain, which we present and validate. This tool allowed us to realistically reproduce numerically one of the Greek earthquakes studied as well as the propagation of the resulting T-waves up to Sicily.

We also present a two-stage parametric study of the influence of seafloor slope in a typical T-wave generation/conversion scenario. The energy and duration of these waves is particularly sensitive to the environment. In particular, the slopes and characteristics of the seabed play a crucial role for both solid-fluid and fluid-solid conversion. These characteristics can mislead localization algorithms. Likewise, the depth and position of the earthquake relative to the slope is of great importance, with the presence of privileged areas for the generation of T-waves, which we have mapped. In addition, in the case of the conversion of an acoustic wave on a coast, our simulations predict that in some cases a strong Rayleigh wave can be generated, whose signal, recorded inland, is very sensitive to the slope and to the characteristics of the environment, but not very sensitive to the modal structure of the incident wave. This phenomenon may have interesting implications that we discuss.

However, our studies confirm that at regional distances (< 1000 km) the sound speed profile in the ocean is only a second-order parameter. To evaluate its impact we have developed a procedure for the calculation of transmission-loss and time-dispersion maps from full-wave numerical simulations in the time domain. In the configurations studied, the presence of the SOFAR channel slightly limits the time dispersion but only introduces a gain in terms of energy transmission of a few thousandths of dB per kilometer.

In a second step, we show that a medium-sized commercial vessel, as there are tens of thousands nowadays in the oceans of the globe, can generate by diffraction some T-waves of significant amplitude (of the order of those created by downslope conversion on a slope of 12°) and of low dispersion. This mechanism of T-wave generation, to our knowledge undocumented, must be particularly frequent in areas in which maritime traffic is substantial and could explain some abyssal T-waves that are still not well understood. Taking the atmosphere into account in these simulations, we realized that the presence of these vessels could also produce guided infrasound in the lower layers of the atmosphere. This mechanism of infrasound production could be an alternative explanation to the evanescent coupling proposed by Evers et al. [2014] to explain the waves observed in Tasmania following an earthquake on the Macquarie Ridge.

Finally, we presented and validated some numerical tools to calculate the acoustic field created by a moving source. The method was applied to a light aircraft flying over the ocean. This configuration, presented by Buckingham [2010], can be used to estimate the pressure wave speed in marine sediments.

Résumé

Cette thèse mêle observations, simulations et développement d'outils numériques haute performance dans le domaine de l'acoustique sous-marine, et notamment pour l'étude des ondes T.

Le terme ondes T est généralement associé à des signaux acoustiques générés par des événements sismiques et qui se déplacent ensuite horizontalement dans l'océan à la vitesse du son. Après une revue thématique de la littérature sur les ondes T nous avons analysé des données réelles enregistrées en Sicile et en Calabre à la suite de tremblements de terre survenus près de la côte ouest de la Grèce. Afin de modéliser le phénomène nous avons développé un solveur éléments spectraux axisymétriques (2.5-D) dans le domaine temporel, que nous présentons et validons. Cet outil nous a permis de reproduire numériquement de façon réaliste un des séismes grecs étudiés ainsi que la propagation des ondes T résultantes jusqu'en Sicile.

Nous présentons également une étude paramétrique en deux temps de l'influence de la pente du plancher océanique dans un scénario typique de génération/conversion d'une onde T. L'énergie et la durée de ces ondes s'avère être particulièrement sensible à l'environnement. En particulier nous avons vu que les pentes et les caractéristiques du fond marin jouaient un rôle capital autant sur la conversion solide - fluide que fluide - solide. Ces particularités peuvent d'ailleurs tromper les algorithmes de localisation. De même, la profondeur et la position du tremblement de terre vis-à-vis de la pente s'avèrent être de grande importance, avec la présence de zones privilégiées pour la génération des ondes T, que nous avons cartographiées. En outre, dans le cas de la conversion d'une onde acoustique sur une côte, nos simulations prédisent dans certains cas la création d'une forte onde de Rayleigh dont le signal, enregistré à l'intérieur des terres, est très sensible à la pente et aux caractéristiques de l'environnement, mais très peu sensible à la structure modale de l'onde incidente. Ce phénomène peut avoir des implications intéressantes que nous discutons.

Cependant, nos études confirment qu'aux distances régionales (< 1000 km) le profil de vitesse dans l'océan s'avère n'être qu'un paramètre de deuxième ordre. Pour en évaluer l'impact nous avons développé une procédure pour le calcul de cartes de perte de transmission et de dispersion à partir de simulations numériques en forme d'onde complète dans le domaine temporel. Dans les configurations étudiées, la présence du canal SOFAR limite légèrement la dispersion temporelle mais n'introduit un gain en termes de transmission énergétique que de l'ordre de quelques millièmes de dB par kilomètre.

Dans un second temps nous montrons qu'un bateau commercial de taille moyenne, comme il y en a aujourd'hui des dizaines de milliers sur les mers du globe, peut créer par diffraction des ondes T d'une d'amplitude conséquente (de l'ordre de celles créées par conversion « downslope » sur une pente de 12°) et de faible dispersion. Ce mode de génération d'onde T, encore non documenté, doit être particulièrement fréquent dans les zones où le trafic maritime est important et pourrait expliquer certaines ondes T abyssales encore incomprises. En prenant l'atmosphère en compte dans ces simulations nous nous sommes aperçu que la présence de ces mêmes navires pouvait également générer des infrasons guidés dans les couches basses de l'atmosphère. Ce mode de production d'infrasons pourrait constituer une explication alternative au couplage évanescent proposé par Evers et al. [2014] pour expliquer les ondes observées en Tasmanie à la suite d'un tremblement de terre sur la dorsale Macquarie.

Pour finir, nous avons présenté et validé des outils numériques pour calculer le champ acoustique créé par une source en mouvement. La méthode a été appliquée au cas d'un avion léger volant au-dessus de l'océan. Cette configuration, présentée par Buckingham [2010], peut permettre d'estimer la vitesse des ondes de compression dans les sédiments.

Contents

Summary of the research done, or not done, in this thesis

The reader will find a brief definition of the terms that will appear in blue in the thesis in Appendix C.

T-waves

In underwater acoustics, T-waves have been the subject of much attention since their discovery in the 1940s (Linehan [1940]). This thesis falls within this area of interest. As is often the case in a substantial body of literature, the term "T wave" has sometimes been used in reference to various phenomena and in various contexts. For that reason, in order to avoid confusion, it seemed important to us to set once and for all the vocabulary in the context of our work.

In our definition, a T-wave is an acoustic signal generated following a seismic event that travels horizontally in the sea at the speed of sound in the water.

This definition, which may seem rather vague, may be the most appropriate; as we will see in these pages, T-waves cannot be described in all their diversity by their mode of propagation or their dispersion properties for example. One has to note in particular the term "seismic event", which applies to both earthquakes and man-made seismic sources but not to underwater explosions for instance. Indeed, some authors speak of T-waves to refer to signals generated in water by any mechanism (Shapira [1981]; Cansi & Bethoux [1985]; Okal & Talandier [1986]; Koyanagi et al. [1995]; Piserchia et al. [1998] for example). It should also be noted that no propagation distance has been specified. We will call "T wave" a signal recorded at 150 km as well as signal recorded at 15000 km from the source, as long as it propagated at more or less 1500 $m.s^{-1}$. Let us note that the term "T-phase" also appears in the literature. T-wave and T-phase are often used interchangeably. In this document we will sometimes also use the term T-phase but only when referring to a recorded signal and not to the physical phenomenon itself.

Figure A illustrates the generation of T-waves by earthquakes.

An earthquake, the eruption of a volcano or the explosion of an atomic bomb generate seismic waves. We distinguish compression waves ("P" waves, as "Pressure", also called sound waves), shear waves ("S" waves as) and surface waves. When a seismic event occurs near an ocean basin, some of the energy produced can be channeled into the water layer and then travel horizontally in this natural waveguide at the speed of sound in the water. These guided waves are called T-waves and

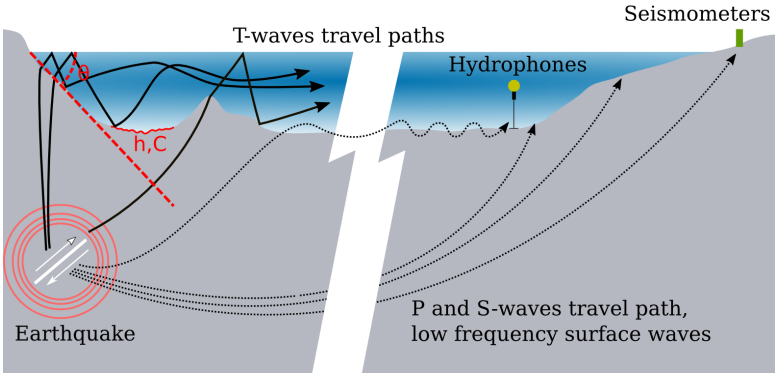

Figure A – Illustration of the generation of T-waves by earthquakes. The two main known coupling mechanisms are shown in the figure: generation at a sloping seafloor (angle θ) or at a local bathymetric high, and generation at rough interfaces (correlation length C and average height h).

typically have a frequency range between 1 and 100 Hz. The conversion of seismic waves into T-waves can occur mainly in two ways: by successive reflections between the sea surface and a sloping seabed, or by diffraction by roughness or by heterogeneities. Each conversion mode has its own specific characteristics.

Once channeled into the water layer, T-waves can travel particularly far for several reasons. First, by propagating in the ocean, they spread in an almost cylindrical fashion, which causes less losses than in the case of spherical geometrical spreading in free space as for P and S waves (see Fox & Dziak [1998]). In addition, the attenuation of acoustic waves in water is particularly low at the frequencies considered. Finally, due to the fact that temperature and pressure vary with depth, the speed of sound waves in the ocean typically presents a minimum around 1000 m in the Atlantic. This feature, known as the "SOFAR channel", makes it possible, under certain conditions, to further improve energy transmission. T-waves can therefore propagate over very large distances, in practice only limited by the size of ocean basins (see Okal & Talandier [1997]; Metz et al. [2016] for example). Even a moderate seismic event can be detected thousands of kilometers away if it has generated T-waves. Thus, the event detection threshold can be improved by one to two orders of magnitude by using a few instruments at sea (hydrophones or OBS) rather than large terrestrial seismic networks (Johnson & Northrop [1966]; Fox et al. [1994]; De Groot-Hedlin et al. [2004]; Pan & Dziewonski [2005]; Dziak et al. [2011]). It should be noted, however, that these instruments pose other problems related, for example, to their location or to the transmission of recorded data.

After their oceanic path, T-waves have thus good chance of reaching the coasts. On arrival on the continental slope, they convert back into seismic waves that can be detected by inland seismometers, even exceptionally by those located far from the shoreline (Tolstoy & Ewing [1950]; Båth & Shahidi [1971]; Cansi & Bethoux [1985]; Cook & Stevens [1998]; Stevens et al. [2001]). Although harmless, T-waves can sometimes be felt by coastal populations (Talandier & Okal [1979]; Leonard [2004]). Since sound travels more slowly in water than in the ground, converted T-waves typically arrive after compression waves (P-waves) and shear waves (S-waves), hence their name "T" as Third. Figure B shows a typical example of a T-wave seismogram recorded in Sicily following an earthquake of magnitude $M_w = 4.7$ on the Greek west coast.

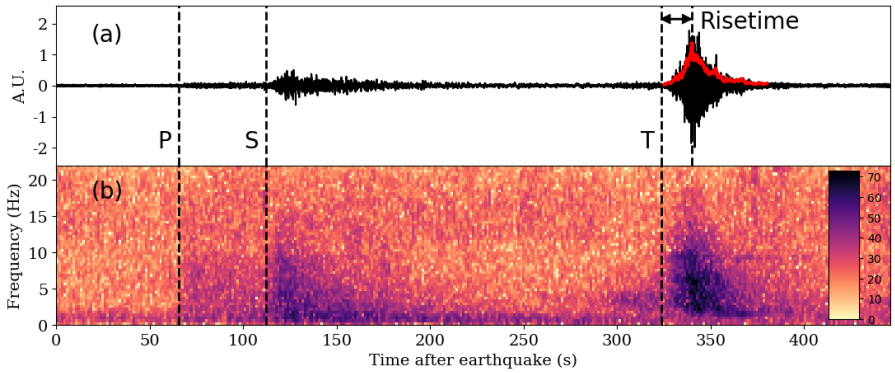

Figure B – Example of a T-wave signal recorded in Sicily following an earthquake that occurred near the west coast of Greece (distance ∼ 520 km). Origin time of the earthquake: 2013/05/23 at 14:09:07.40, latitude: 38.6488, longitude: 20.5813, moment centroid depth: 2 km, $M_w = 4.7$. The earthquake location is shown as a red star in Figure 2.1 (top). (a) Vertical component displacement seismogram (arbitrary displacement unit) recorded at the Sicilian seismic station HCRL (latitude: 37.2831, longitude: 15.0325), which is the station immediately northwest of station SSY in Figure 2.1. P, S and T-waves arrivals are clearly visible. An example of filtered T-phase envelope is shown in red. The T-phase rise time is defined in the figure. (b) Power Spectral Density (in dB) as a function of time and frequency. Note the high frequency content of the T-phase.

In this example the three arrivals P, S and T are clearly visible. However, in many cases, such as small seismic events along mid-ocean spreading ridges, only T-waves are detected. They are the only available piece of information on these events (see for example Fox et al. [1994]). T-waves are therefore used in many fields of geosciences. Since the 1960s, thousands of T-waves have been recorded and located (seeJohnson [1966]; Duennebier & Johnson [1967]; Fox et al. [2001]) and algorithms now exist for their automatic recognition (Sukhovich et al. [2014]). Although the location of the conversion zone is sometimes difficult, these measurements have made it possible to identify volcanic eruptions (Dietz & Sheehy [1954]; Norris & Johnson [1969]; Talandier & Okal [1987a]; Schreiner et al. [1995]; Fox & Dziak [1998]; Bohnenstiehl et al. [2013]) or to monitor eruptive processes in real time (Fox et al. [1995]; Dziak et al. [2011]). These detections therefore contributed greatly to our understanding of hydrothermal and microbial processes in ocean ridges (Delaney et al. [1998]; Cowen et al. [2004]; Wilcock et al. [2014]). T-waves are also very useful for detecting small intra-plate earthquakes in very remote regions (Fox et al. [2001]) and for studying seafloor expansion or magma intrusion at ocean spreading ridges (Hammond & Walker [1991]; Fox et al. [1994]; Schreiner et al. [1995]; Blackman et al. [2000]) that affect the ocean and marine ecosystems (Dziak et al. [2011, 2012]).

For large earthquakes in oceanic regions, the T-waves received can be used together with P and S waves to map the different components of the fault rupture (see Graeber & Piserchia [2004]; De Groot-Hedlin [2005]; Guilbert et al. [2005]; Tolstoy & Bohnenstiehl [2005, 2006]). Moreover, some links between T-waves and tsunamis have now been established and could potentially be used in a warning system (Ewing et al. [1952]; Tolstoy & Bohnenstiehl [2006]; Salzberg [2008]). Finally, acoustic signals recorded in the oceans have been used for several years to distinguish between anthropogenic and natural sources such as nuclear explosions and volcanoes, in particular under the Comprehensive Nuclear-Test-Ban Treaty (CTBT) adopted by the United Nations General Assembly in 1996 (see De Groot-Hedlin & Orcutt [1999, 2001c])). Indeed, although easily detectable from surface waves, nuclear explosions generate only weak P and S waves (see Adams [1979]) because they happen very close to the Earth surface. T-wave signals can also provide information on the earthquake that generated them (Dziak [2001]; Talandier & Okal [2016]), on the surface seismic characteristics of coastal regions (Koyanagi et al. [1995]; Kosuga [2011]) or on the deep structure of the Wadati-Benioff zone (Okal [2001b]). In the future, T-waves may also be used to study mesoscale variations in ocean properties (Evers & Snellen [2015]).

At the interface between seismology and underwater acoustics, the T-wave phenomenon involves complex and diverse processes whose mechanisms are poorly understood, which limits the possibilities for in-depth theoretical analysis. These processes include viscoelasticity, seismic to acoustic and acoustic to seismic conversion, diffraction, guided propagation in the ocean, high frequencies, 3-D effects or complex geometries. In this context, it is still difficult to correctly assess the influence of the characteristics of the earthquake, the seabed or the ocean, for example. These issues are still open nowadays. The spectrogram presented in Figure B is typical and shows that, overall, T-waves have a much higher frequency content than corresponding P and S waves. Indeed, high frequencies are particularly less attenuated during propagation in the ocean than during propagation in the Earth's crust and mantle. This characteristic is interesting because the high frequency part of the spectrum is sensitive to the fine structure of the earthquake, ocean and seabed and is absent from long-distance P and S wave seismograms. Thus, more information is potentially contained in T-waves than in P and S waves from that point of view, and that this information can be detected from far away (see Dziak et al. [2004a]). Unfortunately, the scientific community currently does not fully understand how to use this information. In this context, as in many other research areas, numerical simulation seems to be an appropriate approach for the study of T-waves.

Sediment sounding from flying aircrafts

Figure C – Diamond Star DA40 aircraft (three-blade propeller, 180 shaft horse power). Taken from scripps.ucsd.edu/labs/buckingham/research/aircraft-sound.

It has been known for many years that the sound from large aircrafts is detectable beneath the ocean surface (Urick [1972]; Medwin et al. [1973]; Richardson et al. [2013]). More recently, Buckingham et al. [2002a,b] performed experiments with a light and low-flying aircraft (similar to the one shown in Figure C) to establish whether the sound from such an airborne source could be used to recover the acoustic properties of the seabed in shallow water. The authors showed that the sound from the propeller was detected not only at a microphone in the air and at hydrophones below the sea surface but also at an instrument buried about 1 m deep in the sediment. The received signals experience a significant Doppler shift due to the motion of the aircraft. The amplitude of such a frequency change in the seabed depends on the speed of sound. Later studies (Buckingham [2003]; Buckingham & Giddens [2006]) provided a deeper understanding of the physics behind the Doppler-shifted field in the channel and the sediments. This work opened the door to inversion of the Doppler-shifted modes associated with each harmonic in order to estimate the sound speed in the sediment and also other geoacoustic parameters (shear speed, porosity, density and grain size), even using only receivers moored in the water. Conveniently for such inversion purposes the sound of light aircrafts appears to contain low frequency harmonics (down to ∼80 Hz), the intensity of which varies only weakly throughout the angular range (Buckingham et al. [2006]). This unusual acoustic inversion

technique is known as geoacoustic Doppler spectroscopy (Buckingham [2010]). Recently, Bevans & Buckingham [2017] presented another original technique using a low-flying light helicopter and an inversion procedure using the coherence function of the head wave generated at the ocean-sediment interface. The sound produced by the rotors has an even broader frequency bandwidth than the propeller noise of aircrafts, rich in low frequencies (down to about 13 Hz and up to 2.5 kHz) and thus constitutes a great low-frequency sound source. In addition, this new inversion techniques seem more efficient than geoacoustic Doppler spectroscopy because it uses the whole frequency spectrum and thus seems more suitable in noisy environments. For such configurations there exist relatively simple mathematical models for stratified fluid media. However, as complexity increases (slopes, elasticity, roughness...) the theoretical analysis becomes particularly challenging. Here again, numerical methods can be beneficial.

Supercomputers, High-Performance Computing (HPC), and numerical methods

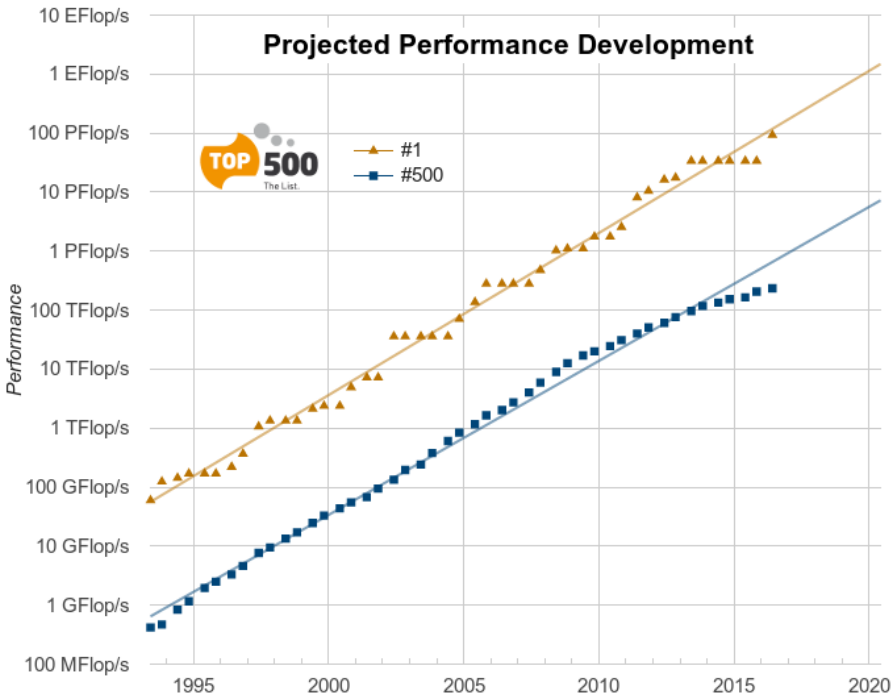

Figure D – Performance measured in flop/s (number of floating-point operations per second) of the world's fastest supercomputer (in orange) and its projected evolution over the years, as well as the speed of the 500th, i.e. a typical machine in regional computing centers and therefore easily accessible to any researcher. In logarithmic scale, adapted from `www.top500.org`.

Understanding, predicting, imaging. Numerical simulation is nowadays one of the pillars of science, together with observation, experimentation and theory. It is now indispensable for the study of most complex systems. In this context, numerical methods and supercomputers are essential for all applications requiring high computing power, such as weather or climate prediction, aerodynamics, seismology, molecular chemistry, genetics, astrophysics, cryptanalysis, finance and insurance, etc. These approaches are known as HPC (High Performance Computing). The reader can find an overview of this field e.g. in Nagel et al. [2018]. It is also worth citing the article of Gropp & Sterling [2015] on the future evolution of HPC.

Since the 1960s and the development of the first supercomputers, the performance of the largest

high performance computers has increased from 10^6 to 10^{17} Flop/s (floating-point operation per second) following an almost perfect exponential law (Figure D). This law predicts, for example, that by about 2020, the first exascale/exaflops machine (10^{18} Flop/s) will appear somewhere in the world (orange line). More importantly, this figure shows that until now, it took about nine years to move from the world's largest supercomputer to a regional or local infrastructure easily accessible to many researchers. The trend is expected to continue. In recent years, intra-node parallelism in supercomputers has continued to improve, either because of the increasing number of cores available on CPUs (Central Processing Units), or because of computing units such as GPU (Graphics Processing Units Computing) graphics cards or Intel accelerators (Intel Xeon Phi, Intel Many Integrated Core Architecture "Knights Landing" i.e. MIC KNL). One can therefore predict with some confidence that expensive numerical methods now will become the standard in a fairly well-predicted future, as the machines to run them will most probably become widely available.

For this thesis we will focus on the propagation of acoustic waves in complex environments. In this field, the evolution of supercomputers has enabled several academic and industrial laboratories to use so-called "full-wave" methods, which were still impractical because too expensive a decade ago. These methods have the advantage of directly discretizing the fundamental equations of elastodynamics without introducing any additional approximation. This of course comes with a high calculation cost. They are therefore typically used when the problems considered require high accuracy and when the cost of calculation can be afforded. These methods were mostly initially developed in the late 1960 and in the 1970s to meet the needs of the oil industry, which has always been interested in seismic methods for detecting oil and gas reservoirs. Finite-difference (FD) methods were first developed (Alterman & Karal Jr [1968]; Boore [1972]; Kelly et al. [1976]; Virieux [1986]; Levander [1988]). For spatial discretization, variational methods also soon emerged (Lysmer et al. [1972]; Strang & Fix [1973]), in particular because they limit the problems of numerical instabilities and make it possible to more easily deal with heterogeneous environments and boundary conditions. A large number of such Finite Element Methods (FEM) then appeared. Among the most widely used nowadays one can cite the Spectral Element Method (SEM, Seriani & Priolo [1994]; Komatitsch & Vilotte [1998]; Cohen & Fauqueux [2000]; Bécache et al. [2000]; Jenkins et al. [2002]), the Discontinuous Galerkin method (Rivière & Wheeler [2003]; Chung & Engquist [2006]; Grote et al. [2006]; Käser & Dumbser [2006]; Käser & Dumbser [2008]) and to a lesser extent Finite Volume Methods (Dormy & Tarantola [1995]; Dumbser et al. [2007]). These methods have gradually become standard in the field of seismology at both global and regional scales (Tromp et al. [2008]; Gokhberg & Fichtner [2016]; Monteiller et al. [2015]; Wang et al. [2016]). In underwater acoustics however, the use of full waveform methods is still uncommon. Indeed the problems studied, such as T-waves or geoacoustic Doppler spectroscopy, typically involve very high frequencies over long propagation distances, which often make these kinds of approaches unaffordable. However, the evolution of computer performance is now changing the situation and opening up an immense field of study (see for example Isakson & Chotiros [2011]; Cristini & Komatitsch [2012]; Jamet et al. [2013]; Bottero et al. [2016a]; Isakson [2018]), of which we intend to explore a small part in this PhD. The numerical method that we will use is a SEM. The SEM is a continuous Galerkin technique, which can easily be made discontinuous; it is then close to a particular case of the discontinuous Galerkin technique, with optimized efficiency because of its tensorized basis functions. In particular, it can accurately handle very distorted mesh elements. The SEM has very good accuracy and convergence properties. It admits spectral rates of convergence and allows exploiting *hp*-convergence schemes. It is also very well suited to parallel implementation on very large supercomputers as well as on clusters of GPU accelerating graphics cards. The SEM can also handle triangular (in 2-D) or tetrahedral (in 3-D) elements as well as mixed meshes, although with increased cost and reduced accuracy in these elements, as in the discontinuous Galerkin method (see references and details in Komatitsch [2018]).

What *is* covered in this thesis

This manuscript is composed of six chapters mixing observations, simulations and development of numerical tools. The first chapter contains a review of the literature on T-waves, which spans 90 years of research, from early observations to current numerical simulations. We then present a data study carried out in collaboration with Dr. Emanuele Casarotti at the Istituto Nazionale di Geofisica e Vulcanologia (INGV, National Institute of Geophysics and Volcanology) of Rome, Italy (Chapter *2*). In that work we analyzed seismograms recorded in Sicily and Calabria following earthquakes that occured near the west coast of Greece. This led us to identify general trends on the generation and propagation of T-waves in that region. In order to model the phenomenon we then developed an axisymmetric (2.5-D) spectral-element solver in the time domain, which we present and validate in Chapter *3*. This tool allowed us to numerically reproduce one of the Greek earthquakes studied and the propagation of T-waves all the way to Sicily. Comparing the real data with the numerical results enabled to exhibit the most significant physical parameters (Chapter *4*). We also tried to perform 3-D simulations but failed to generate a suitable mesh. This unsuccessful attempt is described in Appendix B. Chapter *4* also contains a two-step parametric study of the influence of the slope on a typical T-wave generation/conversion scenario. We first study the amount of acoustic energy channeled from an earthquake occurring under an sloping seabed. We then model the reflection/transmission of a guided wave at shore. The influence of the properties of the water layer and of marine sediments is discussed.

Chapter *5* describes a procedure for calculating transmission loss and dispersion maps from full-wave numerical simulations performed in the time domain. We then use these maps to study the efficiency of the SOFAR channel in terms of energy channeling as a function of the sound speed profile in the water layer, of the type of source and of the nature of the seabed. Finally, Chapter *6* presents and validates a full-wave numerical approach based on spectral elements in the time domain to model in the acoustic field created by a moving source. The method is applied to geoacoustic Doppler spectroscopy of marine sediments. In the second part of that chapter we also propose a new T-wave generation mechanism and an alternative explanation to the waves observed by *Evers et al. [2014]* at sea and in the atmosphere following a 2004 earthquake in the Macquarie Ridge.

What *is not* covered in this thesis but could have been

1. 3-D effects

T-waves travel in the seas and oceans. They originate from seismic waves that are converted in part into acoustic waves, which in turn are redirected by irregular geometric features in such a way that they propagate horizontally in the ocean. The role of bathymetry in this process is crucial, implying that the observed signals are affected by 3-D effects (Talandier & Okal [1979]; Graeber & Piserchia [2004]; Chapman & Marrett [2006]; Bohnenstiehl [2007]; Chapman & Marrett [2007]; Heaney & Campbell [2016]; Heaney et al. [2017]). Nevertheless, we quickly realized that full-wave ocean acoustics in the time domain is still in its early stage. Therefore, much remains to be learned from 2-D numerical simulations before having to deal with growing complications stemming from 3-D models (model meshing in particular, and extremely high computational cost). We nonetheless attempted 3-D simulations at some point in this thesis, however not very successfully; this attempt is reported in Appendix B.

2. Sensitivity of T-waves to the source radiation pattern

This topic has been addressed by Balanche et al. [2009] and Jamet et al. [2013], who discussed the effects of the source radiation pattern on T-wave structure. Some qualitative results were obtained

based on 2-D Cartesian simulations. Although interesting, these simulations did not provide quantitative results because the radiation pattern and geometrical spreading of a source in 2-D Cartesian coordinates cannot properly describe 3-D situations. Using 2-D axisymmetric simulations might be a solution. However, even if the geometrical spreading in axisymmetric geometries is 3-D, it requires the source radiation pattern to be axisymmetric too, which makes the correct study of the influence of source characteristics on T-waves more complicated.

3. Localization of earthquakes from T-phases

Accurately locating a source from T-phases remains a challenging issue for the study of remote earthquakes in oceanic environments. Does the transmission point location found by simple triangulation always match the epicenter of the earthquake? Which part of the signal should be used for triangulation: first arrivals, maximum energy pick or the entire envelope (Yang & Forsyth [2003])? Although we did not address this topic in this PhD work, it would definitely deserve a numerical study.

4. Influence on T-waves of the variations with range of the acoustic properties of the ocean

Typical of ocean currents, gyres, eddies or fronts for example, range-dependent sound-speed oscillations from internal waves cause sound scattering effects that cannot be explained in the framework of normal-mode theory. The problem is not specific to T-waves and has been the subject of numerous studies in ocean acoustics (for example Lichte [1919]; Foreman [1983]; Scully-Power & Stevenson [1985]; Desaubies et al. [1986]; Schmidt et al. [1995]; Colosi & Flatté [1996]; McDonald [1996]; Brekhovskikh & Godin [1999]; Gavrilov & Mikhalevsky [2001]; Spiesberger [2007, 2010]; Hegewisch & Tomsovic [2011]). This topic, although interesting, was considered less crucial and was thus not addressed in this thesis.

5. Inversions

Inverting for the source properties or the acoustic properties of the ocean from recorded T-phases would be of great interest. Although all the necessary tools are already available in our software package SPECFEM because they have been developed for other projects in the past (Favier et al. [2004]; Xie et al. [2014]; Monteiller et al. [2015]; Wang et al. [2016]; Komatitsch et al. [2016]) we decided to favor parametric studies rather than inversions to begin the exploration of the phenomenon in the time domain. It seemed important to us to start working with forward simulations on different types of models before maybe going into inverse problems in future work.

Résumé des recherches effectuées, ou non effectuées, dans cette thèse

Ceci est une version en français de l'introduction précédente en anglais.

Les ondes T

Dans le domaine de l'acoustique sous-marine, les ondes T ont été beaucoup étudiées. Le terme "onde T" a parfois été utilisé en référence à des phénomènes et des contextes d'observation variés. Afin d'éviter toute confusion, il nous a paru important de fixer une bonne fois pour toutes la définition utilisée dans le contexte de notre travail.

Selon notre définition, une onde T est un signal acoustique, généré à la suite d'un événement sismique et qui voyage horizontalement dans l'eau de mer à la vitesse du son

Cette définition, qui peut sembler assez floue, nous semble la plus adaptée ; comme nous le verrons dans ces pages, ces ondes ne peuvent être décrites dans toute leur diversité par un mode de propagation ou par des propriétés de dispersion par exemple. Notons surtout le terme "événement sismique" qui s'applique aussi bien aux tremblements de terre qu'aux sources sismiques d'origine humaine, mais pas aux explosions sous-marines par exemple. En effet, certains auteurs parlent d'ondes T pour évoquer des signaux générés dans l'eau par n'importe quel mécanisme (Shapira [1981]; Cansi & Bethoux [1985]; Okal & Talandier [1986]; Koyanagi et al. [1995]; Piserchia et al. [1998] par exemple). Soulignons également que nous n'avons pas introduit de distance de propagation. Nous appellerons aussi bien "onde T" un signal enregistré à 150 km qu'à 15000 km de la source, du moment qu'il s'est propagé globalement à plus ou moins 1500 $m.s^{-1}$.

Pour rester dans le vocabulaire, nous pouvons noter que le terme "phase T" apparaît également dans la littérature. Onde T et phase T sont souvent utilisés indifféremment. Dans ce document nous utiliserons parfois également le terme phase T, mais seulement quand nous ferons référence à un signal enregistré et non au phénomène physique en soi.

La Figure A illustre la génération des ondes T par les tremblements de terre. Un tremblement de terre, l'éruption d'un volcan ou l'explosion d'une bombe atomique, génèrent des ondes sismiques. On distingue les ondes de compression (ondes "P", comme Pression ou comme Premières, appelées aussi ondes sonores), les ondes de cisaillement (ondes "S" comme cisaillement, "Shear" en anglais,

ou Secondes) et les ondes de surface. Quand un événement sismique a lieu à proximité d'un bassin océanique, une partie de l'énergie produite peut se retrouver canalisée dans la couche d'eau et voyager ensuite horizontalement dans ce guide d'onde naturel à la vitesse du son dans l'eau. Ce sont ces ondes guidées que l'on appelle les ondes T. Elles ont des fréquences typiquement situées dans la bande de fréquence allant de 1 à 100 Hz. La conversion en ondes T des ondes sismiques peut se faire principalement de deux façons : par réflections successives entre la surface de la mer et un fond marin en pente, ou bien par diffraction sur une rugosité ou des hétérogénéités. Chaque mode de conversion a ses spécificités. Une fois canalisées dans la couche d'eau, les ondes T peuvent s'y propager particulièrement loin, et ce pour plusieurs raisons. Tout d'abord, en se propageant dans l'océan, elles possèdent une divergence géométrique cylindrique, ce qui provoque moins de pertes que pour une divergence sphérique en espace libre comme pour les ondes P et S (voir Fox & Dziak [1998]). De plus, l'atténuation des ondes acoustiques dans l'eau est particulièrement faible aux fréquences concernées. Enfin, il faut également mentionner que grâce au fait que la température et la pression varient avec la profondeur, la vitesse des ondes sonores dans l'océan présente un minimum typiquement aux alentours de 1000 m dans l'atlantique. Cette particularité, connue sous le nom de canal SOFAR, permet dans certaines conditions d'améliorer encore la transmission d'énergie. Les ondes T peuvent donc se propager sur des distances très grandes, en pratique uniquement limitées par la taille des bassins océaniques (voir Okal & Talandier [1997]; Metz et al. [2016] par exemple). Un événement sismique de taille même modérée peut ainsi être détecté à des milliers de kilomètres s'il a généré des ondes T. Ainsi, le seuil de détection des événements peut être amélioré d'un à deux ordres de grandeur en utilisant quelques instruments installés en mer (hydrophones ou OBS) plutôt que de grands réseaux sismiques terrestres (Johnson & Northrop [1966]; Fox et al. [1994]; De Groot-Hedlin et al. [2004]; Pan & Dziewonski [2005]; Dziak et al. [2011]). Notons malgré tout que ces instruments posent d'autres problèmes liés par exemple à leur localisation (pour leur maintenance par exemple) ou à la transmission des données enregistrées.

Après leur parcours océanique, les ondes T ont donc toutes les chances d'atteindre les côtes. À l'arrivée sur un talus continental elles se convertissent en ondes sismiques détectables par les sismomètres situés à l'intérieur des terres, même exceptionnellement par ceux installés très loin de la façade littorale (Tolstoy & Ewing [1950]; Båth & Shahidi [1971]; Cansi & Bethoux [1985]; Cook & Stevens [1998]; Stevens et al. [2001]). Bien qu'inoffensives, les ondes T peuvent parfois être ressenties par les populations côtières (Talandier & Okal [1979]; Leonard [2004]). Comme le son voyage plus lentement dans l'eau que dans le sol, les ondes T converties arrivent typiquement après les ondes de compression (ondes P) et de cisaillement (ondes S) d'où leur nom "T" comme Troisième. La Figure B montre un exemple typique de sismogramme d'onde T enregistré en Sicile suite à un tremblement de terre de magnitude $M_w = 4.7$ s'étant produit sur la côte ouest grecque. Dans cet exemple les trois arrivées P, S et T sont clairement visibles. Cependant, dans de nombreux cas, comme par exemple pour les petits séismes le long des dorsales océaniques, seules les ondes T sont détectées. Elles sont alors le seul élément d'information disponible (voir par exemple Fox et al. [1994]). Les ondes T sont donc utilisées dans de nombreux domaines des géosciences. Depuis les années 1960, des milliers d'ondes T ont été enregistrées et leurs sources de création localisées (voir Johnson [1966]; Duennebier & Johnson [1967]; Fox et al. [2001]) et des algorithmes existent pour les répertorier automatiquement (Sukhovich et al. [2014]). Bien que la localisation de la zone de conversion soit parfois délicate, ces relevés ont permis notamment d'identifier des éruptions volcaniques (Dietz & Sheehy [1954]; Norris & Johnson [1969]; Talandier & Okal [1987a]; Schreiner et al. [1995]; Fox & Dziak [1998]; Bohnenstiehl et al. [2013]) ou de suivre en temps réel des processus éruptifs (Fox et al. [1995]; Dziak et al. [2011]). Ces détections ont donc contribué grandement à notre compréhension des procédés hydrothermaux et microbiens au niveau des dorsales océaniques (Delaney et al. [1998]; Cowen et al. [2004]; Wilcock et al. [2014]). Les ondes T sont également très utiles pour la détection des tremblements de terre intra-plaques tectoniques de faible amplitude dans les régions très éloignées (Fox et al. [2001]), pour l'étude de l'expansion des fonds océaniques ou bien de l'intrusion du magma au niveau des dorsales océaniques (Hammond & Walker [1991]; Fox et al. [1994]; Schreiner et al. [1995]; Blackman et al. [2000]). Autant de phénomènes qui

affectent l'océan et les écosystèmes marins (Dziak et al. [2011, 2012]).

Dans le cas des grands séismes en région océanique, les ondes T reçues peuvent être utilisées en complément des ondes P et S pour cartographier les différentes composantes de la rupture de la faille concernée (voir Graeber & Piserchia [2004]; De Groot-Hedlin [2005]; Guilbert et al. [2005]; Tolstoy & Bohnenstiehl [2005, 2006]). De plus, certains liens entre les ondes T et les tsunamis sont désormais avérés et pourraient être potentiellement utilisés dans le cadre d'un programme d'alerte aux tsunamis (Ewing et al. [1952]; Tolstoy & Bohnenstiehl [2006]; Salzberg [2008]). Pour finir, les signaux acoustiques enregistrés dans les océans sont utilisés depuis plusieurs années pour faire la distinction entre les sources anthropiques telles que les explosions nucléaires et naturelles telles que les volcans, en particulier dans le cadre du Traité d'interdiction complète des essais nucléaires (TICE) adopté par l'Assemblée Générale des Nations Unies en 1996 (voir De Groot-Hedlin & Orcutt [1999, 2001c]). En effet, bien que facilement détectables à partir des ondes de surface, les explosions nucléaires ne génèrent que de faibles ondes P et S, notamment parce que la source est localisée très près de la surface de la Terre (voir Adams [1979]). Les signaux des ondes T peuvent également fournir des informations sur les mécanismes des tremblements de terre qui les ont générés (Dziak [2001]; Talandier & Okal [2016]), sur les caractéristiques sismiques superficielles des régions côtières (Koyanagi et al. [1995]; Kosuga [2011]) ou sur la structure profonde de la zone Wadati-Benioff (Okal [2001b]). Dans le futur, les ondes T pourraient également être utilisées pour étudier les variations méso-échelle des propriétés de l'océan (Evers & Snellen [2015]).

À l'interface entre la sismologie et l'acoustique sous marine, le phénomène des ondes T met en jeu des procédés complexes et variés dont les mécanismes sont actuellement mal connus, ce qui limite les possibilités d'analyse théorique approfondie. On peut évoquer la viscoélasticité, les conversions sismiques vers acoustiques et acoustiques vers sismiques, la diffraction, la propagation guidée dans l'océan, les fréquences élevées, les effets 3-D, ou les géométries complexes. Dans ce contexte il est encore difficile d'évaluer correctement l'influence des caractéristiques du séisme, du fond marin ou de l'océan par exemple. Ces problématiques restent en grande partie ouvertes de nos jours. Le spectrogramme présenté dans la Figure B est caractéristique et montre que globalement les ondes T ont un contenu fréquentiel bien plus élevé que les ondes P et S qui les précédent. En effet, les hautes fréquences sont moins atténuées lors d'une propagation dans l'océan que lors d'une propagation dans la croûte et le manteau terrestre. Cette caractéristique est intéressante car la partie haute fréquence du spectre est sensible à la structure fine du séisme, de l'océan et du fond marin et est absente ou fortement réduite dans les sismogrammes des ondes P et S à longue distance. De ce fait, une plus grande quantité d'informations sont potentiellement contenues dans les ondes T que dans les ondes P et S, et celles-ci peuvent être détectées de très loin (voir Dziak et al. [2004a]). On ne sait malheureusement pas aujourd'hui comment bien utiliser cette information. Comme dans beaucoup d'autres domaines de recherche, la simulation numérique semble donc être une approche appropriée et prometteuse pour l'étude des ondes T.

Sondage de sédiments à partir d'aéronefs

On sait depuis de nombreuses années que le son des gros avions est détectable sous la surface de l'océan (Urick [1972]; Medwin et al. [1973]; Richardson et al. [2013]). Plus récemment, Buckingham et al. [2002a,b] ont effectué des expériences avec un avion à hélice léger volant à basse altitude (semblable à celui illustré sur la Figure C) afin de déterminer si le son d'une telle source volante pouvait être utilisé pour déterminer les propriétés acoustiques du fond marin en eau peu profonde. Les auteurs ont montré que le son de l'hélice est détecté non seulement par un microphone dans l'air et par des hydrophones dans l'eau, mais aussi par un instrument enterré à environ 1 m de profondeur dans les sédiments. Les signaux reçus présentent un important décalage Doppler provoqué par le mouvement de l'avion.

Il est facile de voir que l'amplitude d'un tel changement de fréquence dans le fond marin dépend de la vitesse du son. Des études ultérieures (Buckingham [2003]; Buckingham & Giddens [2006]) ont permis d'approfondir la compréhension physique du phénomène. Ces travaux ont ouvert la voie à l'inversion des modes Doppler associés à chaque harmonique afin d'estimer la vitesse du son dans les sédiments mais aussi les autres paramètres géoacoustiques (vitesse des ondes de cisaillement, porosité, densité et granulométrie) et cela même en n'utilisant que des récepteurs placés dans l'eau. Pour ces inversions, le son des avions légers s'avère contenir des harmoniques de basse fréquence (jusqu'à ∼80 Hz) dont l'intensité ne varie que faiblement sur toute la plage angulaire (Buckingham et al. [2006]). Cette technique inhabituelle d'inversion acoustique est connue sous le nom de spectroscopie Doppler géoacoustique (Buckingham [2010]). Récemment, Bevans & Buckingham [2017] ont présenté une autre technique originale utilisant un hélicoptère léger volant à basse altitude et une procédure d'inversion utilisant la fonction de cohérence de l'onde latérale générée à l'interface océan-sédiment. Le son produit par les rotors a une largeur de bande de fréquence encore plus grande que celle du bruit des hélices des avions, riche en basses fréquences (à partir d'environ 13 Hz et jusqu'à 2,5 kHz) et il constitue donc une excellente source sonore basse fréquence. De plus, la nouvelle technique d'inversion semble plus efficace que la spectroscopie Doppler géoacoustique parce qu'elle utilise tout le spectre de fréquences. Cette méthode est donc plus adaptée aux environnements bruyants. Pour ce genre de méthodes il est possible de construire des modèles mathématiques pour des milieux fluides stratifiés. Cependant, dès que la complexité augmente (pentes, élasticité, rugosité...) l'analyse théorique devient particulièrement ardue. Là encore les méthodes numériques peuvent être d'une grande utilité.

Les supercalculateurs, le Calcul Haute Performance (HPC) et les méthodes numériques

Comprendre, prévoir, imager. La simulation numérique est maintenant l'un des piliers de la science, aux côtés de l'observation, l'expérimentation et la théorie. Elle est maintenant essentielle à l'étude de la plupart des systèmes complexes. Dans ce contexte, les méthodes numériques et les supercalculateurs sont incontournables pour toutes les applications nécessitant une très grande puissance de calcul, telles que les prévisions météorologiques ou climatiques, l'aérodynamique, la sismique et la sismologie, la chimie moléculaire, la génétique, l'astrophysique, la cryptanalyse, les finances et assurances, etc. Ces approches sont connues sous l'acronyme anglais HPC (Calcul haute performance). Le lecteur trouvera par exemple dans Nagel et al. [2018] un tour d'horizon complet. Il convient également de citer l'article de Gropp & Sterling [2015] sur l'évolution future du HPC. Depuis les années 1960 et l'apparition des premiers supercalculateurs, la puissance de calcul des plus gros ordinateurs à haute performance est passée de 10^6 à 10^{17} Flop/s (opération en virgule flottante par seconde) suivant une loi exponentielle quasi parfaite (voir Figure D). Cette loi prévoit par exemple qu'en 2020 environ la première machine exascale/exaflops (10^{18} Flop/s) apparaîtra quelque part dans le monde (ligne orange). Plus important encore, ce chiffre montre qu'il faut seulement environ neuf ans pour passer du plus gros supercalculateur du monde à une infrastructure régionale ou locale de même puissance accessible à un très grand nombre de chercheurs. La tendance devrait se poursuivre. Ces dernières années, le parallélisme intra-nœud sur les supercalculateurs n'a cessé de s'améliorer, soit en raison du nombre croissant de cœurs disponibles sur les processeurs CPU, soit en raison des unités de calcul telles que les cartes graphiques GPU (Graphics Processing Unit computing) ou les accélérateurs de type Intel (Intel Xeon Phi, Intel Many Integrated Core Architecture "Knights Landing" c'est-à-dire MIC KNL). Nous pouvons donc prédire avec une certaine confiance que les méthodes les plus coûteuses actuellement deviendront la norme dans un avenir pas trop lointain et assez bien déterminé, car les machines pour les utiliser deviendront très probablement largement disponibles.

Pour cette thèse, nous nous intéresserons à la propagation des ondes acoustiques dans les milieux complexes. Dans ce domaine l'évolution des supercalculateurs a permis l'émergence des méthodes dites

"en forme d'onde complète" dont l'utilisation, il y a une dizaine d'années, se limitait encore au niveau mondial à quelques laboratoires seulement en raison de leur coût. Ces méthodes ont l'avantage de discrétiser directement les équations fondamentales de l'élastodynamique sans introduire d'approximation supplémentaire, au prix bien entendu d'un coût de calcul important. Elles sont donc typiquement utilisées lorsque les problèmes exigent une grande précision et que l'on peut se permettre de payer un tel coût de calcul. Ces méthodes ont pour la plupart commencé à se développer dans les années 1970 pour répondre notamment aux besoins de l'industrie pétrolière, qui s'est depuis toujours intéressée aux méthodes sismiques pour la détection des réservoirs de pétrole ou de gaz. Des méthodes de différences finies ont d'abord été développées (Alterman & Karal Jr [1968]; Boore [1972]; Kelly et al. [1976]; Virieux [1986]; Levander [1988]). Concernant la discrétisation spatiale, des méthodes variationnelles ont commencé à émerger à la même période (Lysmer et al. [1972]; Strang & Fix [1973]), notamment parce qu'elles limitent les problèmes d'instabilités numériques et permettent de traiter facilement les milieux hétérogènes et les conditions aux limites. Un grand nombre de ces méthodes par éléments finis (FEM) sont alors apparues. Parmi les plus utilisées aujourd'hui, on peut citer la méthode des éléments finis spectraux que nous avons utilisée dans cette thèse (SEM, Seriani & Priolo [1994]; Komatitsch & Vilotte [1998] ; Cohen & Fauqueux [2000]; Bécache et al. [2000]; Jenkins et al. [2002]), les méthodes de Galerkin discontinues (Rivière & Wheeler [2003]; Chung & Engquist [2006]; Grote et al. [2006]; Käser & Dumbser [2006]; Käser & Dumbser [2008]), et dans une moindre mesure la méthode des volumes finis (Dormy & Tarantola [1995]; Dumbser et al. [2007]). Ces méthodes sont progressivement devenues incontournables dans le domaine de la sismologie tant à l'échelle de l'ensemble de la Terre qu'à l'échelle régionale (Tromp et al. [2008]; Gokhberg & Fichtner [2016]; Monteiller et al. [2015]; Wang et al. [2016]). Dans le domaine de l'acoustique sous-marine cependant, l'utilisation des méthodes en forme d'onde complète reste encore limitée. En effet, les problèmes qui y sont étudiés, tels que les ondes T ou la spectroscopie Doppler géoacoustique, impliquent typiquement des fréquences très élevées et sur de grandes distances de propagation, ce qui rend actuellement ce genre d'approches souvent inaccessibles car trop coûteuses. L'évolution des moyens informatiques est aujourd'hui en train de changer rapidement cette situation et ouvre un champ d'étude très important (voir par exemple Isakson & Chotiros [2011]; Cristini & Komatitsch [2012]; Jamet et al. [2013]; Bottero et al. [2016a]; Isakson [2018]). Avec cette thèse nous souhaitons aller dans cette même direction et participer aux efforts de la communauté scientifique dans ce domaine. La méthode numérique qui sera utilisée est basée sur les éléments spectraux (SEM). La SEM est une méthode de Galerkin continue, qui peut facilement être rendue discontinue si nécessaire ; elle est alors proche d'un cas particulier de la méthode de Galerkin discontinue, avec une efficacité optimisée grâce à ses fonctions de base tensorisées. En particulier, elle peut fonctionner avec précision sur des maillages très déformés. La méthode des éléments finis spectraux a de très bonnes propriétés de précision et de convergence. Elle a une convergence quasi-spectrale et permet d'exploiter des schémas de convergence de type hp (haut degré polynomial pour les bases de fonctions, et maillage de densité moyenne). Elle est également très bien adaptée au calcul parallèle sur de très gros supercalculateurs ainsi que sur des clusters de cartes graphiques GPU. La SEM peut également traiter des éléments triangulaires (en 2-D) ou tétraédriques (en 3-D) ainsi que des maillages mixant les deux, bien qu'avec un coût accru et une précision réduite pour ces éléments, comme d'ailleurs dans la méthode Galerkin discontinue (voir les nombreuses références sur ces différents points dans Komatitsch [2018]).

Ce qui a été abordé dans la thèse

La thèse est composée de six chapitres combinant observations, simulations et développement d'outils numériques. Le premier chapitre contient un historique thématique de la littérature sur les ondes T, la littérature disponible couvrant 90 ans de recherches, des premières observations jusqu'aux simulations numériques actuelles. Ce travail de documentation est suivi par une étude de données faite en col-

laboration avec le Dr. Emanuele Casarotti à l'Istituto Nazionale di Geofisica e Vulcanologia (INGV, Institut national de Géophysique et de Volcanologie) de Rome en Italie (Chapitre 2), dans laquelle nous avons analysé des sismogrammes enregistrés en Sicile et en Calabre à la suite de tremblements de terre survenus près de la côte ouest de la Grèce. Cela nous a amené à identifier des tendances générales sur la génération et la propagation des ondes T dans cette région. Afin de modéliser le phénomène nous avons alors développé un solveur éléments spectraux axisymétriques (2.5-D) dans le domaine temporel, que nous présentons et validons dans le Chapitre 3. Cet outil nous a ensuite permis de reproduire numériquement un des séismes grecs étudiés ainsi que la propagation des ondes T jusqu'en Sicile, puis de comparer les données avec les résultats numériques et de déterminer les paramètres physiques les plus importants rentrant en jeu dans ce cas (Chapitre 4). Nous avons également tenté de faire des simulations 3-D, mais nous n'avons pas réussi à générer un maillage approprié. Cette tentative infructueuse est décrite dans l'annexe B. Le Chapitre 4 contient quant-à-lui une étude paramétrique en deux temps de l'influence de la pente du plancher océanique dans un scénario typique de génération/conversion d'une onde T. Dans un premier temps, nous étudions la quantité d'énergie acoustique canalisée à partir d'un séisme profond sous un fond marin incliné. Nous modélisons ensuite la réflexion/transmission d'une onde guidée sur une côte. L'influence des propriétés de la couche d'eau et des sédiments marins est discutée. Le Chapitre 5 décrit une procédure pour le calcul de cartes de perte de transmission et de dispersion à partir de simulations numériques en forme d'onde complète effectuées dans le domaine temporel. Nous utilisons ensuite ces cartes pour étudier l'efficacité du canal SOFAR en termes de canalisation de l'énergie en fonction du profil de vitesse dans l'eau, du type de source, et de la nature du fond marin. Pour finir, le Chapitre 6 présente et valide une méthode numérique basée sur les éléments spectraux dans le domaine temporel pour modéliser en forme d'onde complète le champ acoustique crée par une source en mouvement. La méthode est appliquée à la spectroscopie Doppler géoacoustique des sédiments marins. Nous proposons également à la fin de ce chapitre un nouveau mécanisme de génération d'ondes T ainsi qu'une explication alternative aux ondes observées par Evers et al. [2014] en mer et dans l'atmosphère à suite d'un tremblement de terre de 2004 dans la dorsale de Macquarie.

Ce qui n'a pas été abordé dans cette thèse, mais qui aurait pu l'être

1. Effets 3-D

Les ondes T se propagent dans les mers et les océans. Elles proviennent d'ondes sismiques qui sont converties en ondes acoustiques, lesquelles sont à leur tour redirigées par les structures géométriques irrégulières de telle sorte qu'elles se propagent horizontalement dans l'océan. Le rôle de la bathymétrie dans ce processus est crucial et suggère que les signaux observés sont affectés par des effets 3-D (Talandier & Okal [1979]; Graeber & Piserchia [2004]; Chapman & Marrett [2006]; Bohnenstiehl [2007]; Chapman & Marrett [2007]; Heaney & Campbell [2016]; Heaney et al. [2017]). Néanmoins, nous nous sommes vite rendu compte que l'acoustique sous-marine dans le domaine temporel n'en était encore qu'à ses débuts et que de ce fait beaucoup restait encore à apprendre de simulations numériques 2-D avant d'avoir à faire face aux grandes complications techniques apparaissant dans le cas de modèles 3-D (maillage précis de ces modèles en particulier, et coût de calcul extrêmement élevé). Néanmoins, au cours de la thèse comme mentionné ci-dessus nous avons tenté quelques simulations en 3-D, et cette expérience est décrite dans l'annexe B.

2. Sensibilité des ondes T au diagramme de rayonnement de la source

Ce sujet a été abordé par Balanche et al. [2009] et Jamet et al. [2013], qui ont discuté les effets du diagramme de rayonnement de la source sur la structure des ondes T. Des résultats qualitatifs ont été obtenus à partir de simulations Cartésiennes 2-D. Bien qu'intéressantes, ces simulations ne fournissent pas de résultats quantitatifs car le diagramme de rayonnement et la divergence géométrique d'une source

en coordonnées Cartésiennes 2-D ne peuvent pas décrire correctement la réalité 3-D. L'utilisation de simulations axisymétriques bidimensionnelles pourrait être une solution. Cependant, même si la divergence géométrique est 3-D en géométrie axisymétrique, il faut également que le diagramme de rayonnement de la source soit également axisymétrique. Cela rend pour l'instant compliquée l'étude correcte de l'influence des caractéristiques des sources sur les ondes T.

3. Localisation des tremblements de terre à partir d'ondes T

Localiser avec précision une source à partir d'ondes T reste un défi pour l'étude des tremblements de terre éloignés en milieu océanique. L'emplacement du point de conversion obtenu par simple triangulation correspond-il toujours à l'épicentre du séisme ? Et quelle partie du signal devrait être utilisée pour la triangulation : les premières arrivées, le pic d'énergie ou l'enveloppe entière (Yang & Forsyth [2003]) ? Bien que nous n'ayons pas abordé ce sujet dans notre travail, il mériterait certainement une étude numérique dans le futur.

4. Influence des variations des propriétés acoustiques de l'océan le long du trajet de propagation des ondes T

Typiques des courants océaniques, des gyres, des tourbillons de turbulence ou des fronts par exemple, les oscillations de la vitesse du son dues aux ondes internes provoquent des effets de diffusion du son qui ne peuvent pas être expliqués dans le cadre de la théorie des modes normaux. Le problème n'est pas spécifique aux ondes T et a fait l'objet de nombreuses études en acoustique sous-marine (voir par exemple Lichte [1919]; Foreman [1983]; Scully-Power & Stevenson [1985]; Desaubies et al. [1986]; Schmidt et al. [1995]; Colosi & Flatté [1996]; McDonald [1996]; Brekhovskikh & Godin [1999]; Gavrilov & Mikhalevsky [2001]; Spiesberger [2007, 2010]; Hegewisch & Tomsovic [2011]). Ce sujet, bien qu'intéressant, a donc été considéré comme moins crucial et n'a pas été abordé durant la thèse.

5. Inversions

L'inversion des propriétés de la source ou des propriétés acoustiques de l'océan à partir des ondes T serait d'un grand intérêt. Bien que tous les outils nécessaires soient déjà disponibles dans notre logiciel SPECFEM en raison de leur développement dans le contexte d'autres projets (Favier et al. [2004]; Xie et al. [2014]; Monteiller et al. [2015]; Wang et al. [2016]; Komatitsch et al. [2016]), nous avons décidé, dans un premier temps, de privilégier les études paramétriques plutôt que les inversions pour commencer l'exploration des phénomènes étudiés dans le domaine temporel. Il nous a semblé important de commencer à nous forger une opinion grâce à des simulations directes sur différents types de modèles avant de nous lancer éventuellement dans l'étude de problèmes inverses dans le futur.

Chapter 1

History of research on T-waves

In this chapter we will recall how T-waves have been discovered and used. Most of the analysis and affirmations here come from bibliographical search. In order to avoid the repetition of previous reviews I have tried to construct a personal view of previous works on T-waves. Let me of course cite the reviews of Okal [2001a, 2007, 2011a], which have all been very helpful.

1.1 First observations and research

T-wave identification and first research go back to the first decades of the 20th century, during the golden age of seismology. With the arrival of the first short period damped seismometers the prospects offered, notably for the study of the terrestrial structure, were large. The number of seismic stations recordings and seismologists to interpret them was rising sharply all over the world. The first documented observations of T-waves has been published in 1930 in a weekly science leaflet called The Volcano Letter made at the Hawaiian Volcano Observatory (Jaggar [1930]; Okal [2007]). Its founder, American volcanologist T.A. Jaggar, presented a seismogram recorded after a great Alaskan earthquake of October 1927. Richter scale did not yet exist but this earthquake magnitude was later rated as 7.1 (Mpas: Mpas: "Pasadena Magnitude" is described in Gutenberg & Richter [1954]. It is often the only available quantification information for non shallow earthquakes that occurred before the establishment in 1963 of the WWSSN, the first World-Wide Standardized Seismographic Network. Before that date there were only about 700 seismographic stations around the world, which were equipped with instruments of various types exhibiting different frequency responses (Okal [1992]).). After the main seismic waves arrivals the Bosch-Omori mechanical seismometer (period of 7 seconds, Okal [2001a]) recorded high frequency oscillations, later identified as corresponding to a T-phase, which were incorrectly interpreted as resulting from a local Hawaiian earthquake. Indeed, high frequencies were known to undergo more attenuation than low frequencies, which suggested that these observed oscillations were coming from a close source, such as a collapse or a slump, which could have been touched off by the predominant teleseismic waves. A few years later, a bulletin from the Berkeley university seismographic stations (Byerly & Wilson [1936]) also reported a “most peculiar” short-period phase, interpreted as of local origin, that would later prove to be a T-phase from an Hawaiian earthquake (Byerly & Herrick [1954]). At the same time, the Harvard university Seismograph Station bulletin Collins [1936] reported a T-phase as a third “unusual” arrival in a seismogram recorded in September 1935, following P and S waves[1]. This time the phase is just described as surprising and is not interpreted as a local arrival.

It is in Linehan [1940]) that the term “T”-phase (for Tertiary) was coined in the literature and that the phenomenon was clearly interpreted as originating from distant events. The author correctly

[1]We thank Prof. Miaki Ishii from Harvard University for providing us a copy of this hard-to-find bulletin.

picked T-phases on many seismograms from the Weston, Massachusetts observatory and set them apart as due to a single, but still unknown, propagation mechanism, remarking that they were not arriving as a function of P and S-waves arrival times. Linehan just offered speculation as to their nature, hence these late arrivals could not be interpreted using available travel time tables. That very same year Ravet [1940] independently came to the same conclusion while working on recordings of Aleutian earthquakes from Faiere Observatory, Tahiti. Ravet even interpreted the recorded waves as surficial and estimated their group velocity at 1500 m/s but did not relate this measurement to the speed of sound in water.

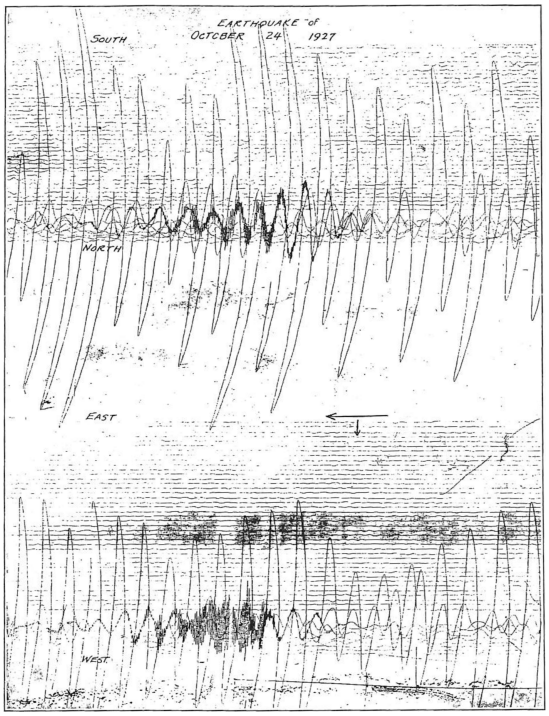

Figure 1.1 – Taken from Jaggar [1930]. First-ever published T-phase. The earthquake occurred a few miles offshore the Alaskan Pacific coast and was recorded in Hawaii. Up: north-south motion. Time goes from top to bottom and from left to right. Down: Same drawing but for east-west motion. The T-wave is the high frequency wave packet. It is visible on both seismograms. The horizontal arrow represents approximately 23 s.

With the development of active sonars during WWII, ocean acoustics made significant progress. The post-war article of Ewing et al. [1946] summarizes these results among which the most important might be the discovery of the deep sound channel for which the authors imagined many civilian applications such as naval communication, sandbanks localization or deep sea volcanism monitoring. They also described a potential maritime distress system called "SOFAR: SOund Fixing And Ranging" experimented even before the end of WWII by the U.S. Navy and that later gave its name to the deep sound channel. See the box below for the description and history of the SOFAR channel. Thereafter in their classical article Ewing & Worzel [1948], the authors described their deep water experiments of long range sound transmission and interpreted them with ray theory. In parallel, soviet ocean physicist Brekhovskikh [1949] was writing its own independent theory in the USSR. Note here that this theory predicts that a signal guided through the SOFAR channel by refraction of acoustic rays is supposed to exhibit low normal dispersion (Johnson & Norris [1968b]; Porter [1973]; Okal & Talandier [1986]).

These years also saw the publication of Pekeris [1948] who made considerable theoretical advances for modeling of sound propagation in the ocean. Using modal decomposition Pekeris described the wavefield created from a monochromatic submarine source in a simplified oceanic waveguide, which now carries his name, and which is made up of a fluid layer overlying a semi-infinite fluid bottom. His

work was quickly extended to handle elastic seabed by Press & Ewing [1950].

By using the new Pekeris framework to study coastal earthquakes, Press et al. [1950] together with Tolstoy & Ewing [1950] introduced a temporary little confusion between the newly discovered T-waves and Airy waves.

Airy waves are predicted from Pekeris theory which, contrary to guided ray theory (Ewing & Worzel [1948]), predicts dispersive signals. They are associated with the minimum group velocities of each propagative mode. Therefore it exists one Airy wave for each mode. As T-waves, they result from a conversion from seismic to acoustic energy, they are theoretically high frequency waves propagating in the water layer, however they travel with a velocity of ~ 0.7 the speed of sound in water, they are supposed to be quickly attenuated, they always come with quicker wave packets and, more importantly, they can only be generated following very shallow earthquakes (Press uses the term seaquakes). Nevertheless, and for the first time, the authors claimed that T-waves corresponded to short-period compressional waves traveling through the water.

All in all, Tolstoy & Ewing [1950] can be seen as the first comprehensive work about T-waves for several reasons. Indeed by documenting several Atlantic and Pacific T-phases recorded in the USA the authors brought strong evidence on the nature of T-waves. Even if they kept focusing on the Airy phase they also suggested other seismic to acoustic conversions, foreseeing, for deep earthquakes, the possibility of T-waves generation by scattering on rough seabed or by downslope conversion (both described below), and also identifying the basis of acoustic to seismic conversion of T-waves at shores. They also showed an uncommon T-phase measured 700 km inland from the shore line and supposed that T-waves could be used to locate earthquake more precisely because of their low velocity compared to the velocity of seismic waves. They also made an interesting statement that is worth citing: "The short-period phase predicted by the normal-mode theories of Pekeris [1948] and Press & Ewing [1950] assumes a constancy of velocity with depth in the ocean and can also account for a T-phase with periods of one second or less. It is uncertain whether sound-channel propagation or normal-mode propagation is principally responsible for the T-phase." We will come back to that important remark in the section 1.5, indeed the two theories can explain long distance acoustic energy propagation, which can lead to confusion. The authors finally suggested that these waves could perhaps be used for the prevention of tsunamis, which gave rise to a long series of controversies to which we shall return later. Finally, as would be done routinely thereafter, Tolstoy & Ewing [1950] suggested that a hydrophone moored into the SOFAR channel may record many T-waves.

Likewise, the interpretation of T-waves as propagating in the water column failed to gain unanimous support among the community at the time. The works of Tolstoy and Ewing were criticized very strongly by Leet, Linehan and Berger (Leet et al. [1951]) in particular, who considered that the phenomenon was due to shear wave propagation in the sedimentary layer at the bottom of the oceans, an idea already expressed by Coulomb & Molard [1949]. On his side, Biot [1952] considered that T and Stoneley-Scholte interface waves (Stoneley [1924]; Scholte [1947]) may have similar dispersion curves at high frequency and suggested that a coupling effect may exist between the two types of waves.

However, Ewing et al. [1952] later provided additional evidence that T-waves were propagating in the water body of the oceans. The authors presented numerous signals of better quality and exhibiting limited, if any, inland propagation. Moreover the sources were known more precisely, reducing the uncertainties. Part of the data were recorded at sea, which constitutes, to the best of our knowledge, the first published T-phases recorded with hydrophones. These instruments would subsequently become the preferred means of recording T-waves. Ewing et al. [1952] measured the speed of 1.47 +/- 0.01 km/s in the Pacific ocean. In addition they documented a shadow effect of the islands on T-waves. Indeed, if an island is located between the earthquake and a hydrophone, they observed that the hydrophone did not record anything even if a signal have been recorded on the island. This constituted further evidence of the nature of T-waves. In their second article about T-waves, Coulomb & Molard [1952] made similar findings but highlighted the importance of S to T conversion, an observation shared a year later by Wadati & Inouye [1953], who published all the

observational data of T-phase obtained up to the date by the Japanese seismological network and also insisted on the role played by steep bottom slopes in seismic to acoustic conversion. In 1954 Båth [1954] showed the first observations of T-waves in Europe and in the polar region, where the SOFAR channel is known to be surficial in winter. His measurements confirmed the conclusions of Ewing et al. [1952] and were in agreement with the observations of Coulomb & Molard [1952] and Wadati & Inouye [1953] concerning the importance of steep bathymetry in the vicinity of earthquake epicenters in the generation mechanism of T-waves. Furthermore he showed the first observation of reflected T-waves and made the interesting observation that strong T-phases are recorded when the epicentral distance to the continental slope and the depth of the hypocenter are approximately the same, which later turned to be in agreement with ray-based modeling (Johnson et al. [1963]).

The advances made in the early 1950s on understanding T-wave phenomena led Dietz & Sheehy [1954] to the first teleseismic detection and identification of volcanic activity from hydroacoustic signals. The authors documented a deadly submarine volcanic eruption in Japan from signals recorded at a hydrophone moored off California. This probably constitutes the first result obtained through the record of T-waves. Let us cite here also the work of Shurbet [1955]; Shurbet & Ewing [1957] who published recordings of T-waves with very large continental path (up to 5600km) showing, in these exceptional cases, that only P waves (and sometimes surface waves) were likely to be transformed to T-waves and that the conversion took place at steep continental slopes. The large-scale program of hydrophone monitoring in the 1960s (see for example Johnson et al. [1963]; Johnson [1966]; Johnson & Northrop [1966]; Duennebier & Johnson [1967]; Johnson & Norris [1968a]; Northrop [1970]) ended the controversy about the nature of T-waves. Note also that Soviet researchers Solovyev Voronin and

Voronina published in 1967 a review on T-waves and tsunamis (Solovyev et al. [1968]).

The SOFAR channel

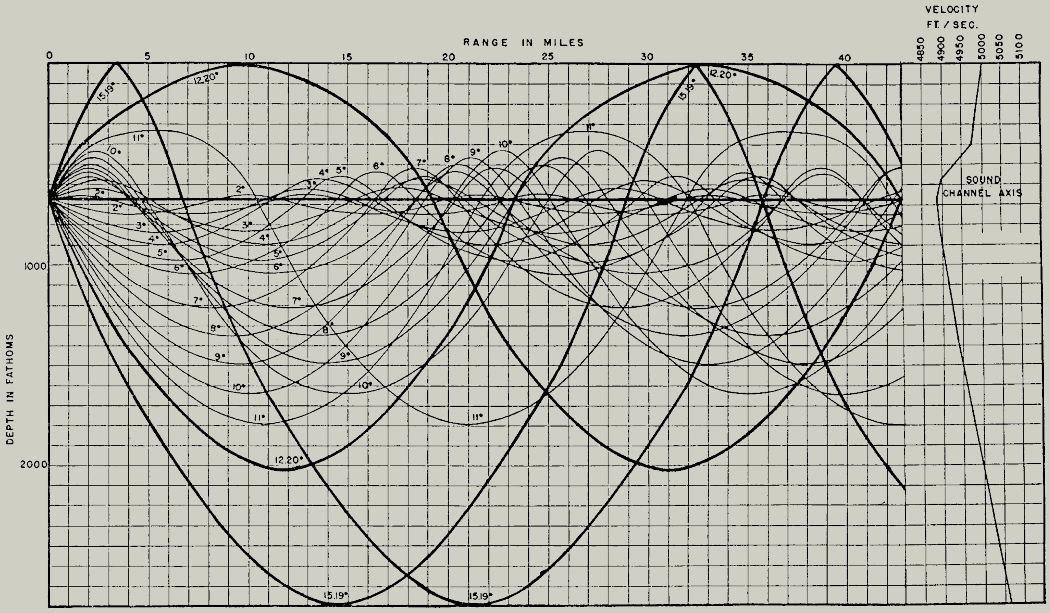

Figure 1.2 – Ray diagram for a typical Atlantic Ocean sound channel. The variation of sound speed with depth is shown on the right. Appart from guided rays the diagram also shows refracted surface-reflected rays. From Ewing & Worzel [1948].

The speed of sound in seawater has a nominal value of 1500 m.s^{-1} in temperate and equatorial oceans but has variations with depth explaining the existence of the SOFAR channel. When the hydrostatic pressure increases in a fluid the sound velocity also increases. Similarly when temperature decreases the sound velocity decreases and the compressibility increases, making it more sensitive to an increase in pressure. Due in particular to competition between these effects, sound speed in most parts of the deep ocean has a minimum at medium to shallower depth. A simple empirical expression for the variation of the sound speed c including the effect of salinity is due to Mackenzie [1981]:

$$c = 1448.96 + 4.591 \cdot T - 0.591 \cdot T - 0.05304 \cdot T^2 + 2.374 \times 10^{-4} \cdot T^3 + 1.340 \cdot (S - 35) + 0.0163 \cdot z \\ + 1.675 \times 10^{-7} \cdot z^2 - 0.01025 \cdot T \cdot (S - 35) - 7.139 \times 10^{-13} \cdot T \cdot z^3$$

Where T is temperature in degrees Celsius, S is salinity in parts per thousand, and z is depth in meters. This equation is valid for temperatures between -2°C and 30°C for all depths to 8000 m and for salinities between 25 and 40%. This particular shape of the sound speed profile with depth has an important influence on the propagation of sound in the ocean. Hence as a sonic wave propagates in an increasingly faster environment it is refracted back towards slower parts. Therefore if a sound source is close to the depth where the sound velocity is minimal, the waves generated, whether moving towards the seabed or the surface, can be refracted to their original depth, which they will cross before being refracted again. Thus, part of the energy will propagate, oscillating around the depth of minimum sound speed which can be seen as the axis of a "sound channel" in the deep ocean.

The SOFAR channel (continuation)

This natural waveguide is particularly efficient to transport over very large distance (>5000 km) acoustic signals with frequencies between ~2 Hz and ~500 Hz because it allows a portion of the waves to propagate with no interaction with the seafloor which is, at these frequencies, the main potential source of energy losses due to attenuation and scattering. This is the SOFAR channel. As an illustration, in the experiment of Ewing & Worzel [1948], no reflected sounds were detected over 300 km. It is important to note that the signals trapped in the channel have the characteristic of exhibiting low dispersion.
Note also that below ~1 Hz the waves cannot be trapped into the waveguide and that above 100 Hz the seawater viscoacoustic attenuation is not negligible anymore for long distance propagation (Francois & Garrison [1982]; Ainslie & McColm [1998]). The reader will find in Chapter 5 a study on the channeling efficiency of the SOFAR channel against range.
As can be expected, oceanographic parameters vary according to seasonal and geographical parameters. Consequently, the deep sound channel varies in depth and shape with time and location (Johnson & Norris [1968b]).
The deep sound channel was discovered and characterized independently twice in the 1940' by American scientists M. Ewing and J. Worzel following an experiment carried in the spring of 1944 (Ewing & Worzel [1948]) and by Soviet ocean physicist L. M. Brekhovskikh and his colleagues (Brekhovskikh [1949]) from offshore experiments in the sea of Japan carried by Rozenberg in 1946 (Rozenberg [1949]).

1.2 Downslope conversion

Research on T-waves in the late 1950s and the beginning of the 1960s had indicated that continental slopes were probably instrumental in the generation of T-phases (e.g. Tolstoy & Ewing [1950]; Ewing et al. [1952]). It was also noticed that many of the observed T-waves were generated by non-surficial earthquakes and exhibited low dispersion. These observations precluded their interpretation as Airy waves, as originally suggested. In his textbook on sound propagation in the ocean, Officer [1958] summarized the state of the art of American research of the last decade (Pekeris, Tolstoy, Ewing, Press...), propagation in the sound channel, rays, Pekeris waveguide and normal modes, and proposed an alternative model for the propagation of a SOFAR-guided ray across a sea bottom dipping up from source to receiver. A similar concept was used by Milne [1959] when comparing the spectra of an earthquake T-phase with similar signals coming from nuclear explosions, both recorded from a boat. Milne [1959] wrote that acoustic energy from a nuclear explosion "entered into deep water after first having been refracted into the Earth's crust and having undergone multiple reflections between the sea surface and its downsloping bottom", this reasoning allowing him to constrain the explosion location to the interior of an atoll. These early works allowed Johnson et al. [1963] to write the first article detailing a generation mechanism for T-waves generated by non-surficial earthquakes. That article proposes that seismic energy can be trapped into the SOFAR channel after successive reflections between a downsloping seafloor and the sea surface, allowing it to travel horizontally (see Figure A on page 12). This scenario, which they called downslope conversion, is based entirely on geometrical optics. Their model also suggests that the top of continental slopes would be more prone to generate T-waves than its bottom, and that steep slopes would favor strong T-waves by allowing the rays to be trapped into the SOFAR channel after few, if any, reflections. Thirty years later this concept have been investigated by Chiu [1994] in the modal framework and by Sperry et al. [1996] using a hybrid wave-number-integration approach.

1.3 Hydrophone arrays

The 60s have seen the operation of the Pacific Missile Range/Missile Impact Location System (PMR / MILS) by the Hawaiian institute of Geophysics. This hydrophone network consisted of instruments spread all over the Western Pacific to hear, originally, the impacts of missiles launched from Vanden-

berg Air Force Base in California. The sensors were installed in the ocean near Midway Island, Wake Island, Enewetak Atoll and Oahu. While the missiles crashed into the ocean they triggered a small explosive charge which was then recorded by the hydrophones in the network. By triangulation the military were then able to determine the point of impact and thus assess the accuracy of the missile (Walker [2001]). It was the first large hydrophone array operated by civilian researchers. With access to this new network, the team of the Hawaiian Institute of Geophysics, probably headed by D. A. Johnson at that time, was able to locate T-waves routinely. They have localized more than 20000 T-waves between 1964 and 1967 (see Johnson [1966]; Duennebier & Johnson [1967]). The amount of data collected was massive, and was useful to many researchers until the 1990s (for example Hammond & Walker [1991]; Walker & Bernard [1993]). Let us note here that this unprecedented monitoring led to the discovery of a submarine volcano at the end of the Austral Island chain (Norris & Johnson [1969]).

Subsequently, other hydrophone arrays were made available to scientific community. We can mention the northeast Pacific ocean and Atlantic ocean SOSUS hydrophones declassified in the 90s, which were operated by the U.S. Navy since the 1950s for antisubmarine warfare (Fox et al. [1994]; Slack et al. [1999]) and managed since then by the NOAA/Pacific Marine Environmental Laboratory, or the global IMS network installed in the early 2000s to monitor compliance with the Comprehensive Nuclear Test Ban Treaty as part of the International Monitoring System IMS to detect and locate events that generate hydroacoustic phases worldwide (De Groot-Hedlin & Orcutt [1999]). Let us also mention the French Polynesian Seismic Network, RSP (Talandier & Kuster [1976]), consisting of seismometers installed on Pacific islands and in use since the 1970s, and also the HUGO and H2O T-phase stations (Caplan-Auerbach & Duennebier [2001]; Chave et al. [2000]) operational from the 1990s to 2002, 2003.

1.4 Abyssal T-waves

In the 60s the operation of the PMR/MILS hydrophone network in the western Pacific allowed Johnson et al. [1967] to make interesting observations of the so-called abyssal T-waves that would after keep the researchers busy for a long time. Indeed, since their discovery T-phases have also been recorded at teleseismic or regional distance ($<$ 500 km) from earthquakes located far below smooth abyssal oceanic plains, apart from any significant bathymetric feature. If the hypocenter of an earthquake is not in the immediate viciniPty of the seabed, and is therefore not within the scope of Airy waves, other non geometrical processes are required to explain those waves. In such cases that cannot be explained by downslope conversion, geometrical optics asserts that the rays coming from the source cannot end-up guided by the SOFAR channel. In fact, due to the large velocity contrast between water and rock, Snell's law indicates that seismic energy generated by the earthquake must experience severe refraction toward vertical when crossing the seafloor interface to get into the overlying water column. Still, data shows that T-waves can be generated at the epicenter or close by and then travel horizontally at the speed of sound in water. More surprisingly, this remains true even when the seafloor is far below the conjugate depth (also called critical depth) below which ray theory predicts that no ray can be trapped into the sound channel (Williams et al. [2006]). Scattering was suspected to play a role in T-wave generation from deep earthquakes since the very first articles (for example Tolstoy & Ewing [1950]) but it is Johnson and his team who first detected (Johnson et al. [1963]) and described (Johnson et al. [1967]) the characteristics of abyssally-generated T-waves. Johnson et al. [1967] presented a meaningful illustration of the phenomenon. They showed the T-wave of a coastal, 23 km deep, earthquake exhibiting two distinct arrivals: a first arrival created by downslope conversion and an "abyssal" arrival. The signal showed that the abyssal wave arrived before the "downslope wave", indicating that abyssally-generated waves were less delayed than the waves generated by downslope conversion which suffer successive reflections. The authors suggested a simple theoretical model to

explain the observed increase in T-phase rise time with earthquake depth. The abyssal mechanism is documented to be of similar efficiency as the downslope generation mechanism at high frequency, although its efficiency decreases at low frequency (Duennebier [1968]). Moreover, compared to the impulsive downslope wave, the abyssal wave was of lower amplitude but with higher frequency content and exhibited an emergent wave train that is often described as "spindle shaped" in the literature. Johnson and his team first suggested that abyssal arrivals were due to scattering by reflection on the rough sea surface (Duennebier & Johnson [1967]) before highlighting also reflection scattering on a rough seabed (Johnson et al. [1967]; Johnson & Norris [1968a]), unlikely volume scattering on velocity inhomogeneities in the ocean, or a coupling phenomenon between SOFAR-channel waves and surface waves as suggested by Biot [1952], which, nevertheless, cannot explain the absence of low frequencies in the abyssal T-phase spectrum. Keenan & Merriam [1991] later added the possibility of generation by scattering under the ice-cap at the highest latitudes.

The mechanism responsible for abyssal T-waves remained uncertain for decades, and it was not until the late 1990s with the articles of De Groot-Hedlin & Orcutt [1999, 2001a] that a model capable of explaining the phenomenon gained some consensus in the community. As already succinctly suggested in Fox et al. [1994], the authors considered radiation of seismic waves energy at the seafloor interface. They assumed secondary point sources distributed over the seabed, and exciting low-order acoustic modes proportionally to the acoustic modal amplitude and also to the ground motion resulting from the earthquake evaluated at the local ocean depth. This way they modeled T-phase envelopes for intermediate depth earthquakes, which were found to be in good agreement with the measured ones. The remaining deviations are supposed to come from uncertainties in bathymetry, mode coupling and radiation effects. They also conjectured that scattering shall often be the predominant phenomenon compared to downslope conversion. Thus, even in the presence of a sloping seabed, T-waves created by scattering could be observed especially if the slope is moderate and the bottom is made of unconsolidated sediments. Indeed, their theory predicts that the excitation of T-waves mainly depends on depth rather than on slope at the vertical of the earthquake. It also predicts that abyssal T-wave are composed of high-order modes, a fact that was partly confirmed by observations (D'Spain et al. [2001]).

The same year, Park & Odom [1999] proposed a perturbation-based theory of elastic wave scattering from stochastic rough surfaces that they later successfully applied to abyssal T-waves modeling (Park et al. [2001]), illustrating the effect of seafloor roughness on their modal content for different seafloor geometries and source depths. By introducing mode coupling, their model explains the main characteristics of most T-waves, such as low dispersion (Okal & Talandier [1986]).

Odom & Soukup [2002, 2004] later showed that the scattering efficiency is improved with the presence of a sedimentary layer at the bottom of the ocean, covering the higher seismic velocity oceanic crust. Their analysis also predicts that normal-fault earthquakes are poor generators of T-waves, which is in agreement with the observations of Dziak [2001].

The simple model proposed by De Groot-Hedlin & Orcutt [1999, 2001a] allowed to explain T-waves due to earthquakes at depth of several tens of kilometers. However, in its initial form, it was not suitable for the shallow earthquakes studied by Yang & Forsyth [2003]. Indeed, it did not take into account the S-wave displacement field which was supposed to be of minor importance in the scattering generation process compared to the downslope conversion case. However, in the case of shallow and/or subduction earthquakes below rocky shores a P→T-phase and a S→T-phase are commonly observed (Talandier & Okal [1998]; Lin [2001]). Depending on the incidence angle of the seismic waves (Lin [2001]) the amplitude of S→T-waves is then often greater than that of P→T-waves[2]. In order to simulate T-waves generated by shallow earthquakes in regions with low sedimentary thickness, Yang & Forsyth [2003] extended the De Groot-Hedlin and Orcutt model by including the contribution of

[2]This is not true if the epicenter is at a great distance (hundreds or thousands of kilometers) from the conversion zone, as documented by Shurbet [1955]. In these exceptional cases and all the more so if the earthquake is deep, S waves are attenuated before reaching the shore (Shearer [2009] 6.6.5) and S→T-waves cannot be generated.

S waves to seabed motion at the conversion points. More importantly, they did not assume that the entire incident field was scattered, but assigned only 1% of its energy to direct conversion into low-order acoustic modes. They considered the possibility for the remaining energy to bounce between seabed and sea surface while being re-scattered at each seafloor reflection. These updates to the De Groot-Hedlin and Orcutt model allowed them to qualitatively model T-phase with asymmetric long-duration envelopes recorded at regional distances by an array of ocean-bottom seismometers.

De Groot-Hedlin [2004] later provided important improvements to De Groot-Hedlin & Orcutt [1999, 2001a] by 1. considering several subsequent seafloor reflections, 2. addressing the question of how finely-discretized seafloor bathymetry should be to accurately model T-phase excitation, and 3. by taking S waves into account. By comparing T-waves arrival times for smooth and rough sloping models, she concludes that scattering is the dominant mechanism for T-phase excitation, even in regions of high impedance contrast. Indeed, synthetic T-waves created with smooth models, therefore by downslope conversion, arrived too late compared to the T-phase created with rough models which are of lower amplitude but whose calculated arrival time is correct. See also De Groot-Hedlin et al. [2004] for other details on the implementation of their method.

Schmidt et al. [2004] proposed a new explanation for abyssal T-waves. They developed a wave-number integration technique coupled with a Galerkin approach (see Jensen et al. [2011]) and a virtual source approach (Schmidt [1995]; Goh et al. [1997]) and used them to model abyssal T-phases. Using Rayleigh–Kirchhoff approximation for the rough interfaces they stressed that abyssal T-waves can be interpreted as originating from the coupling of crustal shear body-waves into seismic interface waves, or seabed Stoneley-Scholte waves (Stoneley [1924]; Scholte [1947]), which subsequently scatter into the waterborne modal spectrum. Their theory is also in agreement with the observations of Dziak [2001] that the T-waves produced by earthquakes with high dip-slip motion are generally weak. Indeed, it predicts that T-waves produced by earthquakes generating strong crustal SV waves are significantly stronger than those produced by earthquakes that mainly produce P-waves.

Despite numerous studies on the subject, abyssal T-phases are still an unresolved problem. Hence, the more sophisticated theories described above predict T-waves to be very sensitive to water depth at the epicenter. However, T-phases recorded in the north Atlantic ocean for example (Williams et al. [2006]), do not vary much in amplitude with epicentral ocean depth. Moreover, even if it is true that abyssal T-waves contain more high-order modes than downslope T-waves, the first mode is often dominant in terms of energy contribution (D'Spain et al. [2001]). This is unfortunately not in agreement with De Groot-Hedlin & Orcutt [1999, 2001a] and presupposes the existence of a mode coupling mechanism as suggested by Park et al. [2001]. However this last model does not explain neither the generation of T-wave composed of low-order modes in the case of epicenters substantially below the critical depth.

Additionally, it is unlikely that all the mechanisms by which T-waves can be generated have been discovered. We will propose one more in Chapter 6.

1.5 Dispersion of T-waves and influence of the SOFAR channel: on the importance of going beyond ray theory

As the SOFAR channel is more than often associated with T-wave propagation, we chose to dedicate part of this introduction to its influence. Indeed, we believe that a small confusion has gradually appeared in the literature between the two phenomena, still many authors seem to consider, as we shall see, the existence of the SOFAR channel as a necessary condition for the generation of T-waves. It is necessary to return to the origin to enlighten the apparent misunderstanding. To do this, we will now distinguish "regional" T-waves recorded at less than about 1500 km from the conversion point from "teleseismic" T-waves recorded further away. Apart from the observations of the team in charge at the Morne des Cadets observatory in Martinique (Coulomb & Molard [1949, 1952]; Aubrat

[1963, 1965]) who have studied regional T-waves since the 1940s, the first recordings of T-phases (Jaggar [1930]; Linehan [1940]; Ravet [1940]; Tolstoy & Ewing [1950]; Ewing et al. [1952]) concerned teleseismic T-waves. It was only later that the first regional T-waves (Wadati & Inouye [1953]; Båth [1954]; Shurbet [1955]; Milne [1959]) were documented. The efficiency of explosive sound transmission in the ocean at teleseismic distances has been known since the Second World War (Ewing et al. [1946]; Brekhovskikh [1949]), and is no longer to be demonstrated. Hence the explosion of a small bomb near the channel axis can be recorded by receivers placed at the same depth and up to distances in practice only limited by the size of the ocean basins, while no reflected signal is recorded typically after a few hundreds kilometers. This kind of propagation in the SOFAR channel gives to the signals thus recorded a typical signature described in the following manner by Ewing et al. [1946]: "It sounds like kettle drums, starting very gradually and faintly. The tempo and the intensity both increase to the very end of the signal, which is an abrupt cut-off from maximum intensity to complete silence."

Nevertheless, as is known since Pekeris [1948], this **does not mean** that no transmission is possible without the existence of the channel, and this even more so at the regional scale and at low frequency (<10 Hz). Note that there are even configurations in which a homogeneous water layer is more efficient in transmitting signals at several hundred kilometers than a SOFAR channel, as shown in Figure 1.3.

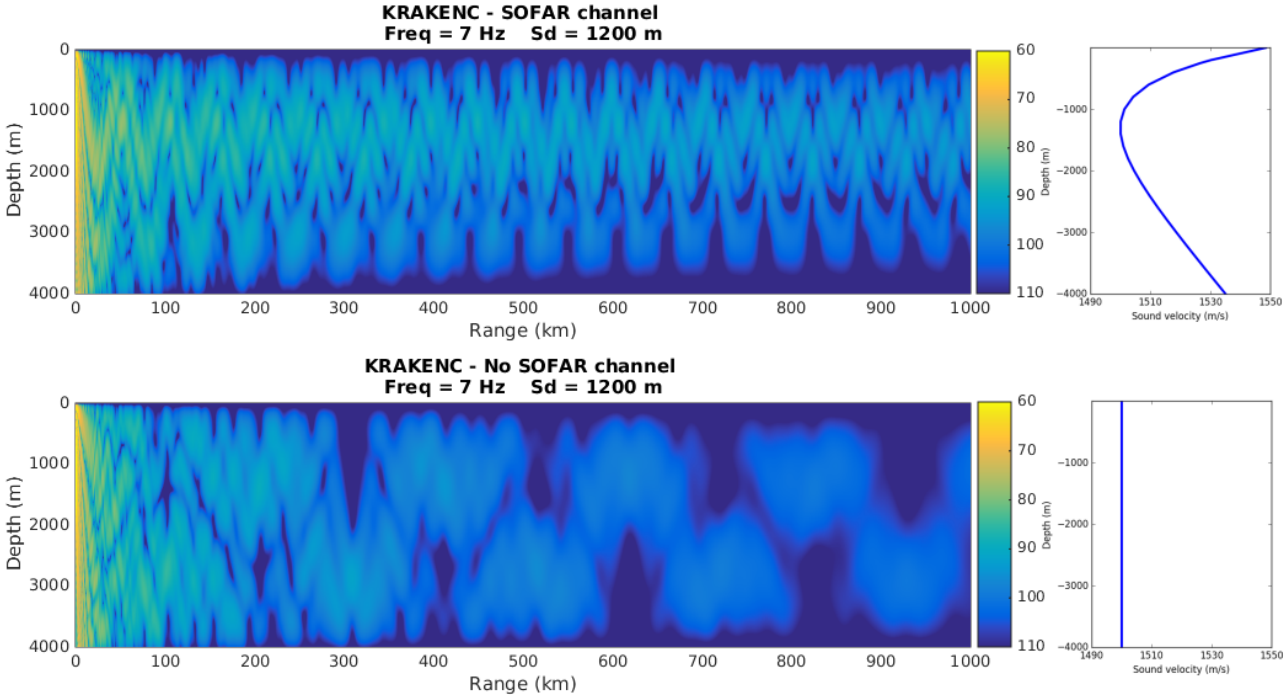

Figure 1.3 – Monochromatic transmission losses in dB as a function of range and depth calculated with the normal mode program Kraken(c) (Porter & Reiss [1984, 1985]) for two different ocean models. One with SOFAR channel and one without. The model is axisymmetric, with the axis at the left edge. The source is located on the axis at depth 1200 m. It is a monochromatic source at 7 Hz. The seabed (depth below 4000 m, not shown) is considered semi infinite and elastic with compressional wave speed: 2500 m/s, shear wave speed: 1500 m/s, density: 2200 kg/m^3, compressional wave attenuation 0.2 dB/λ_p, shear wave attenuation 0.2 dB/λ_s . Right: sound speed profile in the ocean for the two different models. The water density is constant at 1000 kg/m^3. Although it is clear that the SOFAR channel (up) favors long-distance transmission, **we see that its absence does not prevent in any way the propagation**, and that the signals may even be favored in certain places by the absence of the channel (see range 700 km and depth 3800 m for example).

Consequently, as early as the 50s, when T-waves were identified as traveling in the water layer, it is naturally that the first investigators (for example Tolstoy & Ewing [1950]) questioned their mode of propagation. When analyzed it seemed then to be explained by one or the combination of the following two mechanisms:

1. Normal modes such as newly theorized by Pekeris [1948]. The theory does not require the presence of a minimum of sound speed in the water to explain T-waves and may explain the observed T-waves with a frequency smaller than one Hertz. The predicted signals feature different forms of dispersion, both normal (with the higher frequencies traveling faster than lower ones) and inverse. Let us mention that even if the seabed is not considered as attenuating, which is not physical, a large part of the modes will eventually propagate without losses by successive total internal reflections, and the transmitted energy will be overestimated.

2. Guided rays in the SOFAR channel with no interaction with the seafloor. These signals theoretically have a small normal dispersion (see Porter [1973]; Talandier & Okal [2016] and simulations of Chapter 5). The phenomena, however, are unable to explain the part of the observed T-wave spectrum typically below 1 Hz (wavelength of 1500 m in water) but is known to explain the transmission of sound from remote underwater explosions. Ray tracing models are known to generate false caustics and to produce shadow zones whose boundaries are unrealistically sharp. Moreover, shear waves in an elastic bottom are rarely taken into account (Buckingham [1992]).

Over time the second interpretation gradually took precedence over the first in the literature, notably because of its conceptual simplicity and its ability to readily explain teleseismic propagation and T-wave generation from downslope conversion (Johnson et al. [1963]; Talandier & Okal [1998]). Therefore the question has been set aside. However, teleseismic propagation obviously does not exist in the case of regional T-waves and downslope conversion proved explainable as a coupled-mode mechanism using a modal framework (Sperry et al. [1996]; Park et al. [2001]; D'Spain et al. [2001]). Moreover, observations that cannot be tackled with ray tracing have been accumulated decade after decade, suggesting that T-wave should be considered as a shallow-water acoustics problem, even in deep water, the bottom being inherently part of the problem. In the following we list 6 points that cannot be explained using rays guided in the SOFAR channel:

- T-waves often exhibit inverse dispersion (Ewing & Press [1953]; Aubrat [1963, 1965]; Båth & Shahidi [1971]; Hamada [1985]; D'Spain et al. [2001]; Graeber & Piserchia [2004]...) or a typical "Christmas tree" spectrum shape (Northrop [1962]; Keenan & Merriam [1991]; Walker et al. [1992]; Talandier & Okal [2016]...). Few T-waves in the literature present the normal dispersion typical of explosions at sea (we can cite Solarino & Eva [2007]). At present time the dispersion properties of the waterborne signals even constitute a robust way to discriminate between explosions and T-waves (Talandier & Okal [2016]), the former presenting normal dispersion while the last do not.

- T-waves are routinely recorded by Ocean Bottom Seismometers (OBS) in ray shadow zones far below the deepest guided ray predicted by ray theory (Shimamura & Asada [1975][3]) even at teleseismic distances (Ito et al. [2012]). T-waves are also observed at borehole instruments, hundreds of meters below the seafloor of abyssal plains (Butler & Lomnitz [2002]; Araki et al. [2004]; Butler [2006]). In that case the authors suggested that the recorded signals were due to a different type of interface wave that they labeled Ti, which would travel through marine sediments as predicted by Biot [1952]. However the high anelastic attenuation known to be present in these surficial layers at the frequencies considered makes this hypothesis unlikely. Note that these observations may be related to unexplained deep sea floor arrivals in long-range acoustic propagation documented by Stephen et al. [2009, 2013] following explosive manmade source in the ocean. In any case, this implies the existence of coupling between the sound channel and the bottom, however ray theory does not take into account any interaction when the water depth is below the critical depth.

[3]Note that the authors suggested that these arrivals could be different from the T-waves already documented, and may consist of multiply-reflected water waves detected because of the high sensitivity of the instruments used.

- T-wave can be generated following earthquakes below abyssal plains, which are situated well below the SOFAR channel critical depth (Shimamura & Asada [1975]; Williams et al. [2006]). Ray tracing predicts that no ray initiating at the seafloor can be channeled in that case, yet strong T-waves are generated. Furthermore, no dependence of T-wave amplitude on water depth at the conversion point has been documented in the North Atlantic ocean (Williams et al. [2006]). This issue can be considered reciprocal of the previous point.

- Propagation as channeled rays cannot explain the lowest frequency part of T-wave signals (below 2 Hz) that has been observed and noted since the very first articles (Aubrat [1965]; Solarino & Eva [2007]).

- While observing T-waves at four ocean-bottom seismometers (two above and two below the SOFAR channel axis) Hamada [1985] showed that T-waves exhibit prograde particle motion in the vertical direction at stations both above and below the SOFAR channel axis. However Sato [1978] indicated that the particle motion induced by a wave trapped into the SOFAR channel was supposed to be retrograde above the channel axis and prograde below.

- The SOFAR channel has no essential influence on the amplitude of regional T-waves computed numerically based on the first Cartesian 2-D full-wave time domain simulations (Jamet et al. [2013]).

Because of all these points and because of the additional observations made during this PhD (see Chapters 4, 5 and Appendix A), the framework of ray theory nowadays seems unsuitable to go further into the understanding of this phenomenon, and even seems to be a conceptual obstacle potentially leading to flawed or biased interpretations, even more so in the case of regional T-waves. Unfortunately, to date, it is still invoked from the first line of the abstract in many articles dealing with T-waves, even at a regional scale and at frequencies below 10 Hz.

Lin et al. [2014] is an illustration of that. The article unfortunately shows a misunderstanding of the phenomenon, probably stemming from the apparent causality relation between the SOFAR channel and T-waves suggested in some of the literature. The authors describe regional T-waves recorded (at 250 km) by an ocean bottom seismometer “outside the SOFAR channel” and state that they gain new insight by explaining these arrivals using a numerical analysis based on ray tracing. Unfortunately they did not consider seabottom attenuation and hence think they provide an alternative to “SOFAR channel” propagation for the “mechanism of T-wave energy preservation across long distances” by mentioning multiple total internal reflections. Using the same method, Chen et al. [2017] is also problematic from that point of view. The authors do not mention total reflections but think that they explain the observations of Butler & Lomnitz [2002] or Williams et al. [2006] by explaining propagation “out of the SOFAR channel” at short range (< 250 km). We can also cite Ghalib et al. [1983], who observed T-waves at distances between 70 and 400 km and said that "these events enter the T-phase window along the inner trench slope at a more favorable angle for downslope propagation, since several bottom reflections are required before SOFAR propagation is achieved". Another example is Wilcock et al. [2014], who show T-waves at 30 km but describe them as a signal traveling “as a ducted wave in the ocean sound channel”. These articles (among many others) illustrate the confusion that has arisen in the community on that aspect.

Wave propagation models based on modal expansion and including coupled modes (for example Park et al. [2001]; D’Spain et al. [2001]), seem promising for the future. Similarly several numerical methods are efficient at modeling T-waves, as we shall detail in Section 1.10.

We shall present in this document additional numerical studies based on full waveform modeling showing that the SOFAR channel plays only a marginal role in the propagation of regional T-waves compared to the very existence of the water layer. Especially in polar regions or in the Mediterranean sea where the SOFAR channel is known to be surficial or narrow. Indeed, the channel mainly introduces

a reorganization of the energy in the water layer, which probably becomes crucial only at teleseismic distance.

1.6 Conversion and reflection of T-waves at shore

After their propagation in the ocean, T-waves finally reach the coast and are reflected and converted into seismic waves. In fact, it is thanks to inland seismic stations that they were first detected and studied (Linehan [1940]; Ravet [1940]), long before the use of the first hydrophones. The conversion and reflection processes of an acoustic wave guided in a water layer are complex and are not limited to T-waves phenomena. The problem of the penetrable wedge is a classical benchmark in underwater acoustics (Jensen & Kuperman [1980]; Jensen & Ferla [1990]; Buckingham [1992]; Jensen et al. [2011]).

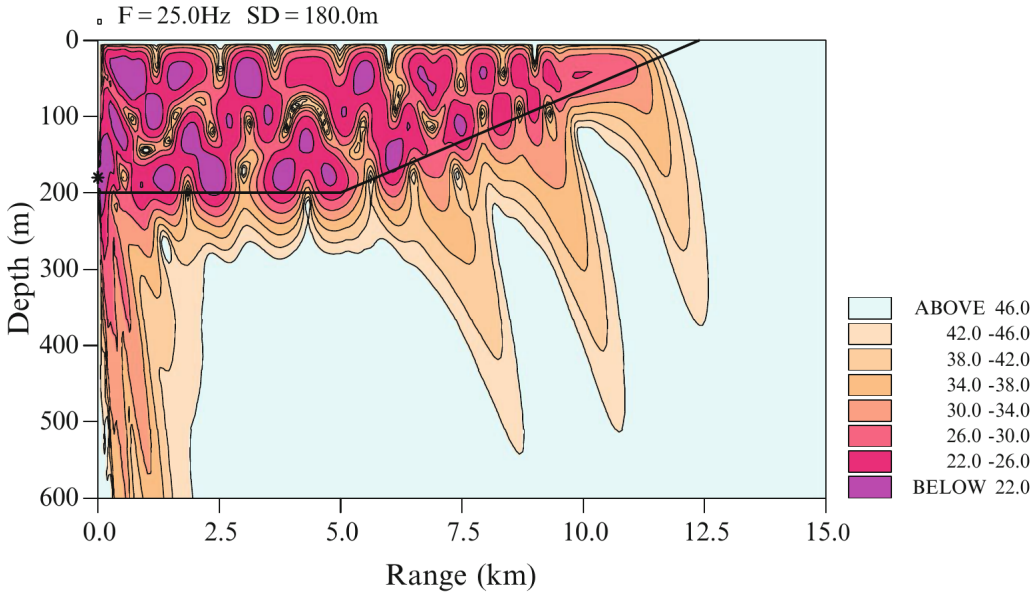

Figure 1.4 – Mode cutoff during upslope propagation in a wedge-shaped ocean with a penetrable bottom. After Jensen et al. [2011].

Figure 1.4, which has become famous, describes the phenomenon at stake. When they reach the wedge the modes are reflected and their incidence angle steepens by twice the seafloor inclination at each cycle of seabed and sea surface reflections. This eventually leads to supercritical incidence interaction for the guided modes also, which induces a leak of the energy of the modes into the sloping bottom at certain depths. In the fluid-fluid case, this behavior was observed experimentally by Coppens & Sanders [1980], and simulated, the same year, by Jensen & Kuperman [1980] using the parabolic approximation (see the box below for a description of the method). Numerous articles based on analytical techniques have been subsequently published, among which we can cite Pierce [1982, 1983]; Evans [1983]; Arnold & Felsen [1983, 1984]; Buckingham [1987]; McDonald [1996]; Abawi [2002]; Chunmei et al. [2016]. Theoretically speaking, difficulties arise because the Helmholtz equation describing the propagation of sound waves in a fluid (1.1) is not separable for the case of a fluid overlying a sloping bottom. For that reason, all models necessarily involve a form of approximation, usually adiabatic. It should be noted that in the case of simulations based on the parabolic equation a number of shadow areas remain, in particular regarding the staircase step chosen for the finite-difference scheme or regarding boundary conditions (Xu et al. [2016]).

Qualitatively, the prediction given by the parabolic equation has the correct form, but it is difficult to know to what extent the results obtained represent the actual interference structure. This illustrates the issue that is often associated with the use of the parabolic equation. We shall come back to these

points later in Chapter 5.

Note that the penetrable elastic wedge case was later studied by Deane & Buckingham [1993], who calculated the 3-D sound field in the water using the method of source images. The authors used it in conjunction with an spatial Fourier extension of Brekhovskikh & Lysanov [1982]; Brekhovskikh & Godin [2013] of the reflection of a spherical wavefield from a planar interface, which they modified to include a coordinate system tilted by an arbitrary angle with respect to the reflecting boundary. The field in the elastic bottom was calculated theoretically by Abawi & Porter [2007] using the technique of the virtual source, and by Godin [2007] who considered the shear wave speed in the bottom as a perturbation of the fluid case. As for the fluid case, they show that the coupling between surface and body waves occurs primarily near mode cutoffs. Godin [2007] also shows that P and S wave arrivals on shore increase with increasing slope angle and increasing impedance contrast. He predicts the generation of a surface wave when the slope is low and the impedance contrast is high. When the slope increases surface wave should logically decreases and tend to zero. The same thing should happen when the slope decreases.

In the real case of T-waves reaching an irregular coast the phenomenon is all the more complex and the literature is often contradictory. Converted T-waves are used by some authors to evaluate the seismic properties of the surficial layers of the coast (seismic velocities and attenuation) and also allow for the use of coastal seismic stations to study underwater signals. In what follows, we are going to try to summarize the main papers published to date on this topic. Following Piserchia et al. [1998] we will call "seismic T-wave" the seismic waves resulting from the conversion of an "hydroacoustic" T-wave at shore.

The first article dealing with the conversion of T-waves to seismic waves is Tolstoy & Ewing [1950], long time before the first theoretical works on the penetrable wedge. From the beginning they made the hypothesis that the T-phases they observed in the US coast (Northeast and California) corresponded to a short-period compressional wave traveling in water as far as the continental shelf, and transmitted from there into short-period elastic waves traveling through the sediments and basement of the continent. The nature of the seismic T-wave produced after the conversion was unclear. The motion recorded is said to be complex, often exhibiting a strong transverse component, and is interpreted as probably originating from successive P and S arrivals. The authors suggested that these components were coming from from the incident acoustic wave at a series of points all along the shelf, assuming the largest transfer of energy to occur at the depth of the SOFAR channel axis where, the continental slope is also the steepest. This interpretation explained the main features of some of the recorded seismic T-phases, including the very slow amplitude build-up and decrease, more or less continuous around the main body of the T-phase. Note that this article predicted the possibility for T-waves to be reflected at shore, as would be observed thereafter by e.g. Båth [1954]; Shurbet & Ewing [1957]; Aubrat [1963]; Cooke [1967]; Northrop [1970].

Båth [1954] showed seismic T-waves in polar regions propagating as Pg waves, seismic T-waves propagating as Sg, and again seismic T-waves that they interpreted as possible S waves in soft surficial layers of the upper crust. Båth & Shahidi [1971] later documented the furthest in-land detection of T-waves to that date, more than 1000 km from coast in Sweden and drew the same conclusions, but now interpreting the last type of T-waves as Rayleigh surface waves. As Tolstoy & Ewing [1950] they documented a dominant transverse (horizontal) motion within the T→Sg arrivals, and also low vertical displacements compared to T→Pg. The conversion point was found around 200 m depth. They used these phase to estimate the attenuation of T-waves as they travel through the Scandinavian crust. Shurbet & Ewing [1957] examined two phases recorded at Palisades, Halifax, and Ottawa and showed that the phases observed resulted from transformation of a T-phase to a transverse wave traveling (up to 840 km) through the continent with a velocity of about 3.5 km/sec, which they interpreted as a Lg wave or a possible Sg at short distance. Note that compared to the observation made in Europe and North America, Leet et al. [1951]; Coulomb & Molard [1952]; Nguyen & Nguyen [1961] calculated a very low velocity value for the converted regional T-waves (around 1.7± 0.5 km/s) in the

Bermuda-Antilles region and in the Philippines, and interpreted these phases as transverse (vertical) waves propagating in the shallowest sedimentary layer.

Green [1962] later reported apparent inconsistencies in the seismic T-phases recorded by the Tasmanian seismic network following an earthquake in New-Zealand. Some of the signals seemed to have traveled with P-wave speed across the state while other were more suggestive of surface wave velocities. Moreover the velocity appeared to be varying across the island. The author suggested that this could be explained by the "irregular contact between the continental shelf and the SOFAR channel".

Let us also cite Galanopoulos & Drakopoulos [1974], which is probably the first article dealing with T-waves in the Mediterranean sea. It reported the observation of a vertically-polarized high-frequency phase (probably > 15 Hz) recorded by a coastal strong-motion seismograph after an $M_s = 6$ earthquake whose epicenter was estimated around 10-15 km offshore from the instrument. The authors interpreted this arrival as a T-wave because no aftershock with fitting arrival times were recorded at two other seismic stations located 100 km away. The signal observed in this article would probably correspond to a T-wave which exhibits the shortest acoustic path published in the literature. However, after examination, this interpretation seems a little far-fetched due to the uncertainties associated with the epicenter location, the media characteristics and the timing of the phases. Moreover the estimated epicenter position/conversion point in the immediate vicinity of the coast, on a smooth and gentle continental slope orientated seaward, does not seem prone to generate T-waves, even more so toward the continent. Finally, they suggested that the T-wave traveled as a P-wave after the conversion, which is not consistent with the vertical polarization of the recorded phase. If of natural origin we would rather suggest that this high-frequency tremor was generated following the earthquake and was attenuated before reaching the two other instruments.

One year before the publication of the first theoretical works on the penetrable wedge, Talandier & Okal [1979] published the very first article documenting T-waves felt by a coastal population. They studied the conversion of T-waves to seismic waves in the framework of ray theory, considering the incident acoustic wave as composed of rays trapped in the channel SOFAR. They therefore assumed several possible reflection points on the coast on which refraction was possible, and considered the generation of P, S and Love surface waves after the conversion. Note that they also document an unusual T-wave which was recorded surprisingly small at Rarotonga compared to Tahiti after its propagation from the Tonga archipelago. Indeed Rarotonga is at shorter epicentral distance than Tahiti, the coastal slopes of the islands are similar and Rarotonga is not masked by any bathymetric blockage. They suggest that the high amplitudes recorded at Tahiti are due to favorable 3-D geometrical conditions.

Although not specifically dealing with T-waves, in the sense in which I defined them at the beginning of this document, the work of Shapira [1981] has to be mentioned here. He studied the conversion at shore of acoustic waves generated by thirty three underwater controlled explosions off the coast of Israel (at distances up to 280 km) and recorded at three seismograph stations located at a few kilometers from the coast (up to 15 km). He identified three converted waves. The first two were interpreted as P waves and the last as S or surface waves. Indeed, assuming, as the previous researchers, that the conversion from acoustic to elastic waves occurred where the continental slope crossed the SOFAR channel axis, they measured horizontal velocities of 2.5 km/s or lower for the converted wave. These low velocities are consistent with the existence on the site of an already documented unconsolidated material of significant thickness through which the waves could propagate. Unfortunately, he lacked measurements of the horizontal components of the T-waves and thus was not able to confirm this with the signal polarization. He also proposed three semi-empirical laws linking peak-to-peak converted wave amplitude, distance between shot and station, sea depth at the shot point, frequency, seismic velocities, attenuation coefficients and wave train duration. They were then able to obtain a value for the crustal quality factor for the coastal regions considered.

Cansi & Bethoux [1985] studied the conversion at shore of acoustic waves generated by two explosions at sea, as well as by an earthquake, which were characterized by their exceptionally long inland propagation path (>1000 km). Analysis of travel times and particle motion showed that the observed

seismic waves were mainly composed of Pg and Sg (or Lg) waves. Assuming that the converted wave was the sum of discrete arrivals from various points along the continental slope, they computed the first T-wave synthetic seismograms that were in relative agreement with the measured ones. For the seismic T-wave generated by the documented earthquake, two distinct pulses were visible, the second one had the largest amplitude and was interpreted as being composed of Sg waves. This article suggests that the transmission of energy from the ocean to the continental crust is mainly due to diffraction and shows that the duration of the signals is considerably affected by the bathymetry of the continental slopes.

Koyanagi et al. [1995] later used three teleseismic T-phases recorded by a rather dense seismic network in Hawaii to map the near-surface attenuation over most of the island. They found quality factor values ranging from 30 to 200, which were significantly lower than existing estimates suggesting that seismic T-waves may be sampling the very near surface. They documented velocities around 2 km/s which are consistent with S or surface wave propagation. As Adams [1979] and Talandier & Okal [1979] they reported a focusing effect of T-phases resulting from a favorable bathymetry of the continental slope.

Cook & Stevens [1998] documented a number of T-phases recorded inland Australia at long distances from the coast (up to 1600 km, which constitutes the current record). The travel times were all consistent with propagation as Pn waves. In a more theoretical paper dealing with acoustic to seismic conversion at shore of waves created by an explosion at sea, Piserchia et al. [1998] compared real signals with synthetic signals calculated using ray tracing coupled with a 2-D axisymmetric finite-difference method. Their numerical simulations showed realistic phases mainly composed of P waves followed by Rayleigh waves comparable in size. They stressed that the duration of seismic and hydroacoustic phase is linked with the explosion depth and insisted on the importance of the bathymetry of the continental slope and of the distance between the coast and the receiver.

Their results are in agreement with the observations of Talandier & Okal [1998] in French Polynesia published simultaneously. These authors studied downslope and upslope propagation of acoustic waves at very steep island shore ($> 45°$) by establishing scenarios based on ray-tracing considerations that explain the main characteristics of observed signals. Assuming that the seismic properties of the ground on the receiver side were known, they obtained theoretical relationships between wave propagation time inland and distance between conversion point and station. They compared these relations for P, S and surface waves with data from various sources. The fit was excellent for P waves at long distance and for S or surface wave at short distance (<10 km from conversion point to station). However they stated that their reasoning are no longer valid for moderate slopes, which explains, according to them, the differences with the observations of Koyanagi et al. [1995]. They also noted that seismic T-waves converted on gentle slopes last longer than those observed after conversion on steep slopes.

With the developments of computational capabilities these years were particularly rich of articles dealing with upslope T-wave conversion. Let us mention the work of De Groot-Hedlin & Orcutt [2000], who modeled upslope propagation of acoustic energy at a sloping wedge model using a 2-D adiabatic elastic parabolic equation (PE) method in the frequency domain and interpreted the results in terms of mode coupling. For seafloor exhibiting low shear velocity (50 m/s) they reported a strong decrease of transmitted signal energy with increasing frequency, especially for low slope angles and high-frequency sources with high mode number content, such as explosions in the deep ocean. For such sources the influence of slope angle is shown to be of particular importance on transmitted energy compared to low frequency, shallow sources whose energy couples with seafloor close to the wedge apex. The authors however predict the slope angle to be particularly influential on signal duration. In the case of significant shear velocity at the bottom the simulation predicted that strong surface waves can be generated and are quickly attenuated. However, and as they worked in the frequency domain, they did not analyze the arrival times of the phases nor their duration or polarization properties.

Similarly, Stevens et al. [2000, 2001] compared data from hydrophones in the ocean with data from the same events recorded by coastal seismometers in California. They defined a transfer function for

the conversion, which they modeled using a 2-D solver based on time-domain finite differences coupled with a normal-mode solution. The seafloor model included shear velocity larger than the velocity of sound in water. For slopes of 30 degrees or less, the first arrival of the synthetic pulses has the largest amplitude and corresponds to retrograde elliptical particle motion, suggesting a propagation as Rayleigh wave. The signal subsequently (or simultaneously) exhibits linearly-polarized waves with vertical particle motions, associated with P waves. This behavior suggests that the acoustic energy is converted to Rayleigh waves along the continental slope interface well before its conversion to body waves (which would arrive first if produced at the same time). This observation seemed contradictory with their observations in California, which were consistent with P-wave propagation in accordance with Talandier & Okal [1998]. Therefore, as suggested by previous authors, they assumed that these strong surface waves observed in their simulation were attenuated quickly after their generation. Note that they also showed results for varying slopes and did not report big differences, which is inconsistent with previous observations (Piserchia et al. [1998]; Talandier & Okal [1998]). They examined the effect of a surficial low velocity layer and finally documented, in line with De Groot-Hedlin & Orcutt [2000], that higher frequencies scatter more strongly than lower frequencies during the conversion, leading to a deficit in high frequencies in coastal signals.

By observing T-waves and airgun shots before and after their conversion at an ocean-continent margin, Rodgers & Harben [2000] also confirmed that the process induced a drastic loss of high frequencies. In addition, they performed 2-D finite-difference simulations that confirmed the earlier observations of Stevens et al. [2000, 2001].

We can recommend De Groot-Hedlin & Orcutt [2001b] . This article examined two distinct cases; the first, characteristic of volcanic island, in which the shear velocity of the seabed is greater than the sound velocity in the fluid, the second more representative of sediment-covered continental margins in which the seafloor is supposed to be gently sloping and exhibits a weak shear wave speed (case later studied theoretically by Godin [2007]). Based on considerations related to modal critical angles, they assumed that the acoustic energy incident at the weakly-elastic gentle slopes coupled to P and S waves with a relative partitioning depending on the slope and on shear wave speed. In the case of a hard seabed the authors mainly predict a coupling with S waves for intermediate slopes (between 10° and 20°) and with P waves only in the presence of the steepest slopes ($> 30°$). Surprisingly, the conversion from T-wave to surface wave is not mentioned. Using almost the same dataset as Stevens et al. [2000, 2001], the authors examined data from an offshore hydrophone and from coastal seismic stations in California. They argued that the converted signals were made of several converted modes arriving almost simultaneously. They thus suggested that modal information contained in the acoustic wave may be destroyed during their conversion into elastic waves at shore, which makes the case that hydrophones are more efficient than inland stations for T-waves studies. The article also contains a study based on signal-to-noise ratios (SNR), which they computed as a function of frequency for each instrument. Not surprisingly, the best signal-to-noise ratio inland was found at stations closest to the shore. Steep slopes along the source-station azimuth were also shown to favor signal-to-noise ratio, as the 3-D configuration of the coast can as well. Indeed, the station exhibiting the largest signal-to-noise ratio lied close to a convex portion of the continental slope, possibly focusing the energy.

More recently, along the same line as Koyanagi et al. [1995] let us cite the work of Kosuga [2011], who observed the propagation inland for a reflected/scattered T-wave (already studied by Obara & Maeda [2009]) using the very dense Japanese seismic network (see Figure 1.5[4]). The seismic T-wave recorded has a rather low dominant frequency (1.5 Hz) and its energy appeared to concentrate in a specific area (northern part of Honshu Island), suggesting strong 3-D effects or non-isotropic radiation from the conversion points. The low frequencies recorded can be explained by the combination of two mechanisms. The first is the particularly high attenuation of high frequencies at shore, as documented by Stevens et al. [2000, 2001]; De Groot-Hedlin & Orcutt [2000] (however the frequency content of

[4]We thank Pr. Kosuga for providing us a high-resolution version of his figure.

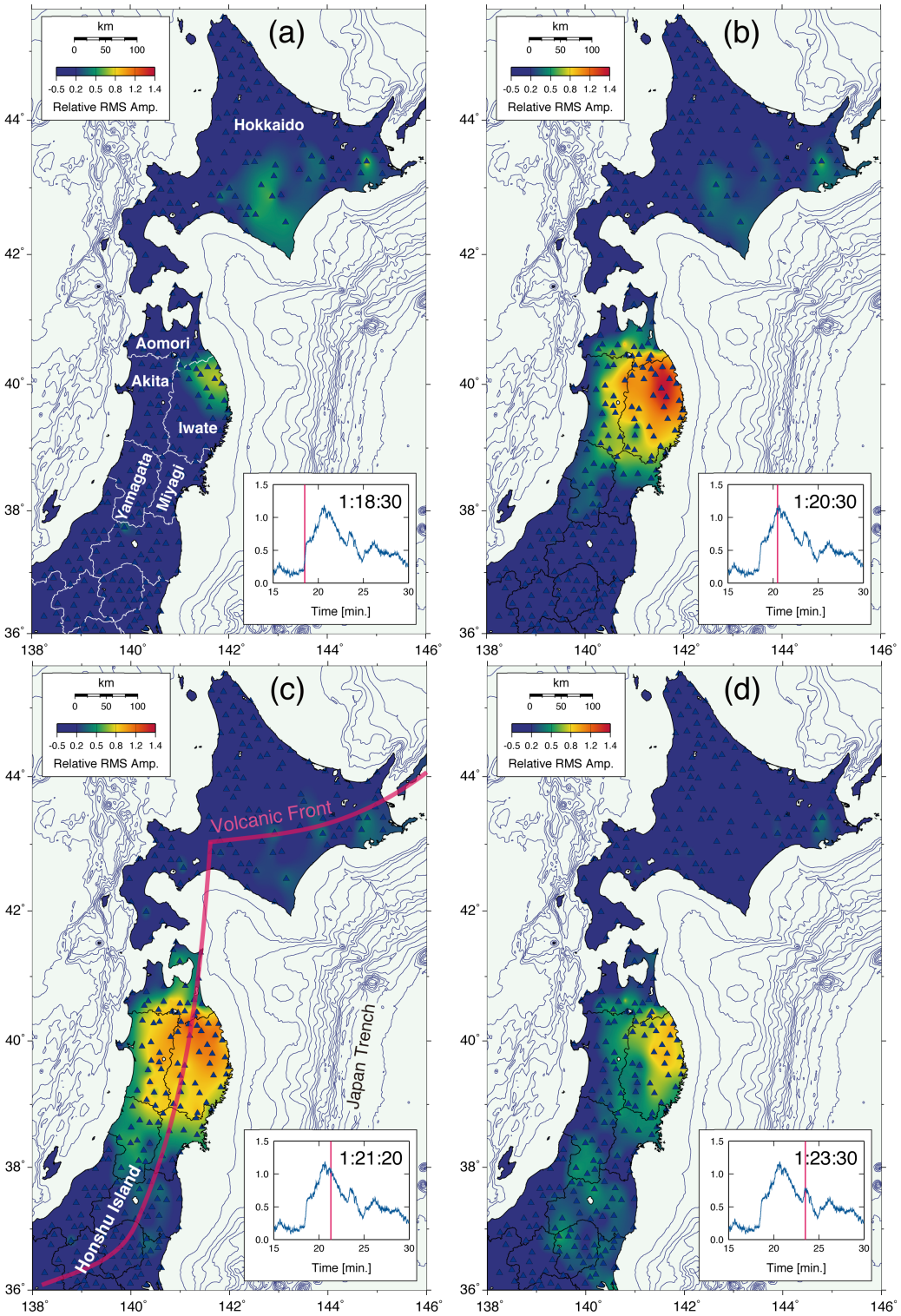

Figure 1.5 – Taken from Kosuga [2011]. Snapshots of T-phase root mean square amplitude distribution in four 10-s time windows. The colour indicates the logarithm of the relative root mean square amplitude measured from the noise level. The triangles indicate the stations used to calculate the amplitude distribution. The lower right box in each panel displays the average root mean square amplitude as a blue line and the start time of the window as a vertical red line.

the signals seems to be similar no matter the distance to the shore), the second mechanism being a possible "low-pass-filter effect" induced by the previous reflection of the incident signal. Hence, low-order modes are supposed to be more easily blocked (and thus possibly reflected) at shallow bathymetric features (De Groot-Hedlin et al. [2004]; Hanson et al. [2006]), letting high frequencies propagate.

The recorded first arrivals shown in Kosuga [2011] have the apparent velocity and polarization characteristics of a Rayleigh wave, in contradiction with earlier works reporting dominance of body waves. In agreement with Talandier & Okal [1998] the author suggests that the gentle slopes in the conversion area may favor the generation of surface waves. Using a source-scanning algorithm he mapped the conversion zone, which appeared to be 100 km large.

As is done in Kosuga [2011], the reflection/scattering of T-waves at shores or bathymetric highs have been often reported. We can also cite Lin [2001], for example, who reported a rare observation of successive T-waves reflections at both sides of a forearc basin east of Taiwan, Hanson & Bowman [2006], who documented the use of reflected waves for event localization, or the following articles that all report T-wave reflections: Båth [1954]; Shurbet & Ewing [1957]; Aubrat [1963]; Cooke [1967]; Northrop [1970, 1974]; Lin [2001]; Graeber & Piserchia [2004]; Obara & Maeda [2009]; Kosuga [2011]... However, to our knowledge, the reflection process has not been studied in detail to date. We can cite Hanson et al. [2006], who compared power spectra for direct and reflected T-waves and documented loss of high-frequency energy in the reflection from bathymetry. These authors were able to predict the amplitude of reflected signals from simple considerations based on bathymetry, SOFAR channel depth, and source/receiver locations. However they were not able to predict observed frequency variations, which may depend on seafloor seismic properties.

Note that Frank et al. [2015] recently showed a parabolic equation solution for the conversion of an abyssal T-wave at shore but without a particular analysis of the process.

To close this Section let us cite the recent article of Buehler & Shearer [2015] who showed that the T-phase was clearly visible (especially above 2 Hz) in global broadband seismogram stacks from land stations of the Global Seismic Network (see Figure 1.6). They showed the evolution in apparent velocity with increasing continental path length but did not draw any conclusion about the converted waves.

1.7 Locating and characterizing T-wave sources

It has been known since WWII (Ewing et al. [1946]) that a point source of sound in the ocean can be located with fair precision (1 km or so) by simple triangulation using multiple remote hydrophones. Furthermore the accuracy improves year after year with the emergence of new localization techniques and the availability of high-resolution sound speed models constructed after decades of measurements in the oceans. This has many applications, in the military field, in geophysics, in animal bio-acoustics and in anthropogenic noise monitoring for example. Such localization has gained particular importance recently in the context of monitoring the Comprehensive Nuclear-Test-Ban Treaty, which requires the capability to detect and locate events that produce acoustic signals in the ocean, and to discriminate between explosions and natural events (De Groot-Hedlin & Orcutt [2001c]).

In the case of T-phases, the localization process gives the position of an area of the seabed considered to be the source area of acoustic waves. This area is commonly called the T-wave conversion zone. In has been pointed out since Tolstoy & Ewing [1950] that because of their lower speed compared to seismic waves, T-waves can provide a more precise location of close events[5]. Nowadays, thousands of

[5]Supposing that the phase picking uncertainties are the same (which is actually not completely true), measuring an arrival time of 45± 5 s for the T-wave is more precise than measuring an arrival time of12± 5 s for the P-wave.

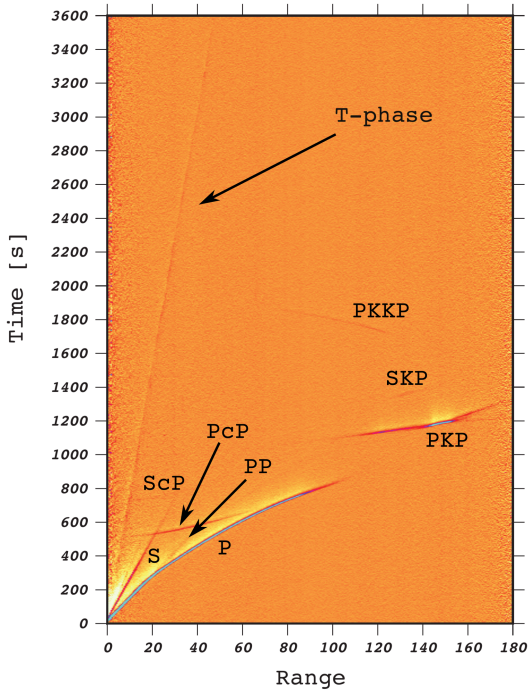

Figure 1.6 – Adapted from Buehler & Shearer [2015]. Global broadband STA/LTA seismogram stack with traces filtered at 2-8 Hz. See Figure G.2 on page 197 for a description of the seismic phases mentioned.

T-waves are routinely recorded and algorithms exist for their automatic recognition (Sukhovich et al. [2014]).

Furthermore, due to the efficiency of the guided propagation in the ocean, T-waves can be detected at long distance from many events that are not recorded by inland stations. Hence the detection threshold of events can be improved by 1-2 orders of magnitude using a few hydrophones set in the ocean rather than large terrestrial seismometer networks (Johnson & Northrop [1966]; Fox et al. [1994]; De Groot-Hedlin et al. [2004]; Pan & Dziewonski [2005]; Dziak et al. [2011]). In addition, as attenuation is highly frequency dependent, the higher-frequency part of the seismic waves (typically > 5 Hz) generated by an earthquake is strongly attenuated during propagation through the Earth and cannot be recorded far from the hypocenter (all the more so if it is deep) by seismic stations set in continents (Dziak et al. [2004a]). Still, provided that the earthquake occurred in an oceanic environment, high frequencies (2-50 Hz) can be transmitted very efficiently to long distance in the ocean in the form of T-waves. Consequently, more information may be obtained on seismic events using hydrophones in the ocean than using land-based seismometers alone. T-waves are also crucial for studying submarine volcanism, eruptive processes (Dietz & Sheehy [1954]; Norris & Johnson [1969]; Talandier & Okal [1987a]; Schreiner et al. [1995]; Fox & Dziak [1998]; Bohnenstiehl et al. [2013]), seafloor spreading or magma intrusion at mid-oceanic ridges (Hammond & Walker [1991]; Fox et al. [1994]; Schreiner et al. [1995]; Blackman et al. [2000]) which all affect the oceans and seafloor ecosystems (Dziak et al. [2011, 2012]). Among the most important breakthroughs made possible by T-waves we can thus cite the real-time observation of several seafloor volcanic eruptions on the Gorda and Juan de Fuca ridges (Fox et al. [1995]; Dziak et al. [2011]). This detection enabled fast response with instrumented ships that have considerably contributed to our understanding of seafloor spreading and subsurface hydrothermal and microbial processes (Delaney et al. [1998]; Cowen et al. [2004]; Wilcock et al. [2014]). T-waves are also particularly useful to detect and monitor small amplitude intraplate earthquakes in very remote areas (Fox et al. [2001]).

However, T-waves are highly sensitive to the environment they cross and their properties depend strongly on their generation mechanisms, which is why locating and characterizing T-wave sources

The parabolic approximation

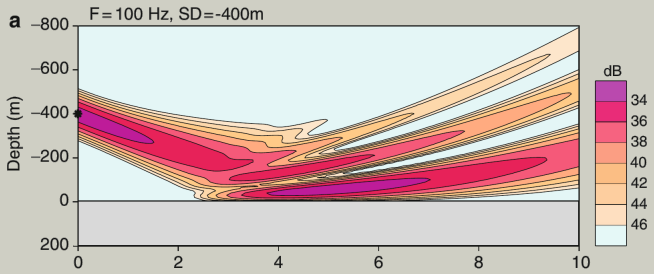

Figure 1.7 – From Jensen et al. [2011]: Transmission losses obtained based on the parabolic approximation and illustrating beam splitting at grazing incidence upon the seafloor.

The parabolic approximation forms the basis of the Parabolic Equation technique, which is probably currently the most popular approach for solving wave propagation problems in ocean acoustics. Since the publications of Tappert [1974, 1977] a considerable number of articles have appeared to improve the accuracy of the method and to extend it to a wide range of 3-D and range-dependent problems. Let us consider an axisymmetric acoustic medium of constant density but of spatially-varying sound velocity c. Supposing harmonic time dependence (constant angular frequency ω), the acoustic pressure expressed in cylindrical coordinate $p(r, z)$ obeys the classical 2-D Helmholtz equation (see e.g. Jensen et al. [2011]):

$$\frac{\partial^2 p}{\partial r^2} + \frac{1}{r}\frac{\partial p}{\partial r} + \frac{\partial^2 p}{\partial z^2} + k_0^2 n^2 p = 0 \tag{1.1}$$

where $k_0 = \frac{\omega}{c_0}$ is a wavenumber, c_0 is some particular value of the sound speed chosen for convenience, and $n(r, z) = \frac{c_0}{c(r,z)}$ is a refraction index. We follow the derivation of Tappert [1977] and make the following set of assumptions:

- $k_0 r$ is large (far field assumption)
- The solution is sought in the form: $p(r, z) = \psi(r, z) H_0^{(1)}(k_0 r)$ where $H_0^{(1)}$ is the Hankel function of the first kind and zeroth order (solution to the problem with a homogeneous medium).
- The envelope function ψ varies slowly with range
- $\frac{\partial^2 \psi}{\partial r^2}$ is much smaller than $k_0 \frac{\partial \psi}{\partial r}$ (paraxial approximation)

These approximations yield the so-called standard parabolic equation:

$$\frac{\partial \psi}{\partial r} = [\boldsymbol{A}(r, z) + \boldsymbol{B}(z)]\, \psi \tag{1.2}$$

where the operators $\boldsymbol{A}$ and $\boldsymbol{B}$ are defined as $\boldsymbol{A}(r, z) = \frac{ik_0}{2}\left(n^2 - 1\right)$ and $\boldsymbol{B}(z) = \frac{i}{2k_0}\frac{\partial^2}{\partial z^2}$.
Since the work of Tappert, many improvements have been achieved in the framework of the parabolic approximation which makes this numerical method, in spite of its limitations, a method of choice for the simulation of wave propagation in ocean acoustics mainly because of its reasonable computational cost even for long ranges or high frequencies numerical simulations. See Jensen et al. [2011]; Brekhovskikh & Godin [2013] for a detailed introduction to the topic.

still faces several obstacles that are under study in the community. We can for example cite D'Spain et al. [2001], who compares, in terms of modal content, T-waves arrivals from a coastal earthquake with arrivals from an earthquake that occurred below an abyssal oceanic plain. It is, in our opinion, one of the best articles dealing with T-waves.

First of all, T-waves are often long duration wave trains, which makes the picking of the phase often required for localization uncertain (Yang & Forsyth [2003]). Indeed the conversion zone is not a point but rather covers an area up to several square kilometers of the seafloor. Second of all, it has been shown (e.g. Johnson et al. [1963]; Johnson [1964]; Northrop [1970]; Graeber & Piserchia [2004]) that this conversion zone does not necessarily match earthquake epicenter[6]. Thus, a single earthquake may produce multiple T-phases, for example if separate slopes or seamounts are present in the vicinity of its focus (Shurbet & Ewing [1957]; Walker et al. [1992]; Freeman et al. [2013]). It is not often clear anyway what seismic wave is responsible for the generation of a given T-wave. This is a reason why, to date, earthquake source parameters are hardly derivable from T-phases, even more so in the case of deep earthquakes. Moreover the link between T-phase amplitude and earthquake magnitude is complex and not understood. Finally, it is worth mentioning that even the oceanic propagation pattern still raises questions (Williams et al. [2006]). We will discuss some of these points in this Section. We also refer to Okal [2007] , who sometime goes into more details, especially into the use of T-waves to explore the seismic source.

1.7.1 The use of T-waves to locate an earthquake epicenter.

Basic triangulation of T-phases (Johnson et al. [1963]), waveform cross-correlation (Graeber & Piserchia [2004]), non linear least squares methods (Hanson et al. [1996]; Slack et al. [1999]; Fox et al. [2001]), Matched-Field Processing/back-azimuth or grid searches (e.g. Lin et al. [2014]) are used to locate the area(s) of the seafloor where underground seismic waves were converted to T-waves. Nowadays thousands of events have been located from T-waves (see Figure 1.8). This is sometimes a difficult task because of their high variability, their long duration, their gradual build-up nature, and their unclear onset (see Figure B on page 13). This raises the question of what part of the signal has to be considered as corresponding to the onset of the T-wave. Most authors use the peak amplitude of the smoothed envelope of the time series as an arrival time and proceed as if a T-wave was an undispersed and unscattered signal arising at a point-source epicenter (e.g. Duennebier & Johnson [1967]; Slack et al. [1999]; Fox et al. [2001]; Stevens et al. [2001]; Dziak et al. [2004a]; Ito et al. [2012]). The choice of considering T-phase peak amplitude as the arrival time of the phase has been tested by Slack et al. [1999] and proven consistent with a generation scenario based on scattering and also consistent with Johnson et al. [1967]; De Groot-Hedlin & Orcutt [1999]; Park et al. [2001] for example who link event depth and T-phase rise time (see Figure B on page 13). We shall return to this particular point in next Subsection. Other authors used the earlier part of the signal (Shimamura & Asada [1975]; Wilcock et al. [1992]; Bohnenstiehl & Tolstoy [2003]; Kosuga [2011]) and stressed that the recorded maximum does not necessarily represent the propagation of a specific phase. However, in that case, the choice of a given emergence time is often equivocal. Recently Ito et al. [2012] compared the two methods, which turned out to give comparable results. Yet, in a shallow hypocenter setting in rather flat areas (e.g. abyssal ridge-transform regions) such approaches have proven not to introduce any apparent bias in epicenter location or, more accurately, moment centroid (Pan & Dziewonski [2005]) which is commonly found with an uncertainty of less than a few kilometers (Slack et al. [1999]; Fox et al. [2001]; Bohnenstiehl & Tolstoy [2003]; Pan & Dziewonski [2005]).

In the case of significant reliefs, slopes (e.g. subduction zone, seamounts) or roughness at the seafloor above the earthquake source, significant discrepancies are also reported between the conversion zone and the epicenter (Northrop [1970]; Walker et al. [1992]; De Groot-Hedlin & Orcutt [2001a]; Freeman et al. [2013]). The T-wave being then commonly sourced toward shallow, steep, bathymetric

[6] A result claimed by Evernden [1970] but found in previous works (e.g. Johnson [1964]). See Johnson et al. [1971].

features (Northrop [1962]; De Groot-Hedlin & Orcutt [2000]) and exhibiting several Peaks, making the location process ambiguous (Williams et al. [2006]). Let us note that, due to the difficulties often associated with the location of conversion areas, some studies documenting such discrepancies have given rise to controversy (Chapman & Marrett [2006]; Bohnenstiehl [2007]; Chapman & Marrett [2007]).

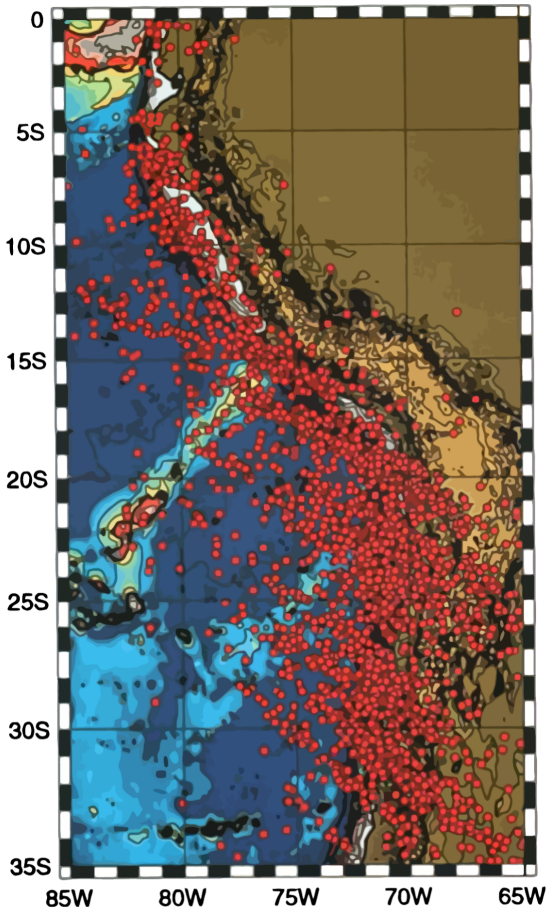

Figure 1.8 – Seismicity of the Peru-Chile trench from May 19, 1996, to May 19, 1999, as determined from T-phases recorded at an autonomous hydrophone array moored in the Pacific Ocean offshore Central America. The red dots represent the calculated conversion points. Some of the acoustic source locations are clearly mislocated on land, which may be due in part to the simplification of the sound speed model made by the authors and also to the great depth of the events within this subduction zone. Adapted from Fox et al. [2001].

A large number of articles deal with improvement of localization from T-phases. Let us cite here Hanson & Given [1998] who further enhanced earthquake azimuths estimations from T-phase envelopes using a nearly automated inversion scheme assuming plane wave propagation. Let us also cite Yang & Forsyth [2003] who developed an empirical function to fit the envelope of T-phases in order to reduce the uncertainties associated with the localization and earthquake magnitude estimation. Using OBS stations to observe T-waves Hamada [1985] confirmed that most parts of recorded T-phases at the sea floor are strongly polarized in the direction of propagation (which is consistent, T-wave being compressional waves in the water). They suggested that this property could be used for T-wave identification and approximate estimation of the direction of the conversion area. Hanson et al. [1996] proposed the combined use of hydrophone arrays and land-based stations, which however raises the issue of the weighting of the different signals (Pavlis [2004]). In order to study the seismicity at the southern East Pacific Rise, Shen [2002] developed an algorithm for automatic identification of seismic T-phases. The author considered commonly Rayleigh waves and T-waves using waveform

cross-correlation and a nonlinear least-square method rather than phase picking, which proved to provide more precise locations.

As it is often ignored in the article of Shen [2002], it is important to recall here that point sources are merely theoretical and do not exist in nature. If looking for a conversion point its position may exhibit a variance of the order of the size of the physical radiator. Furthermore, its position will not necessarily coincide with the earthquake epicenter. For a single earthquake, multiple peaks in the T-phase can appear, each one corresponding to a different conversion point. Presumably, a separate T-phase source location could be established for each peak.

Within that framework Graeber & Piserchia [2004] did not consider a unique point conversion zone but suggested that every detection window of a T-wave can be associated with a specific coupling point. Indeed, the authors observed strong variation of back-azimuth and arrival times while studying six large teleseismic earthquakes using hydro-acoustic triplet stations. By doing so, they mapped point-by-point the areas where elastic-to-acoustic coupling had taken place. Their results are consistent with conversion of P waves by seafloor scattering (De Groot-Hedlin & Orcutt [1999]; Park et al. [2001]). For the strongest events the authors documented areas spanning huge distances (several hundreds of kilometers).

Pavlis [2004] suggested that the use of incoherent beam methods could improve the precision of the location estimation using T-phases. An incoherent beam is a stack of the envelope of an ensemble of time-series data. Incoherent beams have been used widely for analysis of regional phase seismograms in order to increase the efficiency of receiver arrays. Hanson & Bowman [2006] also indicated that the use of reflected waves as synthetic stations for event localization allowed one to reduce location uncertainty and enabled event location even with a single station.

Recently Freeman et al. [2013] used large-aperture horizontal and vertical receiver line arrays to observe a set of 90 T-waves. Their equipment allowed beamforming over the higher frequencies (5 to 50 Hz), which enabled them to confirm the observations of D'Spain et al. [2001] and Baggeroer et al. [2005] that the T-waves had predominantly a first-mode structure. It also brought new evidence that T-waves can be generated at the ocean floor far from the earthquake epicenter. With the objective of improving hydroacoustic localization at long range, Heaney & Campbell [2016] evaluated numerically the impact of mesoscale oceanic variability on teleseismic T-phases based on a two-year time series of ocean state estimations. Their calculations predicted a deviation of back-azimuth of nearly 2° on a 9100 km-long propagation path, for the setting considered, showing that these previously neglected effects could thus lead to errors in localization of several hundreds of kilometers at teleseismic ranges.

1.7.2 Can one infer the source depth from T-waves?

T-phase-based localization methods only provide the area of the seafloor where seismic-to-acoustic conversion took place but give no clue about the depth of the source event. Before the conversion, seismic waves generated by the earthquake travel from the hypocenter to the seafloor. It is not clear which among the seismic waves is mainly converted to T-waves. The phenomenon is diverse and depends on many parameters. Wadati & Inouye [1953] suggested that P or SV waves may generate T-waves, while Shurbet & Ewing [1957] suggested a conversion from P and surface waves. Northrop [1974]; Graeber & Piserchia [2004] later suggested a conversion from P and/or Pn waves. Every configuration seems possible depending on the geometry. Working on regional T-waves, Ghalib et al. [1983] assumed possible $P \rightarrow T$ and $S \rightarrow T$ conversion but were often unable to unambiguously determine which phase contributed mainly to T-phases excitation. However, they found that shallow (< 60 km) earthquakes tend to produce stronger T-waves than intermediate-depth (> 60 km) events. This may be due to the relative closeness of hypocenters to the T-phase waveguide, which allows more energy to be channeled into the waveguide. Okal & Talandier [1997] documented arrivals of S-waves at the conversion area, whereas Talandier & Okal [1998] also observed efficient conversions from P-wave by shallow events. Lin [2001] suggested that the differences are due to the depth of the

earthquake: deep events would be more prone to generate T-waves from their S-waves because of the transverse particle motion produced at the seafloor, which is considered as more efficient in generating horizontally-propagating waves in the ocean.

Furthermore some T-phases clearly exhibit $P \rightarrow T$ and $S \rightarrow T$ phases, the later then being more energetic (Talandier & Okal [1998]).

De Groot-Hedlin et al. [2004] suggested that shear-wave energy transforms to low-order acoustic modes in the case of T-phase excitation at bathymetric relief distant from the epicenter (radiation at seamount or downslope conversion), while abyssal T-waves result from direct conversion of P-waves to higher-order acoustic modes. This is problematic because the observed velocity of the seismic phase coupling to T-phases seems consistent with shear waves in both situations. To explain this inconsistency the authors assume that S-waves are converted to P-waves at the interface between the elastic oceanic crust and the seafloor sediments; which is supported by observations (Spudich & Orcutt [1980]).

In order to qualitatively assess the depth of an earthquake from T-waves, some authors pointed out its possible relationship with T-phase rise time (see Figure B on page 13) and earthquake focal depth (Norris & Johnson [1969]; Schreiner et al. [1995]; Hildebrand et al. [1996])[7].

Deep events generally cause long T-phase rise times, while shallow ones produce sharp peaks (Johnson et al. [1967]). Indeed, supposing a generation scenario based on scattering (Johnson et al. [1967]; De Groot-Hedlin & Orcutt [1999]; Park et al. [2001]), the insonified seafloor areas located closer to the instrument are supposed to generate earlier arrivals compared to regions located farther away. This accounts for the lower amplitudes and long rise time of the wave; arrivals from farther away combine with other scattered signals from the event, resulting in a long decay time (Pan & Dziewonski [2005]). The scattering theory is also supported by the work of Slack et al. [1999] who compared the epicenter location of 100 earthquakes estimated considering the onset of the P-wave as arrival time, and then considering instead the peak amplitude of the T-phase. T-wave arrival-time residuals obtained exhibited a zero-offset Gaussian distribution mean, which implies, as suggested by the scattering hypothesis, that using T-wave peak amplitude is consistent with using the P-wave onset as the earthquake arrival. Based on this hypothesis, decrease of T-phase rise time from successive events generated at ridges was interpreted as shallowing magma dike intrusions (Schreiner et al. [1995]; Dziak & Fox [1999]; Dziak et al. [2004b]).

However Williams et al. [2006] did not confirm these hypotheses in the case studied in the Mid-Atlantic ridge. The authors rather observed a surprising correlation between rise time and water depth above the event, but did not propose a physical explanation. They stressed that the onset time could also be a function of other variables apart from hypocenter depth. They mentioned the efficiency of energy conversion at shallow topography and at low water depth above the event, as suggested by De Groot-Hedlin & Orcutt [1999, 2001a] but also the overlying slope angles. Indeed, downslope propagation along a steep slope may be considered a more efficient coupling mechanism than scattering, and can result in T-phases with low rise times (Johnson et al. [1967]; De Groot-Hedlin & Orcutt [2001a]). However, apart from this observation, their other signals are not in agreement with Johnson et al. [1967]; De Groot-Hedlin & Orcutt [1999, 2001a] (especially in terms of frequency content) and raise many questions on our understanding of T-waves. Likewise, Williams et al. [2006] observed that the length of the propagation path between the conversion point and the instrument did not influence the onset time of the event.

Note that T-phase rise time has also been linked to earthquake fracture length by Eaton et al. [1961] (see also Ben-Menahem & Toksöz [1963]) and is also used to discriminate between explosive submarine eruptions, which exhibit sharper onset, and earthquakes, which exhibit more gradual onset (Talandier & Okal [1987a]).

[7]Let us note that onset time and rise time can be different, for example if the T-phase exhibits multiple peaks (Williams et al. [2006])

Schreiner et al. [1995] suggest that the T-phase frequency content may also be related to source depth: high frequencies may suggest a shallower event and thus less attenuation in the crust. However they also stress that the greater high-frequency content may be due to the smaller size of the earthquake, larger events tending to exhibit lower frequencies (see e.g. Rathje et al. [1998]).

As a conclusion for this section, in the literature there is currently no reliable model to estimate the depth of an earthquake from T-waves.

1.7.3 What information can be obtained on the source?

T-waves result from the conversion at the seabed of seismic waves originating from an earthquake. As such, they should contain interesting information about the source event especially in the high-frequency range (> 2 Hz), which is often missing in conventional seismic wave spectra due to the high anelastic attenuation in the Earth. With the foundations of T-wave phenomena being progressively better understood, and thanks to the abundance of good quality data and newly developed concepts and models, researchers have quickly sought to use T-waves to obtain information about their source. Numerous interesting articles have been published in this regard, both on the theoretical and observational sides. First, it is important to note that acoustic signals recorded in the oceans are used to discriminate between anthropogenic and natural sources such as sub-oceanic explosions and volcanoes, especially for monitoring of the Comprehensive Nuclear Test-Ban Treaty (CTBT). However it is not an easy task. Let us cite for example Milne [1959], Ben-Menahem & Toksöz [1963] and Båth & Shahidi [1971], who all emphasize that signals coming for explosions last less time than T-phases, and De Groot-Hedlin & Orcutt [2001b], for example who did not observe when comparing recordings from a French nuclear test of 1995 with recordings of T-phases. The authors rather stressed that the two types of signals have a similar duration but that the nuclear explosion exhibits higher frequency content, as already observed for a submarine explosive eruption (Talandier & Okal [1987a]). This may be explained by the shallow (if any) depth of these sources, involving minimum path through the attenuating crust.

In this perspective, Talandier & Okal [2001, 2016] are particularly significant because they constructed and enhanced a set of criteria to differentiate man-made explosions from earthquakes (including those occurring inside volcanic structures, called "hotspot earthquakes"), from seismograms recorded at long distance (> 1500 km) at atoll stations of the RSP (Réseau Sismique Polynésien - Polynesian Seismic Network). Their discriminants were based upon the envelope amplitude, signal duration and dispersion properties (see Figure 1.9). Indeed, signals coming from explosive sources in the water always feature an inverse dispersion, with lower frequencies traveling slower, which is not the case for T-phases. Even if still lacking physical justification, the proposed procedure is very precise and it can now be considered that acoustic signals from explosions and T-waves from earthquakes can be differentiated in most cases. These works are thoroughly summarized in Okal [2007].

Note that shallow submarine volcanic activity without associated T-phases is frequently reported, suggesting differences in the physical mechanisms of the eruptions with respect to earthquakes and manmade sources that may explain the very small, if any, T-waves generated Koyanagi et al. [1995].

From a geophysical point of view, the next level would be to use T-waves to get information on the earthquake source, in particular on its magnitude to begin with. However, due to the complexity of T-wave generation and propagation processes, inferring earthquake magnitude from T-phases, if possible, is difficult. Some authors did not even observe any direct relation between T-phase amplitude and earthquake magnitude or source mechanism (e.g. Ghalib et al. [1983]; Walker et al. [1992]; McLaughlin [1997]). Others documented only a rough correlation with seismic magnitude (Johnson & Northrop [1966]; Fox et al. [2001]; Hanson & Bowman [2006]). Nevertheless, ridge events have been shown to generate T-waves whose amplitude better correlates to seismic magnitudes, probably because of the simpler and more consistent acoustic coupling (Hanson & Bowman [2006]). Note that Talandier & Okal [1979], following Geller [1976], stressed that T-waves, due to their high frequency content, are

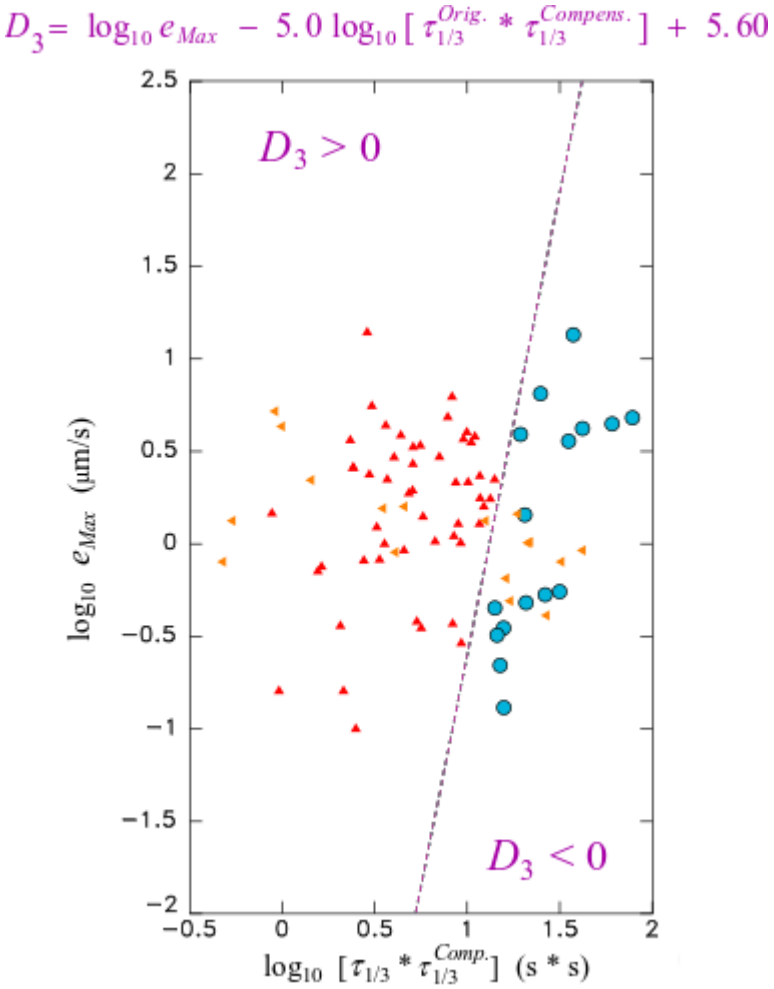

Figure 1.9 – After Talandier & Okal [2016]. Performance of the discriminant D_3 defined at the top of the figure and aimed at differentiating "hotspot earthquakes" (open circles) and manmade underwater chemical explosions (upward-pointing triangles). The dataset comprises 84 records. e_{Max} is the maximum of the envelope of ground velocity in the T-phase (in μm.s^{-1}), and $\tau_{1/3}$ is the duration in seconds during which the envelope is sustained at or above 1/3 of e_{Max}. *Compens.* means that the dispersion of the signal has been compensated by an algorithm. Note that all hotspot earthquake records feature a negative D_3, which separates them reliably from those of underwater chemical shots. However, complex explosions (left-pointing triangles) cannot be identified. See Talandier & Okal [2016] for more details.

greatly affected by interference arising from source size finiteness. They suggested that the amplitude of T-waves would saturate for earthquakes with a magnitude above $M_W = 6$, and that any greater earthquake would generate T-waves of similar amplitude but of longer duration. Studying New Zealand earthquakes in Australia, Leonard [2004] rather suggested a limit above $M_W = 7$ and documented a log-linear relationship between T-phase spectral power and magnitude. For large earthquakes, the saturation effect allows one to get an estimate of the rupture length from T-phase duration (Eaton et al. [1961]; Ben-Menahem & Toksöz [1963]; Johnson & Norris [1968a]; Johnson [1970]) and to obtain an order of magnitude for the seismic moment of the earthquake (Talandier & Okal [1979]). In consequence, empirical scaling laws have been proposed in the literature to link earthquake magnitude and T-phase duration (e.g. Adams [1979]; Okal & Talandier [1986]). They are, to date, probably the simplest and most robust tool for rapid estimation of the size of large submarine earthquakes (Tolstoy & Bohnenstiehl [2006]). Other works rather used T-phase spectral amplitude (e.g. Hiyoshi et al. [1992]; Walker et al. [1992]; Leonard [2004]; Hanson & Bowman [2006]), or combined T-phase amplitude and duration in the form of an energy called the T-Phase Energy Flux (TPEF e.g. Okal et al. [2003]; Ito et al. [2012]). Let us note that Ito et al. [2012] did not observe any correlation between magnitude and duration. Bohnenstiehl et al. [2013] used a similar energy-based procedure (outlined in Hildebrand [2005, 2009]) to get, from T-phases, an order of the magnitude of the acoustic energy released during a volcanic eruption. Most of the proposed laws however differ significantly, suggesting a strong influence of the dataset used (Okal [2007]). For example, in the case of downslope converted T-waves, the seafloor slope above the source must be of particular importance (e.g. Talandier & Okal [1979]). In the context of CTBT we can also cite De Groot-Hedlin et al. [2004], who examined the effect of the precise knowledge of bathymetry and of the seasonal variation in temperature on the accuracy in predicting acoustic transmission. Moreover, because of their ability to propagate high-frequency seismic energy efficiently, T-waves may be used to identify the frequency spectrum and therefore the stress drop of the various sub-events and/or aftershocks (Okal [2001a]). Hence the focal mechanism, such as radiation pattern or fracture speed, may play a big role for transmitted T-waves. However, determining earthquake source parameters from T-waves is still very challenging (Slack et al. [1999]), thus few general trend results have been obtained over the years in this respect.

We have already mentioned Eaton et al. [1961]; Ben-Menahem & Toksöz [1963]; Talandier & Okal [1979], who pointed out that the duration of the T-phase may be used to estimate the length of the ruptured zone. Dziak [2001] went further, studying a total of 179 northeast Pacific ocean earthquakes. The author empirically related T-phase characteristics with earthquake focal mechanisms and concluded that, on average, T-waves would be less energetic for normal and reverse fault earthquakes than for strike-slip events of the same magnitude. He attributed this effect to the fact that a S-wave radiation pattern would more efficient than a P-wave radiation pattern in producing T-waves. More specifically, he observed that T-wave energy tends to decrease when dip-slip motion increases. His observations suggest that fault parameter information is contained within the T-wave signal packet. These results were confirmed by Odom & Soukup [2002, 2004], who also predict that normal-fault earthquakes are poor generators of T-waves. However, Chen et al. [2015] later reported apparently opposite behavior using inland broadband stations in Taiwan and along the Ryukyu Arc to investigate a modest dataset including 17 T-waves that propagated westward through the Philippine sea. Their main finding is the very high probability of excitation of the T-waves by the earthquakes located to the south of the Mariana Arc, whose western shore slope is strongly concave. Almost all these earthquakes are of normal fault type. It is not clear, however, which of the concave bathymetry or the earthquake type is responsible for the high amplitudes observed.

These observations illustrate well the great variability and complexity inherent to T-waves. Note that the presence of a receiver-side acoustic-to-elastic wave conversion makes the analysis even more complicated. In that case the duration of recorded T-phases has proven to be largely affected by the shape of the coast in the acoustic-to-elastic conversion area (e.g. Cansi & Bethoux [1985]).

In the case of large oceanic earthquakes, T-waves received can be used to map the various compo-

nents of the rupture (Graeber & Piserchia [2004]), as often done with body waves (e.g. Walker et al. [2005]). As also mentioned above, Graeber & Piserchia [2004] observed a strong variation of back-azimuth and arrival times when studying six large teleseismic earthquakes using hydro-acoustic triplet stations. This allowed them to map point-by-point the areas (up to several hundred kilometer wide for the strongest events) in which elastic-to-acoustic coupling takes place. This constituted the first use of T-phases for earthquake source tomography. A similar approach was used by De Groot-Hedlin [2005], Guilbert et al. [2005] and Tolstoy & Bohnenstiehl [2005], who simultaneouslyestimated the earthquake rupture along the fault plane of the great Sumatra earthquake ($M_W = 9$) of December 26, 2004 using T-waves. Although using different approaches (compared in Tolstoy & Bohnenstiehl [2006]) these articles all used remote hydrophone(s) in the Indian ocean. They precisely tracked the event rupture for example by following the the variations of signal arrival azimuth with time at each station (Guilbert et al. [2005]). The hydro-acoustic analysis has proven to be a valuable tool in studying the rupture of this large submarine earthquake. Indeed the documented change in rupture speed during this destructive event was not clear from seismic data alone using classical source inversion methods, due to the exceptional fracture duration (more than eight minutes). Since then, a comparable study has been carried out concerning the Tohoku ($M_W = 9$) earthquake of March 11, 2011 Yun & Lee [2013].

1.8 T-waves and tsunamis

Long gravitational waves (tsunamis) propagate at the ocean free surface and are usually generated following submarine earthquakes or submarine mass failures such as landslides and slumps. When reaching the coasts, these extremely long-period waves can cause disastrous human and material loss. Although infrequent, tsunamis are among the most destructive catastrophic events in history. Hence the International Tsunami Information Centre of the UNESCO estimated that they have caused more than 600,000 casualties (228,000 during the 26 December 2004 Sumatra, Indonesia tsunami alone), as a result of the almost 300 recorded events over the past four millennia. The reader is referred to Okal et al. [2009] and Okal [2011b] for recent reviews on the topic. T-waves and tsunamis were suspected to be related since the very first articles dealing with T-waves (e.g. Tolstoy & Ewing [1950]). Indeed, some tsunamigenic earthquakes had produced strong T-waves. Moreover, as discussed in Section 1.1, T-waves, like tsunamis, were suspected to be generated by surficial earthquakes. These considerations led Ewing et al. [1950] to suggest the use of T-phases for tsunami warning. Their theory, however, was early strongly criticized by Leet [1951] and Wadati & Inouye [1953], who disputed the reality of this supposed correlation between T-waves and tsunamis. Also, as we have recalled above, T-waves were also observed after deep earthquakes (e.g. Linehan [1940]; Northrop [1974]; Okal & Talandier [1997]) refuting the hypothesis of Ewing et al. [1950]. Furthermore, tsunami generation is now known to depend only slightly on earthquake depth (Ward [1980]). T-waves and tsunamis result from different parts of the source frequency spectrum. Indeed, tsunami earthquakes are slow events generating low frequencies (typically below 2 mHz, Kanamori [1972]) while T-waves exhibit higher frequencies (> 1 Hz Okal et al. [2003]). Nevertheless the possible link between the two phenomena has generated interest in the scientific community for years (Eaton et al. [1961]; Walker et al. [1992]; Okal et al. [2003]; Salzberg [2008]). Johnson [1970] and Okal & Talandier [1986] suggested that the length of the T-phase wave train, rather than its amplitude, may be associated to seismic moment, and thus to tsunamigenic potential (Kanamori [1972]; Abe [1973]) and examined the possible application to tsunami warning. However, afterwards, Walker et al. [1992] and Walker & Bernard [1993] suggested some connection between T-wave spectral amplitude and tsunamis, but using a rather sparse dataset (Okal et al. [2003]). A noteworthy improvement regarding T-waves with regards to tsunamigenesis has been made after the catastrophic Papua New Guinea tsunami of 17 July 1998 (10-15m high, 3000 people killed),

triggered after a rather weak earthquake ($M_w = 7.1$). The normal rupture speed of this earthquake[8] challenged our understanding of tsunamis and resulted in the development of new models of tsunami generation that more realistically represent the reality. It is now accepted by most scientists that that tsunami was due to a massive submarine slump that occurred following the earthquake (Tappin et al. [2008]). This model is consistent with the characteristics of a T-wave, recorded by a hydrophone next to Wake Island, whose long duration and complex spectrum can hardly be attributed directly to the earthquake (Okal [1999, 2003]). Therefore, T-waves may be useful to detect sedimentary resonances involved in compaction, slumpage, or submarine landslide (Caplan-Auerbach et al. [2001]) and causing rapid displacements of the seafloor that may be sometimes responsible for tsunami generation (Walker et al. [1992]).

Using T-waves, Okal et al. [2003] determined the timing of the 1998 Papua New Guinea event and suggested that these waves are too sensitive to small-scale details of the source process to reliably estimate the overall, lower-frequency earthquake source properties controlling tsunami excitation (Kozdon & Dunham [2014]). Nevertheless they showed that many tsunami earthquakes exhibited relatively low energetic T-waves compared to their seismic moment, which would be, to them, a consequence of the slow fracture speed ascribed to these events.

Therefore, some links are nowadays known to exist, and could likely be used for tsunami warning. Studying the great Sumatra-Andaman earthquake of December 2004, Tolstoy & Bohnenstiehl [2006] emphasized the usefulness of hydro-acoustic data as a tool for rapid assessment of the size and character of large submarine earthquakes. The authors sadly remarked that all the monitoring stations in the Indian Ocean basin recorded T-phases exhibiting a duration of more than ten minutes, which could thus have been seen as a sign of danger. Comparison with existing duration-moment data (e.g., Okal & Talandier [1986]) would have identified the great size and tsunamigenic potential of this event within 45 min of the start of the rupture and may have saved many lives. In this regard, T-phases could also be used to identify earthquake involving splay-faulting, which also explains some extreme local tsunamis in events that produce only moderate tsunamis at large distance (Salzberg [2008]).

More recently, in the context of tsunami characterization problems, Caplan-Auerbach et al. [2014] estimated, based on T-waves, the speed of the submarine landslide that occurred during the West Mata eruption in 2010.

It is worth mentioning that, apart from T-waves which are purely acoustic modes in the ocean, researchers also study another type of acoustic waves associated with tsunamigenesis and commonly called hydro-acoustic waves (HAW). These highly-energetic waves are emitted by the water column above the tsunami generation zone, which, due to its compressibility, acts as an oscillatory generator for these quasi-horizontally traveling waves (Prestininzi et al. [2016]). As T-waves, these waves travel long distance at the speed of sound in water but exhibit lower characteristic frequencies (around 0.1 Hz). HAWs are considered as another potential means of enhancing the promptness and the accuracy of tsunami early warning systems (Abdolali et al. [2015]). HAWs might be observable with hydrophones, if these instruments do not clip on the large-amplitude waves generated by megathrust events (Kozdon & Dunham [2014]).

1.9 Study of the properties of the propagating media using T-waves

After passing through the Earth's crust in the form of seismic waves, T-waves travel in the ocean and are sometime converted back into seismic waves before being recorded by sensors. Consequently, fingerprints of their journey through the different environments in which they propagated may be present within their structure, and may thus be used to gather information about these media in which they propagated. Of course this topic also depends strongly on the issues mentioned in previous sections because it is difficult to deduce any information on the propagation media e.g. if the source

[8] Other similar observations have been made since then, for example for the 2011 Tohoku earthquake (Okal [2013])

position is poorly known or if the propagation mechanisms are ambiguous. That is why there are only a few articles showing such results. In what follows we will distinguish between the study of the (visco)elastic media below the ocean floor or on the ground and the study of the ocean.

1.9.1 Studying the earth with T-waves

We have already mentioned in Section1.6 the research works dealing with the converted T-waves observed after conversion at a coast. These signals can provide information on the properties of the upper continental crust (e.g. Koyanagi et al. [1995]; Kosuga [2011]). Apart from these studies let us mention the work of Shimamura & Asada [1975], who showed recordings of T-waves generated by deep-focus earthquakes (between 200 and 500 km) and recorded 1000 km away from the epicenter by an array of ocean-bottom seismometers deployed in the deep western Pacific ocean, well below the SOFAR channel axis. They used these data to estimate the attenuation of the seismic waves in the lithosphere, between the earthquake hypocenter and the sea surface, which was found to be very small in order to explain their observations.

The same kind of reasoning regarding seismic attenuation and T-waves later led Okal & Talandier [1997] to obtain an important indication of the continuity of a south American slab. Indeed, the authors reported a $S \rightarrow T$ wave generated following the great Bolivian deep earthquake of June 9, 1994 in the south American subduction zone. The frequency content of the documented T-phases and the timing of their most energetic arrival required channeling of the S wave from the hypocenter to the conversion point through weakly attenuating material, which in turn added supportive evidence for the mechanical continuity of the down-going slab, at least beneath this particular part of the South American plate, despite the observed aseismic zone between 300 and 600 km. At the same period Fox & Dziak [1999] observed the internal deformation of the Gorda plate based on the monitoring of generated T-waves.

Let us also mention Dziak et al. [2004a], who used T-phases to estimate the velocity of Pn waves waves along the east and west flanks of the mid Atlantic ridge.

1.9.2 Studying the ocean with T-waves

Compared to electromagnetic waves for example, the propagation of sound in the ocean is particularly effective and sensitive to variations of temperature and/or pressure (see Frosch [1964]). Hence controlled, manmade acoustic waves have been used successfully to image the ocean, from large mesoscale variability (the first acoustic observation is Hamilton [1977]), internal tides (Dushaw et al. [1995]; Ogasawara et al. [2008]), El Niño and Southern Oscillation (ENSO, e.g. Ogasawara et al. [2006]) to fine structures (e.g. Holbrook et al. [2003]; Dunn [2015] or Dushaw et al. [2016]). Long-range acoustic transmission is also considered in the context of a recent and important field: measuring climate change and its impact in the ocean. Indeed, as the speed of sound in the ocean depends on the water temperature, long-distance recordings of controlled sound sources might allow the community to estimate the average temperature over the wave path (see Figure 1.10). The idea has been suggested in the late 1980s by Munk & Forbes [1989], who underlined the fact that the ocean warming induced in the deep ocean by greenhouse gases (estimated at 0.005°C per year at that time) was too small to be measured locally but should be detectable above the gyre and mesoscale noise, given a ten-year campaign of measurements at nearly antipodal distances. In this setting, the anthropogenic temperature increase should result in a decrease in travel time, estimated at 0.1 to 0.2 s per year. The idea has given rise to a feasibility test that was then successfully carried out by Munk et al. [1994], proving that the climatic signal was detectable with fair precision based on teleseismic manmade 57 Hz signals of 3 kW, and the campaign itself was then launched. It was called the Acoustic Thermometry of Ocean Climate (ATOC) campaign, and the results obtained proved comparable with those obtained based on other methods (ATOC Consortium [1998]). The experiment was stopped following a controversy

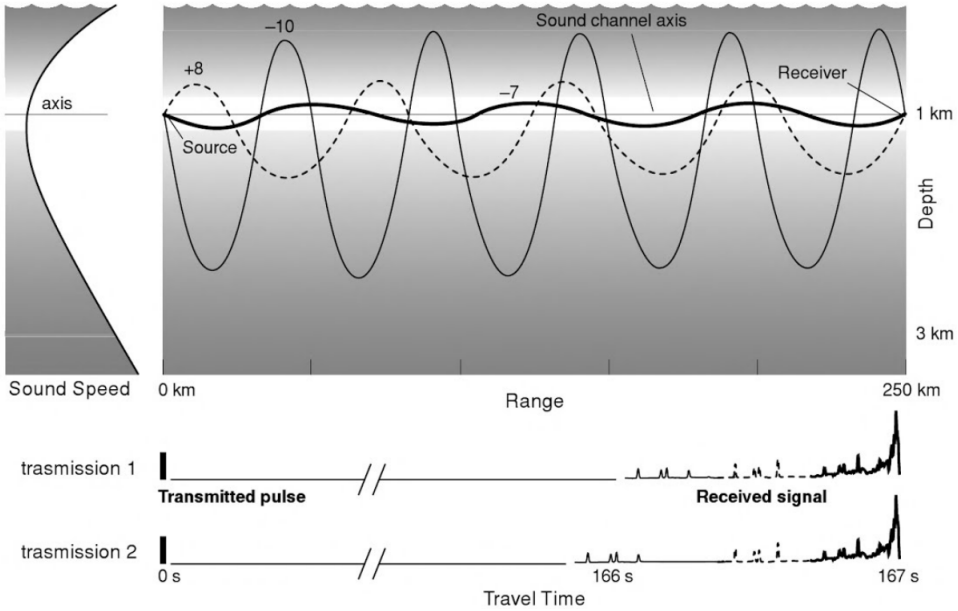

Figure 1.10 – Cartoon of an ocean acoustic tomography method. The minimum in sound speed provides an axis for an acoustic waveguide. The time sequence of ray arrivals is from steep (thin) to moderate (dashed) to flat (heavy) launch angles (flat, axial rays generally cannot be resolved). A representative ray for each of the three classes is shown in the upper panel. Transmission 2 (relative to 1) shows earlier arrivals of steep rays, but no change otherwise. This is consistent with a warming of the upper ocean (or less likely, a warming of the abyssal ocean), with intermediate and axial depth unchanged. After Munk [2006].

with the environmental community (see Munk [2006] for the whole story) but the topic still remains an active field of research nowadays (e.g. Aulanier et al. [2013]).

In the case of T-waves, as the source is a volcanic or seismic event and is consequently not controlled nor located accurately, getting information on the ocean is even more difficult. Of course, once their mode of propagation was understood, T-waves have allowed people to estimate the mean value of the sound velocity along their oceanic path (e.g. Ewing et al. [1952]) but the information is nowadays only of little value, precisely because it is a mean value. As an illustration, seasonal variations in oceanic modal group velocity can involve a time difference of 9 seconds over a 5000 km path, already far below the large errors routinely made in picking T-phase arrival times from earthquakes (De Groot-Hedlin et al. [2004]). Climate change induces differences that are typically 100 times smaller, which is thus currently an unreachable challenge.

Nonetheless, T-waves have been used to study the oceans. Sugioka et al. [2005] for example, following the work of Dushaw et al. [1995], who used manmade sources, used stacking of T-waves generated by underwater volcanoes to study internal waves in the ocean. Diurnal variations in the SOFAR channel were found by analyzing the travel time differences from the source to the receivers. More recently, Evers & Snellen [2015] used T-waves to image the ocean. Their study shows the ability of passively probing the variation of SOFAR channels of the ocean as a function of distance and of latitude using waves resulting from ridge earthquakes. Their results compare well to those obtained with manmade acoustic sources, but are still too noisy to detect seasonal changes, and all the more so to monitor the effect of climate change in the ocean. This is also confirmed by the work of Heaney & Campbell [2016] who evaluated numerically the impact of mesoscale oceanic variability on teleseismic T-phases based on a two-year time series of ocean state estimations. Their calculations predicted a deviation of back-azimuth of 2° on a 9100 km-long propagation path, for the setting considered. This effect is not negligible but would be too small to be detected in the case climate change variability.

This observation is also confirmed by the work of Heaney & Campbell [2016], who numerically assessed the impact of mesoscale ocean variability on teleseismic T-phases based on a two-year time

series of ocean state estimations. Their calculations predict a 2° back-azimuth deviation over a 9100 km-long propagation path, for the case under study. This effect is not negligible but suggests that the influence of subtle temperature variations in the oceans induced by climate change would be too small to detect based on such methods.

1.10 T-waves modeling and numerical simulations

The complexity of phenomenon relates to T-waves, at the interface between seismics and underwater acoustics, limits the possibility of detailed or full theoretical analysis. As many other research areas, ocean acoustics has thus benefited from computer science (Jensen et al. [2011]), leading to progress in T-waves studies. Computers were first involved in T-phase spectrum analysis (Milne [1959]) and in the localization of conversion points based on hydrophone signals (e.g. Johnson [1964]), before being used, since the 1980s, with numerical methods for T-wave simulation. Although simple mathematical models for abyssal T-waves have been proposed since the 1960s (Johnson et al. [1967]), the first synthetic T-phases were computed by Cansi & Bethoux [1985] using a diffraction-based model. They assumed that the seismic T-waves recorded after conversion at the continental slope were the sum of discrete arrivals coming from various points of the shore, and computed synthetic seismograms that were in relatively good agreement with the measured ones.

Following the exponential growth of numerical capabilities, starting in the late 1990s many articles studying T-waves from a numerical point of view have been published. The reader is referred for instance to Jensen et al. [2011] for a description of most of the numerical approaches mentioned here such as ray tracing, finite differences (FD), finite elements (FEM), normal modes, parabolic equation (PE) techniques, or wavenumber integration.

To give a brief summary, we can begin with Sperry et al. [1999], who modeled downslope conversion of T-waves using the 2-D hybrid method of Schmidt et al. [1995]; Goh & Schmidt [1996]; Goh et al. [1997] based on wavenumber integration, finite elements and boundary integrals. The same authors (Schmidt et al. [2004]) later used the virtual source algorithm that they developed (Schmidt [1995]; Goh et al. [1997]) to model the generation of T-waves from scattering at rough interfaces, implemented using a Rayleigh-Kirchhoff approximation.

Using a simple modal framework De Groot-Hedlin & Orcutt [1999, 2001a]; De Groot-Hedlin [2004] computed synthetic T-phases envelope by considering secondary point sources distributed over the seabed and exciting low-order acoustic modes proportionally to the acoustic modal amplitude, and to the ground motion resulting from the earthquake evaluated at the local ocean depth. Synthetic T-waves were later computed using a similar approach by Yang & Forsyth [2003] and Obara & Maeda [2009]. Park et al. [2001]; Odom & Soukup [2002, 2004] instead used a more sophisticated model involving mode coupling induced by seabed roughness. In their work on ocean passive probing with T-waves, Evers & Snellen [2015] used a range-dependent acoustic method based on adiabatic acoustic modes that they developed (Snellen et al. [2011]) to model T-waves generated by shallow earthquakes at ridges. The inferred spatial variations of T-wave velocity obtained were compared to measured ones and proven to be physically relevant.

Let us also mention that methods based on ray tracing, such as Gaussian beam techniques, are still being employed (e.g. by Lin et al. [2014] and Chen et al. [2017]), however the most widely used numerical methods in ocean acoustics are nowadays based on the parabolic approximation because that approximation allows for the computation of long-range acoustic propagation at high frequency at a reasonable computational cost (e.g. Xu et al. [2016]; Sturm & Bonnel [2016]; Heaney & Campbell [2016]; Collins & Siegmann [2017]). First introduced in underwater acoustics by Tappert [1974, 1977], these methods have been extended since then by a large number of contributions in order to be able nowadays to handle range dependence (when it remains not too strong), elastic media, or complex sources (see e.g. Lee et al. [2000]; Xu et al. [2016] as well as the inset above). The domain of T-

waves was no exception. We have already cited the works of De Groot-Hedlin & Orcutt [2000] and Frank et al. [2015], who studied conversion of T-waves at shore based on the parabolic equation. Downslope conversion and abyssal generation of T-waves have recently been modeled based on a 2-D elastic parabolic equation by Frank et al. [2012, 2015]. Teleseismic 3-D acoustic parabolic-equation simulations of T-waves have also been conducted by Heaney et al. [2013, 2017], who showed the contribution of 3-D effects such as bathymetric diffraction, which allowed them to explain observed arrivals in apparent acoustic shadow zones located behind islands and not explainable based on $N \times 2D$ simulations. Parabolic simulations of T-waves were also used by Heaney & Campbell [2016] to study the effect of mesoscale variability on teleseismic propagation.

However, the high computational efficiency of these methods comes at a price in terms of the physics that can be modeled because they rely on an assumption of weak range dependence (see the inset on the parabolic approximation above), and thus become inaccurate when range variation is important. Unfortunately, this may occur in regions of steep bathymetry, or when the impedance contrast between the ocean and the sea bottom is high (De Groot-Hedlin [2008]). This has consequently motivated the use of full wave methods.

T-wave finite-differences calculations have therefore been carried out, apparently since 1997 to the best of our knowledge, with McLaughlin [1997] showing 3-D linear elastic results of downslope conversion from seismic to acoustic, probably in a small computational domain at that time. The complementary part of the propagation, from acoustic to seismic, was modeled a year layer in 2-D by Piserchia et al. [1998] based on innovative code coupling between ray tracing and finite differences. The following years, additional 2-D finite-difference simulations of T-wave conversion at shore were carried out by Rodgers & Harben [2000] as well as Stevens et al. [2000, 2001]. De Groot-Hedlin [2008] later compared, for purely acoustic models, finite-difference results to parabolic equation results, as well as to analytical results when available. Her benchmarks included downslope conversion of acoustic energy, which involves mode coupling. The results indicate that the finite-difference method accurately solves for the acoustic wave field at all propagation angles and is more accurate than the parabolic equation method near the source. However, in addition to their high computational cost, an important drawback of finite-difference methods is their difficulty in handling dipping interfaces, which often have to be modeled as staircases, leading to spurious numerical diffraction by these artificial staircases.

This drawback is fortunately not present in another popular family of full-wave numerical methods: finite element techniques. The approach can be traced back to the 1940s in the structural mechanics field with Hrennikoff [1941] and McHenry [1943], who used one-dimensional elements for the computation of stresses in continuous solids. In its current form in 2-D, it was initially developed by Turner et al. [1956] for the aircraft industry. Some classical textbooks are for example Zienkiewicz & Taylor [1977], with many contributions from Zienkiewicz and his group to that popular technique, Hughes [1987], or Bathe [2006], among others. Finite elements started to be used in underwater acoustics in the late 1970s with Carlson et al. [1976]; Fix & Marin [1978]; Kalinowski [1979]; DeSanto [1979]. The future of finite elements in underwater acoustics is examined by Jensen & Zampolli [2010]. Although recommended for example by Buckingham [1992] for ocean-acoustics propagation modeling, the method has not often been used for T-wave simulations. We can cite Balanche et al. [2009] who investigated, in planar 2-D, the influence of the earthquake source radiation pattern on T-waves. Unfortunately there is sometimes a confusion between T-waves and P-waves. Recently, a particular formulation of the finite-element method called the Spectral-Element Method (SEM), originally coming from the Navier-Stokes community (Patera [1984]) and very popular in seismology (Komatitsch & Tromp [1999]), was introduced for underwater acoustics by Cristini & Komatitsch [2012] and was then used by Jamet et al. [2013] to simulate plane-strain 2-D regional T-waves resulting from ridge earthquakes. Let us mention that the spectral-element method is central to my thesis and will thus be detailed in the next chapters.

As a possible conclusion, and given the relative strengths and drawbacks of each of these numerical methods, it seems to us that strategies coupling full wave methods (FD, FEM, SEM...) in the vicinity

of the source (and/or of 2-D or 3-D objects under study) to parabolic equation techniques for long-range propagation in the ocean could be particularly promising for the near future. This should preclude long-distance propagation of inaccuracies in parabolic equation solutions usually observed near the source (De Groot-Hedlin [2008]), while taking advantage of the computational efficiency of that method for long-range propagation. Of course, 3-D full wave techniques will prevail in the longer future. However they are currently still very expensive at T-waves frequencies for very elongated domains, and will remain so for one or two decades (but not more than that).

Chapter 2

Study of a T-wave dataset in the Ionian Sea

This short chapter presents observations of T-waves in the Ionian Sea made in collaboration with the Istituto Nazionale di Geofisica e Vulcanologia (INGV, National Institute of Geophysics and Volcanology) of Rome, Italy. The data shown here constitute, to us, an instructive illustration of the phenomenon. Moreover few articles deal with T-waves in the Mediterranean sea (we can cite Galanopoulos & Drakopoulos [1974]; Cansi & Bethoux [1985]; Solarino & Eva [2007] and Carmona et al. [2015]).

2.1 Introduction

The Istituto Nazionale di Geofisica e Vulcanologia (INGV, National Institute of Geophysics and Volcanology) was created in September 1999 as a result of the fusion of several geophysical research institutes in the field of seismology, geochemistry and volcanology in Italy. With its headquarters in Rome and important facilities all around Italy, it is currently the largest European entity dealing with research in geophysics and volcanology. INGV also conducts 24-hour seismic surveillance of the whole Italian territory, real-time volcanic monitoring, early warning and forecast activities. Networks of geophysical and oceanographic sensors, including seismometers and hydrophones, deliver a continuous flow of observations to the acquisition centers of Rome, Naples and Catania, were the data are analyzed (website INGV [2017]). It has been recognized for some time by INGV that the Ionian sea, south east of Italy, is an interesting place to observe and study T-waves. Indeed, when an earthquake occurs near the west coast of Greece, which is a particularly active geotectonic zone (Burton et al. [2004]; Kokinou et al. [2005]), INGV seismic stations (including one sea floor observatory) located in Sicily and Calabria often record significant T-waves that have crossed the Ionian sea (∼500 km, see example shown in Figure 2.1), if the magnitude of the earthquake is not too small ($M_w > 3.9$ or so) so that these T-waves can be observed. We have analyzed a large number of seismograms recorded in this area, allowing us to identify general trends for T-waves generation in Greece and their propagation in Italy. We noticed in particular that the Greek peninsula of Paliki is likely to produce strong T-waves.

2.2 T-waves observation

The location of the instruments used is shown in Figure 2.1 (top), which presents a global perspective on T-phase amplitude recorded at each station following a shallow earthquake in Greece. This event of magnitude $M_w = 4.7$ took place on May, 23, 2013 at 14:09:07.40 in the Greek peninsula of Paliki (latitude: 38.6488, longitude: 20.5813). The hypocenter was at a depth of 10 km (National Oceanic and Atmospheric Administration, later labeled as NOAA) but the moment centroid depth was only 2 km (Institute of Geodynamics of the National Observatory of Athens, later labeled as NOA). This earthquake illustrates phenomena related to regional T-waves relatively well. An example of T-phase

recorded on the Sicilian east coast is shown in Figure 2.1 (bottom). The arrival is very impulsive, it exhibits a short rise time and high amplitude compared to P and S-phases. It is similar to those recorded on volcanic atolls (e.g. Talandier & Okal [1998]). However, as expected from the literature (e.g Kosuga [2011]) , the map in Figure 2.1 shows that T-waves in the region are strongly attenuated when propagating inland. The T-phase observed furthest from the coast was recorded by station CLTA located only 120 km inland. It can also be seen from Figure 2.1 that the conversion from hydroacoustic to seismic T-wave is particularly efficient at steep slopes. Indeed, the east Sicilian and Calabrian coasts exhibit strong continental slopes (rarely below 10 degrees) apparently beneficial for T-wave conversion, whereas the gulf of Taranto is characterized by smooth slopes (around 1 or 2 degrees) that seem to preclude any conversion. Anyhow, these observations suggest a strong dependence of seismic T-wave amplitude on slope in the area, in line with the observations of Piserchia et al. [1998] and Talandier & Okal [1998] on Polynesian atolls for example, but not with the simulations of Stevens et al. [2000, 2001] in California. We shall return to this particular point in Chapter 4. It can also be seen that the instruments located in South Sicily are particularly prone to record T-phases following earthquakes in Greece, probably because of favorable bathymetry.

This property allowed us to approximate the seismic velocity of the T-wave recorded in Sicily from its arrival times at the three stations AGST, SSY and MEU, which are fortunately quite well aligned with the source (see Figure 2.1 and 2.2). The value found (4000 ± 1000 m.s^{-1}), although imprecise, is quite high and is close to the average crustal P-wave velocity documented in the area (Finetti [2005]; Accaino et al. [2011]; Calò et al. [2012]) in accordance with the observations of Talandier & Okal [1998] in French Polynesia and or Stevens et al. [2000, 2001] in California, but in apparent contradiction with Koyanagi et al. [1995] in Hawaii or Kosuga [2011] in Japan for example. Let us remark that this is apparently inconsistent with De Groot-Hedlin & Orcutt [2001b] as well, which would also suggest a propagation as S-waves after conversion at the Sicilian high continental slope. However, it is important to note the spreading of the phase along its propagation, showing that it is made of several components traveling at different speeds. The first arrival indeed seems to travel at the P-wave speed but contains little energy. In fact, the peak energy of the signal propagated at lower speed (around 2500 m/s), which is close to the local crustal S-wave velocity or surface wave velocity.

The analysis of particle motion at stations AGST and SSY (see Figures 2.3) confirms this comment. The source-station azimuth is east-west oriented, therefore we can suppose that the main direction of propagation of the wave is from east to west. This figure shows that the seismic T-phase is complex and composed of a mix of phases.

It can be noted however that the first arrival at station AGST is linearly polarized in the longitudinal direction, suggesting a P-wave. Surprisingly however, no clear evidence of a P-wave can be seen in the particle motion in the first arrival at station SSY. The recorded ground movement is rather polarized in the North-South direction, that is to say in the horizontal transverse direction, hinting at arrivals of SH or Love waves. This motion can be explained by refraction in the horizontal plane when the waves are transmitted from ocean to land (see Båth & Shahidi [1971]).

In addition to the seismic stations located inland, INGV operated the seafloor observatory SN-1 deployed at a depth of 2105 m, about 25 km offshore from the Sicilian east coast (see Figure 2.1). It was equipped with a set of geophysical and oceanographic instruments, including a three-component broadband seismometer (Guralp CMG-1T, 0.0027 to 50 Hz bandwidth and 100 Hz sampling rate, see Sgroi et al. [2007]). Following De Groot-Hedlin & Orcutt [2000], signal-to-noise ratios (SNRs) have been computed at stations AGST, SSY and MEU (see Figure 2.4) and compared to SNR for the vertical component recorded at ocean bottom seismometer SN-1. SNRs were computed by dividing the power spectrum of the T-phase by the power spectrum of an interval typical of the ambient noise at each receiver. They are very high compared to those computed in California (De Groot-Hedlin & Orcutt [2000]). No significant differences are observed between the different T-phase displacement components (termed N-S, Up-Down and E-W). Although not affecting much the frequencies below 2 Hz, the upslope conversion at shore and the propagation inland induce a drastic loss of high frequencies

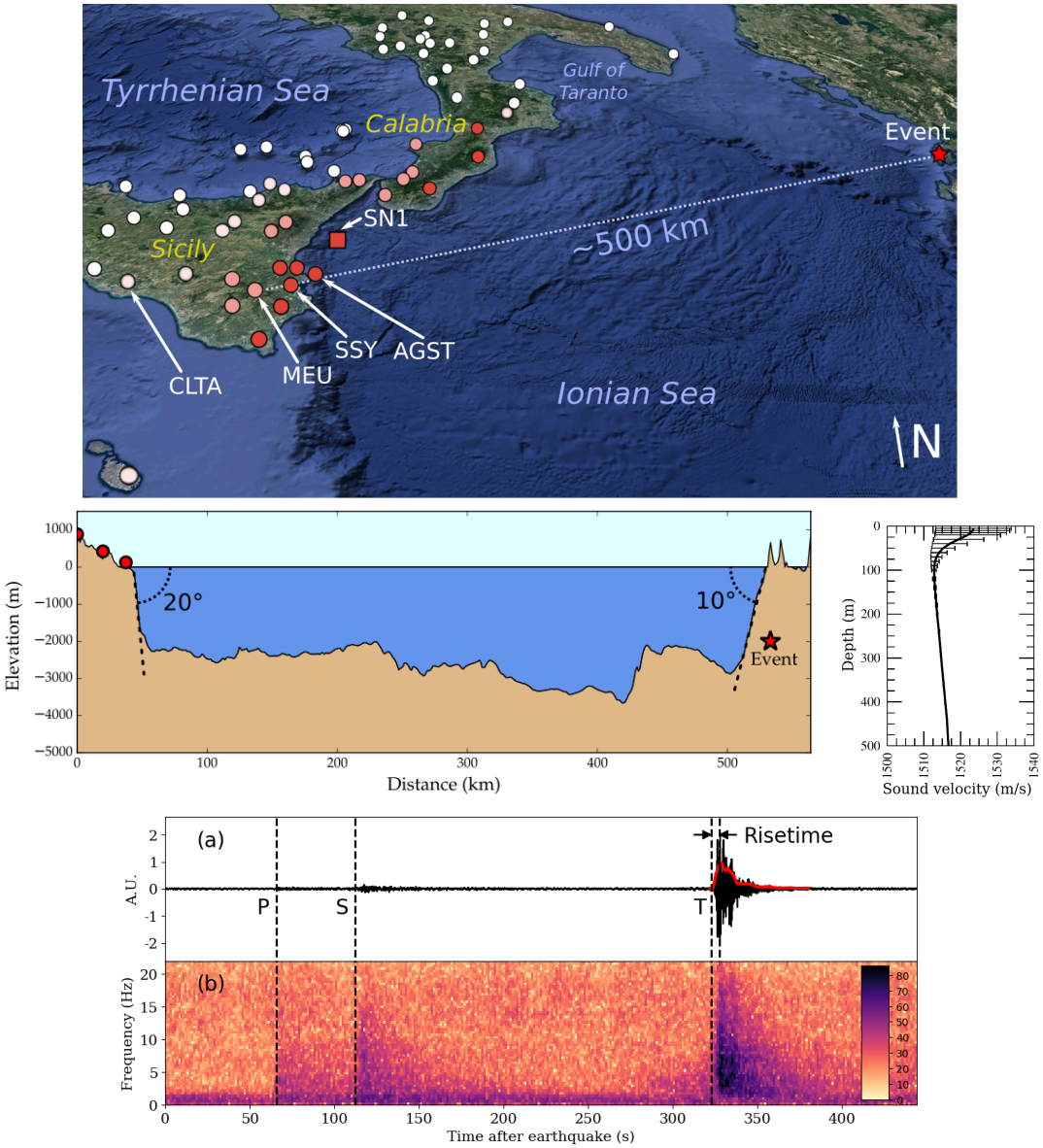

Figure 2.1 – Setting of a shallow Greek T-wave event. Origin time: 2013/05/23 at 14:09:07.40, latitude: 38.6488°, longitude: 20.5813°, hypocenter depth: 10 km (NOAA), centroid depth: 2 km, M_w = 4.7 (NOA). **Top**: Map of the Ionian sea describing the T-phases recorded by INGV stations after this earthquake. The moment centroid is indicated by a star. The red circles indicate stations that have recorded a strong T-phase (maximum amplitude at least twice above those of P and/or S waves), the light-red circles indicate stations that have recorded T-phases whose amplitude was comparable with that of P and S waves, and the circles colored with the lightest shade of red (like that of the CLTA station) correspond to stations that have recorded T-phases with an amplitude lower than that of P and S phases. The white circles indicate stations that have recorded P/S waves for this event but no T-waves. The SN-1 seafloor observatory is indicated by a red square. **Middle**, left: elevation profile corresponding to the light-blue dotted path drawn on the top map. Note that the vertical and horizontal scales are different. The three red circles represent the stations used to estimate the T-wave velocity after its conversion at shore. In increasing order of distance from the coast we find stations AGST, SSY and MEU. Middle, right: annual mean sound speed profile and relative temporal standard deviation in the Ionian sea (from Salon et al. [2002]). Note the different depth scales. **Bottom**: (a) Vertical component displacement seismogram (arbitrary displacement unit) recorded at Italian seismic station AGST. Arrivals of P, S and T-waves are clearly visible. An example of filtered T-phase envelope is shown in red. T-phase rise time is defined in the figure. (b) Power Spectral Density (in dB) as a function of time and frequency. Note the high frequency content of the T-phase.

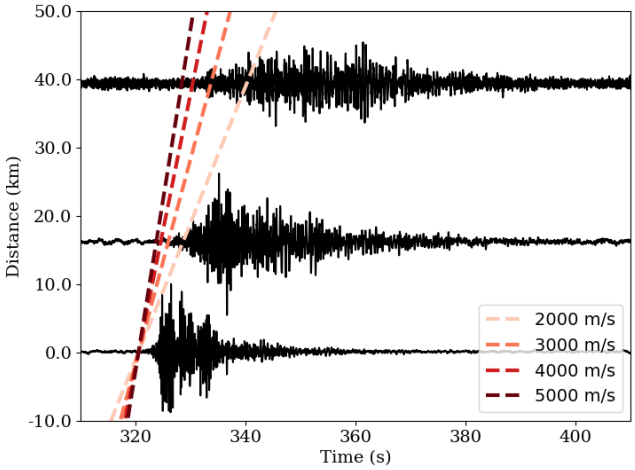

Figure 2.2 – Normalized north-south displacement seismograms at three selected aligned stations in the direction of the source. From top to bottom: MEU, SSY, AGST. The traces are distributed along the vertical axis according to the distance to station AGST of their projection on the blue dotted line in Figure 2.1 (top). The apparent group velocity of the first arrival is seen to be 4000±1000 m/s.

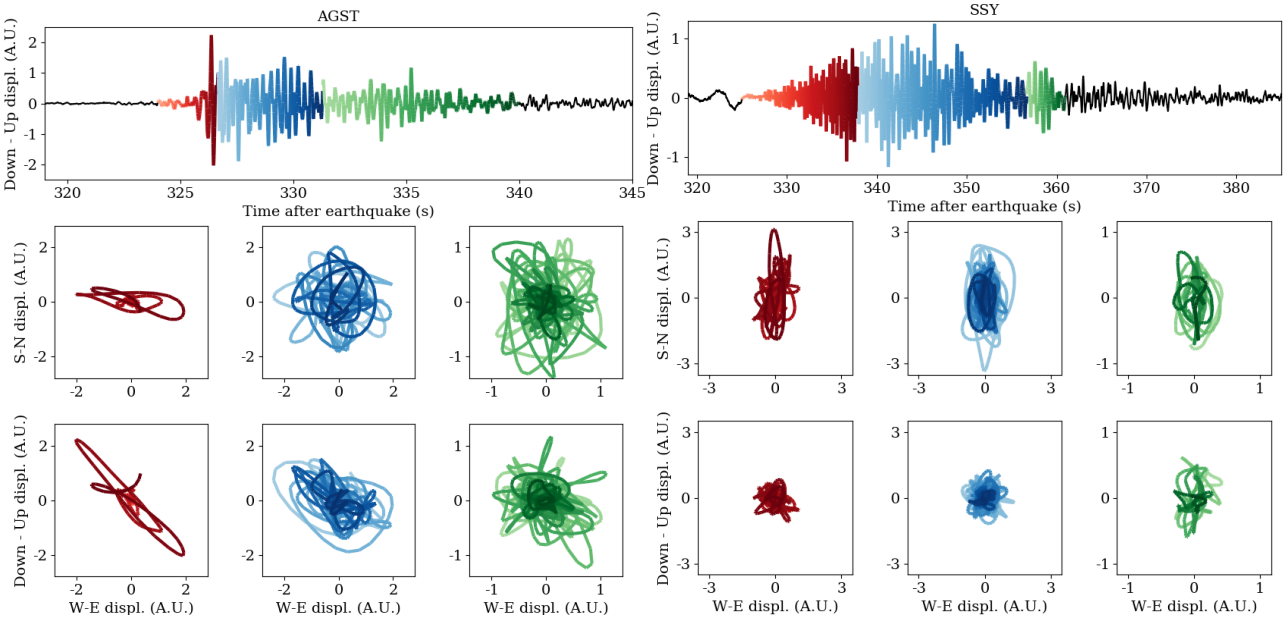

Figure 2.3 – **Left**: T-wave-induced particle velocity at station AGST as a function of time. Top: T-phase north-south displacement at station AGST (arbitrary units) as a function of time. Note the three colored time intervals. Middle and bottom: Corresponding particle motions in the horizontal and vertical planes containing source and receiver, respectively. The colors correspond to the upper image. **Right**: Same but at station SSY. Note the large transverse component.

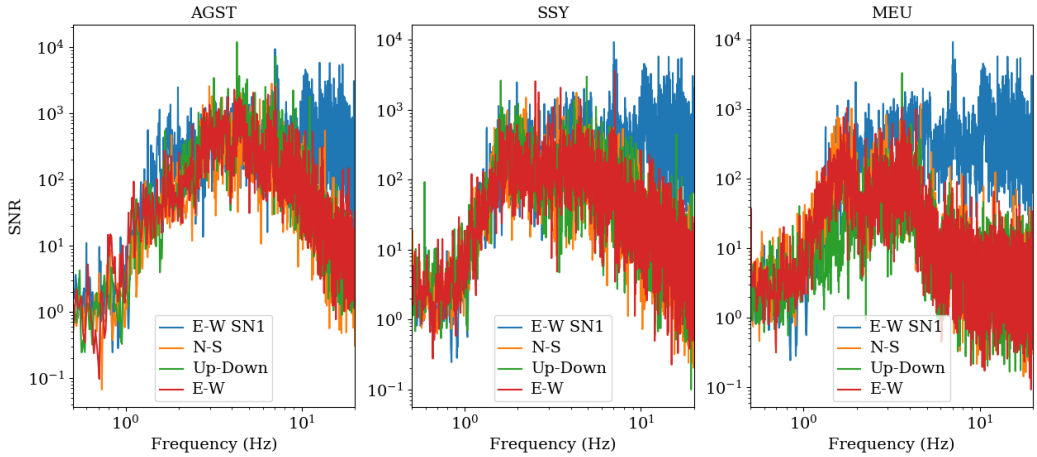

Figure 2.4 – Signal-to-noise ratios (SNR) at stations AGST, SSY and MEU, in log-log scale. SNRs were computed by dividing the power spectrum of the T-phase by the power spectrum of an interval typical of the ambient noise at each receiver. SNRs for the East-West (red), North-South (orange), and vertical components (green) are shown, compared to the SNR for the vertical component recorded at ocean bottom seismometer SN-1 (blue). Note the drastic fall of high frequencies involved with the conversion at shore, and the subsequent gradual losses with increasing distance from the coast.

(above 7 Hz), confirming the observations ofStevens et al. [2000, 2001], De Groot-Hedlin & Orcutt [2000] and Rodgers & Harben [2000].

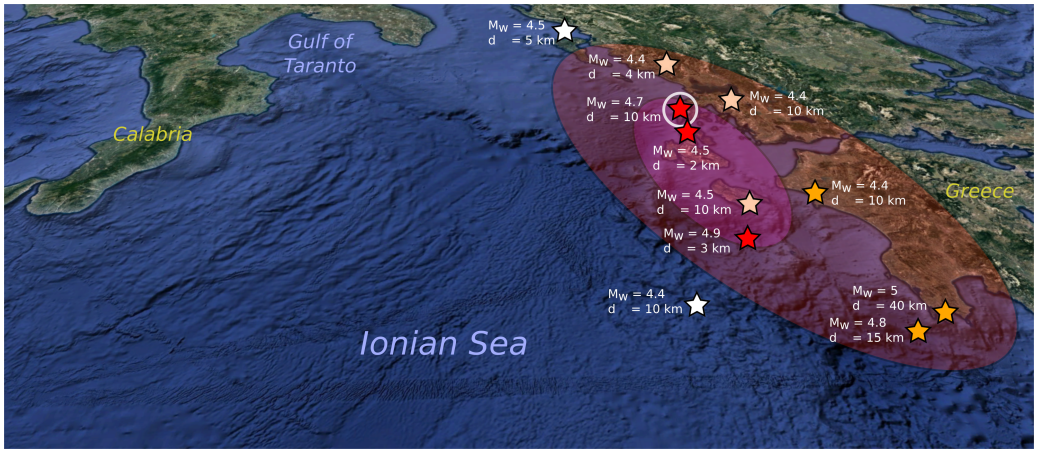

Figure 2.5 – For each earthquake indicated on the above map (star), both the characteristics from NOAA (magnitude and hypocenter depth d) and the quality of the generated T-waves are detailed. The classification has been made from the same kind of map than the one presented in Figure 2.1. Red stars: more than 5 Italian stations have recorded strong T-phases ("red" stations), orange stars: some Italian stations have recorded strong T-phases, light orange stars: T-phases recorded by several Italian stations, white stars: no T-waves visible. Earthquakes occurring in the red area are prone to generate T-waves. Earthquakes occurring in the purple area are particularly prone to generate strong T-waves. That area corresponds to the Greek peninsula of Paliki. The circle indicates the earthquake shown above.

For the sake of brevity we have only detailed here our observations for the earthquake studied above, however other events in Greece have been examined with respect with the T-wave that they have produced in Italy. The observations are summarized in Figure 2.5. We first selected a set of events for which P and S waves were recorded by Italian seismic stations, and then, for each selected event, we built the same map as the one shown in Figure 2.1. This allowed us to classify the earthquakes according to the T-phase recorded subsequently at Italian stations and thus to define the areas in which strong T-waves are likely to be generated. Figure 2.5 reveals that strong T-waves in this area are, for the most part, generated following earthquakes that occurred near the Greek peninsula

of Paliki, which is a particularly active tectonic area (see Kokinou et al. [2005]) characterized by steep continental slopes. We did not observe any T-phase following the earthquakes located below flat seabeds (see Johnson et al. [1967] or D'Spain et al. [2001] for example), which suggests that the preferred T-wave generation mechanism in that area is downslope conversion, described in Section 1.2. The three most powerful T-waves were generated following very shallow earthquakes (depth < 3 km), which suggests a strong relationship between T-wave strength and earthquake depth in the area.

Let us note that in our study T-phases were never observed on the Tyrrhenian Sea islands, although rather big T-phases were recorded on the Sicily and north Calabria coasts (see the top map in Figure 2.1). This suggests that no conversion can occur from seismic T-wave to hydroacoustic T-wave, which results in a very efficient bathymetric blockage.

2.3 Conclusions

The Ionian sea is a convenient place to observe T-waves. Indeed the Greek west coast is an active geotectonic zone in which a significant number of shallow earthquakes occur, and it exhibits steep slopes that prove to favor T-wave generation by downslope conversion. On the other side of the basin, Sicily and Calabria present steep eastward continental slopes fostering the conversion into seismic waves. All these features imply that most of the Greek earthquakes produce strong T-waves that are then recorded particularly well by the inland Italian seismic network.

More specifically, the coastal stations in Sicily and Calabria record very clear T-phases exhibiting exceptionally-high signal-to-noise ratios in the frequency band 1-7Hz, even compared to a seafloor seismic station. However, T-wave conversion at shore and the subsequent inland propagation do not come without an important loss of high frequencies. In any case the influence of slopes on T-waves is seen to be of crucial importance in the area, both on the source and receiver sides. The study of arrival times at three aligned stations proved that the first wave packet of a seismic T-wave in Sicily travels at the speed of the P-wave but that the most energetic part is slower. Particle motion revealed the generation of a Rayleigh wave in the conversion, but also showed that the main part then propagates as SH waves until it is completely absorbed. Let us mention that the Mediterranean sea is characterized by a shallow and narrow SOFAR channel compared to the one in the oceans (e.g. Salon et al. [2002] and middle right curve in Figure 2.1). However, the simulations that we will perform in Chapters 4 and 5 (see also Appendix A) will show that this parameter is only of secondary importance for understanding this regional phenomenon.

In conclusion, this data set review allowed us to identify inconsistencies with previous observations. Hence the phenomena involved in conversion at slopes, both on the source and receiver sides, are complex, site-dependent and poorly understood. This led us to develop a numerical code able to take into account all the complexity involved, such as steep slopes, long range propagation, fluid-solid coupling etc. 2-D parametric studies of the influence of slopes on T-wave generation and conversion at shore will thus be discussed in Chapter 4, and details on 3-D full-wave simulation attempts that we have made for the earthquake studied above are shown in Appendix B. The data used in our study were all downloaded from the public site `cnt.rm.ingv.it`.

Chapter 3

An axisymmetric time-domain spectral-element method for full-wave simulations

This chapter has been published as an article in: A. Bottero, P. Cristini, D. Komatitsch and M. Asch, An axisymmetric time-domain spectral-element method for full-wave simulations: Application to ocean acoustics, Journal of the Acoustical Society of America, vol. 140(5), p. 3520-3530 (2016).

At the interface between geophysics and underwater acoustics, T-wave complexity makes its characterization challenging. Among the parameters that need to be considered we identify complex geometries, fluid-solid coupling, attenuation, high frequencies, long-range propagation, 3-D effects, etc. Hence it is often difficult to deduce from field T-phases data what characteristics of the media have influenced them (see Chapter 1 and 2). With this aim in mind, numerical simulations seem to be a suitable, and nowadays necessary, approach.

As discussed in Chapter 1 many numerical results on T-waves were obtained with ray tracing techniques. This historical numerical method (still extensively used) has enabled researchers to draw the first conclusions on T-waves kinematics but failed to model abyssal T-wave, shadow zone arrivals, or T-wave amplitudes. Solvers based on normal-mode solutions or parabolic equations provided new hints (e.g. Frank et al. [2015]; Heaney et al. [2017]...) but at the price of strong assumptions (e.g. far field, small horizontal variations, no back scattering...), significant complexity in resolution as well in the interpretation of the results. Ideally one should turn to 3-D full-wave simulations in the time domain to correctly model the phenomenon. These numerical solutions of the full-wave equation are already known to be significantly more accurate and flexible than the parabolic wave equation (see for example De Groot-Hedlin [2008] for a comparison in the case of upslope acoustic wave conversion at shore, or Pinton & Trahey [2008] in the case of an ultrasound transducer) at the price of a much greater computational cost. However, given the high frequencies and distances involved, no numerical modeling of this kind has been performed yet. Although some attempts are in progress e.g. at Woods Hole Laboratory (USA), only pioneering 2-D simulations has been produced so far (see section 1.10 of this document). Though inconceivable some years ago because of their prohibitive computational cost, accurate 3-D simulations are nowadays contemplated. In the field of T-waves however, real 3-D simulations are still beyond current reach. Nevertheless, some attempts have been made though and are described in appendix B. Indeed, the ongoing drastic increase in computing capabilities (Komatitsch et al. [2002], Magnoni et al. [2014]) will bring the most expensive calculations made nowadays within the reach of any laboratory in ten years, as shown by the extrapolation of supercomputer power evolution that can be made for instance based on the data available in the Top500 database of the 500 fastest supercomputers in the world at a given time (Strohmaier et al. [2017]). Hence it seems to us important to start working right now on these topics, as full-wave time domain simulation will surely become standard soon and will most likely shed light on remaining issues

in underwater acoustics. Among other techniques, the spectral-element method in the time domain (SEM, Patera [1984], Komatitsch & Vilotte [1998], Tromp et al. [2008]) is an accurate and efficient option. It is based upon a high-order piecewise polynomial approximation of the weak formulation of the wave equation. It has been the subject of active research and developments in geophysics over the last 20 years. Particularly suited for high-performance computing, this method is now widely used for regional and global seismic wave propagation simulations (see e.g. Tromp et al. [2008] for a review) to solve both forward and inverse (i.e., imaging) problems. In ocean acoustics, Cristini & Komatitsch [2012] have already emphasized the high potential of the SEM. 2-D and 3-D versions of an efficient and widely-used implementation of this method in the so-called SPECFEM software package are available open source on the Computational Initiative in Geophysics (CIG) website. This code is particularly tuned for high-performance computing, and used by hundreds of laboratories in the world. For instance, SPECFEM is one of the twelve codes used by the UEABS (Unified European Application Benchmark Suite) to benchmark the new European supercomputers (`www.prace-ri.eu/ueabs`).

With the goal of studying T-waves dynamics, in my thesis I have developed an axisymmetric (2.5-D) version of SPECFEM. This chapter introduces and validates this numerical technique based on an axisymmetric formulation of the spectral finite-element method in the time domain for heterogeneous fluid-solid media. Note that SPECFEM 2.5-D includes fluid-solid coupling, viscoelasticity, anisotropy, high-order time schemes and the improved absorbing Perfectly Matched Layers (PML) of Xie et al. [2014, 2016]. Taking advantage of axisymmetry enables us to study relevant 3D configurations at a moderate computational cost. The axisymmetric spectral-element formulation is first presented, and validation tests are then performed. A typical application of interest in ocean acoustics showing upslope propagation above a dipping viscoelastic ocean bottom is then shown. The method correctly models backscattered waves and explains the transmission losses discrepancies pointed out in Jensen et al. [2007]. Finally, a more realistic application to a double seamount problem is considered.

3.1 Introduction

Among all the numerical methods that can be used to model acoustic wave propagation in the ocean (see e.g. Jensen et al. [2011] for a comprehensive review), finite-element techniques are methods of choice for solving the momentum equation in the time domain or the Helmholtz equation very accurately, and for handling complex geometries (Komatitsch & Tromp [1999]; Fichtner [2010]; Jensen et al. [2011]). They have for instance been used to study acoustic scattering by rough interfaces (e.g. Isakson & Chotiros [2011, 2015]), which is a topic of importance in reverberation studies and ocean bottom sensing, and for the study of diffraction by structures immersed or embedded within the oceanic medium (Zampolli et al. [2007]). When time signals are needed they can be obtained by Fourier transform from frequency-based simulations, or else obtained directly by solving the wave equation in the time domain. In this case, spectral-element methods (Cristini & Komatitsch [2012]; Jamet et al. [2013]) are of interest for performing numerical simulations because they lead to accurate results and an efficient implementation (Komatitsch & Tromp [1999]; Fichtner [2010]; Komatitsch [2011]; Peter et al. [2011]). In addition, they are well adapted to modern computing clusters and supercomputers (Tromp et al. [2010]). However, finite-element models have the drawback of requiring large computational resources compared to approximate numerical methods that do not solve the full-wave equation, for instance the parabolic approximation (Pinton & Trahey [2008]). Despite the recent development of very efficient perfectly matched absorbing layers for the study of wave propagation in fluid-solid regions (Xie et al. [2016]), which allows for a drastic reduction of the size of the computational domain, performing realistic 3D simulations in ocean acoustics still turns out to be difficult because of the high computational cost incurred. The main reason for this lies in the size of the domains classically studied in ocean acoustics, which often represent thousands of wavelengths. A first attempt was presented at low frequency in Xie et al. [2016], but when higher frequencies are required in the context

of full-wave simulations, 2-D simulations are currently still the only realistic option. In the case of underwater acoustics, Cristini & Komatitsch [2012] used a 2-D Cartesian (plane strain) version of the spectral-element method. This type of 2-D simulation has the disadvantage of involving line sources, i.e. nonphysical sources that extend in the direction perpendicular to the 2-D plane (Pilant [1979]). Physical effects and amplitudes are thus enhanced in an artificial manner and may lead to erroneous interpretation. For the same reason, comparisons with real data are difficult because amplitudes and waveforms are unrealistic.

A more realistic approach thus consists in resorting to axisymmetric simulations. If the source is located on the symmetry axis then this allows for the calculation of wavefields having 3D geometrical spreading with the cost of a 2-D simulation. Nevertheless, solving the weak form of the wave equation in cylindrical coordinates leads to a difficulty because of the potential singularity in elements that are in contact with the symmetry axis, for which $r = 0$ at some of their points and thus a singular $1/r$ factor. Several strategies have been proposed to overcome this difficulty. One approach consists of increasing the accuracy of the numerical integration when an element is close to the axis or lies on the axis and slightly shifting its position away from the axis (Clayton & Rencis [2000]). However, in such a case the source cannot be put on the axis, making simulations of point sources impossible. A better strategy was developed by Bernardi et al. [1999], who proposed to use a Gauss-Radau-type quadrature rule to handle this problem and remove the singularity. This approach was successful and several subsequent articles have implemented axisymmetric simulations using this strategy. For instance, Fournier et al. [2004] used axisymmetric cylindrical coordinates to simulate thermal convection in fluid-filled containers, and Nissen-Meyer et al. [2007, 2008, 2014] used a clever combination of four runs performed in cylindrical coordinates to simplify the computations of seismic wavefields in spherical coordinates in fluid-solid or in purely solid regions. However, to our knowledge ocean acoustics configurations with axisymmetric cylindrical coordinates have never been addressed. In this chapter we thus present an axisymmetric spectral-element method in cylindrical coordinates for such fluid-solid models that is particularly well-adapted to underwater acoustics.

The chapter is organized as follows: In Section 3.2 we describe the implementation of an axisymmetric spectral-element method in cylindrical coordinates for fluid and solid regions. Section 3.3 is then devoted to the validation of this implementation by providing comparisons with results obtained with analytical or other numerical methods. We first consider a flat bottom configuration, and then analyze a sloping bottom configuration that leads to significant backscattering, illustrating the interest of performing full-wave time-domain simulations. Finally, in Section 3.4 we illustrate the importance of taking backscattering into account in acoustic wave propagation in the ocean based on a configuration with two seamounts. This model exhibits strong backscattering effects that can only be modeled based on a full-wave simulation.

3.2 Axisymmetric spectral elements

In this section we will briefly present our axisymmetric spectral-element technique. Interested readers can learn more on spectral element methods in their Cartesian forms by referring to Cohen [2002]; Deville et al. [2002] or Fichtner [2010] for example. Let $\boldsymbol{x}$ denote the position vector. In the general case, the time-dependent displacement field $\boldsymbol{u}(\boldsymbol{x}, t)$ induced by an acoustic source $\boldsymbol{f}(\boldsymbol{x}, t)$ is related to the medium features by the 3D wave equation, which can be written in its strong form as

$$\rho \ddot{\boldsymbol{u}} = \boldsymbol{\nabla} \cdot \boldsymbol{\sigma} + \boldsymbol{f}, \tag{3.1}$$

where $\rho(\boldsymbol{x})$ is the distribution of density, $\boldsymbol{\nabla} \cdot \boldsymbol{\sigma}$ is the divergence of the stress tensor $\boldsymbol{\sigma}(\boldsymbol{x}, t)$, and a dot over a symbol denotes time differentiation. In a typical forward problem the source $\boldsymbol{f}(\boldsymbol{x}, t)$ and the material properties of the medium are known and we are interested in computing the displacement field $\boldsymbol{u}(\boldsymbol{x}, t)$. The reader is referred to Buehler & Shearer [2015] for example, which details how this equation is obtained.

From now on we will choose the cylindrical coordinate system (r, θ, z) - see Figure 3.1. The position vector is then expressed as $\boldsymbol{x} = r\hat{\boldsymbol{r}} + z\hat{\boldsymbol{k}}$ and any vector $\boldsymbol{a}$ is decomposed into its cylindrical components,

$$\boldsymbol{a} = a_r(r, \theta, z, t)\hat{\boldsymbol{r}} + a_\theta(r, \theta, z, t)\hat{\boldsymbol{\theta}} + a_z(r, \theta, z, t)\hat{\boldsymbol{k}}. \tag{3.2}$$

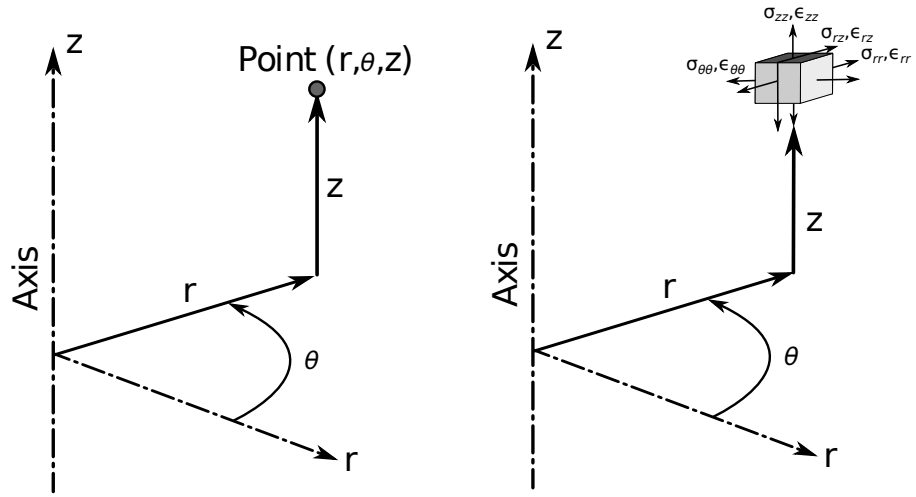

Figure 3.1 – Cylindrical coordinate system and components of the strain tensor $\boldsymbol{\varepsilon}$ and of the stress tensor $\boldsymbol{\sigma}$ in an axisymmetric setting.

At this point we choose the 2.5-D convention: we consider a 3D domain $\breve{\Omega}$ symmetric with respect to the axis $(r = 0)$ and suppose that the important loads are axisymmetric also and are thus independent of θ. Then, all the quantities of interest are independent of θ and, due to the rotational symmetry, the θ-component of the displacement is zero. This yields true axisymmetry resulting in a reduction of the order and the number of equations, while still preserving the possibility of non-zero out-of-plane components of stress, $\sigma_{\theta\theta}$. An example of such a configuration can be seen in Figure 3.2 (left).

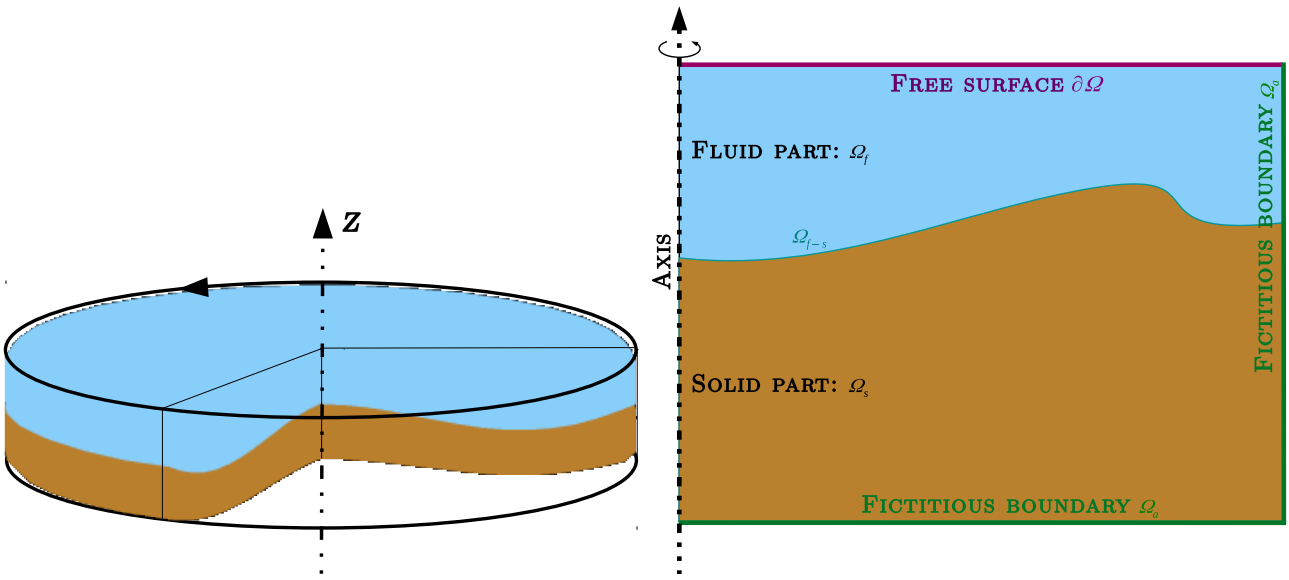

Figure 3.2 – **Left**: Axisymmetric medium generated by rotation of its 2-D meridional shape around the z-axis. **Right**: Meridional 2-D shape Ω and description of our notation.

Following Curie's symmetry principle, the symmetry of a cause is always preserved in its effects. Hence if the acoustic source $\boldsymbol{f}(r, \theta, z, t) = f_r(r, z, t)\hat{\boldsymbol{r}} + f_\theta(r, z, t)\hat{\boldsymbol{\theta}} + f_z(r, z, t)\hat{\boldsymbol{k}}$ does not depend on

θ, working in the 3D domain $\breve{\Omega}$ reduces to working in its meridional 2-D shape Ω, referred to as the transect in underwater acoustics. As shown in Figure 3.2 (right), in the general case, this 2-D meridional shape Ω is composed of a fluid part Ω_f and a solid part Ω_s. The coupling interface between these two sub-domains is denoted Ω_{f-s}. Let us suppose that Ω has a free surface $\partial\Omega$, and fictitious absorbing boundaries Ω_a. These are required because for regional simulations our modeling domain is limited by fictitious boundaries beyond which we are not interested in the wave field and thus acoustic energy reaching the edges of the model needs to be absorbed by our algorithm. In recent years, an efficient absorbing condition called the Perfectly Matched Layer (PML) has been introduced by Bérenger [1994] and is now used widely in regional numerical simulations. Although we have implemented them in our code, the mathematical and numerical complications associated with absorbing boundary conditions will not be addressed here as their implementation in the axisymmetric case is very similar to the Cartesian one. The reader is referred to Martin et al. [2008], Kucukcoban & Kallivokas [2010], Matzen [2011], Xie et al. [2014] or Xie et al. [2016] for example. Let us just mention that grazing incidence problems have been solved by Xie et al. [2014] and these enhanced PML layers are implemented in our code. This allows us to perform simulations on very elongated domains. For the sake of completeness we will note $\Gamma = \partial\Omega \cup \Omega_{f-s} \cup \Omega_a$ all the possible one-dimensional boundaries considered, although we will focus on fluid-solid interfaces Ω_{f-s}. For $\boldsymbol{x} \in \Gamma$ we note $\boldsymbol{n}(\boldsymbol{x})$ the outward unit normal to the surfaces Γ. The spectral-element method, just as the standard finite-element method, is based on a weak form of the wave equation (3.1). This formulation being different in the fluid and solid parts of the model we will present each case separately. It is worth mentioning that unified fluid-solid formulations can be designed if needed (Wilcox et al. [2010]), however they lead to a larger number of calculations on the fluid side.

3.2.1 Fluid parts

In the fluid regions, and ignoring the source term for now, the wave equation (3.1) when written for pressure $P(\boldsymbol{x}, t)$ in a spatially-heterogeneous fluid is (Brekhovskikh & Godin [1990])

$$\frac{1}{\kappa}\ddot{P} = \boldsymbol{\nabla} \cdot \left(\frac{\boldsymbol{\nabla} P}{\rho} \right) , \tag{3.3}$$

where $\kappa(\boldsymbol{x})$ is the adiabatic bulk modulus of the fluid. The linearized Euler equation is valid in a fluid with constant or spatially slowly-varying density (Landau & Lifshitz [1959]; Jensen et al. [2011]) and reads

$$\ddot{\boldsymbol{u}} = -\frac{\boldsymbol{\nabla} P}{\rho} . \tag{3.4}$$

Following Everstine [1981] and then Chaljub & Valette [2004], from a numerical point of view it is more convenient to integrate this system twice in time because that allows for numerical fluid-solid coupling based on a non-iterative scheme. We thus define a new scalar potential,

$$\ddot{\chi} = -P \tag{3.5}$$

and the scalar wave equation (3.3) then becomes

$$\frac{1}{\kappa}\ddot{\chi} = \boldsymbol{\nabla} \cdot \left(\frac{\boldsymbol{\nabla} \chi}{\rho} \right) . \tag{3.6}$$

Equation (3.4) combined with (3.5) leads to

$$\rho \boldsymbol{u} = \boldsymbol{\nabla} \chi , \tag{3.7}$$

i.e. $\rho\boldsymbol{u}$ is irrotational. Adding a pressure point-source at position $\boldsymbol{x}_s$ we obtain the wave equation in fluids,

$$\frac{1}{\kappa}\ddot{\chi} = \boldsymbol{\nabla} \cdot \left(\frac{\boldsymbol{\nabla} \chi}{\rho} \right) + \frac{1}{\kappa} f(t) \delta_{\boldsymbol{x}_s} . \tag{3.8}$$

Let $\boldsymbol{x} \mapsto w(\boldsymbol{x})$ be a real-valued, arbitrary test function defined on Ω_f. One obtains the weak form by dotting the wave equation (3.8) with a scalar test function w and integrating by parts over the model volume Ω_f,

$$\int_{\Omega_f} w \frac{1}{\kappa} \ddot{\chi} \, \mathrm{d}^2\boldsymbol{x} \;=\; -\int_{\Omega_f} \frac{1}{\rho} \boldsymbol{\nabla} w \cdot \boldsymbol{\nabla} \chi \, \mathrm{d}^2\boldsymbol{x} + \int_{\Omega_{f-s}} \frac{1}{\rho} w \boldsymbol{n} \cdot \dot{\boldsymbol{u}} \, \mathrm{d}\Gamma + \frac{1}{\kappa(\boldsymbol{x}_s)} w(\boldsymbol{x}_s) f(t) \,. \tag{3.9}$$

Note that the infinitesimal surface is now $\mathrm{d}^2\boldsymbol{x} = 2\pi r \mathrm{d}r\mathrm{d}z$. Remark that the part of the contour integral along the free surface $\partial\Omega$ has vanished. Indeed, the pressure-free surface condition is $P(\boldsymbol{x}, t) = -\ddot{\chi}(\boldsymbol{x}, t) = 0$ for all times and all $\boldsymbol{x} \in \partial\Omega$, and thus $\dot{\chi}(\boldsymbol{x}, t) = 0$ as well, hence $\boldsymbol{n} \cdot \dot{\boldsymbol{u}} = \boldsymbol{n} \cdot (\frac{1}{\rho} \nabla \dot{\chi}) = 0$, making the contour integral along the free surface $\partial\Omega$ vanish naturally.

The first term of (3.9) is traditionally called the mass integral, the second is the stiffness integral and the third is the fluid-solid coupling integral. The last term is the (known) source term, and will be dropped for convenience. It should be noted that both the test function $w(r, z)$ and the radial derivative of the potential $\frac{\partial \chi}{\partial r}(r, z, t)$ have to vanish on the axis (Bernardi et al. [1999]). Let us now present the discretization of this equation based on the time-domain spectral-element method. This is somewhat similar to the 2-D planar spectral-element implementation (of e.g. Cristini & Komatitsch [2012]), thus for the sake of conciseness we detail here the differences only. We recall that the model Ω is subdivided into a number of non-overlapping quadrangular elements Ω_e , $e = 1, \ldots, n_e$, such that $\Omega = \bigcup_{e=1}^{n_e} \Omega_e$. As a result of this subdivision, the boundary Γ is similarly represented by a number of 1-D edges Γ_b, $b = 1, \ldots, n_b$, such that $\Gamma = \bigcup_{b=1}^{n_b} \Gamma_b$. The $\bar{n}_e$ 2-D elements that are in contact with the axis need to be distinguished, they will be noted $\overline{\Omega}_e$. Similarly we will note $\overline{\Gamma}_b$ the 1-D horizontal edges that are in contact with the axis by one point (Figure 3.3). For simplicity we also assume that the mesh elements that are in contact with the symmetry axis are in contact with it by a full edge rather than by a single point, i.e. we exclude cases such as that of Figure 3.4.

This amounts to imposing that the leftmost layer of elements in the mesh be structured rather than non structured, while the rest of the mesh can be non structured.

The integrals in the weak form (3.9) are then split into integrals over the elements, in turn expressed as integrals over 2-D and 1-D reference elements $\Lambda = [-1, 1] \times [-1, 1]$ and $[-1, 1]$ thanks to an invertible mapping between global coordinates (r, z) and reference local coordinates (ξ, η):

$$\begin{aligned}
\int_{\Omega_e \text{ or } \bar{\Omega}_e} w \frac{1}{\kappa} \ddot{\chi} \, r\mathrm{d}r\mathrm{d}z &= \int_{\Lambda} w \frac{1}{\kappa} \ddot{\chi} \, |\mathcal{J}_e| \, r\mathrm{d}\xi\mathrm{d}\eta, \\
\int_{\Omega_e \text{ or } \bar{\Omega}_e} \frac{1}{\rho} \boldsymbol{\nabla} w \cdot \boldsymbol{\nabla} \chi \, r\mathrm{d}r\mathrm{d}z &= \int_{\Lambda} \frac{1}{\rho} \boldsymbol{\nabla} w \cdot \boldsymbol{\nabla} \chi \, |\mathcal{J}_e| \, r\mathrm{d}\xi\mathrm{d}\eta, \\
\int_{\Gamma_e \text{ or } \bar{\Gamma}_e} w \boldsymbol{n} \cdot \dot{\boldsymbol{u}} \, r\mathrm{d}\Gamma &= \int_{-1}^{1} w \boldsymbol{n} \cdot \dot{\boldsymbol{u}} \, \frac{dr}{d\xi} r\mathrm{d}\xi,
\end{aligned} \tag{3.10}$$

where $|\mathcal{J}_e|$ is the Jacobian of the invertible mapping. It then remains to calculate these integrals. The spectral-element method is based upon a high-order piecewise polynomial approximation of the weak form of the wave equation. For non axial elements, integrals along ξ and η are computed based upon Gauss-Lobatto-Legendre (GLL) quadrature. The integral of a function is expressed as a weighted sum of the values of the function at N specified collocation points called GLL points (containing -1 and 1) as described in textbooks on the spectral-element method (e.g. Cohen [2002]; Deville et al. [2002]; Fichtner [2010]). The N GLL points along ξ will be noted ξ_i, and those along η are noted η_i, the integration weights associated are noted ω_i and the basis functions are $\xi \mapsto \ell_i(\xi)$ or $\eta \mapsto \ell_i(\eta)$. In the axisymmetric case, following Bernardi et al. [1999], Gerritsma & Phillips [2000], Fournier et al. [2004], Nissen-Meyer et al. [2007] and Nissen-Meyer et al. [2008] we use a different quadrature for the integration in the ξ-direction for elements that are in contact with the symmetry axis. Indeed one can see that the factor r in the infinitesimal surface $r\mathrm{d}\xi\mathrm{d}\eta$ would lead to undetermined equations, $0 = 0$, if the integrands were to be evaluated at $\xi_0 = -1$. To deal with this issue the easiest solution

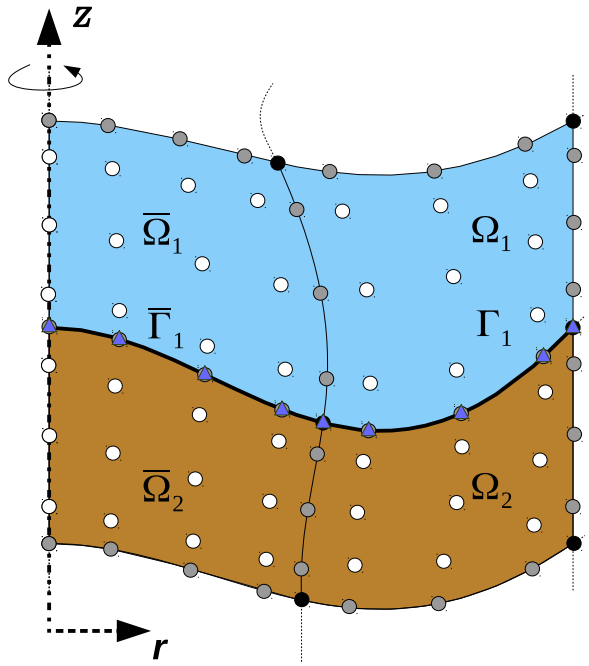

Figure 3.3 – Typical setup along the symmetry axis for a 2-D model containing two media. Four 2-D elements of polynomial degree $N = 4$ are shown. The two elements at the top ($\overline{\Omega}_1$ and Ω_1) lie in a fluid medium, the two at the bottom ($\overline{\Omega}_2$ and Ω_2) lie in an elastic medium, and two 1-D edges ($\overline{\Gamma}_1$ and Γ_1) are used to describe the coupling along the interface. The circles represent the GLL points, or the GLJ points along the direction r in the case of the elements that are in contact with the axis. The triangles are the GLL/GLJ points on the 1-D edges. Each 2-D spectral element contains $(N+1)^2 = 25$ GLL (or GLJ) points, which constitute the local mesh for each element. The difference between local and global grids appears here: points lying on edges or corners are shared between several elements, and thus the contributions to the global system, computed separately for each element, have to be summed (i.e. assembled) at these common points represented by black or gray circles.

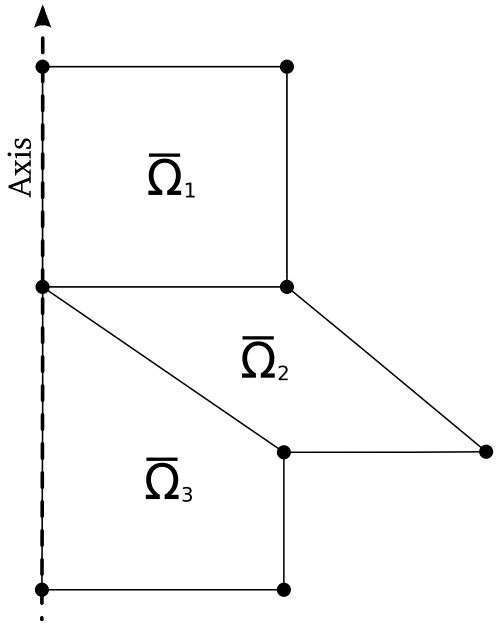

Figure 3.4 – For simplicity we exclude cases in which the mesh elements that are in contact with the symmetry axis are in contact with it by a single point instead of by a full edge, such as element $\bar{\Omega}_2$ here. This amounts to imposing that the leftmost layer of elements in the mesh be structured rather than non structured; The rest of the mesh can be non structured.

would be to shift the edge of the mesh by a small distance away from the axis (see e.g. Kampanis & Dougalis [1999] or Clayton & Rencis [2000]) but this convenient solution is not very meaningful for most physical problems because the source, not being on the axis, has to have a circular shape and thus an nonphysical radiation pattern. Bernardi et al. [1999] introduced a convenient way to tackle this issue, which has now become the classical approach for axisymmetric spectral-element problems (Gerritsma & Phillips [2000]; Fournier et al. [2004]; Nissen-Meyer et al. [2007, 2008]). In the η direction (the vertical direction) nothing different has to be done, but in the ξ direction one resorts to Gauss-Lobatto-Jacobi (GLJ) quadrature $(0,1)$. One first defines the set of polynomials $\overline{P}_N$ based on N^{th}-degree Legendre polynomials P_N following the relation,

$$\overline{P}_N(\xi) = \frac{P_N(\xi) + P_{N+1}(\xi)}{1+\xi}. \tag{3.11}$$

The $N+1$ GLJ points $\overline{\xi}_i$ are then the $N+1$ zeros of $\xi \mapsto (1-\xi^2)\dfrac{d\overline{P}_N}{d\xi}(\xi)$, and one computes the GLJ basis functions (Nissen-Meyer et al. [2007]) $\xi \mapsto \overline{\ell}_i(\xi)$,

$$\overline{\ell}_i(\xi) = \begin{cases} \dfrac{2(-1)^N(\xi-1)\dfrac{\partial \overline{P}_N(\xi)}{\partial \xi}}{N(N+1)(N+2)}, & i = 0, \\ \dfrac{1}{N(N+2)\overline{P}_N(\overline{\xi}_i)} \dfrac{(1-\xi^2)\dfrac{\partial \overline{P}_N(\xi)}{\partial \xi}}{\overline{\xi}_i - \xi}, & 0 < i < N, \\ \dfrac{(1+\xi)\dfrac{\partial \overline{P}_N(\xi)}{\partial \xi}}{N(N+2)}, & i = N. \end{cases} \tag{3.12}$$

Any function $g : (r,z) \mapsto g(r,z)$ on $\overline{\Omega}_e$ can be decomposed on its values at the GLJ and GLL points,

$$\forall \boldsymbol{\xi} = (\xi,\eta) \in \Lambda \quad g(\boldsymbol{x}(\boldsymbol{\xi})) \approx \sum_{\alpha=0}^{N}\sum_{\beta=0}^{N} g(\boldsymbol{x}(\overline{\xi}_\alpha,\eta_\beta))\overline{\ell}_\alpha(\xi)\ell_\beta(\eta) \equiv \sum_{\alpha,\beta=0}^{N} g^{\overline{\alpha}\beta}\overline{\ell}_\alpha(\xi)\ell_\beta(\eta), \tag{3.13}$$

where we have noted $g^{\overline{\alpha}\beta} \equiv g(\boldsymbol{x}(\overline{\xi}_\alpha,\eta_\beta))$ the value of g at the GLJ/GLL points $(\overline{\xi}_\alpha,\eta_\beta)$. It is worth mentioning the important property $\overline{\ell}_i(\overline{\xi}_j) = \ell_i(\xi_j) = \delta_{ij}$ as well as the fact that the points -1 and 1 still belong to the set of collocation points: the continuity with non-axial elements is thus ensured, and the mass matrix remains diagonal. We evaluate the surface integrals with the following quadrature rule,

$$\int_\Lambda g \,\mathrm{d}\xi\mathrm{d}\eta \approx \sum_{i,j=0}^{N} \overline{\omega}_i\omega_j \frac{g^{\overline{i}j}}{\overline{\xi}_i + 1}, \tag{3.14}$$

where the $\overline{\omega}_k = \int_{-1}^{1} \overline{\ell}_k(\xi)\,\mathrm{d}\xi$ are the GLJ integration weights. As the GLJ points, they are computed easily once and for all. All functions g considered in axial elements satisfy $g^{\overline{0}\beta} = 0$, consequently the singularities involving the terms $\frac{g^{\overline{i}j}}{\overline{\xi}_i+1}$ are easily removed with l'Hôpital's rule (Bernardi et al. [1999]),

$$\lim_{\xi\to\overline{\xi}_0} \frac{g(\boldsymbol{x}(\overline{\xi},\eta))}{\xi+1} = \frac{\partial g}{\partial \xi}(\boldsymbol{x}(\overline{\xi}_0,\eta)) = \sum_{\alpha,\beta=0}^{N} g^{\overline{\alpha}\beta}\overline{\ell}'_\alpha(\overline{\xi}_0)\ell_\beta(\eta). \tag{3.15}$$

The 1-D integrals on horizontal edges of axial elements (the only ones that are different from the Cartesian formulation) are computed in the same way, forgetting the variable η. For any function $g : (r) \mapsto g(r)$ on $\overline{\Gamma}_e$,

$$\forall \xi \in [-1,1] \quad g(r(\xi)) \approx \sum_{\alpha=0}^{N} g(r(\overline{\xi}_\alpha))\overline{\ell}_\alpha(\xi) \equiv \sum_{\alpha=0}^{N} g^{\overline{\alpha}}\,\overline{\ell}_\alpha(\xi) \tag{3.16}$$

and

$$\int_{-1}^{1} g \, \mathrm{d}\xi \approx \sum_{i=0}^{N} \overline{\omega}_i \frac{g^{\bar{i}}}{\overline{\xi}_i + 1}. \tag{3.17}$$

After substituting these representations in the wave equation (3.9), a last step has to be performed to deal with GLL/GLJ points lying on the sides, edges or corners of an element that are shared between neighboring elements (see Figure 3.3). Therefore, the grid points that define an element (the local mesh) and all the grid points in the model (the global mesh) need to be distinguished and mapped. Efficient routines are available for this purpose from finite-element modeling. Before the system can be marched forward in time, the contributions from all the elements that share a common global grid point need to be summed. In traditional finite-element this is referred to as the assembly of the system. For more details on the matrices involved and on the assembly of the system the reader can refer e.g. to the Appendix of Komatitsch & Tromp [1999] or to Fichtner [2010]. Using the fact that the relations must hold for any test function w, one obtains a global algebraic system of equations,

$$\ddot{\boldsymbol{\chi}} = (\boldsymbol{M})^{-1} \boldsymbol{F}_{int}(t), \tag{3.18}$$

in which $\boldsymbol{\chi}$ gathers the value of the potential and $\boldsymbol{F}_{int}(t)$ gathers all the interior forces at any unique GLL/GLJ point. The term $\boldsymbol{M}$ is the mass matrix. By construction in the spectral-element method this matrix is diagonal and its inversion is thus straightforward and does not incur any significant computational cost. Hence time discretization of the second-order hyperbolic ordinary differential equation (3.18) can be based upon a fully explicit time scheme. In practice we select an explicit second-order-accurate finite-difference scheme, which is a particular case of the Newmark scheme (Hughes [1987]). This scheme is conditionally stable, and the Courant stability condition is governed by the maximum value of the ratio between the compressional wave speed and the grid spacing. The main numerical cost associated with the spectral-element method is related to small, local matrix-vector products between the local field and the local stiffness matrix, not to the time-integration scheme (Tromp et al. [2008]).

3.2.2 Solid parts

In linear elastic solids the strain tensor $\boldsymbol{\varepsilon}(\boldsymbol{x}, t)$ is calculated from the displacement vector $\boldsymbol{u}$ by

$$\boldsymbol{\epsilon} = \frac{1}{2}(\boldsymbol{\nabla u} + (\boldsymbol{\nabla u})^{\top}). \tag{3.19}$$

The stress tensor $\boldsymbol{\sigma}(\boldsymbol{x}, t)$ is then a linear combination of the components of the strain tensor (Hooke's law):

$$\boldsymbol{\sigma} = \boldsymbol{c} : \boldsymbol{\epsilon}, \tag{3.20}$$

where the colon denotes a double tensor contraction operation. The elastic properties of the medium are described by the fourth-order elastic tensor $\boldsymbol{c}(\boldsymbol{x})$, which can have up to 21 independent coefficients. In this document, for simplicity, we will consider isotropic media and put aside the more general anisotropic relationship (3.20). However anisotropy can readily be implemented (see for instance Komatitsch et al. [2000]). In elastic isotropic media the stress tensor field reads

$$\boldsymbol{\sigma} = \lambda \mathrm{Tr}(\boldsymbol{\epsilon}) \boldsymbol{I} + 2\mu \boldsymbol{\epsilon}\,, \tag{3.21}$$

where $\boldsymbol{I}$ is the 3×3 identity tensor and $\mathrm{Tr}(\boldsymbol{\epsilon})$ is the trace of the strain tensor. The Lamé parameters of the medium are denoted by $\lambda(\boldsymbol{x})$ and $\mu(\boldsymbol{x})$. They are related to the pressure wave speed c_p, shear wave speed c_s and density ρ by the expressions $\mu = \rho\, c_s^2$ and $\lambda = \rho\, c_p^2 - 2\rho\, c_s^2$.

Likewise we will avoid the numerical complications associated with attenuation (viscoelasticity), however attenuation is implemented in our code (Komatitsch & Tromp [1999]; Cristini & Komatitsch

[2012]) and we will use it in the numerical validation tests and examples of Section 3.3. Let us just recall that in an anelastic medium the stress $\boldsymbol{\sigma}(\boldsymbol{x},t)$ at time t is determined by the entire strain history $\boldsymbol{\epsilon}(\boldsymbol{x},t)$, and Hooke's law becomes (Aki & Richards [1980]; Dahlen & Tromp [1998])

$$\boldsymbol{\sigma}(\boldsymbol{x},t) = \int_{-\infty}^{t} \frac{\partial \boldsymbol{c}}{\partial t}(t-t') : \boldsymbol{\epsilon}(\boldsymbol{x},t')\,\mathrm{d}t'. \tag{3.22}$$

As in the fluid part, one obtains the weak form by dotting the wave equation (3.1) with a test function $\boldsymbol{w}$ and integrating by parts over the model volume Ω. The only difference with the fluid formulation is that the test function is vectorial $\boldsymbol{x} \mapsto \boldsymbol{w}(\boldsymbol{x}) = (w_r(\boldsymbol{x}), w_z(\boldsymbol{x}))$. One obtains,

$$\int_{\Omega_s} \boldsymbol{w} \cdot \rho \ddot{\boldsymbol{u}}\, \mathrm{d}^2\boldsymbol{x} = -\int_{\Omega_s} \boldsymbol{\nabla w} : \boldsymbol{\sigma}\, \mathrm{d}^2\boldsymbol{x} + \int_{\Omega_{f-s}} \boldsymbol{w} \cdot (\boldsymbol{\sigma} \cdot \boldsymbol{n})\, \mathrm{d}\Gamma, \tag{3.23}$$

where

$$\boldsymbol{\nabla w} : \boldsymbol{\sigma} = \sigma_{rr}\frac{\partial w_r}{\partial r} + \sigma_{zz}\frac{\partial w_z}{\partial z} + \sigma_{zr}\left(\frac{\partial w_r}{\partial z} + \frac{\partial w_z}{\partial r}\right) + \sigma_{\theta\theta}\frac{w_r}{r}, \tag{3.24}$$

$$\boldsymbol{w} \cdot (\boldsymbol{\sigma} \cdot \boldsymbol{n}) = (\sigma_{rr}n_r + \sigma_{rz}n_z)w_r + (\sigma_{zr}n_r + \sigma_{zz}n_z)w_z. \tag{3.25}$$

The important difference with a 2-D planar model is the presence of the "hoop stress" term, $\sigma_{\theta\theta}$ - see Figure 3.1. Here again the traction-free integral along the free surface $\partial\Omega$ has vanished naturally. For simplicity we have supposed that there is no source in the elastic part of the model. It has to be noted that the terms u_r/r and w_r/r appear and are problematic in axial elements for the GLJ point that is located exactly on the axis, i.e. at $r = 0$. However, on the axis, by symmetry considerations $u_r = 0$ and, by definition of the test functions in axisymmetric domains (Bernardi et al. [1999]), $w_r = 0$. Thus L'Hôpital's rule can be applied, as in the fluid case. For any g, which can represent u_r or w_r in practice, we define

$$\frac{g^{\bar{\sigma}\nu}}{r^{\bar{\sigma}\nu}} \equiv \begin{cases} \dfrac{g^{\bar{\sigma}\nu}}{r^{\bar{\sigma}\nu}}, & \sigma \neq 0, \\ \left(\left.\dfrac{\partial r}{\partial \xi}\right|^{0\nu}\right)^{-1} \displaystyle\sum_{\alpha,\beta=0}^{N} g^{\bar{\alpha}\beta}\bar{\ell}'_{\alpha}(\bar{\xi}_0)\ell_{\beta}(\eta_\nu), & \sigma = 0. \end{cases} \tag{3.26}$$

Following similar steps as for the fluid part of the model, after assembling the system one obtains a similar global system of equations,

$$\begin{cases} \ddot{\boldsymbol{U}}_r = (\boldsymbol{M}^g)^{-1}\, \boldsymbol{F}^g_{r,int}(t), \\ \ddot{\boldsymbol{U}}_z = (\boldsymbol{M}^g)^{-1}\, \boldsymbol{F}^g_{z,int}(t), \end{cases} \tag{3.27}$$

where the $\boldsymbol{U}_i$ gather all the values of the (unknown) displacement and the $\boldsymbol{F}^g_{i,int}(t)$ gather all the interior forces at every GLL/GLJ point.

3.3 Numerical validations

We have tested the accuracy and efficiency of the technique and benchmarked it against reference solutions calculated with the wavenumber integration software package OASES (Schmidt & Jensen [1985]; Jensen et al. [2011]) version 3.1 as well as with the commercial finite-element code COMSOL. The two examples include fluid-solid coupling, attenuation and PML absorbing layers; they are extracted from Jensen et al. [2007] and described in Figure 3.5.

Our code computes time-domain signals but the results are shown both in time and frequency domains as an illustration. For information, these examples ran in a few seconds (2 minutes maximum depending on the configuration chosen) on 12 processor cores of an Intel Xeon® E5-2630 multi-core PC.

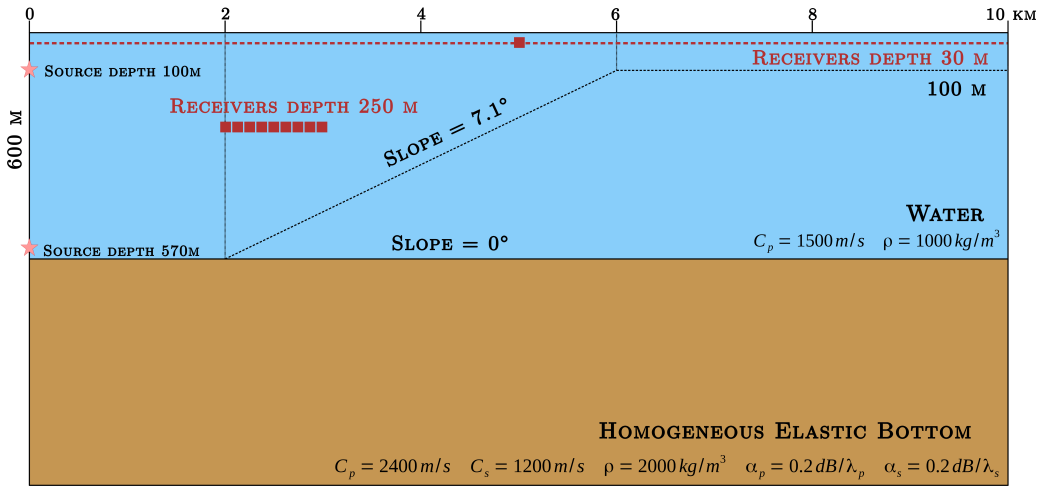

Figure 3.5 – Setting of the validation simulations. The vertical and horizontal scales are different. The properties of the two homogeneous media are given in the figure. Slope = 0° corresponds to the flat bottom benchmark case of Section 3.3.1, in which the water depth is constant and equal to 600 m. In this case the source depth is 100 m and the receiver depth is 30 m. The receiver that records the signal of Figure 3.6 (right) is shown as a square at range 5 km and depth 30 m. For the upslope case presented in Section 3.3.2 the model has a constant water depth (600 m) up to 2 km followed by a constant bottom slope of 7.1° up to 6 km. The depth remains constant and equal to 100 m hereafter. In this case the source depth is 570 m and the receiver depth is 30 m. The horizontal antenna that records the pressure time series of Figure 3.7 (right) is shown as squares at depth 250 m and at ranges 2–3 km. The horizontal size of the computational domain is 12 km, but it includes an absorbing layer (PML) on the right side, which we purposely do not represent because the wavefield in it is by definition non physical; The figures only show the physically-meaningful region, i.e. a domain of size 10 km.

3.3.1 Flat-bottom benchmark case

Let us first compare the results of our spectral-element technique with those from the OASES wavenumber integration code for a flat-bottom benchmark case. We consider an axisymmetric half-space composed of a semi-infinite homogeneous viscoelastic medium lying 600 m below a homogeneous sea layer. The properties of the homogeneous viscoelastic part are given by $\rho = 2000$ kg.m^{-3} for the density, $c_p = 2400$ m.s^{-1} for the pressure wave speed, $c_s = 1200$ m.s^{-1} for the shear wave speed and $\alpha_p = 0.2$ dB/λ_P^{-1}, $\alpha_s = 0.2$ dB/λ_S^{-1} the corresponding attenuation coefficients. In the acoustic domain we set the density to $\rho = 1000$ kg.m^{-3} and the pressure wave speed to $c_p = 1500$ m.s^{-1}. We set $z = 0$ m at the fluid surface. The pressure source is located on the symmetry axis in the acoustic part of the medium, in $(r_s, z_s) = (0,\text{-}100$ m); its source time function is a Ricker (i.e. the second derivative of a Gaussian) wavelet with a dominant frequency $f_0 = 5$ Hz and a time shift $t_0 = 1.2/f_0$ in order to ensure null initial conditions. The wavefield is computed up to a range of 12 km and down to depth 1800 m, the energy coming out of this box being absorbed by PMLs. The mesh is composed of 170×60 spectral elements whose polynomial degree is $N = 4$. The total number of unique GLL/GLJ points in the mesh is $(170N + 1) \times (60N + 1) = 164,121$. The minimum number of grid points per shear wavelength in the solid is 5.2 and the minimum number of points per pressure wavelength in the fluid is 6.8. We select a time step $\Delta t = 1.56$ ms and simulate a total of 6000 time steps, i.e. 9.36 s. The pressure is recorded at $z = -30$ m by 1000 receivers uniformly distributed between $r = 0$ m and $r = 10$ km. The pressure time series at 5 km and $z = -30$ m, normalized to unit pressure at a distance of 1 m from the source, computed with OASES and with the spectral-element method are shown in Figure 3.6 (right) and transmission losses in dB at 5 Hz and $z = -30$ m are shown in Figure 3.6 (left).

The transmission losses for the spectral-element method have been obtained from the time signals by Fourier transform. Very good agreement is found between the two codes in both the time and frequency domains, thus validating our technique for this benchmark case.

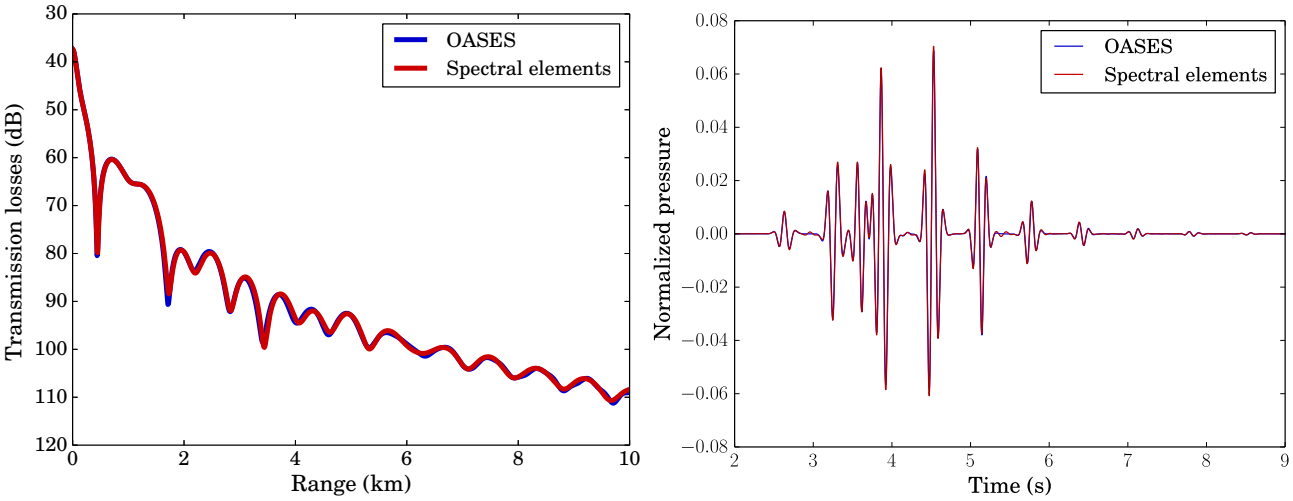

Figure 3.6 – Comparison between the wavenumber integration code OASES and the spectral-element method for the flat-bottom benchmark case. **Left**: Transmission losses in dB at 5 Hz and $z = -30$ m as a function of range in km. **Right**: Normalized pressure (unit pressure at 1 m distance from the source) as a function of time at 5 km and $z = -30$ m.

3.3.2 Validation, including for backscattering

In this section we examine the results of our spectral-element method for the upslope case (slope = 7.1°) described in Figure 3.5. These results are compared to those from the commercial finite-element code COMSOL and to a parabolic equation method with coordinate rotation (ROTVARS, Outing et al. [2006]), specifically designed to handle variable slopes in bathymetry. Both reference results were computed by Jensen et al. [2007] and are reproduced here. The properties of the media are the same as those used in the previous section. The source depth is 570 m in order to excite a significant interface wave of Stoneley-Scholte type, the shear wave speed being lower than the speed in water. The source is still a pressure acoustic Ricker pulse with a dominant frequency $f_0 = 5$ Hz and a time shift $t_0 = 1.2/f_0$. The wavefield is computed up to a range of 15 km and down to depth 3000 m, the energy coming out of this box again being absorbed by PMLs. The mesh is composed of 9039 spectral elements whose polynomial degree is $N = 4$ and the total number of unique GLL/GLJ grid points is 169,064. The number of grid points per shear wavelength in the solid is around 5.3 while the minimum number of grid points per pressure wavelength in the fluid is around 5.5. The time step chosen is $\Delta t = 1.62$ ms and the total number of time steps is 8000 in order to compute 12.96 seconds of simulation. The pressure is recorded at $z = -30$ m by 1000 receivers uniformly distributed between $r = 0$ m and $r = 10$ km and by a horizontal antenna containing nine receivers (the squares at depth 250 m in Figure 3.5). The transmission losses in dB at 5 Hz and $z = -30$ m computed with COMSOL, ROTVARS and with the spectral-element method are shown in Figure 3.7 (left).

An almost perfect fit is found between COMSOL and the spectral-element method, even if the first is implemented in the frequency domain while the second is in the time domain. All complex physical phenomena, including Stoneley-Scholte waves, are correctly modeled. However the parabolic code ROTVARS does not line up because the slope bottom causes non negligible back-propagating waves that are not taken into account by parabolic equation methods. This is illustrated in Figure 3.7 (right) showing the pressure time series recorded by the horizontal antenna. This explains the differences already pointed out in Jensen et al. [2007] and illustrates the advantage of going beyond the parabolic solution for these kinds of problems.

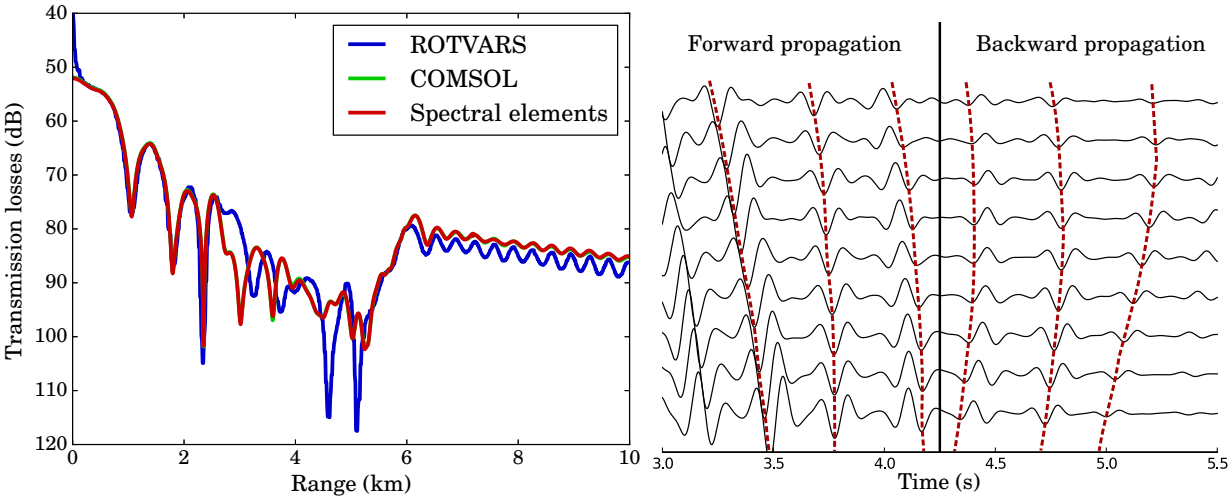

Figure 3.7 – **Left**: Transmission losses in dB as a function of range in km. The first curve has been calculated with ROTVARS, the second with COMSOL (both taken and adapted from Jensen et al. [2007], Fig. 7), and the third with the spectral-element method. Note that the COMSOL and spectral-element results are almost perfectly superimposed. **Right**: Pressure time series recorded by the receivers of the horizontal antenna ($z = -250$ m) shown in Figure 3.5. The upper trace is the pressure recorded by the receiver located at $r = 2$ km, the lower trace is the pressure recorded by the receiver located at $r = 3$ km. In the left part of the picture ($t < 4.25$ s) the noticeable arrivals are recorded first at the leftmost receivers, thus corresponding to forward energy propagation. In the right part of the picture ($t > 4.25$ s) the noticeable arrivals are recorded first at the rightmost receivers, thus corresponding to significant backward energy propagation (which cannot be computed by parabolic equation techniques for instance).

3.4 Example of a more realistic application to seamounts

In this section we present an example of a more realistic application to illustrate the possibilities offered by full-wave simulations. The objective is to observe the wavefield behavior at long range created by an explosive source in an ocean with ocean-floor topography. The model is described in Figure 3.8.

Performing a 2-D axisymmetric simulation is very interesting for such cases with moderate azimuthal aperture (Spiesberger [2007]). Indeed, if the source emits far from the seamounts, later effects are negligible and thus the results will be almost the same as those of a fully 3-D calculation, whose cost would still be prohibitive even on current large supercomputers due to the high frequencies and large propagation distances involved[1]. We keep the media properties identical to those of the previous section. We again set $z = 0$ m at the fluid surface. The pressure Ricker pulse source is located in $(r_s, z_s) = (0,\text{-}590$ m) and has a dominant frequency $f_0 = 100$ Hz and a time shift $t_0 = 1.2/f_0$. The wavefield is computed up to a range of 5 km and down to depth 1000 m, the energy coming out of this box again being absorbed by PMLs. The mesh comprises 1600×360 spectral elements of polynomial degree $N = 4$, leading to a total number of unique GLL/GLJ points in the mesh of $(1600N + 1) \times (360N + 1) = 9,223,841$. The minimum number of points per shear wavelength in the solid is 5.7 and the minimum number of points per pressure wavelength in the fluid is 6.5. We use a time step $\Delta t = 0.046$ ms and compute a total of 90,000 time steps, i.e. 4.14 s. Here for simplicity we have chosen homogeneous media but media with complicated variations of their material properties can easily be accommodated (see e.g. Komatitsch & Tromp [1999]).

Figure 3.8 illustrates the complexity of the wavefield structure obtained for this configuration. We consider two spatial windows, one covering a region close to the source in which the sea floor is flat and another one that includes both seamounts. For each region we present snapshots of the

[1] this will remain so for at least a decade, as shown by the extrapolation of supercomputer power evolution that can be made for instance based on the data available in the Top500 database (Strohmaier et al. [2017])

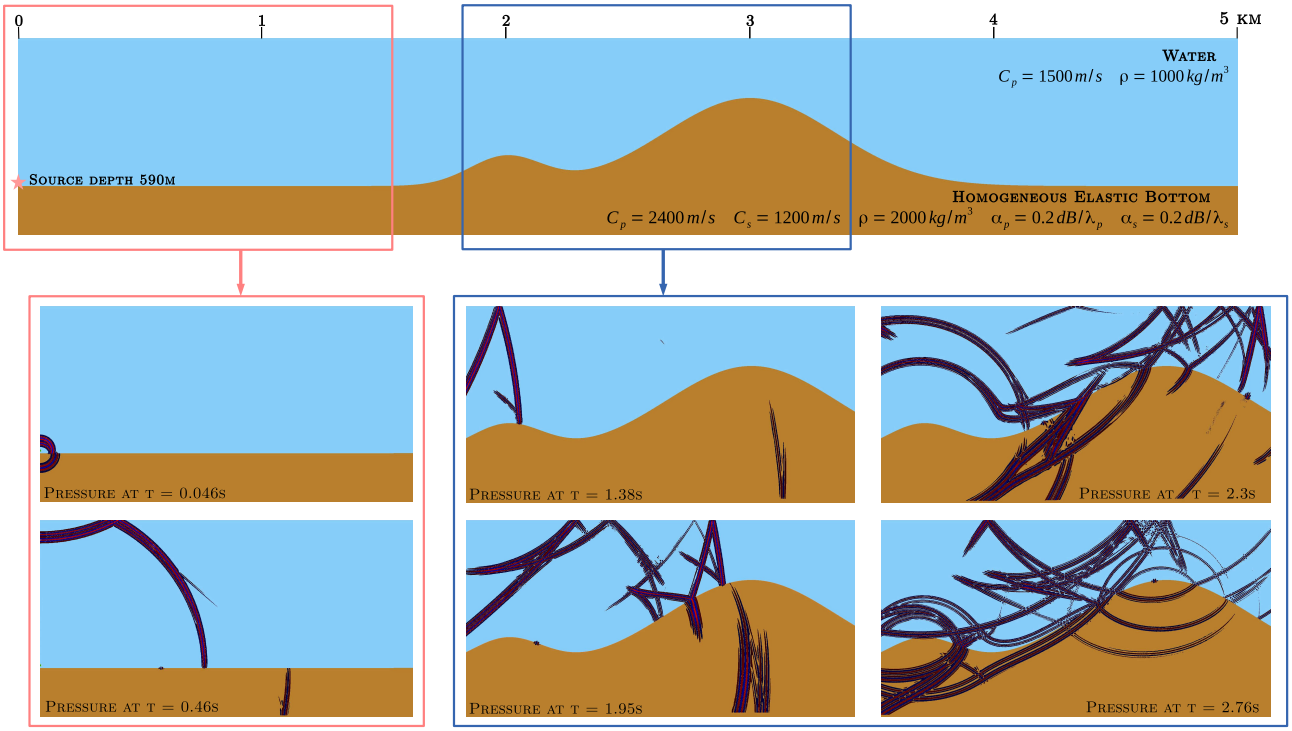

Figure 3.8 – Wavefield snapshots for an explosion with dominant frequency 100 Hz. The vertical and horizontal scales are different. The properties of the two homogeneous media are given in the upper figure. On the axis the water depth is 600 m, and the source is located right above the ocean bottom, at a depth of 590 m.

wavefield at different times. The first spatial window extends from the origin up to a range of 1.5 km. It shows the beginning of the propagation of the wavefield in a section of the waveguide that is flat. The snapshot at time $t = 0.046$ s shows the direct and reflected wavefronts very close to one another because of the proximity of the source to the water-sediment interface, as well as a transmitted wavefront propagating into the sediment. In the snapshot at time $t = 0.46$ s the reflected and direct wavefronts have reached the water-air interface, considered as a free surface in the simulation. A small wave packet that propagates along the interface, now separated from the two other wavefronts and that corresponds to a surface wave of Stoneley-Scholte type, can be observed. It can be identified because it propagates at a speed that is slower than all the wave speeds of the two media in contact ($c_{\text{Stoneley}} = 1005$ m.s^{-1}). The second spatial window covers a region starting at range 1.8 km and ending at range 3.4 km. The snapshot at time $t = 1.38$ s exhibits a wavefront propagating in the sediment (associated to the pressure wave) reaching the position of the second seamount while the wavefront propagating in the water reaches the position of the first seamount. These wavefronts are the first arrivals. At time $t = 1.95$ s the influence of the two seamounts starts to affect wave propagation in the waveguide. A triplication can be observed in the upper-left part of the snapshot owing to the shape of the first seamount. In the sediment, two wavefronts can be observed. The first is associated to the first reflected wavefront from the water-air interface transmitted into the sediment while the second comes from a transmission occurring at the first seamount because of the curvature change. The same type of transmission into the sediment through the second seamount is beginning and can be seen half way to the top. Some energy starts to penetrate into the sediment. This process continues and can be seen after the top of the second seamount at time $t = 2.3$ s. Two wavefronts above the first seamount correspond to the beginning of the significant backscattering that occurs in this configuration. At time $t = 2.76$ s multiple reflections generated between the water-air interface and the two seamounts interact and lead to a complex wavefield structure. These multiple reflections are clearly seen at the top of the second seamount together with the interface wave that was generated

at the beginning of the simulation. Strong backscattering is observed.

For information, this example ran on 180 processor cores of a computing cluster in $\sim$ 30 minutes and could have run on a current classical high-end PC in less than a night. It is worth mentioning that the spectral-element method exhibits almost perfect computing scaling i.e. almost perfect parallel efficiency on modern parallel computers (Tromp et al. [2010]; Komatitsch [2011]) when increasing the number of processors used (mostly because its mass matrix is diagonal and thus no linear system needs to be inverted).

In terms of limitations of the approach let us mention again that the model being axisymmetric, calculations are made for seamounts whose 3-D shape is annular. This has to be kept in mind for axisymmetric simulations in particular when dealing with backscattered energy for objects located close to the symmetry axis because for this geometrical reason backscattered energy gradually grows when coming closer to that axis and is then reflected back into the model after having reached it; this comes from the fact that the radial component of displacement is zero by symmetry on the symmetry axis and thus acts as a Dirichlet condition (perfectly reflecting condition) for the radial component of the field. This is nonphysical and constitutes a model error. A way of avoiding such fictitious "backscattering of the backscattering" by the axis could maybe be to adopt a quasi-cylindrical formulation (Takenaka et al. [2003]; Toyokuni et al. [2012]). Another limitation of the approach is the type of sources that can be modeled if the source is located in the solid part of the model. Since explosive sources have an axisymmetric shape they are perfectly modeled, whether they are located in the fluid or in the solid, which allows for the study a large number of physical problems; however point force sources or moment tensor sources in solids (Tromp et al. [2010]) are limited to cases in which they have an axisymmetric radiation pattern.

3.5 Conclusions

We have presented and validated a numerical method based on time-domain spectral elements for coupled fluid-solid full-wave propagation problems in an axisymmetric setting, including in cases with significant backscattering, which cannot be modeled e.g. based on the parabolic equation approximation. Our calculations have included viscoelastic ocean bottoms, and we have used PML absorbing layers to efficiently absorb the outgoing wavefield. An advantage of this method is its versatility and its relatively low computational cost compared to a truly 3-D calculation while allowing simulations with realistic 3-D geometrical spreading. An application to the calculation of the full wavefield at long range created by a high-frequency explosive source in an ocean with sea-floor topography has also been presented. Our SPECFEM spectral-element software package, which implements the spectral-element method presented above, is collaborative and available as open source from the Computational Infrastructure for Geodynamics (CIG); it includes all the tools necessary to reproduce the results presented in this document.

Chapter 4

On the influence of slopes, seabed and water column properties on T-waves

Slope angles play a crucial role in both T-wave generation and conversion at shore. This important aspect is often mentioned in the literature (see Chapter 1) and was also confirmed by the observations we made in the Ionian sea in Chapter 2. This chapter starts from the modeling of a T-wave event in the Ionian sea, examining the influence of soft sediments, of source depth and of the SOFAR channel on T-waves. It then proceeds with two parametric studies, on each side of the oceanic basin. The first one deals with the influence of slope angle, media properties and source position on T-wave energy created by downslope conversion, and the second one focuses on the conversion of an acoustic wave at an elastic wedge. The influence of sediments and of source frequency content is also discussed.

4.1 Modeling of T-waves in the Ionian sea

4.1.1 Settings of the simulations

With the numerical tool developed in the previous chapter, we propose to perform 2-D axisymmetric full-wave numerical simulations of the event studied in Chapter 2. The numerical model we use is described in Figure 4.1 and corresponds to the 2-D cutplane shown as the blue line in Figure 2.1 (top). As we are only interested here in the T-wave, the curvature of the Earth is neglected to avoid increasing the computational cost (72,000 CPU hours instead of 360,000 CPU hours for all simulations of this section).

The bathymetry is extracted from the SRTM30_PLUS model (see Becker et al. [2009]; Sandwell et al. [2014]), which has 0.5 arc-minute resolution (approximately 700 m in the area), and the properties of the elastic media are defined following Finetti [2005]. The velocity profile in the water column is shown in Figure 4.2. It is an extrapolation of the measured mean annual sound speed profile in the Ionian sea given by Salon et al. [2002] (Figure 2.1, middle, right). The chosen source is a point force located on the symmetry axis, its source time function is a Ricker (i.e. the second derivative of a Gaussian) wavelet with dominant frequency $f_0 = 6$ Hz and a time shift $t_0 = 1.2/f_0$ in order to ensure null initial conditions.

The mesh is composed of ~ 1.1 million spectral elements whose polynomial degree is $N = 4$. The total number of unique GLL/GLJ points in the mesh is approximately 18 millions. Depending on the velocity profile used in the fluid, the number of points per wavelength slightly varies. In the worst case 99.9% of the acoustic elements ensure at least 5 grid points per pressure wavelength in the fluid, and 99.9% of elements in the viscoelastic part ensures at least 6.5 points per shear wavelength. We select a time step $\Delta t = 0.2$ ms based on the stability and accuracy conditions of the explicit, conditionally-

stable time scheme, and simulate a total of 2.5 million time steps, i.e. 500.0 s. The energy coming out of the domain under study, shown in Figure 4.2, is absorbed by PML layers. Frequencies up to ~20 Hz are resolved. The displacement vector is recorded at the different locations shown in the figure. Each simulation performed took approximately 10 hours on 1440 processor cores of a parallel supercomputer equipped with Intel ® Xeon® E5-2690 v3 processors (which is 14,400 CPU hours. It would have cost $\sim$ 70,000 CPU hours without neglecting the Earth curvature).

Four simulations were made in order to test the sensibility of the results to the addition of a small sediment layer, to the presence (or not) of the SOFAR channel, and to the source depth. The simulations made are labeled Case 1, 2, 3 and 4 and are summarized in Table 4.1.

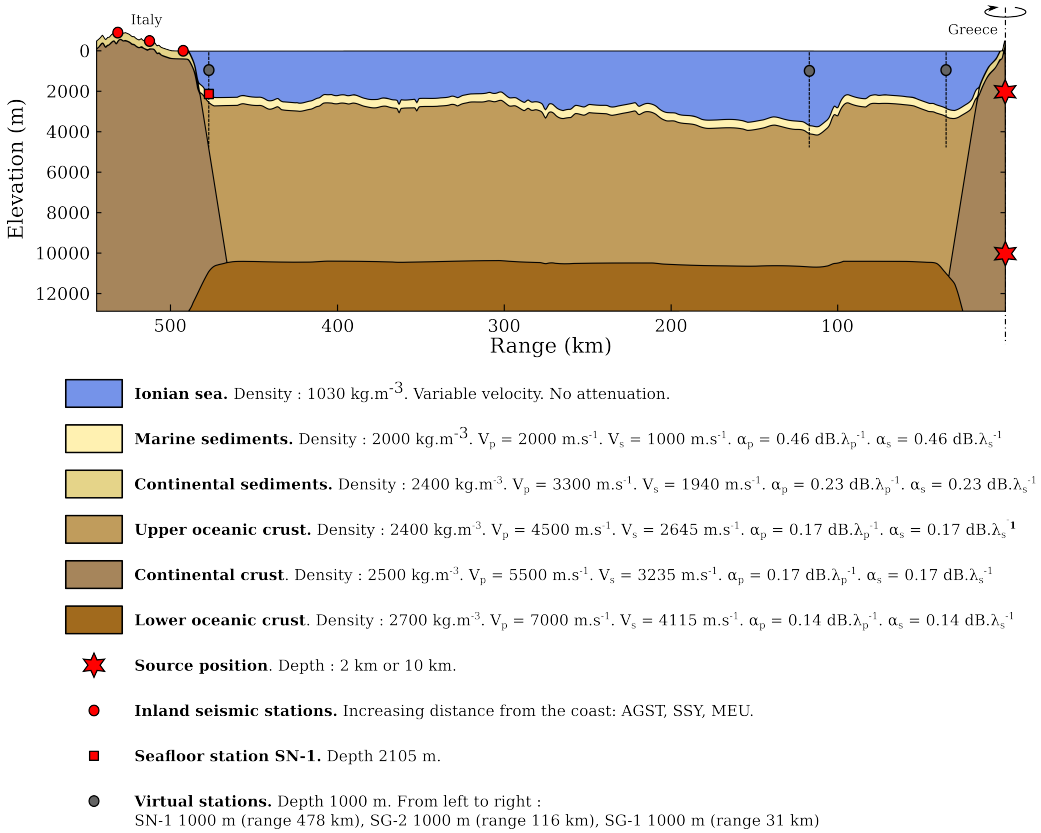

Figure 4.1 – Setting of the axisymmetric spectral-element numerical simulation corresponding to the event studied in Chapter 2. The symmetry axis is shown on the right. The velocity profile in the water is either a constant velocity (1500 m.s^{-1}) or a variable velocity depicted in Figure 4.2. The seismic stations at which the wave field is recorded and that correspond to real stations installed in the field are shown in red, while stations that are only numerical, with no corresponding real stations in the field, are shown in gray. V_p is the compressional wave speed, V_s is the shear wave speed, and α_p and α_s are the corresponding attenuation coefficients expressed in dB per wavelength.

4.1.2 Results and observations

4.1.2.1 Comparison of real and synthetic signals at station AGST

Figure 4.3 shows a comparison between three of the synthetic signals (cases 1, 2 and 3) and the real one for station AGST. Let us first remark that synthetic P and S phases have wrong timing and amplitude compared to the T-phase. In fact, in the almost 600 km-long real configuration considered the straight line between the source and the receivers is shorter than the one that we considered. Moreover, it passes through depths of up to 30 km, that is to say through quicker and less attenuating media.

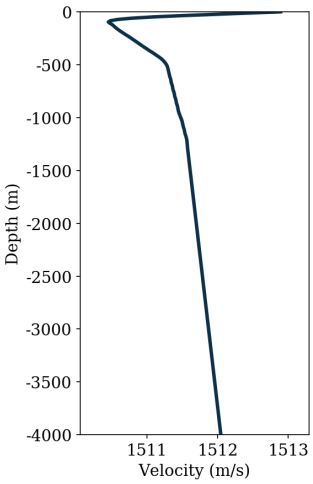

Figure 4.2 – Sound speed profile in the sea used for the numerical simulations in Cases 1, 3 and 4 described in Table (4.1). It has been extrapolated from the measured mean annual sound speed profile in the Ionian sea given by Salon et al. [2002] (see Figure 2.1, middle, right).

	Label used in Figure	Description
Case 1	SOFAR and sediments	It is exactly the case described in Figure 4.1, with source depth 10 km and the sound speed profile in the sea shown in Figure 4.2.
Case 2	No SOFAR	Same as Case 1 but with a constant sound speed of 1500 $m.s^{-1}$ in the sea.
Case 3	No sediments	Same as Case 1 but with no marine nor continental sediments (replaced with the properties of the oceanic and continental crust, respectively).
Case 4	Source depth 2 km	Same as Case 1 but with a source depth of 2 km.

Table 4.1 – Description of the four simulations that we have performed.

The apparent velocity of the actual P and S waves recorded at station AGST is then $\frac{496}{62} \sim 8$ km.s^{-1} and $\frac{496}{108} \sim 4.6$ km.s^{-1} respectively, which is therefore above the values used and corresponds rather well to the properties of the upper mantle as documented in Finetti [2005]. Contrary to the synthetic body phases, the synthetic T-phases in the cases 1 and 2 are particularly realistic (see also Figure 4.4 and 4.5). Although less impulsive, the duration and spectral shape of the synthetic T-phases are consistent. Note for example the low frequency tremor preceding the main arrivals, or the characteristic double peak in the frequency domain.

Furthermore, the synthetic T-phase appears to arrive a bit too early, maybe suggesting that the velocities proposed by Salon et al. [2002] (Figure 4.2) based on temperature, salinity, and pressure measurements was too high at the frequencies considered. We would then propose a value around 1495 m.s^{-1}, largely outside the margin of error of Salon et al. [2002]. This slight discrepancy could most likely be explained by supposing that the rather weak synthetic first peak arrival does not correspond to the real one, which is supposed to be the most energetic in reality. Indeed, the timing of the modeled T-phase second peak in case 1 matches almost perfectly the timing of the actual T-phase first peak. However, if the first synthetic peak is attenuated in reality and does not correspond to a real phenomenon, this means that the second peak observed in the data is either not modeled at all, absorbed too quickly in the propagation, or unrealistically suppressed in the conversion, for example due to missing bathymetric features or unrealistic continental slope.

4.1.2.2 Comparison of real and synthetic signals at the other stations, and influence of the sediments and of the SOFAR channel

This hypothesis is supported by the synthetic signals simulated at station SN-1 in cases 1, 2 and 4 (see Figure 4.4), which do exhibit a third peak before the conversion. In addition, the results of the simulation of Case 4 (see Figure 4.5) show that the first peak amplitude relatively to second peak increases strongly with source depth, keeping in mind that source depth is not precisely known (hypocenter depth is estimated at 10 km, but moment centroid depth is estimated at 2 km).

We failed to identify the origin of this apparent double peak in the spectrogram. The time shift between the two peaks is too important to correspond to $P \rightarrow T$ and $S \rightarrow T$ arrivals. It is very likely due to the sediment layers, as we do not observe such a phenomenon in case 3. This last case illustrates the importance of the presence of sediments in T–phase amplitude and shape, in particular when the sediments are of sufficient thickness. T-phases without sediments are more impulsive, of higher amplitude, of longer duration and do not exhibit several peaks. The longer duration observed for this situation with a high impedance contrast was expected from previous studies (e.g. De Groot-Hedlin [2004]). Figure 4.6 shows snapshots of the horizontal displacement field structure obtained for cases 1 and 3 (with and without sediments) at time $t = 40$ s. The amplitude scales are different for the two snapshots, however one can see that the relative distribution of energy between the water layer and the seabed varies. Low-velocity sediments damp the impedance contrast at the sea bottom and allow for more energy to leak from the waveguide along the propagation.

Surprisingly, Figures 4.3 and 4.4 highlight the fact that the SOFAR channel is not seen to contribute much to the T-phase structure at the distances and frequencies considered. This is in apparent contradiction with most of the studies on the subject. This important observation, also made by Jamet et al. [2013] from their simulations led us to propose to study the efficiency of the SOFAR channel in terms of energy transmission. It will be presented in Chapter 5.

4.1.2.3 Waveforms simulated inland after conversion

Figure 4.7 shows the comparison between the synthetic inland T-wave speed (case 1) and the observed data. The apparent velocity of the first synthetic arrival is seen to be 3000±1000 m/s, which is realistic but significantly lower than the apparent velocity of the first real arrival, which is seen to be 4000±1000

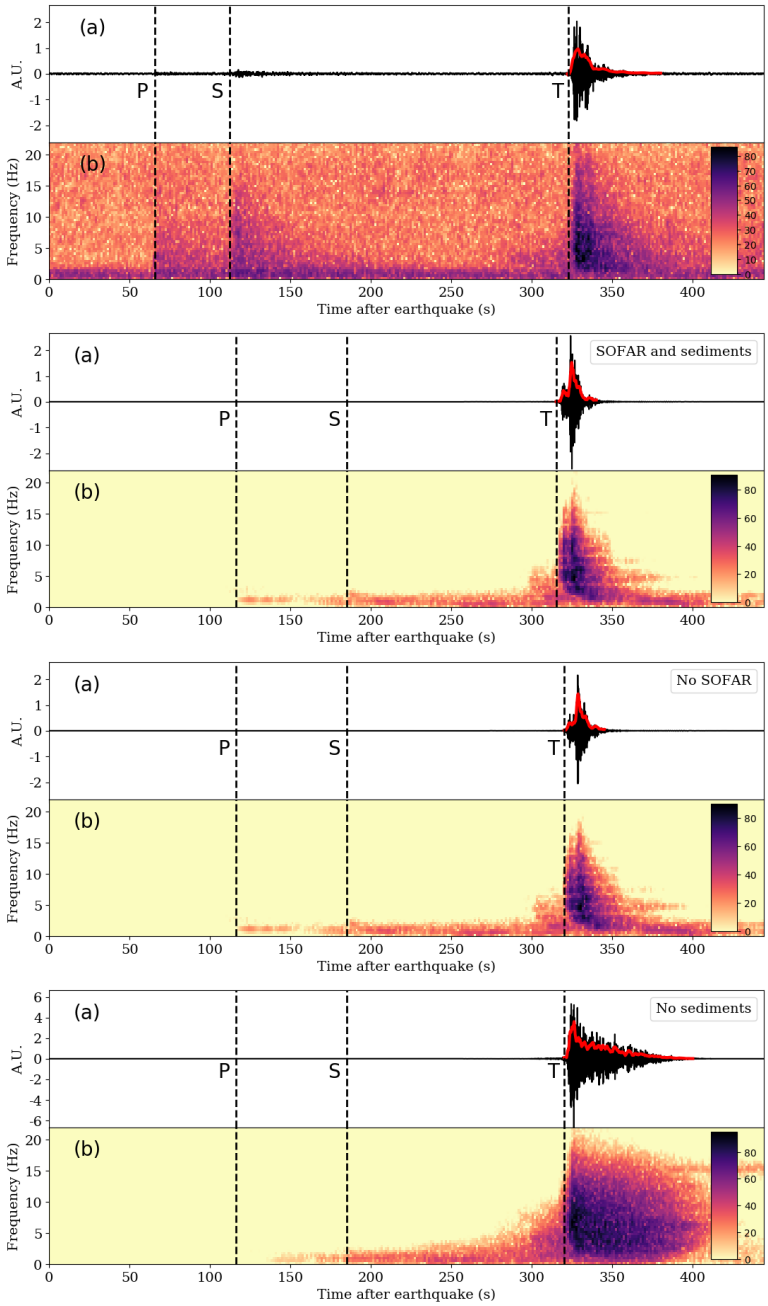

Figure 4.3 – Comparison of the synthetic signal to the real one for station AGST. The top figure is the real signal, the others are the synthetic ones (cases 1, 2 and 3, from top to bottom). For the four pictures: (a) Vertical component displacement seismogram (arbitrary displacement unit) recorded at the Italian seismic station AGST. Although arbitrary, the displacement unit used for the synthetic signals is the same. Thus, the relative amplitudes are preserved (see e.g. the high amplitude of T-waves for the case with no sediments). The red line is an example of filtered T-phase envelope. (b) Power Spectral Density (in dB) as a function of time and frequency. The monochromatic noise (15 Hz) visible on the bottom figure (case 3) is probably of numerical origin.

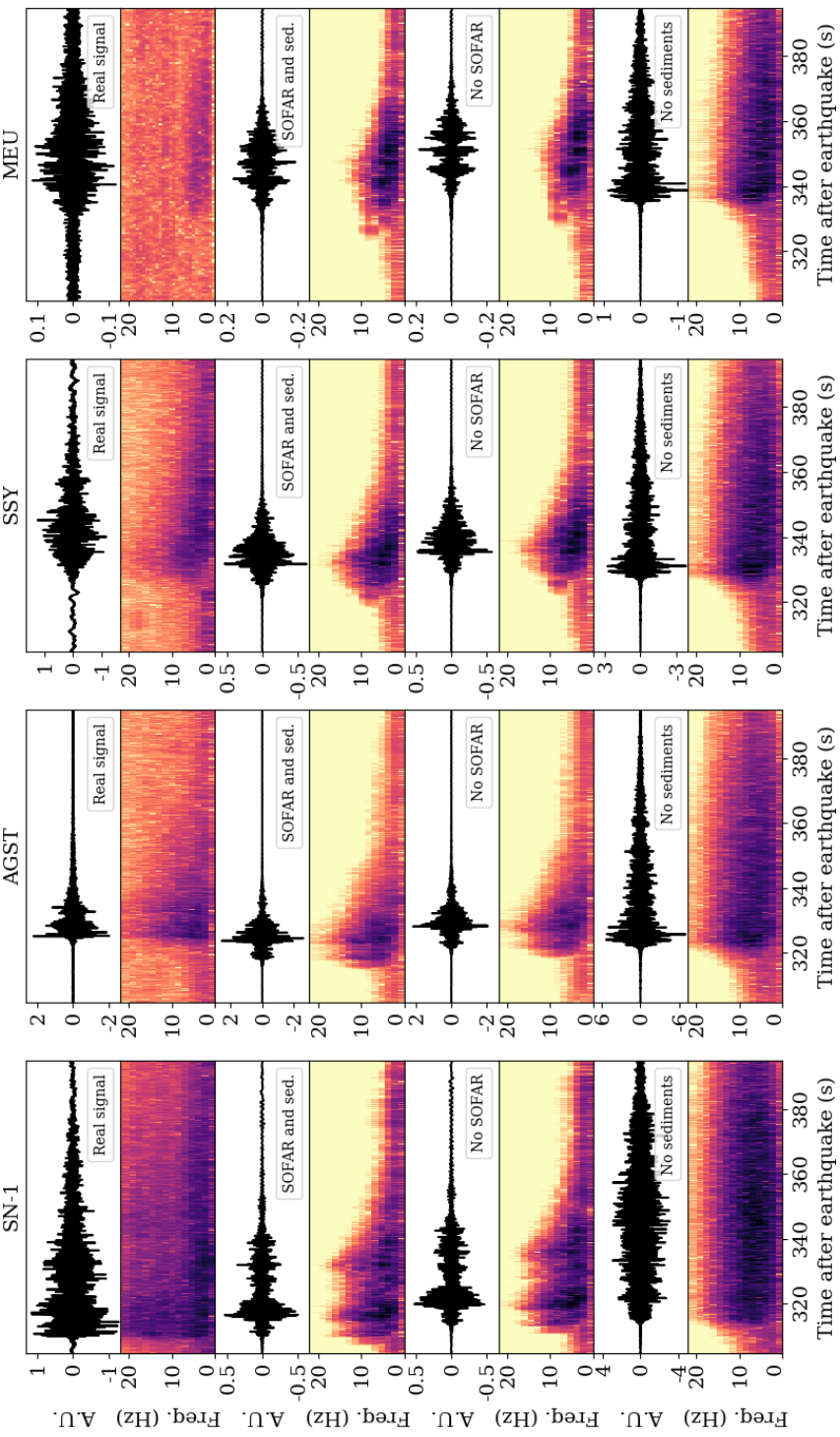

Figure 4.4 – Same as Figure 4.3 but for four seismic stations (columns) and zoomed on the T-phase. Cases 1, 2 and 3 are shown.

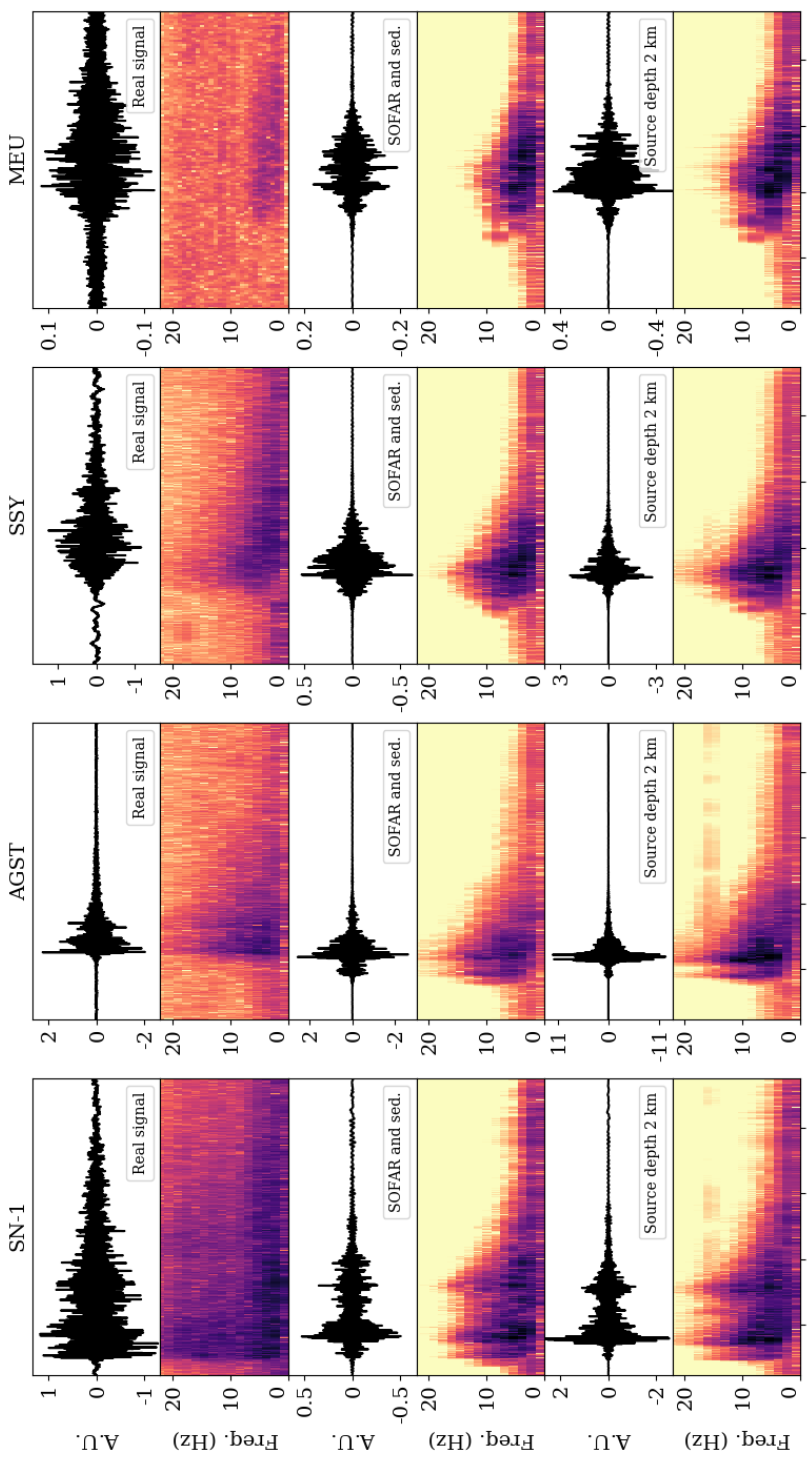

Figure 4.5 – Same as Figure 4.4 but including the effect of source depth (case 4). The second line is simulated for a source depth of 10 km, the last one for a source depth of 2 km. The monochromatic noise (15 Hz) visible on the bottom line (case 4) is probably of numerical origin.

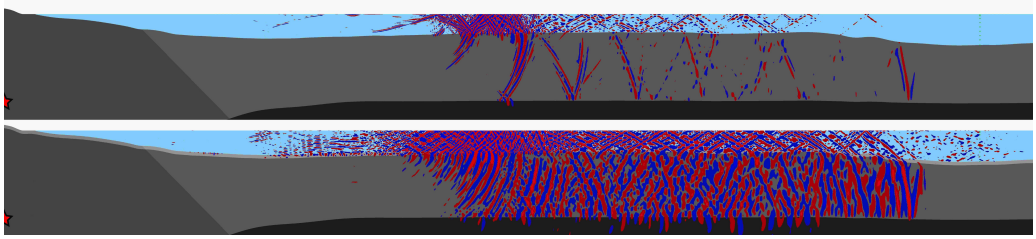

Figure 4.6 – Snapshots of the horizontal displacement field at time $t = 40$ s, showing the effect of the presence of sediments. Blue: negative horizontal displacement, red: positive horizontal displacement. The symmetry axis is at the left-hand side of the figures, and the source position is shown as a (partly cut) red star on the symmetry axis. **Top**: no sediments (case 3). **Bottom**: with sediments (case 1). The amplitude scales used in each case are different, the display being independently normalized to the maximum amplitude of a given figure.

m/s, suggesting that the actual velocity of the upper continental crust and sediments is locally higher than the one extrapolated from Finetti [2005]. Figure 4.7 also suggests that the synthetic signals are slightly less spread in time than the real signals. This may come from the same issue, i.e. too low synthetic velocity values in the continental sediments, or inaccurate attenuation values in the model.

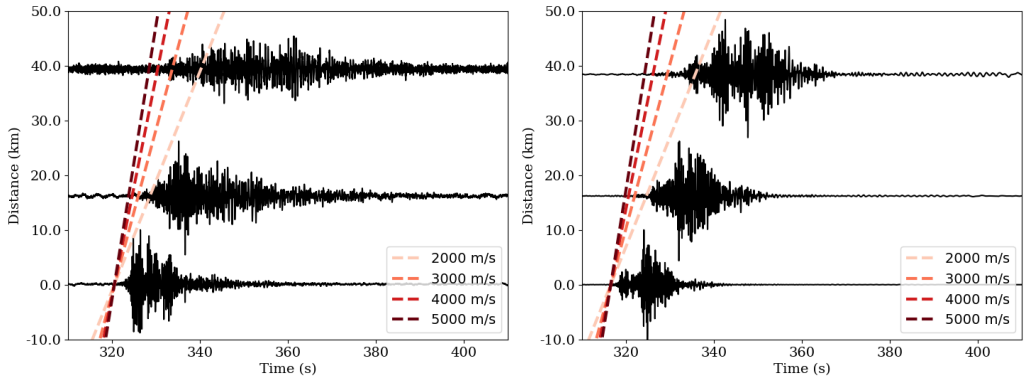

Figure 4.7 – Comparison between the observed inland T-wave speed for the synthetic (case 1) and real cases. The traces are the normalized north-south displacement seismograms at stations MEU, SSY and AGST, from top to bottom. The traces are distributed along the vertical direction according to the distance to station AGST of their projection on blue dotted line in Figure 2.1 (top). **Left**: real signals. **Right**: synthetic signals (configuration with a SOFAR channel, sediments, and a source depth of 10 km). The apparent velocity of the first real arrival is seen to be 4000±1000 m/s, while the apparent velocity of the first synthetic arrival is seen to be 3000±1000 m/s.

Figure 4.8 is a comparison of particle motion at station AGST and SSY for the synthetic (case 1) and real signals. The real components have been rotated in order to match those of the synthetic signals. Nevertheless, in spite of the small differences in orientation between the longitudinal direction and the East-West azimuth, the axis will still be labeled “East-West” in the figures and the transverse component will be labeled “North-South”. Unfortunately, based on geometrical considerations, axisymmetric 2-D simulations cannot handle out-of-plane motion if the source is located on the symmetry axis, and this will force us to perform the comparison in the longitudinal vertical plane (Down - Up / West - East) only. At station AGST the first part of the synthetic signal does not seem to correspond to the real one in terms of particle motion. However, the slight subsequent tilt towards the Up - West direction appears to be modeled. This observation strengthens the hypothesis that the first part of the synthetic signal (shown in red in Figure 4.8) does not correspond to the first part of the actual signal. At station SSY the particle motion analysis does not provide much information. One can still note that the small vertical polarization of the last part of the signal is reproduced.

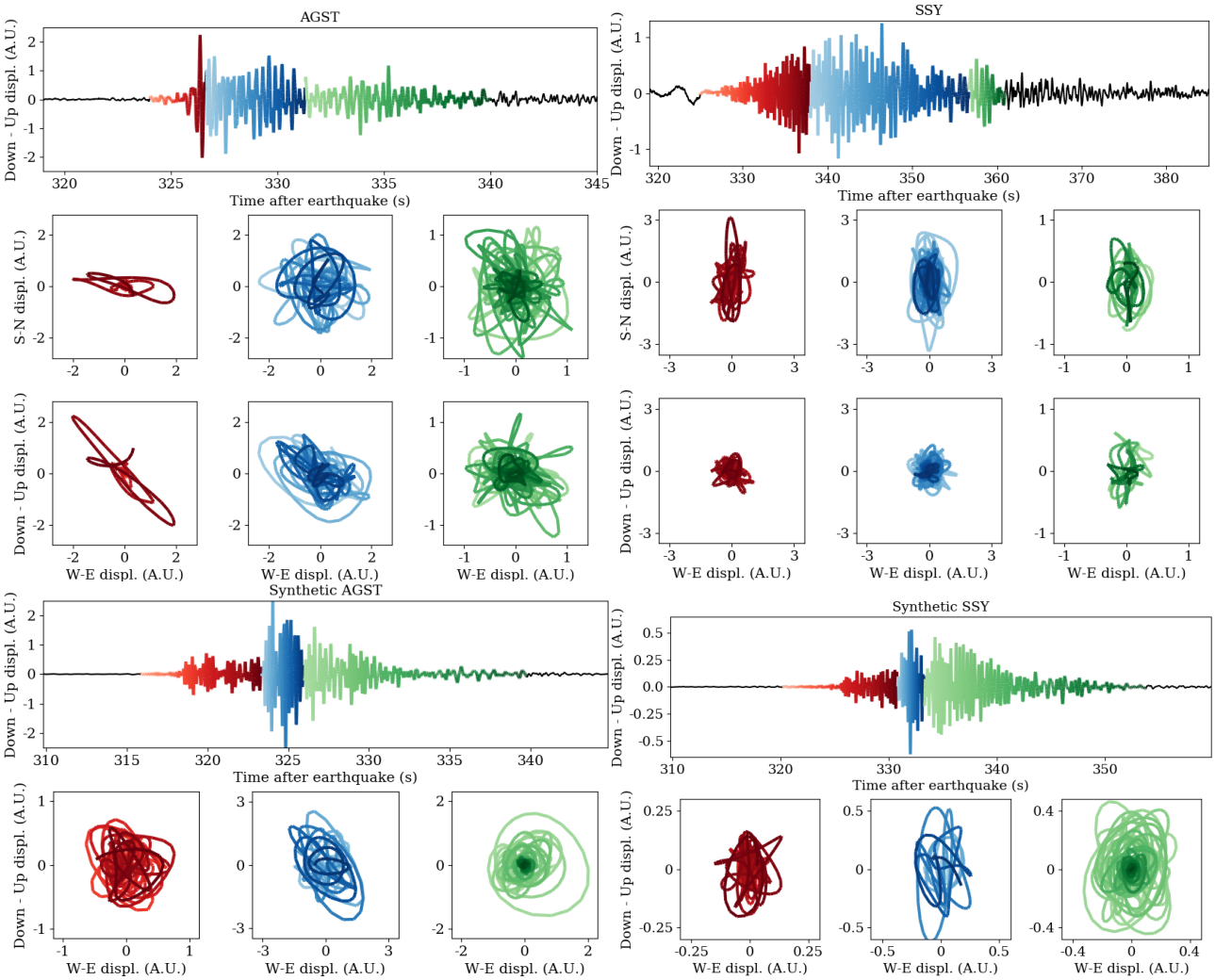

Figure 4.8 – Comparison between synthetic (with sediments, a SOFAR channel, and a source depth of 10 km) and real signals. **Top left**: T-phase north-south displacement at station AGST (arbitrary units) as a function of time. **Bottom left**: same but for the synthetic signal. The simulation being axisymmetric 2-D, the transverse component (S-N) has not been simulated. The real components have been rotated in order to match those of the synthetic signals. Hence we will directly compare the horizontal component of the synthetic signals to the West-East component of the real signals. The sub-figures in the squared boxes correspond to particle motions in the longitudinal planes: horizontal (West-East / South-North, only available for real signals) and vertical (West-East / Down-Up). **Right**: same but at station SSY.

4.1.2.4 Signal-to-noise ratios at inland stations

Figure 4.9 is a comparison of synthetic (cases 1 and 3) and real Signal-to-Noise Ratios (SNR) for stations SN-1, AGST, SSY and MEU. Real SNRs were computed by dividing the power spectrum of the T-phase by the power spectrum of an interval typical of the ambient noise at each receiver. Synthetic SNRs were computed by dividing the power spectrum of the T-phase by the power spectrum of an interval typical of the roundoff noise of the numerical scheme. Although the global structure and behavior along inland propagation of the synthetic SNRs is preserved in case 1, some remarks can be made: one can note that in the synthetic case with sediments (case 1) the SNRs exhibit clearly notches that are not present in the real data. It is tempting to relate the main synthetic notch (at 2 Hz) to the actual one observed around more or less the same frequency at station MEU. However, the two phenomena involved are probably different because, in the real case, the observed notch appears gradually while the wave propagates inland, while the synthetic notch is observed in the water before the conversion. Figure 4.10 shows that the synthetic notch gradually increases along the oceanic propagation path. The figure shows synthetic SNRs computed using the East-West component (horizontal component) for the virtual stations SN1-1000m, SG2-1000m and SG1-1000m (see Figure 4.1) at depth 1000 m and at respective ranges 31 km, 116 km and 478 km. Figure 4.9 (bottom) shows that the notches are not observed when no sedimentary layer is present. It is unclear why these notches do not appear in the data, since our tests show that they are not very sensitive to source depth, nor to the sound velocity profile in the ocean. We suggest that this may come from a difference between the synthetic and virtual sediment properties (velocities or density).

Another remark can be made regarding Figure 4.9. Apart from the notches, another difference between synthetic and real data lies in the high-frequency behavior of the signal at SN-1. While the real signal still exhibits a lot of energy above 10 Hz, the synthetic spectrum appears to be lacking high frequencies. This can be explained by the frequency content of the source used: its source time function is the second derivative of a Gaussian wavelet, with dominant frequency $f_0 = 6$ Hz, and thus has little energy above 15 Hz.

4.1.2.5 Influence of source depth and radiation pattern

To close this section let us go back to Figure 4.5 and discuss a bit more on the influence of the source depth. As expected from the data studied in Chapter 2, the influence of source depth on T-wave amplitude appears to be significant in the setting considered, with simulated amplitudes at station AGST increasing by a factor of 5 when changing the source depth from 10 to 2 km. In some respects, simulations with a source depth of 2 km corresponding to the estimated moment centroid (case 4, estimated by NOA) appear to be more realistic than for case 1 with a source depth of 10 km corresponding to the estimated hypocenter depth (estimated by NOAA).

The decrease in T-phase amplitude along its inland propagation path between stations AGST, SSY, and MEU (see Figure 4.5) is indeed more accurate in the case of a shallow source. Moreover, as already mentioned, the first T-phase synthetic arrivals, presumed to be irrelevant based on considerations related to arrival times, are relatively more damped in this case. For these reasons the simulation with the shallow source (Case 4) appears to be more realistic than the other ones. Let us also note that the simulated T-phases shown in this section seem to make sense in spite of the fact that the source implemented is not entirely realistic. In the model considered, a simple point-source vertical force was used rather than an extended source, while the difference in depth between hypocenter and moment centroid would rather suggest an extended fracture zone. Moreover the time function chosen is simple and not based on an inversion of the real source time signal. This may suggest that the actual source was actually close to a simple point-source vertical force or that the source radiation pattern has a rather weak influence on T-wave, at least in the case that we have studied.

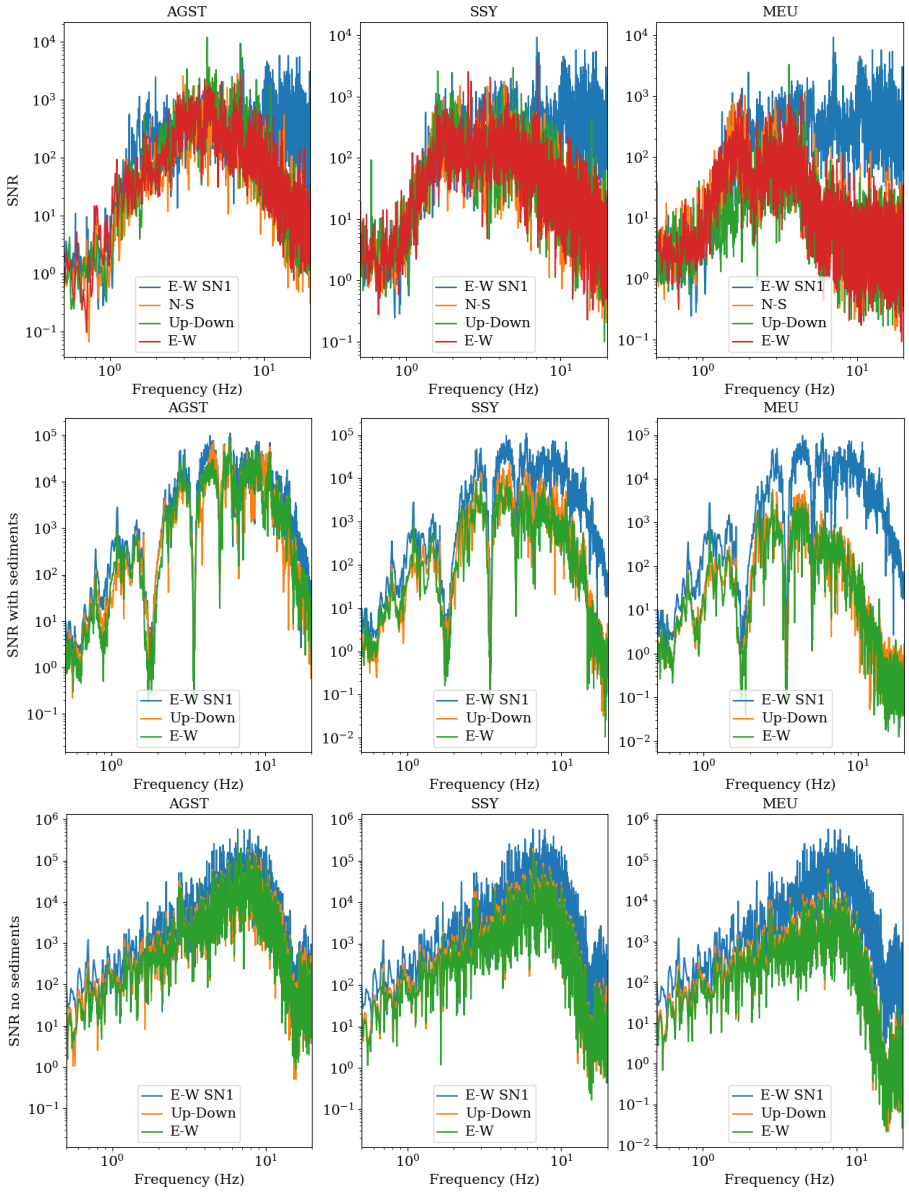

Figure 4.9 – Comparison of synthetic and real Signal-to-Noise Ratios (SNR) for stations AGST, SSY and MEU, in log-log scale. Real SNRs were computed by dividing the power spectrum of the T-phase by the power spectrum of an interval typical of the ambient noise at each receiver. Synthetic SNRs were computed by dividing the power spectrum of the T-phase by the power spectrum of an interval typical of the numerical noise. SNRs for the East-West (red), North-South (orange, not taken into account in our 2-D simulation), and vertical components (green) are shown. In each plot the SNR for the vertical component recorded at ocean bottom seismometer SN-1 is shown in blue. The middle line shows the results in the presence of sediments, while the bottom line is the case without sediments. Note the presence of notches in the synthetic spectra in the synthetic case with sediments.

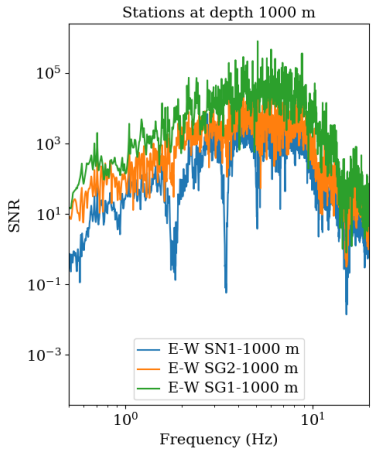

Figure 4.10 – Synthetic signal-to-noise ratios computed using the East-West component (horizontal component) for the virtual stations SN1-1000m, SG2-1000m and SG1-1000m (see Figure 4.1). Note the gradual formation of notches along the oceanic propagation path.

4.1.2.6 What was learned from the above simulations

In this section we have illustrated the fact that a quantitative comparison between real 3-D data and synthetic axisymmetric 2.5-D T-phases involving solid-fluid and fluid-solid conversion is feasible. For the real regional problem considered we have shown that the most significant parameter for T-wave characteristics was the impedance contrast at the sea bottom, much more than the velocity profile in the sea or the source radiation pattern, both appearing to have second-order effects. In particular, the weak contribution of the presence of the SOFAR channel to the T-phase (at the distances and frequencies considered) is in apparent contradiction with most of the studies on the subject. This particular point will be further investigated in Chapter 5. There are of course many remaining open questions. For instance, how can the observed double peak shaped T-phase be explained? From which thickness, in term of the incident wavelength, sediments can be neglected? Why are the robust notches observed in the simulated signal spectra not observed in the real data? etc ... The study of inverse (i.e. imaging) problems would thus be of great interest to investigate these issues, attempting to fit real data and determine more precisely what physical parameters influence the T-phase, and to what extent.

Although all the numerical tools necessary are already available in the software package SPECFEM that we use (Favier et al. [2004]; Xie et al. [2014]; Monteiller et al. [2015]; Wang et al. [2016]; Komatitsch et al. [2016]), in this thesis in a first step we have decided to favor parametric studies rather than inversions, in order to start analyzing the main parameters that play a role based on forward simulations rather than immediately going into significantly more expensive inverse problems. These simulations are indeed the first steps into the exploration of the phenomenon in the time domain. It should also be noted that 2.5-D simulations were supposed to be initial results before going to more realistic 3-D configurations and comparing their results with the INGV data presented in Chapter 2, however for now we have failed at the meshing step, as described in Appendix B.

In Chapters 1 and 2 we saw that slopes play a crucial role in downslope generation and upslope conversion of T-waves. For that reason, in the remainder of this chapter we will perform two parametric numerical studies to evaluate more quantitatively the influence of bathymetry and of sea-bottom impedance contrast on these processes.

4.2 Parametric study of T-wave downslope generation

In this section we will study the influence of the slope and sediment properties on T-wave energy received at a receiver line for a simplified downslope conversion scenario (Figure 4.11). The model consists of a homogeneous elastic semi-infinite bottom overlaid by a 400 m-thick homogeneous elastic sedimentary layer, covered by an acoustic layer. The seafloor has a finite slope of constant horizontal size $d = 5$ km. The seismic source is placed right below its upper end. Contrary to a similar study carried out by Frank et al. [2015], we have chosen to keep the horizontal size of the slope constant in order to keep the solid angle from which the source "sees" the slope unchanged (denoted Ω in the figure). For this study we cannot work in axisymmetric 2-D because we would obtain multiply-reflected energy between the highest slopes and the symmetry axis that do not exist in reality[1]. However, fortunately it seems that the use of Cartesian 2-D rather than axisymmetric 2-D is not of high importance for this qualitative study. We set $z = 0$ m at the sea surface and $x = 0$ at the source. Although the Greek earthquakes studied above in this chapter were very shallow, many earthquakes happen deeper. For the sake of generality we thus chose to carry the study in the case of a deeper source located in the elastic part at $Z_s = 30$ km. The receiver line is located at $x = 85$ km.

Three different sediments have been tested, labeled LOW, MED and HIGH (for low, medium or high impedance contrast between the crust and the water). Their properties are given in Table 4.2. Note that the case labeled HIGH matches the semi infinite bottom properties and thus there is no sedimentary layer. Throughout this section the results obtained based on full-wave spectral-element simulations will be compared with those obtained using a simplified model based on ray tracing in order to identify the phenomena that can be expressed geometrically and those that involve a more complex physical process.

Let us also note that in the setting we have chosen the sedimentary layer also covers the synthetic abyssal plain. Therefore it has an influence not only in the conversion process but also all along the subsequent propagation in the flat ocean. This will have to be kept in mind when comparing the results obtained with different sedimentary layers.

In the water layer, the density is equal to 1000 kg.m^3 and the sound velocity is either a constant velocity of 1500 m.s^{-1} or a classical idealized ocean sound-speed profile (Munk [1974], see Figure 4.11, right).

Label used	Description
Semi-infinite bottom	$\rho = 2500$ kg.m^{-3}, $V_p = 5500$ m.s^{-1}, $V_s = 3235$ m.s^{-1}, $\alpha_p = 0.17$ dB.λ_p^{-1} , $\alpha_s = 0.17$ dB.λ_s^{-1}
HIGH	$\rho = 2500$ kg.m^{-3}, $V_p = 5500$ m.s^{-1}, $V_s = 3235$ m.s^{-1}, $\alpha_p = 0.17$ dB.λ_p^{-1} , $\alpha_s = 0.17$ dB.λ_s^{-1}
MED	$\rho = 2200$ kg.m^{-3}, $V_p = 3500$ m.s^{-1}, $V_s = 2060$ m.s^{-1}, $\alpha_p = 0.46$ dB.λ_p^{-1} , $\alpha_s = 0.46$ dB.λ_s^{-1}
LOW	$\rho = 2200$ kg.m^{-3}, $V_p = 2000$ m.s^{-1}, $V_s = 1000$ m.s^{-1}, $\alpha_p = 0.46$ dB.λ_p^{-1} , $\alpha_s = 0.46$ dB.λ_s^{-1}
HIGH, with low density	$\rho = 2200$ kg.m^{-3}, $V_p = 5500$ m.s^{-1}, $V_s = 3235$ m.s^{-1}, $\alpha_p = 0.17$ dB.λ_p^{-1} , $\alpha_s = 0.17$ dB.λ_s^{-1}

Table 4.2 – Properties of the semi-infinite bottom and of the four types of sediments used. ρ is the density, V_p is the compressional wave speed, V_s is the shear wave speed, and α_p and α_s are the corresponding attenuation coefficients expressed in dB per wavelength. Note that the case labelel HIGH matches the semi-infinite bottom properties and thus there is no sedimentary layer in that case.

[1]This could happen, though, in the case of an earthquake occurring right below a volcano or a seamount, but we are not interested in these particular cases here

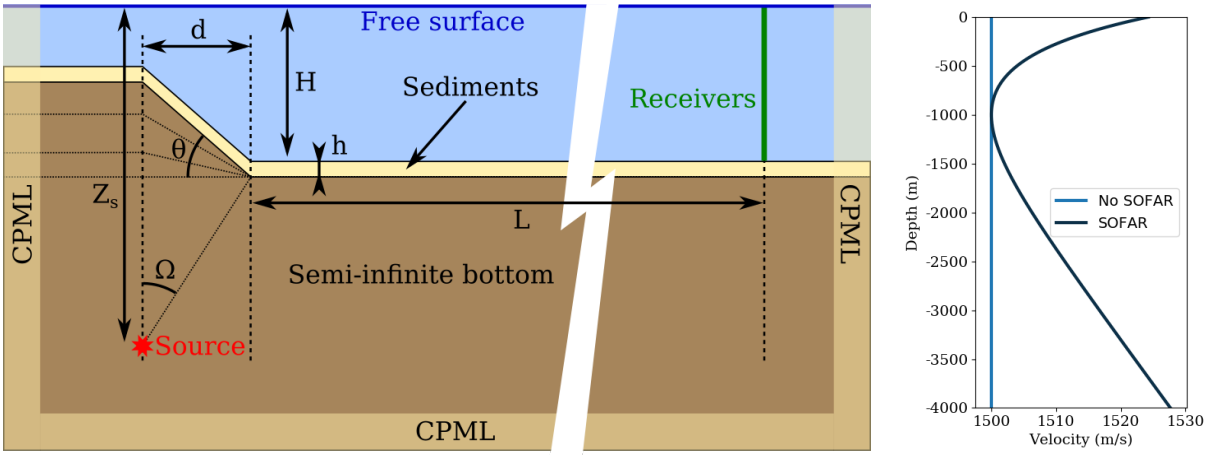

Figure 4.11 – **Left**: Setting of the study. The objective is to analyze the influence of slope angle θ and sediment properties on T-wave energy transmitted at the green receiver line situated at range $L + d = 85$ km. The geometry is 2-D Cartesian. The source is located at depth $Z_s = 30$ km, the sediments are $h = 0.4$ km thick, the abyssal plain is located at depth $H = 4$ km, and the slope has a horizontal size of $d = 5$ km. The receiver line is at $L = 80$ km from the bottom of the slope. In the spectral-element simulations the energy that reaches the edges of the model is absorbed by CPML (convolutional PMLs, see Xie et al. [2016]) absorbing layers. **Right**: Sound speed profiles in the sea used in the numerical simulations. The curve labeled "SOFAR" refers to a classical idealized ocean sound-speed profile (Munk [1974]) with minimum velocity at a depth of 1000 m.

4.2.1 Simple ray model

4.2.1.1 Description of the model

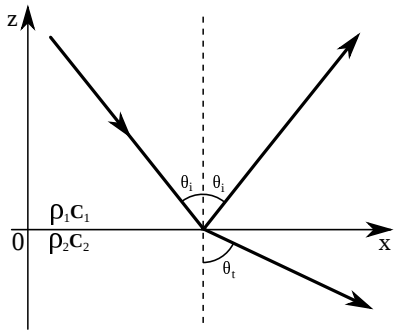

Figure 4.12 – Reflection and refraction of a plane wave at the boundary between two fluid media.

Let us first use a simplified fluid model based on ray tracing in order to discuss qualitative results before switching to full-wave simulations. The elastic parts of the real ocean bottom are replaced with fluid media having the same density and a velocity of either P or S waves. The ocean is considered to have a constant density of 1000 kg.m^{-3} and a sound velocity of 1500 m.s^{-1}. The source emits 100 rays covering the whole sloping interface. The refraction and reflection angles of the rays at an interface obey Snell-Descartes's law (see Figure 4.12):

$$\frac{\sin\theta_i}{c_1} = \frac{\sin\theta_t}{c_2} \tag{4.1}$$

with θ_i the incidence angle of the ray with respect to the normal to the interface, θ_t the transmission angle, and c_1 and c_2 are the velocities of the two media. An example of ray tracing for a source at depth 15 km (instead of 30 km) and with only 5 rays is shown in Figure 4.13.

A unitary energy is assigned to each ray when it leaves the source. When it reaches the slope the ray is divided by its length to account for the cylindrical geometrical spreading (we suppose Cartesian

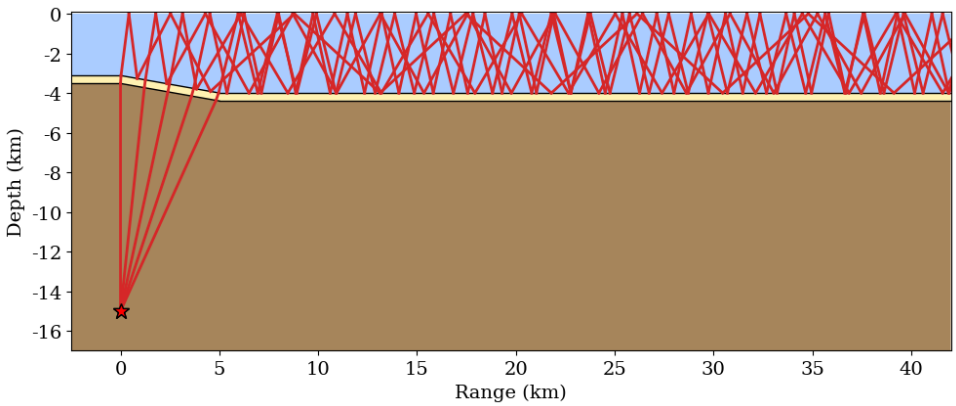

Figure 4.13 – Example of ray tracing for a source at depth 15 km with 5 rays launched at the source and spread over the whole slope ($\theta = 10°$). The sediment properties correspond to the medium labeled MED in Table 4.2.

2-D coordinates). Then, at each refraction/reflection undergone by the ray its energy is multiplied by the corresponding coefficient depending on its incidence angle θ_i and given by Fresnel formulas (Brekhovskikh & Godin [1990] pp.17-24):

$$\begin{aligned} \mathcal{R} &= \left| \frac{c_2\rho_2 \cos\theta_i - \rho_1\sqrt{c_1^2 - c_2^2\sin^2\theta_i}}{c_2\rho_2 \cos\theta_i + \rho_1\sqrt{c_1^2 - c_2^2\sin^2\theta_i}} \right|^2 \qquad \text{Energy reflection coefficient} \\ \mathcal{T} &= 1 - \mathcal{R} \qquad \text{Energy transmission coefficient} \end{aligned} \tag{4.2}$$

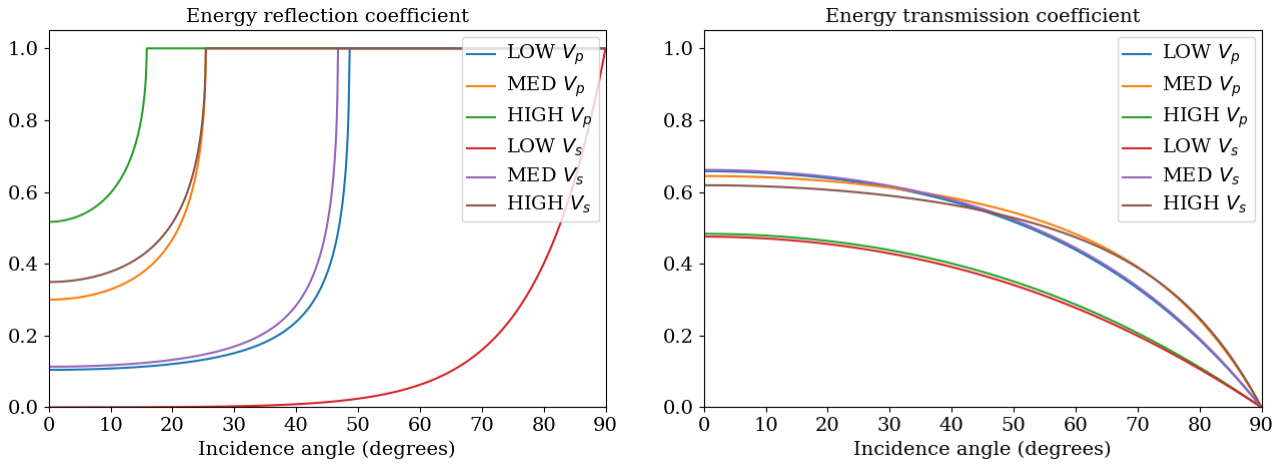

Figure 4.14 – Left: energy reflection coefficient for oceanic rays as a function of incidence angle (with respect to the normal to the interface) at the water-sediments interface. Right: semi-infinite bottom → sediments → water energy transmission coefficient as the function of incidence angle. "LOW V_s" for example means that the sediment density is equal to that of the case labeled LOW in Table 4.2 and that the velocity corresponds to shear-wave velocity of case LOW.

When they cross the receiver line at range 85 km, and to account for the geometrical spreading in the water, the ray energies are finally divided by the horizontal distance between the point where they entered into the water and the receiver line. The sum of all ray energies is then computed and divided by the number of rays launched. This value is noted S, and it has the dimension of an energy. It is important to note that this energy is "incoherent" because it does not take into account the phase and thus the interactions between the rays. We consider that it gives some information on the total energy transmitted at range 85 km. The semi-infinite bottom → sediments → water energy transmission

coefficient as the function of incidence angle (with respect to the normal to the interface) is shown in Figure 4.14 (right); it is an energy transmission coefficient taking into account the two crustal interfaces. The energy reflection coefficient for water → sediments reflections of rays as a function of incidence angle is shown in Figure 4.14 (left).

This simple model does not take attenuation into account. Apart for geometrical spreading, ray energy is assumed to be unaffected by the propagation through the media in the absence of interfaces. This assumption also allows for total internal reflection (unitary energy reflection coefficient) when the incidence of a ray is above a critical angle.

4.2.1.2 Results obtained based on this simple model

The critical angle is highly dependent on the velocity contrast between the two media but only to a lesser extent on density, which mostly drives the amount of reflected energy below the critical angle (see the differences between MED V_p and HIGH V_s in Figure 4.14, left). The results are summarized in Figure 4.15.

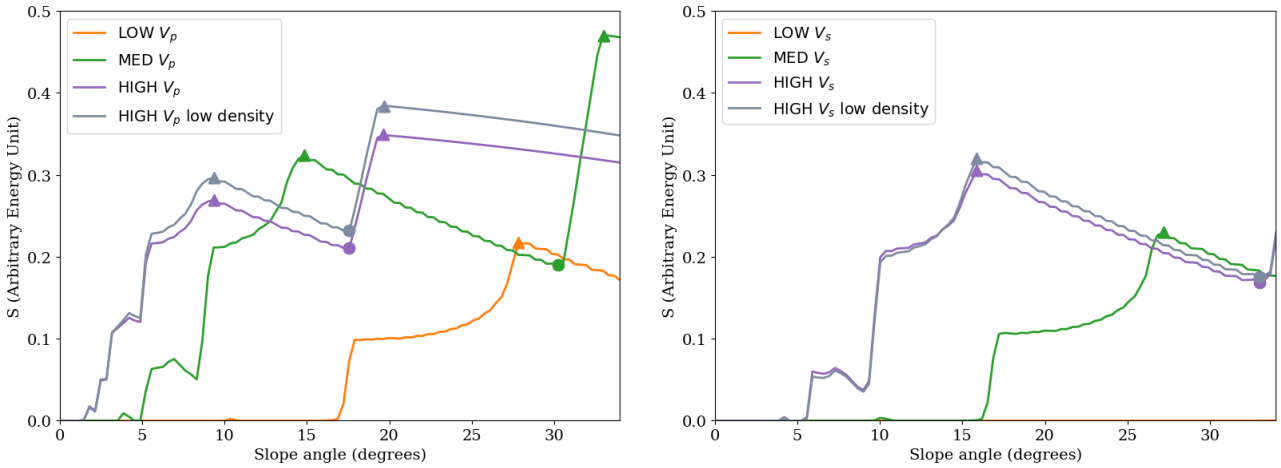

Figure 4.15 – Normalized average ray energy S as a function of slope angle. ρ and V are respectively the sediment density and sound velocity used. **Left**: Properties corresponding to P waves. The fourth case ($V = 5500$ m.s^{-1} and $\rho = 2200$ kg.m^{-3}) does not correspond to any of the cases studied (see Table 4.2) and has been added in order to illustrate the effect of density on transmitted energy. **Right**: Properties corresponding to S waves. "LOW V_s" for example means that the sediment density is equal to that of case LOW (see Table 4.2) and that the velocity corresponds to the shear-wave velocity of case LOW. The circles and triangles indicate particular points of the curves that are discussed in the text.

This figure shows the normalized average ray energy S as a function of slope angle for the three different sediments studied: two curves for each, considering either the P wave velocity (left) or the S wave velocity (right), plus an additional curve showing the effect of a density variation of the sediments (light purple curve in the figure on the left, to be compared to the dark purple one). Low sediment density is seen to slightly favor energy transmission without affecting the global shape of the curve, this being particularly true when high velocities are involved.

The results exhibit several other interesting features. As the rays leave the sediments with an angle equal to their incidence angle, the sedimentary layer properties have no particular effect on the geometric ray tracing results, the number of reflections remains the same, and the differences in transmitted energy at long range are due to the energy coefficients only. Let us first analyze the dark purple curve, corresponding to the case without sediments (HIGH). When increasing the slope angle from 0 to 15°, the number of reflections needed to reach the receiver line first decreases and then

increases, leading to a maximum in transmitted energy (marked with a triangle around slope angle 9°) and corresponding to an optimum geometry in terms of the number of reflections.

From the trough, indicated by a solid circle, the first total internal reflections appear, leading to a sharp rise of energy. Once the second maximum (second triangle) is reached, the evolution of the energy is only driven by the transmission coefficient at the slope, which gently decreases with increasing incidence angle (see Figure 4.14, right) and thus also with increasing slope angle. Note that for these high slopes the number of reflections also increases, which has no effect in this simplified model that includes total internal reflection, but would probably become important for more realistic models. When decreasing the impedance contrast between the water and the sediments, the overall shape of the curve is conserved but is shifted towards higher slope angles. Indeed, the critical angle increases with increasing sound speed in the sediments (see Figure 4.14, left), thus delaying the beginning of the first internal reflections. Note that in this model there is a clear difference between the rays that propagate on the flat part with total internal reflection and rays still experiencing damping. Let us mention again that our simple model here is not meant to be realistic but only to provide a first analysis of the phenomena that may play a role, before switching to far more expensive full-wave numerical simulations in the remainder of the document.

4.2.2 Full-wave model

4.2.2.1 Description of the model

The same settings as in the above section has been simulated based on the spectral-element method, now taking into account S waves in the sea bottom. The chosen source is a vertical force ; its source time function is a Ricker wavelet (i.e., the second derivative of a Gaussian) with a dominant frequency $f_0 = 4$ Hz and a time shift $t_0 = 1.2/f_0$ in order to ensure null initial conditions. The wavefield is computed up to a range of 110 km and down to a depth of 35 km, the energy coming out of this box (shown in Figure 4.11) being absorbed by PML absorbing layers. For each slope angle between 0 and 34° (with an increment of one degree) six simulations are performed, one for each of the four types of sediments in Table 4.2, and for either a constant sound speed in the water or for a typical SOFAR channel (Figure 4.11, right). Each mesh is composed of ~ 0.12 million spectral elements whose polynomial degree is $N = 4$. The total number of unique GLL/GLJ points in the mesh is approximately 2 millions. In the worst case for all these meshes, 99.9% of the acoustic elements ensure a sampling of the signals of at least 5 grid points per pressure wavelength in the fluid, and 99.9% of elements in the viscoelastic part ensures at least 6.5 points per shear wavelength. In this way, frequencies up to ~10 Hz are resolved. We select a time step $\Delta t = 0.72$ ms for the explicit, conditionally-stable time scheme, and simulate a total of 0.2 million time steps, i.e. 140.0 s. The displacement is recorded at the receiver line shown in Figure 4.11, which comprises 20 evenly-spaced receivers. All the simulations ran simultaneously on 10,080 processor cores of the supercomputer that we use. The whole run lasted approximately 2 hours. An example of the horizontal displacement time signal generated in the middle of the receiver line for the case labeled HIGH, with a SOFAR channel and with a slope of $\theta = 20°$ is shown in blue in Figure 4.16, together with the same signal with 0° slope (orange).

P and S wave arrivals (observed after conversion into acoustic waves) are clearly visible on both curves and do not depend on the slope. The T-phase appears only in the presence of the slope, as expected. In order to remove the body waves the reference signal for a zero slope is subtracted from the signal generated with a non-zero slope. Such processing is of course not fully satisfactory, as the signals obtained may also contain energy from other phenomena than T-waves that may overlap with it. However we consider this unlikely, but cannot exclude it theoretically.

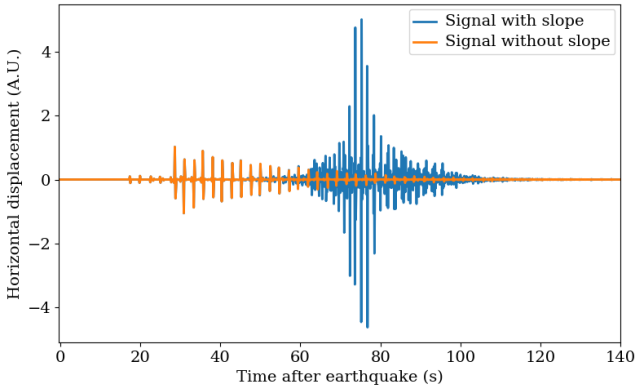

Figure 4.16 – Synthetic horizontal particle displacement recorded at a receiver located in the middle of the receiver line (see Figure 4.11) for the case labeled HIGH, with a SOFAR channel, and a slope of $\theta = 20°$ (blue) or a reference slope of $\theta = 0°$ (orange). For time < 40 s the two signals are almost identical and thus, in order to remove the body waves and to keep only the T-waves, the signal in orange (corresponding to the reference slope of $\theta = 0°$) is subtracted from the signal in blue generated with a non-zero slope.

4.2.2.2 Transmitted energy as a function of slope angle

Let us now introduce some useful quantities. We denote $u_x(\boldsymbol{x}, t)$ and $u_z(\boldsymbol{x}, t)$ the horizontal and vertical T-phase displacement fields and $P(\boldsymbol{x}, t)$ the T-phase pressure field at time t and position $\boldsymbol{x} = (x, z)$, obtained after subtraction of the reference signals. $\dot{u}(\boldsymbol{x}, t) = \sqrt{\dot{u}_x(\boldsymbol{x}, t)^2 + \dot{u}_z(\boldsymbol{x}, t)^2}$ is the norm of the particle velocity of the T-phase. The field that represents the instantaneous T-wave energy per unit volume in the fluid is given by (Jensen et al. [2011] pp.11-12):

$$\mathcal{E}(\boldsymbol{x}, t) = \frac{1}{2}\rho \dot{u}^2(\boldsymbol{x}, t) + \frac{1}{2}\frac{P^2(\boldsymbol{x}, t)}{\rho(\boldsymbol{x})c^2(\boldsymbol{x})}, \tag{4.3}$$

where ρ is the density of water and $c(\boldsymbol{x})$ is the distribution of sound velocity. Let T_f refer to the final time of the simulation, we can then define the integrated T-wave energy field by:

$$E(\boldsymbol{x}) = \int_0^{T_f} \mathcal{E}(\boldsymbol{x}, t)\, dt. \tag{4.4}$$

This quantity is similar to the radiated seismic energy introduced by Boatwright & Choy [1986] and evaluated from body waves measurements, it is a generalization to the T-Phase Energy Flux (TPEF) proposed by Okal [2003] to characterize the energy generated by an earthquake source into a T-wave.

Integrating E over depth along the receiver line (situated at range $L + d$, see Figure 4.11) gives an averaged transmitted energy in the water layer:

$$\langle E \rangle = \frac{1}{H}\int_{-H}^{0} E(L + d, z)\, dz \tag{4.5}$$

$\langle E \rangle$ has been computed as a function of the slope angle for the four different sediments types (described in Table 4.2) and the two different velocity profiles in the ocean (shown in Figure 4.11, right). It is shown in Figure 4.17 (left). The curves have a typical shape exhibiting two maxima (marked with red triangles in the figure) and a trough in between. Let us first remark that the SOFAR channel does not seem to have a significant influence on the results at this range.It can also be seen that low sediment densities slightly favor energy transmission without affecting the global shape of the transmission curves, as expected from ray considerations. In the case with no sediments

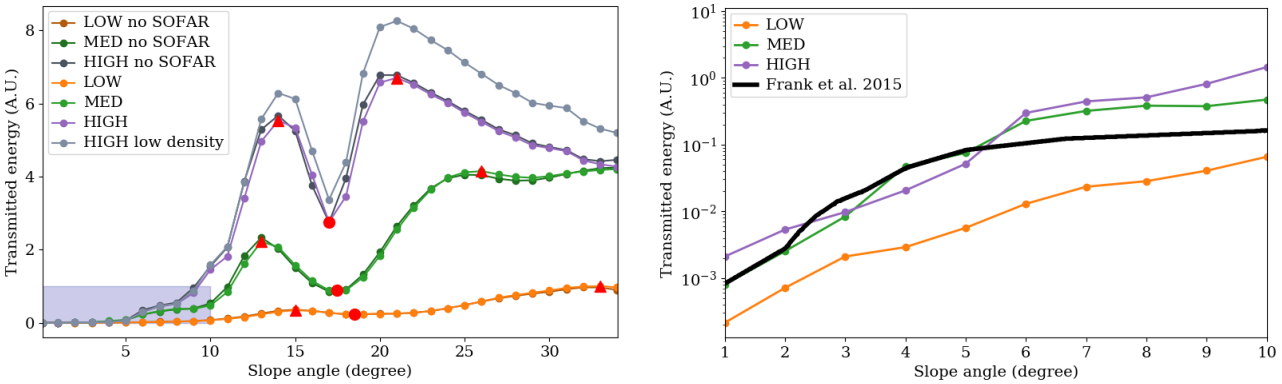

Figure 4.17 – **Left**: Transmitted T-wave energy at 85 km as a function of slope angle for three different sediments of Table 4.2 and for two different sound speed profiles in the ocean (Figure 4.11, right). The red triangles indicate the local maxima, and the red circle indicates the position of the trough. The blue shaded box represents the area studied by Frank et al. [2015]. **Right**: Zoom on the blue shaded area of the left picture, showing also a comparison in logarithmic scale between our results and the curve shown in Frank et al. [2015] (re-scaled).

(labeled HIGH, dark purple curves) the results obtained are in good agreement with ray tracing in the case labeled HIGH V_p (i.e., sediment density equal to that of case HIGH and sediment velocity corresponding to the compressional wave velocity of case HIGH) shown as a dark purple curve in Figure 4.15 (left). The trough and the two local maxima are observed at similar positions: the first maximum transmission was estimated at 9.3° based on ray tracing and is observed at 14° based on the full-wave simulation, and the second was estimated at 19.6° and is observed at 21°. The trough in transmission is observed at 17° instead of 17.6°. Let us note that the first maximum observed with ray tracing in the case HIGH V_s (dark purple curve in Figure 4.15, right) at slope 15.8° is not visible in full-wave simulations. It may coincide with the second peak (at 21°). As predicted, the final decay in transmission observed for slopes above the second maximum is more marked in the full-wave case because of the sea floor attenuation, which impedes total internal reflections. The remaining discrepancies such as the position of the first maximum, the shape of the slopes of the curves, or the depth of the trough can be easily explained by the fact that our simple ray model does not take S waves into account nor, for instance, the possible diffraction at the top edge of the slope. The low angular sampling may also play a role in the observed differences.

On the other hand the results of ray tracing and of full-wave simulations in the cases with sediments (LOW and MED) compare poorly. The curves do exhibit a shape that is similar to that of the case without sediments, and also partly include a characteristic shift that can be explained from the shape of the sea→sediments reflection coefficient (Figure 4.14), but apart from this the other features do not match. Indeed, the first maximum is not shifted towards high slopes and even seems to be shifted to the left in the case labeled MED. The trough and the second peak are shifted to the right but not as much as predicted by ray theory. In addition, transmitted energy substantially increases overall with increasing impedance contrast, which is not obvious in ray-tracing simulations (comparing the purple and green curves of Figure 4.15 and 4.17). Likewise, the reason behind the increase of transmitted energy above 29° for the case labeled MED is unclear and may suggest an effect coming from S waves. These discrepancies suggest that the semi-infinite bottom significantly contributes to the reflection coefficient of the seabed. This can maybe be attributed to the fact that some of the energy crossing the seabed can be reflected at the bottom of the sedimentary layer and can go back into the ocean, increasing the apparent reflection coefficient of the sea bottom.

Figure 4.17 (right) shows a comparison of our results with those of Frank et al. [2015] obtained, for small slopes, based on a parabolic solver. Let us mention that significant differences exist between

their model and ours: they used an axisymmetric geometry[2], they considered an homogeneous sea floor, similar to our case labeled MED but with a lower attenuation of $\alpha_p = 0.05$ dB.λ_p^{-1} , $\alpha_s = 0.10$ dB.λ_s^{-1}, a 5 Hz monochromatic source located at $Z_s = 10$ km (instead of a broadband source with dominant frequency 4 Hz at $Z_s = 30$ km in our case), a receiver line at range 150 km (instead of 85 km) and, more importantly, a different way of parameterizing the slope variations. In their model the depth of the top slope is fixed and the horizontal size of the slope consequently changes for each slope angle. This implies that the solid angle (labeled Ω in Figure 4.11) varies for each slope, thus favoring the lowest slopes (which receive more energy) compared to steepest ones. This is in our opinion the main reason for the slight differences observed between the two models. However, Frank et al. [2015] reached the same conclusion in the slope range 0° to 10° that there is a smooth increase of transmitted energy with increasing slope angle. We have seen in this section that steeper continental slopes involve more complicated physical phenomena than gentle slopes. Yet it is these configurations that are encountered at atolls (see Appendix A) or at the Greek west coast (see Chapter 2 and the first section of this chapter) for example. It is also worth mentioning that, in our study, the differences estimated in energy transmission between a hard (such as our case labeled HIGH for example) gently-dipping seabed (say a 5° slope) and a steeper one (14°) can reach a factor of 100, which could bias localization techniques towards steep slopes. This was already observed and documented in the literature (Northrop [1962]; De Groot-Hedlin & Orcutt [2000]), although not quantified to our knowledge. It is interesting to note that the opposite situation is also possible. Indeed, differences in energy transmission between an optimally-dipping area (i.e. a slope of 14° for our case labeled HIGH for example) and a steeper slope but located in the transmission trough (17°) may sometimes bias the estimated locations towards the lowest slopes.

4.2.3 Influence of source position on T-wave energy and duration

4.2.3.1 Definition of the average transmitted T-wave duration

Let us now consider another aspect of downslope conversion of T-wave and study the influence of the source position on transmitted T-wave energy and duration. Energy and duration are two quantities of equal importance because a large energy distributed over a long period of time can go unnoticed in the presence of noise, and conversely, a limited but concentrated energy over a short period can often be very visible. In equations (4.3), (4.4) and (4.5) we have defined the instantaneous T-wave energy $\mathcal{E}(\boldsymbol{x}, t)$, the integrated T-wave energy $E(\boldsymbol{x})$ and the averaged transmitted T-wave energy $\langle E \rangle$, whose computation has been detailed above. One can also define the maximum T-wave energy field:

$$M(\boldsymbol{x}) = \max_{t<T_f} \mathcal{E}(\boldsymbol{x}, t). \tag{4.6}$$

where T_f is the final time of the simulation. It gives the maximum instantaneous energy at each point and provides a way of defining an "effective" T-wave duration field as follows:

$$\mathcal{T}(\boldsymbol{x}) = 2\frac{E(\boldsymbol{x})}{M(\boldsymbol{x})}. \tag{4.7}$$

This quantity is homogeneous to a duration, which is formally the duration of a signal that is triangular in shape[3]. Computing this field gives information on the temporal and spatial structure of the arrivals, keeping track of their spreading over time at any point of the model. As for the integrated energy, we can then define an averaged transmitted T-wave duration in the water layer:

[2] As the parabolic equation does not take into account back-scattered energy, they do not face the problem of multiple reflections between the slope and the symmetry axis that we mentioned and that prevented us from using axisymmetric calculations in our case.

[3] In the case of triangular signals this effective duration is equal to their actual duration.

$$\langle \mathcal{T} \rangle = \frac{1}{H} \int_{-H}^{0} \mathcal{T}(L+d, z)\, dz, \tag{4.8}$$

which is the average effective duration of the T-waves generated by the earthquake considered and recorded at a horizontal distance $L + d = 85$ km from the top of the slope.

4.2.3.2 Influence of earthquake position on T-wave energy and duration

We have computed the averaged transmitted T-wave energy $\langle E \rangle$ and duration $\langle \mathcal{T} \rangle$ for 351 source positions (324 being below the seafloor). Contrary to the previous sections the slope is now being set at 20°, and the medium properties being those of the case labeled MED in Table 4.2 with a SOFAR channel included. Before being able to compute the instantaneous T-wave energy $\mathcal{E}(\boldsymbol{x}, t)$, the body waves have to be subtracted from the signals (see Figure 4.16). For this purpose, a reference run without a slope is performed for each of the 324 sources below the seafloor. For the sources situated above the ocean floor no subtraction is needed, only T-waves are created in that case. In the transition between these two domains, artifacts can be observed. They are explained by the fact that the body waves generated with and without a slope are not strictly identical anymore for these very shallow source positions. For that reason, we will compare the energies and durations with and without subtraction (i.e. including the body waves in that latter case).

The simulations were run simultaneously on $(351 + 324) \times 12 = 8100$ processor cores and lasted approximately one hour. The results are summarized in Figure 4.18.

Let us first discuss the differences between the quantities computed from the full signal and those computed from the subtracted signals assumed to represent T-waves only. Apart from the artifact at the third line of sources the images are overall very similar, which means that in most cases body waves do not influence the results much. Consequently, the right- or the left-hand side of Figure 4.18 can be used for analysis. The region right below the bottom of the slope and the outset of the abyssal plain are however an exception to note. The results computed there show that T-waves can be generated, by downslope conversion, from earthquakes located beneath the abyssal plain but only above a certain depth, contrary to body waves that can be generated at any depth. It seems that this depth increases with the distance to the slope, although this is to be verified by calculations over a wider area. This phenomenon could have interesting implications and explain some frequent outliers to the rule "epicenters at the lower end, and to seaward, of the continental slope are typically weak or not received" (Johnson et al. [1967]) outside the framework of scattering. Let us note that this implies back-scattering that would prevent the use of parabolic methods.

It can also be noted that the earthquakes that happen in the immediate vicinity of the slope are particularly prone to generate strong and impulsive (short duration) T-waves. This result was of course expected because in that area an important part of the source energy reaches the slope and thus geometrical spreading is minimum. Besides, the angular sector under which the source sees the slope is maximum there. It explains the particularly large T-waves observed in Italy following shallow earthquakes in the Greek peninsula of Paliki that we have analyzed in Chapter 2 (see Figure 2.5 in particular[4]). Looking in more details we can see that the energy and duration maps have an interesting pattern: some regions are favored for T-wave generation and exhibit high energies and short durations. To investigate that more precisely, we constructed the same map using thousands of runs of our simple ray model, using P wave velocity in the semi-infinite bottom and P or S wave velocity from the case called MED (see Table 4.2) in the sediments. That simple ray-tracing technique only takes into account the rays that have a direct path between the source and the slope. The map

[4]The moment centroid depth of the circled earthquake is 2 km.

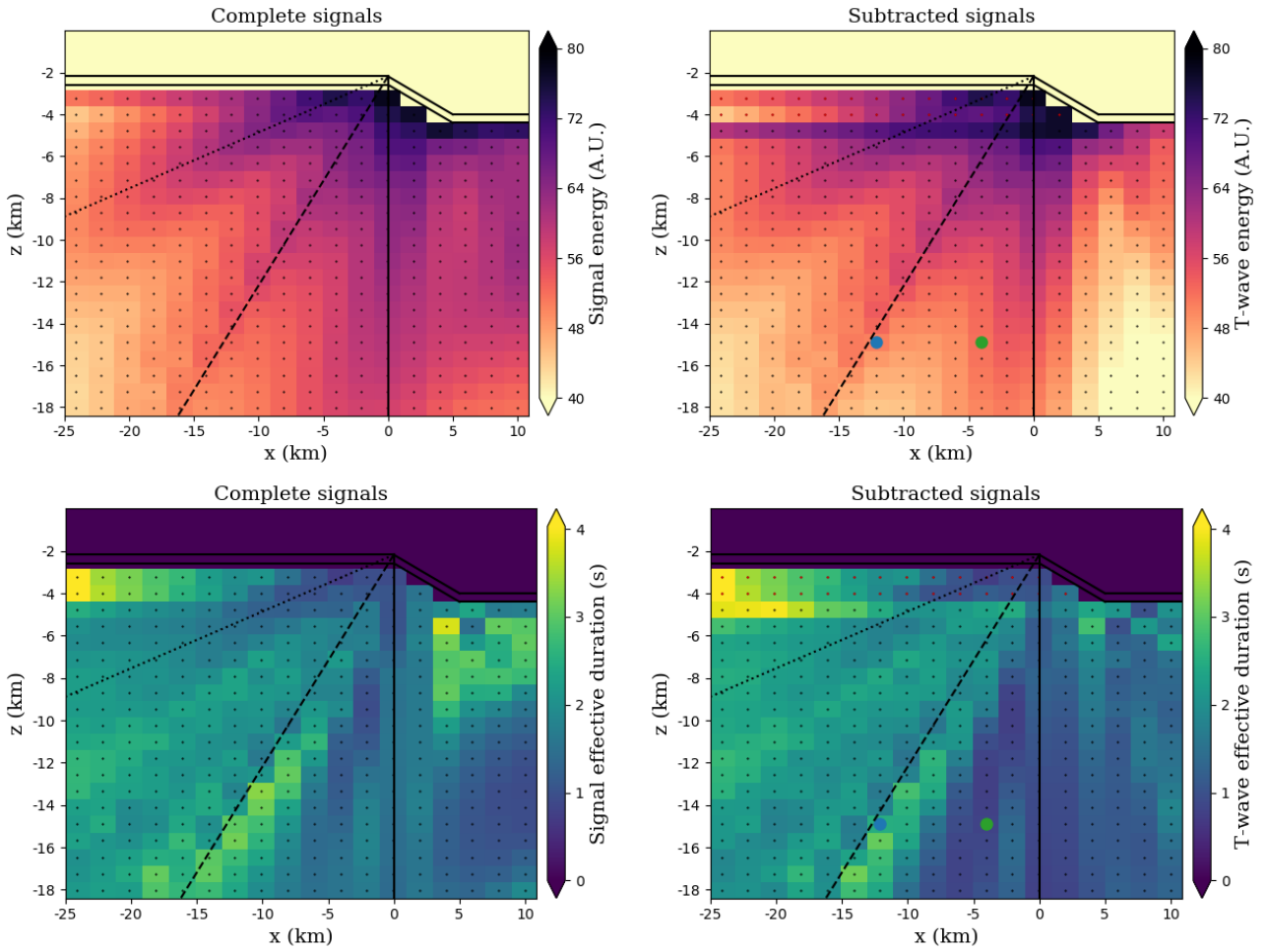

Figure 4.18 – This figure summarizes the energy (top, in arbitrary logarithmic unit) and effective duration (bottom, in seconds) of the signals recorded at a distance of 85 km from the top of the slope for different source positions represented as black or red dots. On the right the body waves have been subtracted for the sources represented in black using the process described in the text. No subtraction has been done for the sources represented in red nor for the pictures on the left. The horizontal and vertical scale are different. The blue and green points indicate the locations at which the signals shown in Figure 4.20 are recorded. The dashed line is tilted by an angle of 45° with respect to the vertical direction represented by the other solid line. The dotted line is tilted by an angle of 75°.

is shown in Figure 4.19 together with three examples of ray tracing (we only considered the sources located in the area shown).

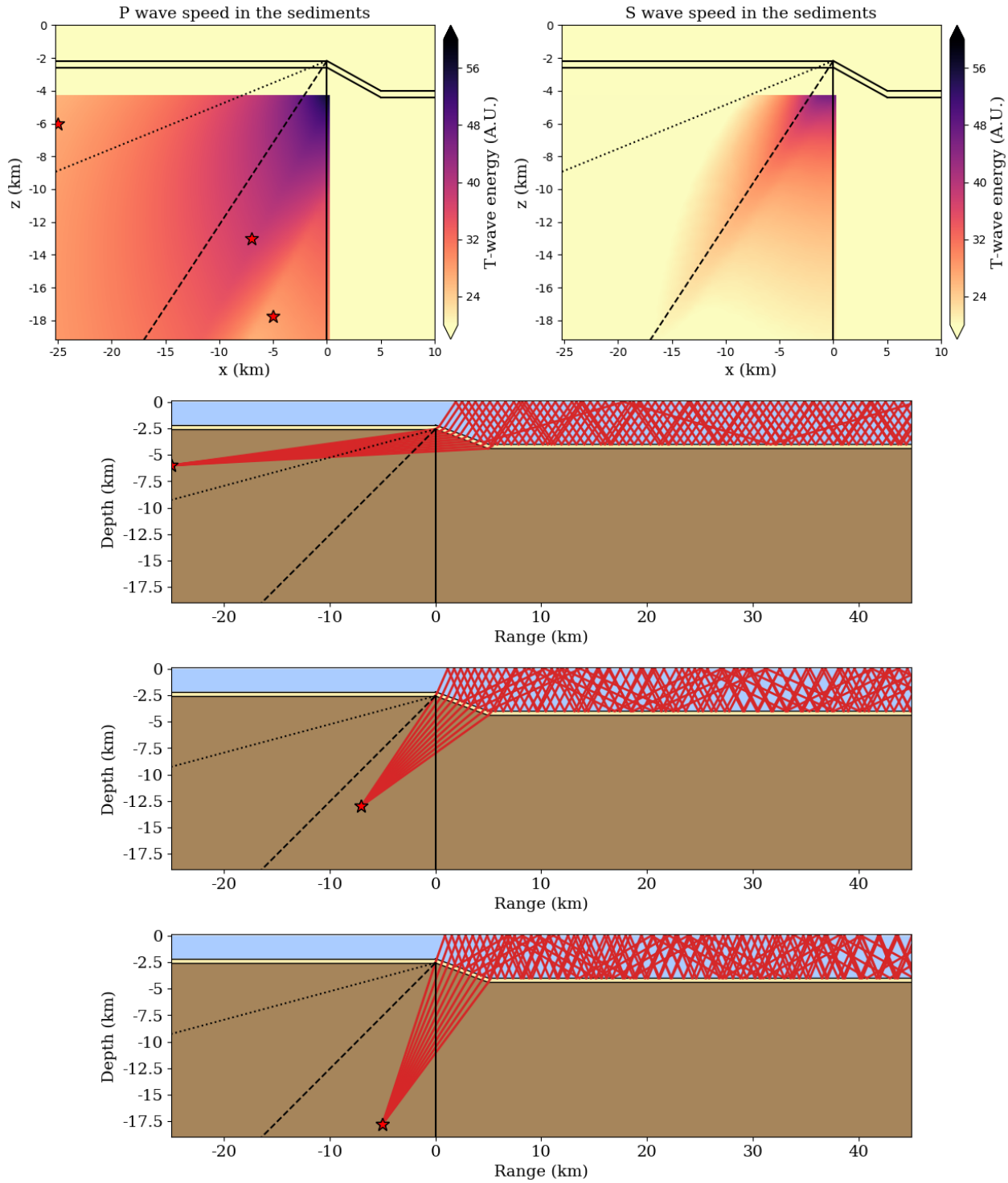

Figure 4.19 – **Top**: figure similar to Figure 4.18 but computed with our simple ray model, considering P wave speed (left) or S wave speed (right) of the case called MED in the sediments. Only the rays having a direct path between the source and the slope are taken into account. The stars represent the earthquakes shown in the three other figures. **Bottom**: Example of ray tracing for each of the sources shown above (in the case of P wave speed).

Let us first note that, in the case considered, both P and S wave speeds in the Earth's crust (sediment and semi-infinite bottom) are greater than the sound speed in the ocean. Consequently, Snell's law (4.1) implies that no ray can propagate in the ocean horizontally directly by refraction,

which means that, even for sources in favored areas, energy transmission implies some reflections. There are three regions that seem to be favored for T-wave generation:

- The first region is situated approximately along the line starting at the top, or at the middle, of the slope and tilted by an angle of 45° with respect to the vertical (dashed line in Figure 4.18 and in the subsequent figures), that is to say when the epicentral distance to the continental slope and the depth of the hypocenter are approximately the same. Figure 4.19 (upper right) shows that this region corresponds to a tradeoff between the number of rays reflected on the slope and thus redirected towards the ocean and the grazing angles of these rays. Above that region the rays reflected on the slope have a smaller grazing angle but are less numerous, while below that region more rays are reflected but have larger grazing angles thereafter. The vicinity of the normal to the slope corresponds to the area where the solid angle from which the source sees the slope is maximum. This favored region has long been known empirically (Båth [1954]) and an interpretation based on ray tracing was made by Johnson et al. [1963]. As in that study, our ray model suggests that the top of slopes are efficient at generating T-waves because they allow more energy to be redirected with low grazing angle. Let us note that $P \rightarrow S$ converted waves in the sediments (case shown at the upper right in Figure 4.19) seem to better match the results obtained with the full-wave method. However, ray theory predicts that at constant initial amplitude they should contribute less to the T-wave than $P \rightarrow P$ converted waves (see the amplitude differences between the upper left and right sub-figures of Figure 4.19). This may be explained by the radiation pattern of the source used in the full-wave simulation. Let us finally note that Figure 4.18 shows that this favored region exhibits relatively homogeneous energy but very different durations, suggesting a variable character of T-waves in that zone.

- The second region of interest is situated along the vertical of the slope, or along a direction slightly oriented leftward (see Figure 4.18). It is in this region that we carried out the parametric study on the influence of the slope. That area allows a maximum number of rays to be reflected on the slope. However, ray theory seems to underestimate the T-waves generated in that zone. Indeed, full-wave simulations predict high amplitude and rather short duration T-waves there. We do not have a definitive explanation for this discrepancy. The biased effective reflection coefficient of the water-sediments interface may again be involved, so as the (little) diffractions observed at the sharp edges in the full-wave simulations, which contribute to the T-wave.

- To a lesser extent, a last favored area is observed in Figure 4.18. It approximately follows a line originating at the top of the slope and oriented at 75° with respect to the vertical (the dotted line in Figure 4.18). The beams emitted from a source in that region and reflected off the slope, although not numerous, have a small grazing angle. More importantly, the earthquakes there are optimally located to generate energy propagating between the shelf and the sea surface and subsequently reflected off the slope. Due to the necessary successive reflections on the shelf, these T-waves have of long duration compared to their energy.

As an illustration, two signals of comparable energy but of different duration (ratio of 1/3) are shown in Figure 4.20. They have been recorded at the blue and green points shown in Figure 4.18.

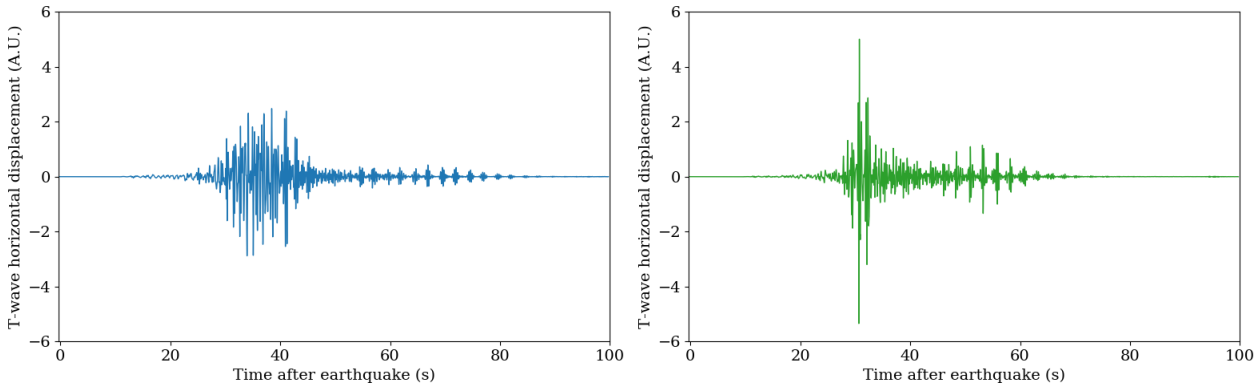

Figure 4.20 – T-wave horizontal displacement (after body wave subtraction) generated by the two earthquakes marked as blue and green circles in Figure 4.18. The green signal is more impulsive.

Let us note that the existence of favored regions for T-wave generation may partly account for the poor correlation observed between earthquake magnitude and T-wave energy. Additionally, if the fracture zone crosses several areas with different transmission potentials, we can presume that only some favored parts of the rupture, but not necessarily the most energetic, will effectively contribute to the T-wave, which makes the phenomenon even more complex. It is also interesting to remark that for the case studied we do not observe any clear trend between source depth and signal duration for downslope generated T-waves. However, T-waves generated at the right of the line passing from the slope and oriented at an angle of 45° with respect to the vertical (dashed line in Figure 4.18) tend to be shorter. If onset time and duration evolve similarly (which is not necessarily obvious), this observation differs from the observations of Williams et al. [2006], who reported a surprising correlation between rise time and water depth above the event. This could suggest that the T-waves observed by Williams et al. [2006] were generated by scattering rather than by downslope conversion.

4.2.4 Conclusions on T-wave downslope conversion

Some interesting observations have been made in this section. We have confirmed and quantified the importance of the sediment properties in the transmission of a two-dimensional T-wave. In particular, at constant source position, downslope generated T-waves have been identified as particularly sensitive to seismic velocity variations in the sediments, which are seen as the most important parameter, at least at close range (85 km from the top of the slope). In particular, the SOFAR channel does not seem to play any significant role at these distances, probably not more than the sea water attenuation which is commonly neglected in ocean acoustics at these frequencies (Jensen et al. [2011]). Low density sediments are seen to favor the generation of T-waves by downslope conversion, as predicted by ray theory. However, simple ray tracing in its most basic form, as used here, fails at conveniently modeling the influence of slope variations on T-waves in the presence of sediments. At constant source position, downslope energy transmission is maximum for typically two slope angles. As more energy can be potentially converted at these slopes, we suggest that this can bias localization algorithms towards them, that is to say not necessarily towards steepest slopes in spite of the fact that it is the most common situation.

Energy and duration maps have been constructed in order to analyze, for a given slope, the influence of source position. This kind of maps can be useful and is easy to construct with full-wave methods in the time domain. In our study they revealed the existence of several favored regions for T-wave generation, which may partly account for the poor correlation observed between earthquake magnitude and T-waves energy. These maps hint that T-waves can be generated, by downslope

conversion, following earthquakes that occur beneath abyssal plains, but only above a certain depth depending on the distance to the slope. This may have interesting implications and explain some outliers to the rule "epicenters at the lower end, and to seaward, of the continental slope are typically weak or not received" (Johnson et al. [1967]). The above results illustrated the complexity of the T-wave phenomena and confirmed that the energy of these waves is at least as sensitive to the magnitude of the earthquake as to the velocity of the sediments, the geometric arrangement of the slope, the depth of the seismic event or the slope of the seabed.

However, many improvements are possible and should be made to address the different limitations of our study. First of all the study has been carried out in 2-D Cartesian coordinates, while to obtain more accurate results it would require an axisymmetric 2.5-D or even better a 3-D setup, to more adequately match the typical real settings and obtain more useful and more quantitative results. However, axisymmetric 2.5-D simulations involve multiple unwanted reflections between the slope and the axis, and full-wave 3-D simulations are currently still too expensive for this kind of parametric study. We could also improve the definition of T-wave durations (see equation 4.6 and 4.7), since using the maximum of T-wave envelope to compute them instead of their maximum amplitude would make the results more reliable and probably easier to interpret. More generally, and in the longer run, inverse problems should also be tackled.

4.3 Parametric study of acoustic wave conversion at shore

After having dedicated the previous section to the source side of a typical T-wave setup, let us now focus on the receiver side and model the conversion of a guided acoustic wave when it reaches a coast. The setting of the study is shown in Figure 4.21.

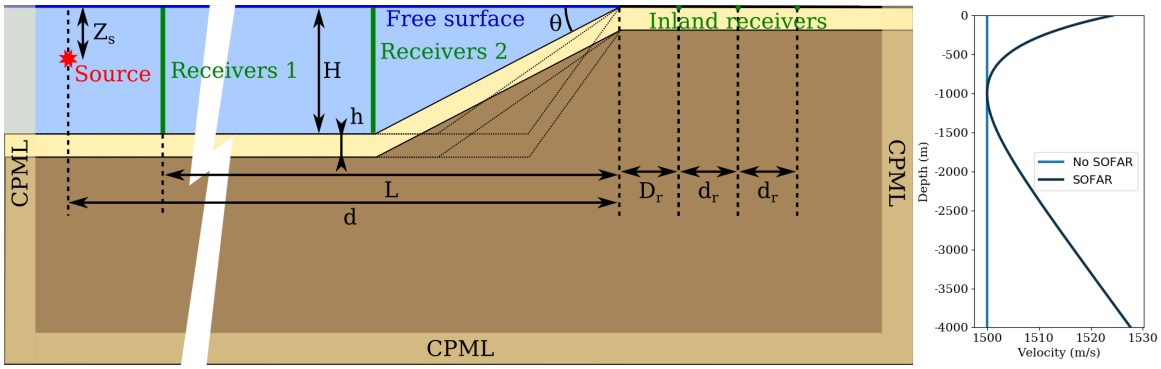

Figure 4.21 – **Left**: Setting of the study. The goal is to study the influence of slope angle θ and sediment properties on the acoustic energy transmitted at the green inland receivers and reflected at the slope. The geometry is Cartesian 2-D. The source is at depth $Z_s = 1200$ m, the sediments are $h = 0.4$ km thick, the abyssal plain is at depth $H = 4$ km and the top of the slope is at a range $d = 195$ km. In addition to the three inland receivers located on the coast ($D_r = 10$ km, $d_r = 40$ km), two receiver lines record the motion. Receivers 1 (receiver set 1) are located at $L = 190$ km from the top of the slope, and Receivers 2 are located at the bottom of the slope and move with it. In the spectral-element simulations the energy that reaches the edges of the model is absorbed by convolutional Perfectly Matched Layers (CPMLs, Xie et al. [2014, 2016]). **Right**: Sound speed profiles in the sea used for the numerical simulations. "SOFAR" is a classical idealized ocean sound-speed profile (Munk [1974]) with minimum velocity at depth 1000 m.

4.3.1 Model description

The model consists of a homogeneous viscoelastic semi-infinite bottom overlaid by a 400 m-thick homogeneous viscoelastic sediment layer, itself covered by a water layer. On the right of the model

the seabed dips towards the sea surface and then becomes flat again when it reaches it. At the outset, note that in this configuration the horizontal size of the slope is not constant but rather varies with the slope angle θ. For this work we chose to work in 2-D Cartesian, this time because this geometry is more realistic in the context of T-waves. Indeed, at a relatively long distance from where they were generated, T-wavefronts can reasonably be considered as planar. We set $z = 0$ m at the sea surface and $x = 0$ at the seismic source, which is placed at depth $Z_s = 1200$ m and at 195 km from the shore. The source is a pressure perturbation with a Ricker wavelet (i.e. the second derivative of a Gaussian) source time function with dominant frequency $f_0 = 5.7$ Hz and a time shift $t_0 = 1.2/f_0$ in order to ensure null initial conditions. Three receivers are located on the coast at the position described in Figure 4.21. The field is also recorded at the two receiver lines shown in the figure. As for the downslope case studied in the previous section, three different sediments will be tested. They are labeled LOW, MED and HIGH (for low, medium or high impedance contrast between the crust and the water). Their properties are given in Table 4.2. Note that the case labeled HIGH matches the semi-infinite bottom properties and thus there is in fact no sedimentary layer in that case. In the water, the density is equal to 1000 kg.m^3 and the sound velocity is either a constant velocity of 1500 m.s^{-1} or a classical idealized ocean sound-speed profile (Munk [1974], see Figure 4.11, right).

In this study, two quantities will be analyzed, one accounting for the energy reflection at the slope and the other describing transmission at the inland receivers. Let us note in the following $X_1 = 5$ km, the range of the first receiver line (labeled "Receivers 1" in Figure 4.11), $X_2(\theta)$ the range of the second receiver line (labeled "Receivers 2" in Figure 4.11) and $\boldsymbol{x}_1 = (205, 0)$ km, $\boldsymbol{x}_2 = (245, 0)$ km and $\boldsymbol{x}_3 = (285, 0)$ km the coordinates of the three inland receivers.

4.3.2 Transmitted energy and reflected energy ratio

We recall that the instantaneous energy per unit volume in the fluid is given by equation (4.3). Using the same notations, the instantaneous energy field per unit volume in a linear isotropic solid medium reads (Achenbach [1973]):

$$\mathcal{E}(\boldsymbol{x}, t) = \frac{1}{2}\rho(\boldsymbol{x})\dot{u}^2(\boldsymbol{x}, t) + \frac{1}{2}\sum_{i,j}\epsilon_{ij}(\boldsymbol{x}, t)\sigma_{ij}(\boldsymbol{x}, t), \tag{4.9}$$

where $\epsilon(\boldsymbol{x}, t)$ and $\sigma(\boldsymbol{x}, t)$ are the second-order strain and stress tensors, respectively and $\rho(\boldsymbol{x})$ is the density.

By integration over the whole duration of the simulation one can compute the integrated energy (defined in equation (4.4)) at the three inland receivers $E(\boldsymbol{x}_1)$, $E(\boldsymbol{x}_2)$ and $E(\boldsymbol{x}_3)$. At the first receiver line the signals typically contain a direct phase and reflected phases clearly separated in time (see Figure 4.22, top). Let T_f refer to the final time of the simulation and $T_i = 150$ s. One can then define the incident and reflected phase energy at this line:

$$E_i(z) = \int_0^{T_i} \mathcal{E}(X_1, z, t)\, dt, \tag{4.10}$$

$$E_r(z) = \int_{T_i}^{T_f} \mathcal{E}(X_1, z, t)\, dt. \tag{4.11}$$

By integration over depth, the average incident and reflected phase energy can then be obtained:

$$\langle E_i \rangle = \frac{1}{H}\int_{-H}^{0} E_i(z)\, dz, \tag{4.12}$$

$$\langle E_r \rangle = \frac{1}{H}\int_{-H}^{0} E_r(z)\, dz. \tag{4.13}$$

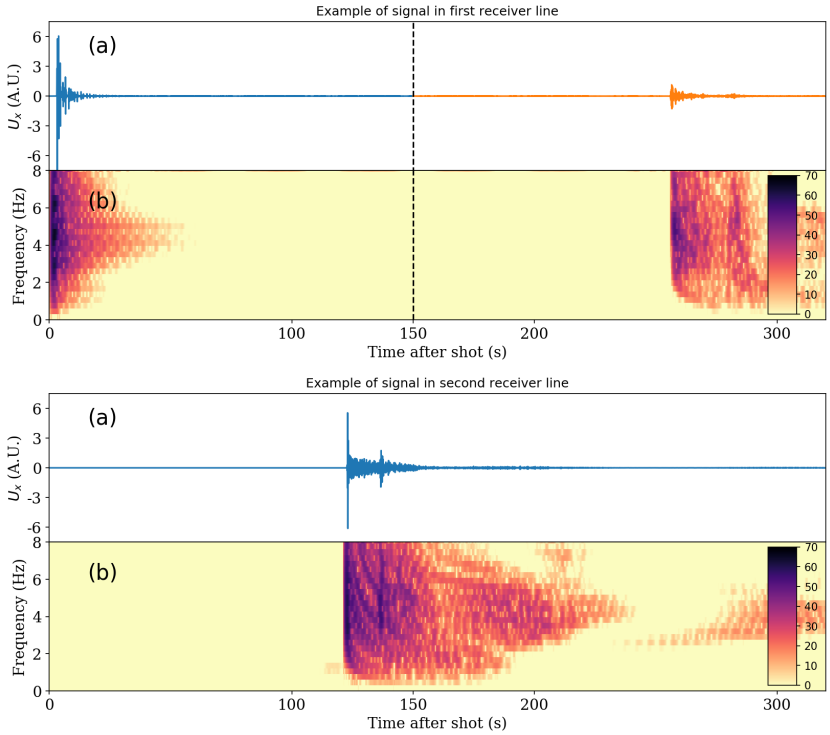

Figure 4.22 – **Upper figure**: (a) Horizontal component displacement seismogram (arbitrary displacement unit) recorded at depth 2105 m at the first receiver line (labeled "Receivers 1" in Figure 4.21) in the case MED with a SOFAR channel and a slope of $\theta = 21°$. Note the incident and reflected phases. The dashed line spots time $T_i = 150$ s used to delineate these two phases. (b) Power Spectral Density (in dB) as a function of time and frequency. **Lower figure**: same but for signals recorded at depth 2105 m at the second receiver line. The reflected phase is visible near time 140 s.

However let us note that in the chosen setting the sedimentary layer also covers the abyssal plain. Therefore it has an influence not only at the conversion at shore, but also all along the foregoing propagation in the flat ocean, whose length depends on the slope. This has to be taken into account when comparing the results obtained with different sedimentary layers. This is the reason why we also use a second receiver line. The field recorded there will be used to normalize the results. At that line, the incident and reflected phases overlap in time and in the frequency domain (see Figure 4.22, bottom), impeding us from properly defining incident and reflected phase energies. We integrate the instantaneous energy recorded there over the full duration of the simulation:

$$E_2(z) = \int_0^{T_f} \mathcal{E}(X_2, z, t)\, dt. \tag{4.14}$$

This allows us to define an average along the line:

$$\langle E_2 \rangle = \frac{1}{H} \int_{-H}^{0} E_2(z)\, dz. \tag{4.15}$$

As the incident field at the second receiver line is much more energetic in most cases (see Figure 4.22, bottom), we assume that $\langle E_2 \rangle$ accounts for the incident field at the slope. An average transmission loss between the two receiver lines can be defined:

$$F = \frac{\langle E_2 \rangle}{\langle E_i \rangle} \tag{4.16}$$

Let us also define three normalized quantities accounting for transmission along the coast $\frac{E(\boldsymbol{x}_1)}{\langle E_2 \rangle}$, $\frac{E(\boldsymbol{x}_2)}{\langle E_2 \rangle}$, $\frac{E(\boldsymbol{x}_3)}{\langle E_2 \rangle}$, and the normalized ratio of reflected energy:

$$R = \frac{\langle E_r \rangle}{\langle E_i \rangle F^2} \tag{4.17}$$

This normalization process is of course not perfect. In particular it has to be noted that the energy of the higher-order modes, if it reaches the slope, travels with larger grazing angles and is therefore more easily reflected. This trend is clearly illustrated in Figure 4.22 (bottom), where one can see that the reflected phase is substantially higher frequency than the incident phase. The reflected phase thus does not have the same modal content as the incident phase. Let us also note that due to mode coupling (energy redirection due to the slope) the reflected phase is not necessarily composed of high-order modes. Anyway the modal content of the reflected and incident phases is not the same, which means that the transmission losses due to the propagation from the first to the second receiver lines (F) are most likely slightly different than for propagation in the opposite direction. However this simplification is considered reasonable for this study.

4.3.3 Influence of slope angle, of sediments, and of the SOFAR channel

The four quantities $\frac{E(\boldsymbol{x}_1)}{\langle E_2 \rangle}$, $\frac{E(\boldsymbol{x}_2)}{\langle E_2 \rangle}$, $\frac{E(\boldsymbol{x}_3)}{\langle E_2 \rangle}$ and R have been computed as a function of the slope angle for the three different sediments and the two different wave speed profiles in the ocean. The results are shown in Figure 4.23.

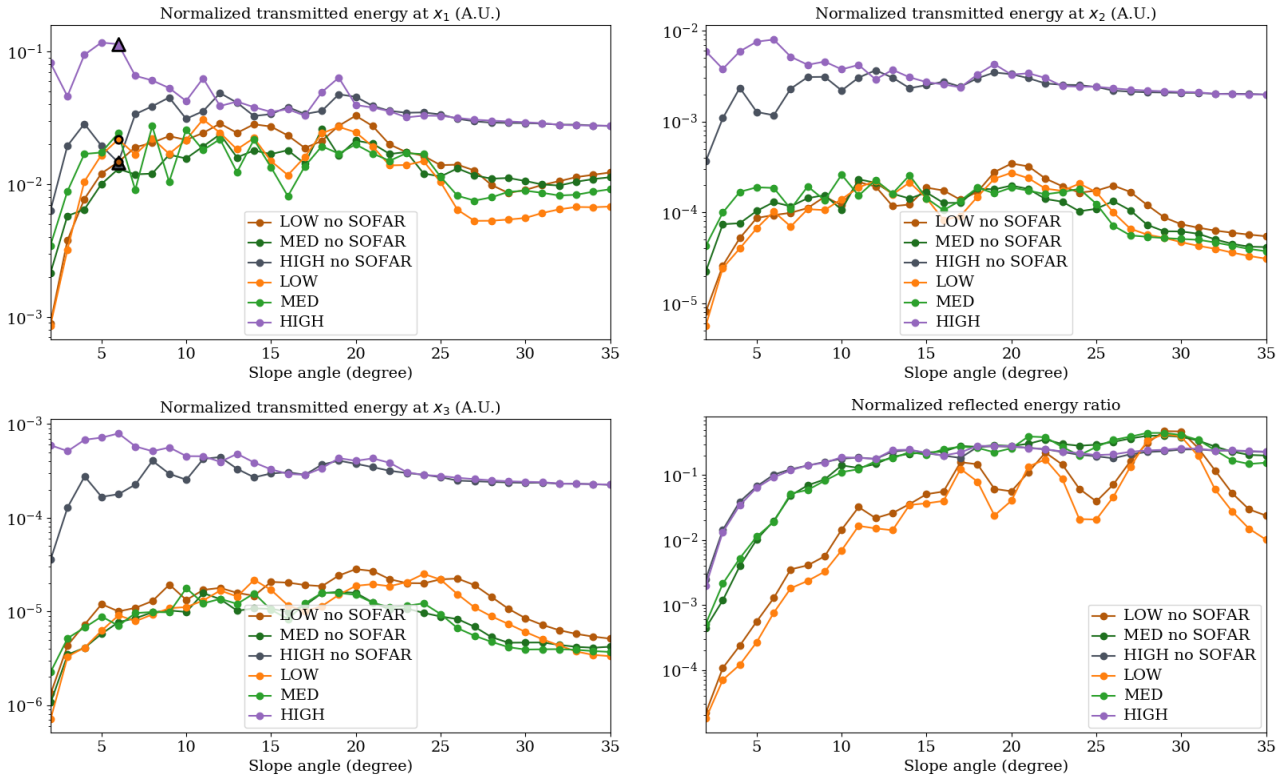

Figure 4.23 – **Top left**: Normalized transmitted energy at the first inland receiver ($\frac{E(\boldsymbol{x}_1)}{\langle E_2 \rangle}$) as a function of slope angle for three different sediments of Table 4.2 and for two different sound speed profiles in the ocean (Figure 4.21, right). The triangular and circular markers indicate the configuration of the signals shown in Figures 4.24 and 4.25, respectively. **Top right**: Same for the second inland receiver. **Bottom left**: Same for the third bottom receiver. **Bottom right**: Normalized ratio of reflected energy R, defined in equation (4.17), as a function of slope angle. All figures are in log scale.

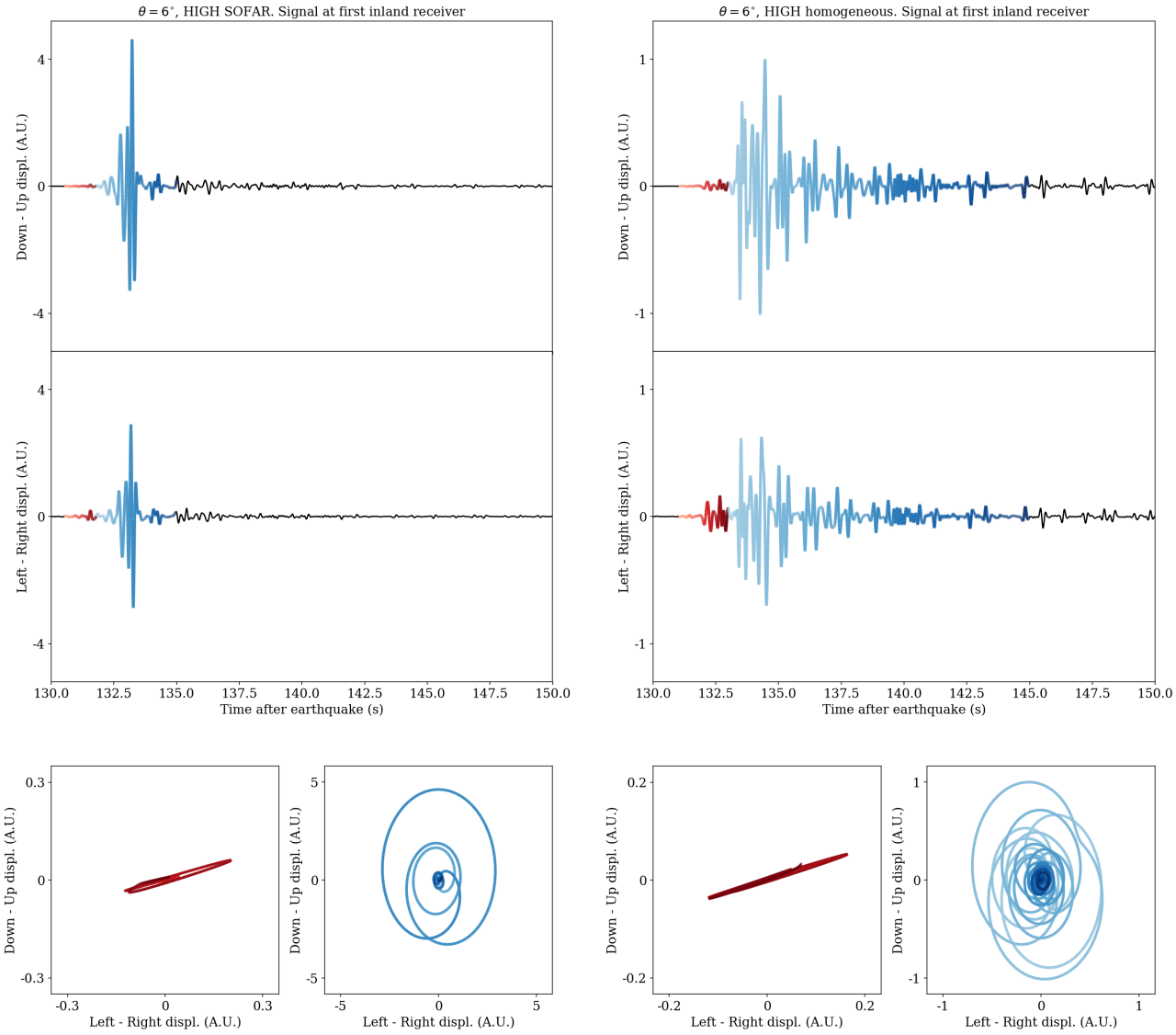

Figure 4.24 – Sketch describing the particle motion at the first inland receiver in the case HIGH and slope 6° with (left) and without (right) a SOFAR channel. These correspond to the configuration indicated by two triangles in Figure (4.23) (top left). First, weak arrivals of P-waves are visible, followed by retrograde particle motion characteristic of Rayleigh waves. Note the important amplitude difference between the homogeneous and SOFAR cases.

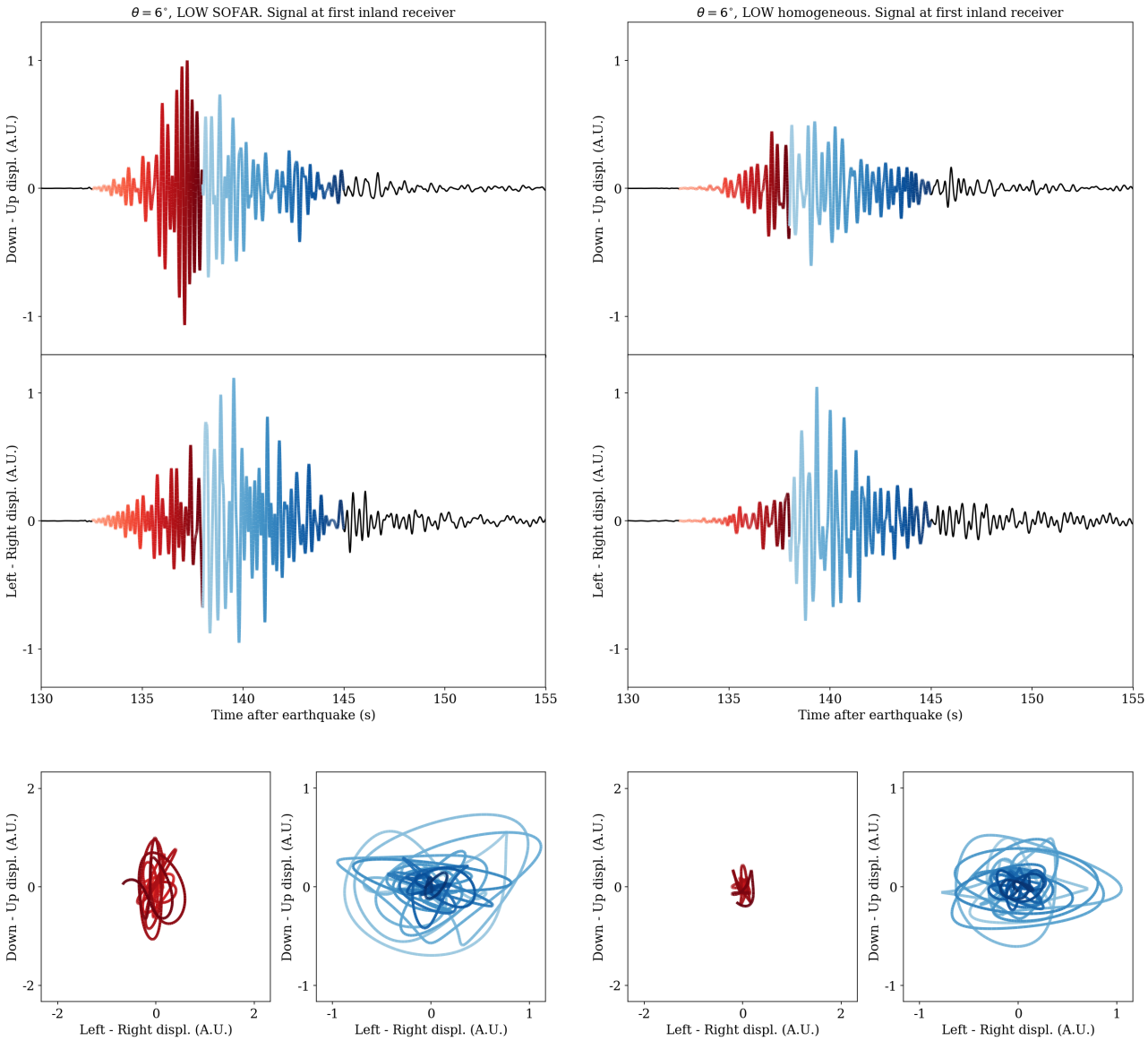

Figure 4.25 – Same as Figure (4.24) but in the case LOW. The arrivals are now composed of a mix of phases consisting mainly of P and S waves.

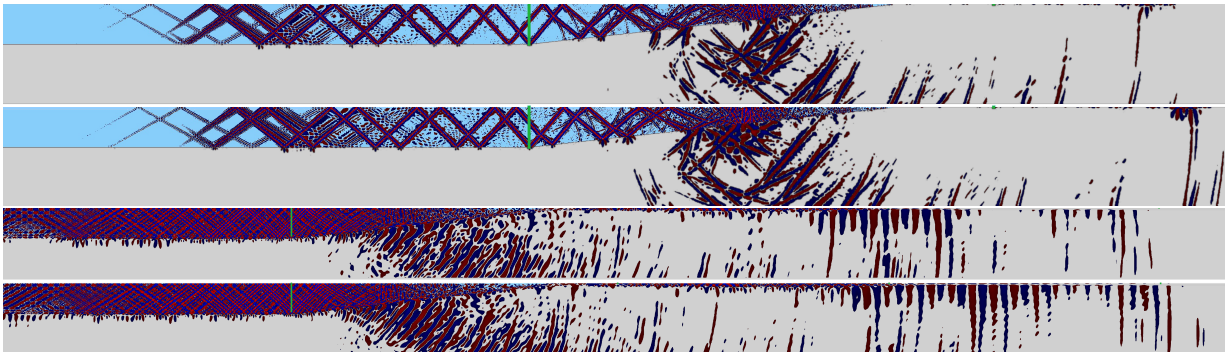

Figure 4.26 – Snapshots showing an example of the horizontal displacement field computed in four different configurations. Only a part of the whole computational domain is shown. From top to bottom: case HIGH with no SOFAR 140 seconds after the triggering of the source, case HIGH with SOFAR 140 s after the triggering of the source, case LOW with no SOFAR 150 s after the triggering of the source, and case LOW with SOFAR 150 s after the triggering of the source. In the cases HIGH the surface waves are clearly visible inland, while the field is a mix of phases in the cases LOW.

These results request several comments. First, even after the normalization process, the amount of energy transmitted along the coast is much greater in the case of a strong impedance contrast between the water and the seabed (HIGH). This may seem counter-intuitive, as one would expect perfect transmission in the case of a zero impedance contrast. However, only the energy arrivals at the surface of the model are taken into account here, and not those that radiate into the bottom and that decrease clearly with the increase of the impedance contrast (see the Figure (4.26) snapshots). We are dealing here with a phenomenon specific to the HIGH case and which, in the case of gentle slope angles, seems particularly sensitive to the seabed tilt as well as to the modal structure of the guided waves in the ocean. Particle motion and displacement field analysis (Figures (4.24), (4.25) and (4.26)) in the case of a 6° slope show, in the HIGH case, the presence of a rather weak P wave followed by a particularly energetic phase with a retrograde elliptical particle motion characteristic of a Rayleigh wave. Note also the strong inverse dispersion of this wave packet. Godin [2007] predicted the generation of such a surface wave by bulk wave conversion at a weakly elastic wedge with bottom compressional wave speed greater than 1500 m.s^{-1}. His approach is based on a perturbation of the fluid-fluid case and assumes low-dipping seabeds and low shear wave speed in the bottom. It shows that the coupling between normal modes in the water and the surface wave occurs primarily near modal cutoff depths. Our simulations confirm that this phenomenon is not limited to gentle slopes, nor to weakly elastic seabeds.

In the LOW case, on the other hand, the signals recorded at the first inland receiver consist of a mix of seismic phases, globally less dispersive. High-amplitude Rayleigh waves are still clearly visible, but the signals are also composed of body waves. The energy received inland does not seem to depend strongly on variations in the environment (only minor differences are noted between the LOW and MED cases).

For the three seabeds considered, as expected the transmitted energy decreases along its propagation inland (comparing energies recorded at the three inland receivers in Figure 4.23). This decrease is however less drastic in the case HIGH due to the cylindrical geometrical spreading of the Rayleigh wave. However, surface waves are typically not recorded after a long inland path (Talandier & Okal [1998]). This apparent inconsistency can be explained by the unrealistic properties of the model HIGH, especially in the shallowest region of the continent in which the surface wave travels and where attenuation is often known to be high. The distance between the coast and the receiver seems to be an important parameter for inland T-phase recording.

Let us also note that in LOW and MED cases the transmitted energy exhibits a plateau between 5 and 20 degrees, which widens towards the highest slopes when one moves away from the coast (receivers $\boldsymbol{x}_1$, $\boldsymbol{x}_2$ and $\boldsymbol{x}_3$). This effect can only be attributed to body waves and can be explained, in part, by a simple geometric effect: by getting away from the coast, the receivers are less sensitive to variations in its slope. However, the reason for the drop in transmission above 20-25° is not very clear. The snapshots in Figure (4.26) for the LOW case show that waves are guided in the sediment layer.

4.3.4 Influence of the modal content of the incident wave and of the thickness of the sedimentary layer

In order to determine the influence of this layer as well as of the modal content of the incident wave, we present another series of simulations, this time made with a homogeneous seabed whose characteristics correspond to the sediments described in Table 4.2. For these simulations the dominant frequency of the acoustic source is set at 2.8 Hz instead of 5.7 Hz. The results are shown in Figure (4.27), left.

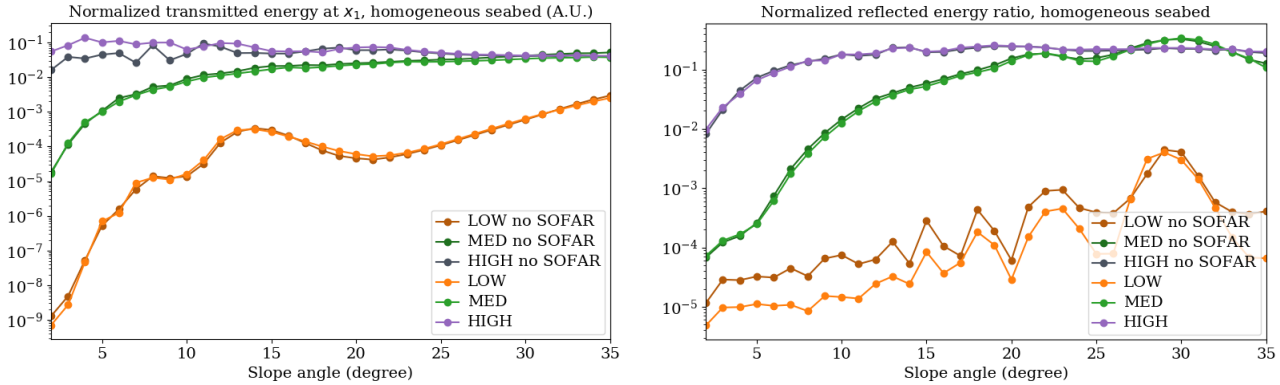

Figure 4.27 – **Left**: Normalized transmitted energy at the first inland receiver ($\frac{E(\boldsymbol{x}_1)}{\langle E_2 \rangle}$) as a function of slope angle for three different homogeneous seabeds, whose properties correspond to the sediments described in Table 4.2, and for two different sound speed profiles in the ocean (Figure 4.21, right). **Right**: Normalized ratio of reflected energy R, defined in equation (4.17), as a function of slope angle in the same configuration. All figures are in log scale.

Let first note that in the HIGH case this figure compares quite well with Figure 4.23, top left. This suggests that the Rayleigh wave produced at the wedge is not very sensitive to the modal content of the incident waves (no sediment layer was set in this case), as predicted by Godin [2007]. This observation is of interest because it implies that the surface wave must mainly contain information on the water column, which may be recovered. However in the cases LOW and MED several differences have to be noted between the new configuration and the previous one. First, as expected, the lower modal content of the incident wave in this new setting makes the transmitted energy less sensitive to the velocity profile in the ocean. Then, the increase in transmission at the lowest slopes is seen to be smoother. Overall, the patterns in the angular transmission curves seem to be shifted right in this second setting compared to the first one. This can be explained by the combination of two phenomena: The source having a lower frequency content in this second setting, it generates relatively more low-order modes. Even if these modes are more attenuated along the propagation, the guided wave approaching the slope will thus have a larger ratio of the energy of its modes propagating with low grazing angles. This energy couples with the seabed relatively further away from the wedge apex, which tends to penalize transmission, especially for the gentler slopes. However the absence of a hard semi-infinite bottom leads to a more efficient orientation of this energy towards the receivers, which particularly favors the steepest slopes.

Let us now discuss the normalized energy ratio R shown in Figure (4.23), bottom right and in Figure (4.27), right. The two figures look similar but exhibit a significant difference: in the case MED and even more so in the case LOW, as expected the reflected energy ratio is seen to be favored by the presence of a hard semi-infinite bottom below the sediments and of higher-order modes in the incident wave. Overall, in both settings, the reflections of the guided waves are seen to increase with the slope and with the impedance contrast, with some preferred angles in the LOW and MED cases. It is especially important to note that the ratio of normalized reflected energy commonly exceeds 10%, and can reach 48% in the case of a slope angle of 29° with a hard bedrock and soft sediments (case LOW without a SOFAR channel in the first configuration of Figure (4.23), bottom right). These values show that the use of parabolic solvers, which by construction neglect backscattered energy, is not suitable for such types of problems (see e.g. the FIG. 11 of Frank et al. [2015]).

The existence of a preferred slope angle for energy reflection can be explained based on simple ray considerations, taking into account the propagation angles of the modes in the water layer. At each cycle of seabed and sea surface reflections, the mode angle steepens by twice the seafloor tilt. If the mode does not lose all its energy in this process its energy can eventually propagate backwards and go down the slope (while possibly coupling to lower-order modes). The amount of reflected energy then depends on the (effective) reflection coefficient of the interface, the slope, and the propagation angle of each of the incident modes. The preferred slope angles for energy reflection correspond to optimum values for the number of reflections necessary for the energy of each mode to leave the slope by being backscattered. This reasoning suggests that high order modes are more easily reflected at the slope (see the difference in frequency content between the direct and reflected phases in Figure 4.22, bottom).

The dependency of seismic T-waves on slope seems to be strongly dependent on the configuration. Our results suggest that this dependency is related to the seabed properties as well as to the range of slopes considered. For the lowest slopes ($< 5°$) and lowest impedance gradients a particularly strong influence of the slope can be expected. The influence is generally less pronounced for the highest slopes, especially in the case of the hardest seabed. This consideration seems to be particularly consistent with our observations in the Ionian Sea (see Figure 2.1, top) and explains why Stevens et al. [2000, 2001] did not find large variations in amplitude with slope in their simulations similar to our MED case.

Note that, as we have observed in the Ionian Sea (Figure 2.3, right), several authors document horizontal transverse waves (e.g. Tolstoy & Ewing [1950]; Shurbet & Ewing [1957]; Båth & Shahidi [1971]; Talandier & Okal [1979] ...) that can be explained by refraction when the waves are transmitted from ocean to land. Unfortunately this 3-D phenomenon cannot be included in our 2-D simulations and thus cannot be simulated in our study.

4.4 Conclusions of this chapter

We have begun by presenting T-wave simulations in the Ionian Sea, in which we studied the influence of the presence of a layer of soft sediments, of the source depth, and of the wave speed profile in the water. Synthetic T-waves have proven to be realistic in both the time and frequency domains, which illustrates the feasibility of a quantitative comparison between real 3-D data and synthetic axisymmetric 2.5-D T-phases involving solid-fluid and fluid-solid conversions. This first study confirms the observations of Jamet et al. [2013]: the SOFAR wave speed channel does not seem to have a major contribution to the amplitude and structure of the T-wave, at least for the distances and frequencies that we have considered. This observation is surprising because it seems to contradict most studies on the subject, even for similar configurations. This will lead us to further study the influence of water layer characteristics on energy transmission in Chapter 5.

Similarly, our study suggests that the T-wave is only slightly sensitive to the radiation pattern

of the source, which may be also a second-order parameter. The properties of the seabed, however, play a crucial role. Thus, in the case studied, T-phases without sediments are more impulsive, of greater amplitude, of longer duration and do not present several peaks in the time-frequency plane. The depth of the source has also an important effect on these synthetic T-waves. As an example, simulated amplitudes at a coastal station increased by a factor of 5 when changing the source depth from 10 to 2 km.

We then performed a parametric study of the influence of slope angle, of the properties of the seabed and water column, and of the position of the source on the energy of downslope converted T-waves. We saw that steep continental slopes (as in atolls, or on the Greek coast, see chapter 2, first section of this chapter and Appendix A) involved more complicated physical phenomena than gentle slopes. Moreover, the estimated differences in terms of energy transmission between a slope of 5° and of 14° of the same bottom and for the same source can exceed a factor of 100, which could bias source location techniques towards the highest slopes. To our knowledge, this had not been quantified in the available literature. We have also shown that the opposite situation is theoretically possible in the case of the steepest slopes, although this is not the most common situation. Indeed, the transmission of energy by downslope conversion decreases beyond a certain tilt of the seabed, which could bias source localization techniques towards gentler slopes.

Energy and time dispersion maps were constructed to analyze, for a given slope, the influence of the source position on the T-waves produced by downslope conversion. These maps revealed the existence of several favored areas for downslope T-wave generation. These areas can probably partly explain why recorded T-wave energy is only weakly correlated to the magnitude of earthquakes. Interestingly, one of these zones extends below the abyssal plain above a critical depth depending on the distance to the slope. This observation may explain some exceptions to the rule stated for example by Johnson et al. [1967] that "epicenters at the lower end, and to seaward, of the continental slope are typically weak or not received".

This type of energy and time dispersion map can be built easily and with no significant additional cost by full-wave computation methods. This concept will be generalized in the next chapter.

The last part of the chapter focused on another parametric study, this time representative of the other side of the ocean basin for a typical T-wave setup. In that study we investigated the influence of slope, of seabed seismic properties and of the water layer on transmission and reflection at a coast of a wave guided in the ocean. An interesting phenomenon was observed, particularly in the case of hard and gently-sloping seabeds. In such configurations we observes the creation of a powerful Rayleigh wave, whose signal, recorded inland, is very sensitive to the slope and to the characteristics of the environment, but only very slightly sensitive to the modal structure of the incident wave. Although coastal receivers usually have far lower signal-to-noise ratios than hydrophones in the water (De Groot-Hedlin & Orcutt [2001b]), and although hard seabeds are likely rare in reality, that phenomenon may have interesting implications. Indeed this surface wave likely carries a lot of information about the water layer, which could probably be recovered. One can for instance imagine determining favored coasts for this type of mechanism and installing seismic stations there. Rayleigh waves created as a result of T-wave arrivals from distant earthquakes could then be used to obtain information on oceanographic processes involved for example. In the hypothesis of the existence of such zones (see Appendix A for a possible example), this would deserve a theoretical study that could be done for instance by generalizing Godin [2007] or based on Keller & Karal Jr. [1960].

All the results and observations presented above illustrate the complexity of the T-wave phenomenon and confirm that the energy of these waves is at least as sensitive to the magnitude of the earthquake as to the seismic wave speeds in the sediments, the geometric configuration of the slopes, or the depth of the earthquake focus. The apparent low influence of the SOFAR channel on the numerical T-waves presented in this chapter led us to investigate the influence of the presence or absence of a SOFAR channel on the energy distribution and transmission of a broadband source in a waveguide. With this objective in mind we developed numerical tools to build broadband transmission losses maps

based on time-domain spectral-element simulations.

Chapter 5

Broadband transmission losses, time dispersion maps and SOFAR channel efficiency

The first part of this chapter has been published as an article in: A. Bottero, P. Cristini, D. Komatitsch and Q. Brissaud, Broadband transmission losses and time dispersion maps from time-domain numerical simulations in ocean acoustics, Journal of the Acoustical Society of America, vol. 144(3), p. EL222-EL228 (2018).

In this chapter, a procedure for the calculation of transmission loss maps from numerical simulations in the time domain is presented. It can be generalized to arbitrary time sequences and to elastic media and provides an insight into how energy spreads into a complex configuration. In addition, time dispersion maps can be generated. These maps provide additional information on how energy is distributed over time. Transmission loss and time dispersion maps are generated at a negligible additional computational cost. To illustrate the type of transmission loss maps that can be produced by the time-domain method, the problem of the classical two-dimensional upslope wedge with a fluid bottom is addressed. The results obtained are compared to those obtained previously based on a parabolic equation. Then, for the same configuration, maps for an elastic bottom and maps for non-monochromatic signals are computed. At the end of the chapter these maps are used to study the efficiency of the SOFAR channel in terms of energy channeling; we investigate the effect of the sound field profile and the influence of the sea bottom nature.

5.1 Broadband transmission losses and time dispersion maps from time-domain numerical simulations in ocean acoustics.

5.1.1 Introduction

In underwater acoustics, wave propagation problems typically involve variable geometry and heterogeneous media, which can generate strong signal fluctuations and make the analysis of time signals difficult. Thus, to measure the acoustic energy emitted by a source distributed inside a complex model, acousticians often present results as frequency-dependent transmission loss (TL) curves or transmission loss maps. These maps are traditionally computed in the frequency domain based on the Helmholtz equation.

Two main approaches coexist in the literature to solve this equation in complex environments. The first consists in performing an approximation, usually parabolic, to obtain a solution at lower computational cost. The second involves discretizing the Helmholtz equation using a full-wave technique (often finite elements), at the cost of a much longer computation time.

This section presents an alternative approach for the calculation of transmission losses via the wave equation expressed in the time domain. When the source is broadband, it allows one to compute time dispersion maps at no additional computational cost compared to the mono-frequency case. To compute transmission loss maps in the time-domain, one can in principle simply store all time signals at all receiver positions and then perform a Fourier transform for each point stored to convert all of them to the frequency domain. However, from a technical point of view this solution is realistic only if the number of receivers is small to moderate because of the amount of storage (in memory or to disk) that the process requires when the number of recording points and/or the number of time steps computed is large to very large. In practice, this limits the generation of frequency-domain results from time-domain simulations to the creation of a small number of transmission loss curves at a limited number of spatial points, preventing the generation of full 2D transmission loss maps.

The objective of this section is thus to present an efficient way of creating transmission loss maps from time-domain numerical simulations that avoids the storage of individual time signals. Since the source time signal can be arbitrary chosen, the transmission loss maps can be evaluated for quasi-monochromatic signals as well as for signals with a wider bandwidth, enabling one to analyze the influence of bandwidth on the distribution of acoustic energy inside the domain. In addition, time dispersion maps can also be calculated on the fly during the simulation, providing an insight into the structure of the received time signals. All these quantities are obtained at a negligible additional numerical cost. It is worth noting that the technique presented is general and can be applied to all methods expressed in the time domain.

Recently, a time-domain spectral-element method (Komatitsch & Tromp [1999]) has been shown to efficiently solve full-wave propagation problems in ocean acoustics (Cristini & Komatitsch [2012]; Bottero et al. [2016a]). Beyond its capability of handling complex geometries and rheologies accurately, as any finite-element technique, the time-domain spectral-element method runs efficiently on very large computers, exhibiting a computer strong scaling that is almost linear with respect to the number of CPUs or GPUs. This property can lead to a drastic reduction of the duration of numerical simulations compared to some more classical time-domain finite-element techniques. Working in the time domain also allows one to consider arbitrary source time functions and to obtain information on the dispersion of the studied signals.

When used in conjunction with the spectral-element method in the time domain, the implementation of the proposed way of computing TL or time dispersion maps thus has the additional advantage that, contrary to full-wave methods in the frequency domain, the time-domain spectral-element method does not exhibit decreasing performance when increasing the number of processor cores used to perform the calculations. Matrix system solvers (linear solvers) are needed when solving the wave equation in the frequency domain, and their known performance scaling issues on large machines above a thousand processor cores or so Xu et al. [2013], which is not that high by current high-performance computing standards, implies that some large problems are numerically difficult to handle in the frequency domain, even on the current largest supercomputers.

The section is organized as follows: subsection 5.1.2 is devoted to the definition of the different physical quantities that we want to study, and to how one can compute them efficiently in a time-domain numerical simulation. Then, in subsection 5.1.3, we provide and discuss some examples of the evaluation of these quantities within the framework of a time-domain spectral-element method. Wave propagation over a fluid and then over an elastic upslope wedge is considered for several source bandwidths. We finally draw some conclusions in subsection 5.1.4.

5.1.2 Generalization of the calculation of transmission losses and evaluation of signal time spreading

In this subsection, we define the different physical quantities that we want to study and show how they can be calculated on-the-fly in a time-domain numerical simulation. These quantities will allow

for the evaluation of the transmission losses and of the time structure of signals at all the discrete points of the spatial domain under study. Let us note $u_x(\boldsymbol{x},t)$ and $u_z(\boldsymbol{x},t)$ the horizontal and vertical displacement field, respectively, and $P(\boldsymbol{x},t)$ the pressure field at time t and position $\boldsymbol{x} = (x,z)$. $\dot{u}(\boldsymbol{x},t) = \sqrt{\dot{u}_x(\boldsymbol{x},t)^2 + \dot{u}_z(\boldsymbol{x},t)^2}$ is the norm of the particle velocity field. The instantaneous energy per unit volume field in the fluid is given by (Jensen et al. [2011] pp.11-12):

$$\mathcal{E}(\boldsymbol{x},t) = \frac{1}{2}\rho\dot{u}^2(\boldsymbol{x},t) + \frac{1}{2}\frac{P^2(\boldsymbol{x},t)}{\rho(\boldsymbol{x})c^2(\boldsymbol{x})}, \tag{5.1}$$

where $\rho = 1000$ kg.m^{-3} is the density of water and $c(\boldsymbol{x})$ is the distribution of sound velocity. Likewise, in a linear isotropic solid medium the instantaneous energy field reads (Achenbach [1973]):

$$\mathcal{E}(\boldsymbol{x},t) = \frac{1}{2}\rho(\boldsymbol{x})\dot{u}^2(\boldsymbol{x},t) + \frac{1}{2}\sum_{i,j}\epsilon_{ij}(\boldsymbol{x},t)\sigma_{ij}(\boldsymbol{x},t). \tag{5.2}$$

where $\epsilon(\boldsymbol{x},t)$ and $\sigma(\boldsymbol{x},t)$ are the strain and stress tensors, respectively. Let T_f refer to the duration that is considered, then the integrated energy field reads:

$$E(\boldsymbol{x}) = \int_0^{T_f} \mathcal{E}(\boldsymbol{x},t)\,dt. \tag{5.3}$$

This physical parameter represents the amount of energy received at a given position inside the model at time T_f. It is similar to the radiated seismic energy introduced by Boatwright & Choy [1986] and evaluated from body waves measurements, or to the T-Phase Energy Flux (TPEF) proposed by Okal [2003] to characterize the energy generated by an earthquake source in the form of a T-wave. Then, knowing the energy E_0 of the emitting source, it is possible to evaluate the transmission losses for time T_f as:

$$TL(\boldsymbol{x}) = -10\log\frac{E(\boldsymbol{x})}{E_0} \tag{5.4}$$

Energy is determined by an integral in time, but with the value that we get we have no knowledge of how this energy is distributed within the time interval that we are considering. For a given energy value, time spreading can be very different depending on the propagation path followed by the signal. It is therefore very useful to get such a piece of information. In order to calculate it, we first define the maximum energy field by:

$$M(\boldsymbol{x}) = \max_{t<T_f} \mathcal{E}(\boldsymbol{x},t). \tag{5.5}$$

This field gives the maximum of the instantaneous energy for each point and provides a way of defining an "effective" time dispersion for a signal as:

$$\mathcal{T}(\boldsymbol{x}) = 2\frac{E(\boldsymbol{x})}{M(\boldsymbol{x})}. \tag{5.6}$$

This quantity is homogeneous to a duration. It represents the duration of the triangle-shaped signal that has the same energy and maximum amplitude as those that we have calculated. It is therefore a measure of the time spreading of the signal. Time-domain numerical simulations provide access to these physical parameters at each time step δt and thus allow for the computation of transmission losses and time dispersion maps on-the-fly during the run at a negligible additional computational cost. In practice, at iteration $i+1$ and position $\boldsymbol{x}$, one can evaluate:

$$E_{i+1}(\boldsymbol{x}) = E_i(\boldsymbol{x}) + \mathcal{E}(\boldsymbol{x},t_{i+1})\delta t \tag{5.7}$$

$$M_{i+1}(\boldsymbol{x}) = \max\left[M_i(\boldsymbol{x}), \mathcal{E}(\boldsymbol{x},t_{i+1})\right] \tag{5.8}$$

$$\mathcal{T}_{i+1}(\boldsymbol{x}) = 2\frac{E_{i+1}(\boldsymbol{x})}{M_{i+1}(\boldsymbol{x})} \tag{5.9}$$

Time domain full-wave numerical methods can thus also provide an at-a-glance view of how the acoustic energy emitted by a source is distributed inside a complex heterogeneous model. In the following subsections, we will show examples of the maps that can be obtained based on the calculation of these physical quantities. In all the examples shown, the final time T_f of the simulations was chosen so that most of the energy produced by the source has left the domain under study.

5.1.3 Validation and examples of transmission loss and time dispersion maps

Below we show three sets of results to demonstrate the ability to compute both TL and dispersion maps from time-domain simulations. In the three cases we consider a fluid layer overlying a sloping sea floor. This configuration illustrates several wave propagation phenomena such as mode conversion and mode cutoff due to a varying water column depth. The first problem serves as a validation of the approach by comparing TL maps obtained by a time-domain method to those computed by a reference method in the frequency domain. The second set of results considers an elastic sea floor. It shows the dual effects on the TL maps of pulse bandwidth and shear stiffness in the sea floor. The third set shows dispersion maps for a broadband pulse propagating along and into a fluid sea floor.

5.1.3.1 Comparisons of the transmission loss maps with a reference solution

In order to illustrate and validate our approach, we choose to investigate the classical two-dimensional (2D) fluid wedge benchmark problem, whose characteristics can be found in Section 6.9.2 of Jensen et al. [2011] and will be described below. In the context of an attenuating fluid bottom, transmission loss maps for a monochromatic source have already been published there and can thus be used for comparison. These previous results were obtained with a split-step implementation of the Thomson-Chapman parabolic equation using a Greene wide-angle source to initialize the solution. No full-wave Helmholtz solution for this problem is available in the literature.

Let us first generate a transmission loss map from a time-domain numerical simulation for exactly the same configuration. The simulation is based on a time-domain spectral-element method (Komatitsch & Tromp [1999]), which has been shown to efficiently solve full-wave fluid/solid propagation problems in ocean acoustics (Cristini & Komatitsch [2012]; Bottero et al. [2016a]). In the spectral-element method, viscoacoustic or viscoelastic effects are represented based upon three generalized Zener standard linear solids placed in parallel, with different relaxation times for each, to mimic a constant Q quality factor over the frequency band under study in the simulation (Komatitsch & Tromp [1999]). In order to avoid spurious reflections from the sides of the computational domain, for all configurations the domain is extended up to a range of 20 km and down to a depth of 1 km and equipped with perfectly matched absorbing layers (PMLs, Xie et al. [2016]).

For this work, we define a source time function signal by:

$$s(t) = \begin{cases} \frac{A}{2}\left(1 - \cos\left(\Delta\pi t\right)\sin\left(2\pi f_0 t\right)\right) & \text{if } 0 < t < \frac{2}{\Delta} \\ 0 & \text{else} \end{cases} \tag{5.10}$$

where A is the maximum amplitude of the source, f_0 is the dominant frequency of the source signal, and Δ is its bandwidth. This type of time sequence will allow us to control the bandwidth of the emitted signal by changing the value of parameter Δ. Quasi-monochromatic signals that will provide results close to frequency-domain calculations as well as narrowband or broadband signals can be generated. We will thus be able, in next subsections, to study the influence of the bandwidth on the spreading of acoustic energy inside the computational domain. In addition to a fluid viscoacoustic bottom, we will also consider a solid viscoelastic bottom by adding a shear velocity of $c_s = 600$ m.s^{-1} and a shear attenuation coefficient $\alpha_S = 0.5$ dB.λ_S^{-1} to the sediment characteristics.

The first results are shown in Figure 5.1, which provides the comparison between a monochromatic TL map (Figure 5.1 (a)) taken from Jensen et al. [2011] and a quasi-monochromatic TL map (Figure 5.1 (b)) generated from a time-domain full-wave numerical simulation. Typically, the results shown in this section were obtained in a few seconds using 128 CPU processor cores of a regional cluster, while results for these models using a parabolic equation method are obtained almost instantaneously.

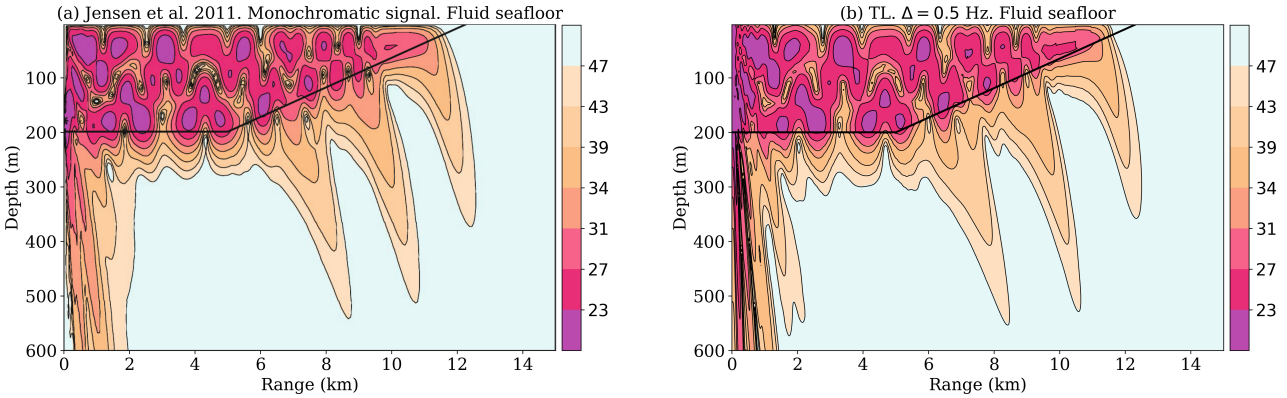

Figure 5.1 – **(a)** Original TL map, in dB, from reference Jensen et al. [2011] page 514. **(b)** TL map from a full-wave time-domain simulation using an quasi-monochromatic source (f_0 = 25 Hz, Δ = 0.5 Hz). Figure (a) is reproduced (slightly modified) from Figure 6.11 of Jensen et al. [2011] with permission from publisher Springer. The black line indicates the seabed interface.

The quasi-monochromatic signal was generated using a bandwidth Δ = 0.5 Hz. We performed several simulations with signals having smaller bandwidth but did not notice any changes in the TL map. We thus consider this value of the bandwidth as a good approximation of a monochromatic signal for this configuration. Note that this is a fluid only configuration. The two TL maps are very similar. Mode cutoff of the three modes, which exist in the flat part of the model, are recovered almost identically in both cases. The main differences are observed for short ranges. This is not surprising since the parabolic equation, which is used to generate the results of Fig 1(a), has angular limitations. Moreover, a source with a limited aperture was used, contrary to our simulation, which implements a point source. Therefore the discrepancies between the two TL maps are attributed to the known inaccuracy for steep angles. Nevertheless, interference structures in the water column are very close, except at the end of the wedge where again the grazing angles are steepened because of the varying depth and thus cannot be handled correctly through numerical modeling based on the parabolic equation method which was used. This comparison may be seen as a first answer to the question raised by Buckingham [1992] on the accuracy of TL maps obtained using the parabolic equation for an upslope fluid wedge. Based on the results that we obtain, it can be considered that the accuracy of the parabolic equation is good. Moreover, parabolic equation methods have made significant progress in the meantime and should thus compare more favorably nowadays. In particular, wide-angle capabilities that have been developed should at least suppress many of the discrepancies observed in the near field. It should also be noted that if several frequencies are of interest, a simulation is necessary for each frequency considered.

5.1.3.2 Effect of pulse bandwidth and sea floor elasticity

Since our numerical method works in the time domain, we can also consider signals with different bandwidths in order to evaluate how this parameter may influence the spreading of energy inside the computational domain. Figure 5.2 (a) represents the TL map for a signal with a bandwidth Δ = 8.0 Hz.

Compared to the monochromatic case (Figure 5.1 (b)), smoothing of the interference structure is observed in the water column mainly from the beginning of the wedge to its end, the reason being

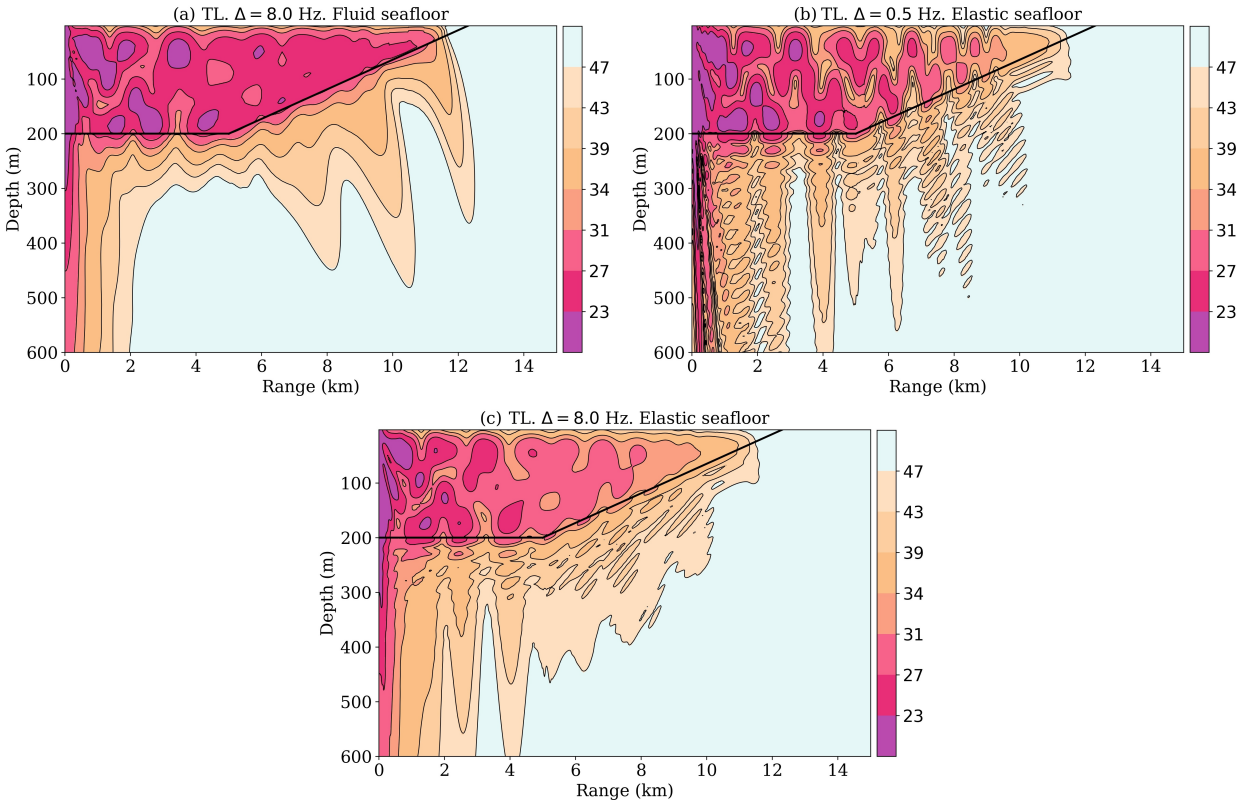

Figure 5.2 – Effect of source bandwidth and bottom elasticity on transmission losses for an upslope wedge. **(a)** TL map, in dB, for a fluid bottom using a broadband source ($f_0 = 25$ Hz, $\Delta = 8.0$ Hz). **(b)** TL map, in dB, for an elastic bottom using a quasi-monochromatic source ($f_0 = 25$ Hz, $\Delta = 0.5$ Hz). **(c)** TL map, in dB, for an elastic bottom using a broadband source ($f_0 = 25$ Hz, $\Delta = 8.0$ Hz).

that for each frequency there is a different modal structure, with different grazing angles and therefore different cutoff depths varying continuously with frequency. This smoothing is also observed in the sediment. The complex structure that was observed below the source also disappears.

Adding a shear velocity to the sea floor leads to a very different structure of the leaking of acoustic energy in the bottom (Figure 5.2 (b)). The leaking of energy associated to the presence of shear waves is strong and dominant. The associated narrow beams are almost vertical because of the low velocity of shear waves in this configuration. Below the sloping interface, it can be seen that the beams exhibit an interference structure due to the leaking, in this case, of both the shear waves and the propagating modes. This structure is also seen in the near field but, in this case, it is generated by the leaking of evanescent modes. Similar results were presented in Abawi & Porter [2007] (top figure of their Figure 1). It can also be noted that the leaking of the first mode is strongly affected by the presence of shear waves, as it does not penetrate deep into the sediment. There is much less energy in the water column at the end of the wedge than in the fluid-only configuration. A large amount of energy is captured by the shear waves of the bottom. The structure of the sound field in the sediment suggests that if another interface is considered, i.e. if we consider an elastic layer over a semi-infinite half-space, the presence of shear waves is critical and may generate complex effects because of the potential interaction between these beams and this interface. As in the pure fluid case, increasing the bandwidth (Figure 5.2 (c)) leads to smoothing of the energy levels mainly in the area of the slope.

5.1.3.3 Broad bandwidth and time dispersion maps

As mentioned in the previous subsection, another type of information can be extracted from time-domain simulations. This piece of information is related to the spreading of energy with time at a receiver location. Indeed, for a given energy level, the time structure of the received signal can be very different and provide additional information on the propagation process that led to this received signal. This is particularly useful e.g. for T-waves analysis because the time structure of a received signal is different depending on the source mechanism that led to the generation of this signal. In order to illustrate the kind of information that is provided by this type of map, we performed a full-wave time-domain numerical simulation for a fluid bottom and a broadband signal ($f_0 = 25$ Hz, $\Delta = 25.0$ Hz).

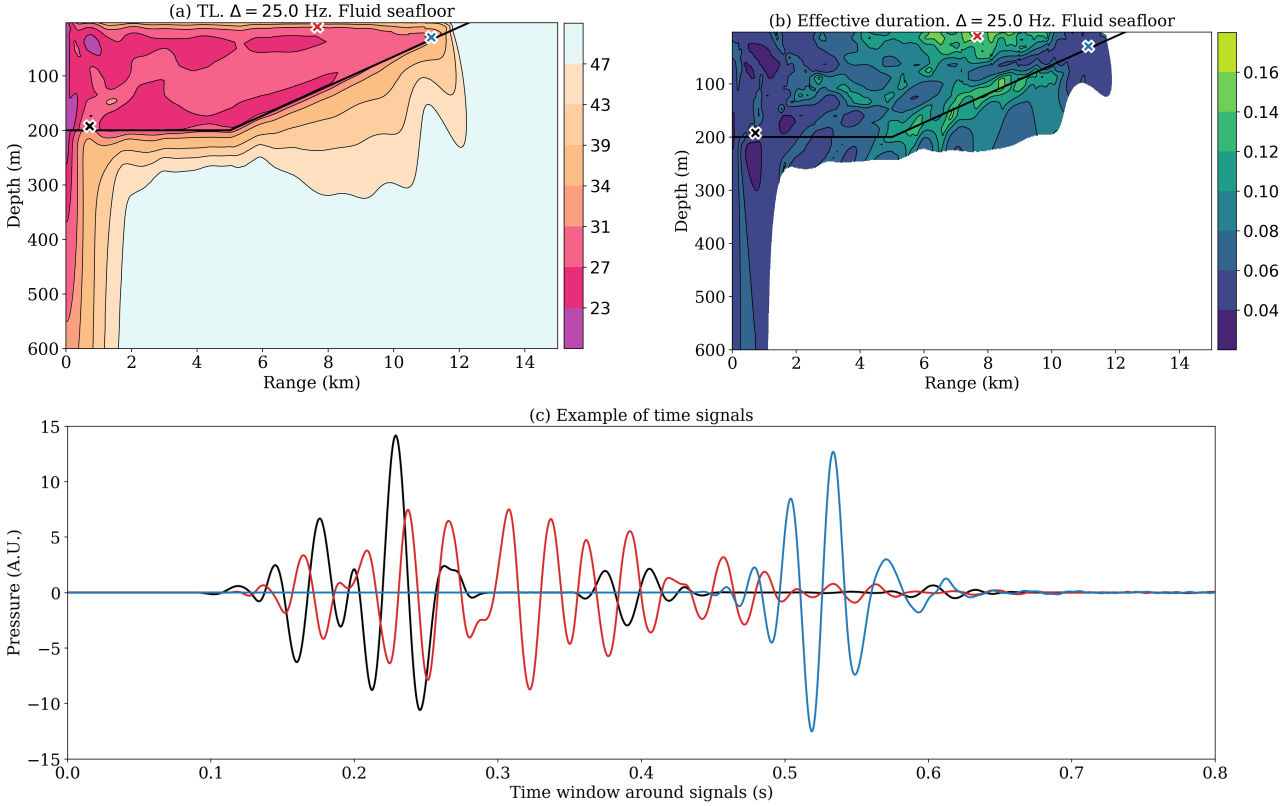

Figure 5.3 – Figure illustrating the use of time dispersion maps. The geometry is the same as in Figure 5.1. **(a)** TL map, in dB, using a broadband source ($f_0 = 25$ Hz, $\Delta = 25.0$ Hz). **(b)** Associated time dispersion map $\mathcal{T}(\boldsymbol{x})$ (in seconds). This field is shown only for transmission losses that are below 43 dB. **(c)** Arbitrary time-shifted pressure signals recorded at the positions indicated by the crosses in (a) and (b). The color of each curve corresponds to the color of the respective cross. The wave energy is about the same at the three positions, but the time dispersion is different.

Figure 5.3 (a) represents the TL map, and Figure 5.3 (b) represents the time dispersion map for TL values lower than 43 dB only in order to avoid showing very weak signals. Finally, Figure 5.3 (c) provides time sequences associated to receivers located at the position of the crosses indicated in Figures 5.3 (a) and (b). These positions were chosen so that the energy level is similar for all positions. The time sequences are arbitrary shifted for visualization purposes. The time dispersion map exhibits complicated structures reflecting the various time structures that can be generated in this configuration. Signals tend to be more dispersed with range, especially right beneath the sea surface or along the interface with the sea bottom. Nevertheless, at the end of the wedge, at the cutoff depth of mode 1, signals tend to be narrower. This effect is clearly visible in Figure 5.3 (c).

5.1.4 Conclusions

We have presented an efficient procedure to compute transmission losses and time dispersion maps from time-domain full-wave numerical simulations. This procedure allowed us to extend the notion of transmission losses to non-monochromatic signals and to elastic media. Some results using this procedure were obtained for a 2D wedge configuration in ocean acoustics. In the case of a simulation in the frequency domain and for a fluid bottom, these results were compared to results previously obtained using a parabolic equation, showing that both methods give similar results. As a result, our approach can provide solutions for configurations for which using a full-wave numerical method is important because of the complexity of the model. Used in conjunction with a spectral element method in the time domain, this procedure may be used in the future to generate full-wave transmission loss maps for problems that are too large for frequency-domain solvers due to their scaling issues. In the next section this approach will be used for T-wave propagation, in which it may bring new insights into the physical mechanisms. See also Appendix A on page 173 and more particularly Figure A.8 on page 181.

5.2 Efficiency of the SOFAR channel in terms of energy channeling in the water column

We have also studied the influence of the deep sound channel on acoustic energy distribution using the tools presented above. Initial observations showing little effect of the SOFAR channel on simulated T-wave energy (at least at regional distance) were intriguing and led us to start the following study on the influence of a Munk-type sound-speed profile (Munk [1974]) on energy distribution. Note that some of the results shown in this section involve layered structures and could thus have been obtained using quasi-analytical methods such as wavenumber integration. For the sake of simplicity, since we were familiar with our existing tool, we chose to nonetheless perform all the calculations based on the spectral-element method.

Let us first summarize the main standard conclusions suggested by the literature on T-waves:

- *The SOFAR channel is a necessary condition for the generation of T-waves.* Note that this assumption has already been discussed in Chapter 1.
- *T-waves have to be generated at conversion points located near the SOFAR channel axis.* Let us recall nevertheless that no dependence of T-wave amplitude on water depth at the conversion point has been documented in the North Atlantic ocean (Williams et al. [2006]).
- *The energy of the hydroacoustic waves trapped in the SOFAR channel is maximum on its axis, corresponding to the minimum propagation speed.* Let us note though that this hypothesis is not in agreement with the observations of D'Spain et al. [2001] in the Pacific ocean.

All these assumptions, which seem well established when reading the literature, are in fact far from being so in reality. Let us try to investigate these points precisely based on our full-wave numerical tool. We will start by studying how the energy of an underwater explosion is distributed in the water layer. The influence of the SOFAR channel on energy transmission will then be discussed depending on the type of seabed considered, and in particular on whether or not it is attenuating. We will then analyze the case of T-waves that are created by earthquakes (thus, occurring in the elastic part).

5.2.1 General description of the configuration studied

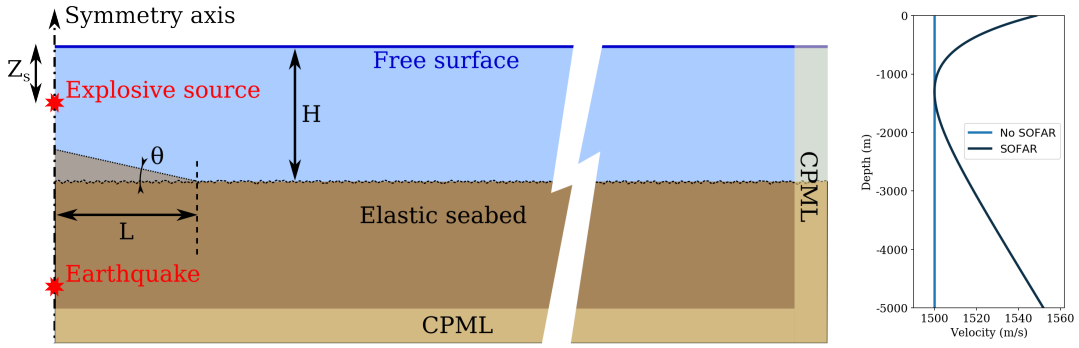

Figure 5.4 – **Left**: this picture depicts the simulations performed in this section. The setup is 2-D axisymmetric. The ocean depth is $H = 5000$ m. **Right**: sound speed profiles in the sea used for the numerical simulations. "SOFAR" means a classical idealized ocean sound-speed profile (Munk [1974]) with a minimum velocity set at depth 1300 m.

All the simulations performed in this section are 2-D axisymmetric and are described in Figure 5.4. The seabed is semi-infinite and (visco)elastic and is situated at depth $H = 5000$ m. Its P and S wave velocities are $V_p = 3400$ m.s^{-1} and $V_s = 1700$ m.s^{-1} respectively and its density is 2200 kg.m^{-3}. The seafloor can either be flat or exhibit a roughness. In this latter case it has a Gaussian height distribution function and a Gaussian autocovariance function, with RMS height equal to 20 m and correlation length equal to 80 m. The seafloor can also be dipping by an angle of $\theta = 9°$ over a length $L = 30$ km. For each simulation the field is computed up to a range of 520 km and down to a depth of 15 km, the energy coming out of this domain being absorbed by PML layers. As shown in Figure 5.4, right, the water layer is either homogeneous ($\rho_w = 1000$ kg.m^{-3}, $c_w = 1500$ m.s^{-1}) or exhibits a variable sound speed with depth (Munk [1974]) with a minimum velocity set at depth 1300 m. This case is labeled "SOFAR".

5.2.2 Explosive source in the water layer

Before considering seismic sources below the seafloor, the simpler case of a pressure source situated in the water column will be tackled. The semi-infinite (visco)elastic seabed, situated at depth 5000 m, will be considered as flat in a first step. The source, initially located at depth $Z_s = 2500$ m, is a point source with a time history corresponding to either a Ricker wavelet (second derivative of a Gaussian) with a dominant frequency f_0 or to a quasi-monochromatic signal. The quasi-monochromatic signal has been defined in equation (5.10). The bandwidth used is in that case is $\Delta = 0.1$ Hz. Three dominant frequencies are considered in the broadband configurations: $f_0 = 0.71$ Hz, $f_0 = 2.83$ Hz and $f_0 = 5.66$ Hz. The spectra of the broadband sources are shown in Figure 5.5. Note that their bandwidth varies with frequency. For each simulation, Transmission Losses (TLs) and effective dispersion maps, as defined in previous section are computed. Some results are shown in Figures 5.6 and 5.7.

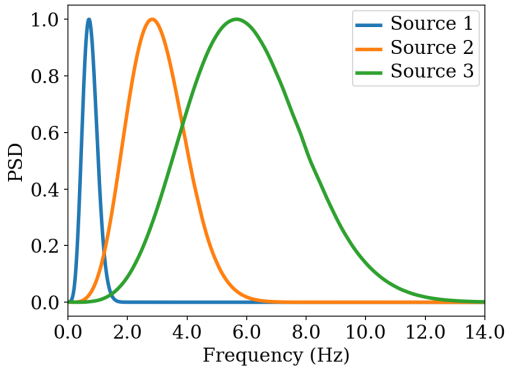

Figure 5.5 – Normalized Power Spectral Density (PSD) of the three broadband signals used. Source 1 has a dominant frequency $f_0 = 0.71$ Hz, source 2 has a dominant frequency $f_0 = 2.83$ Hz, and source 3 has a dominant frequency $f_0 = 5.66$ Hz.

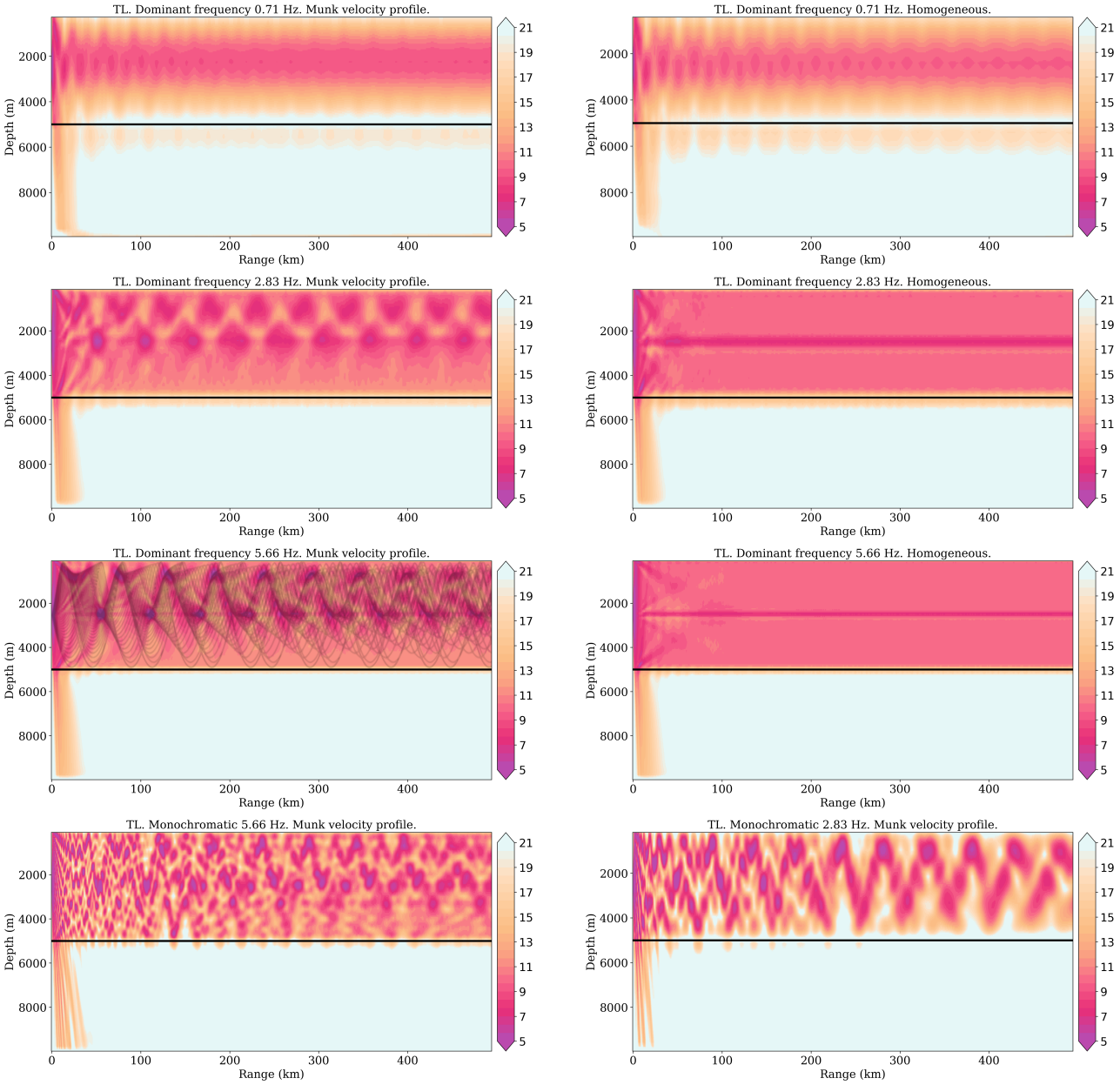

Figure 5.6 – Transmission loss maps for three different broadband sources and two monochromatic sources in the case of a Munk velocity profile in the water layer. The TLs are also shown for a homogeneous water layer (three top-right sub-figures). Ray tracing (black lines) performed with the program Bellhop is superimposed on the figure corresponding to the source with a dominant frequency 5.66 Hz in the case of a Munk velocity profile (third figure from the top left). The source is located at depth $Z_s = 2500$ m.

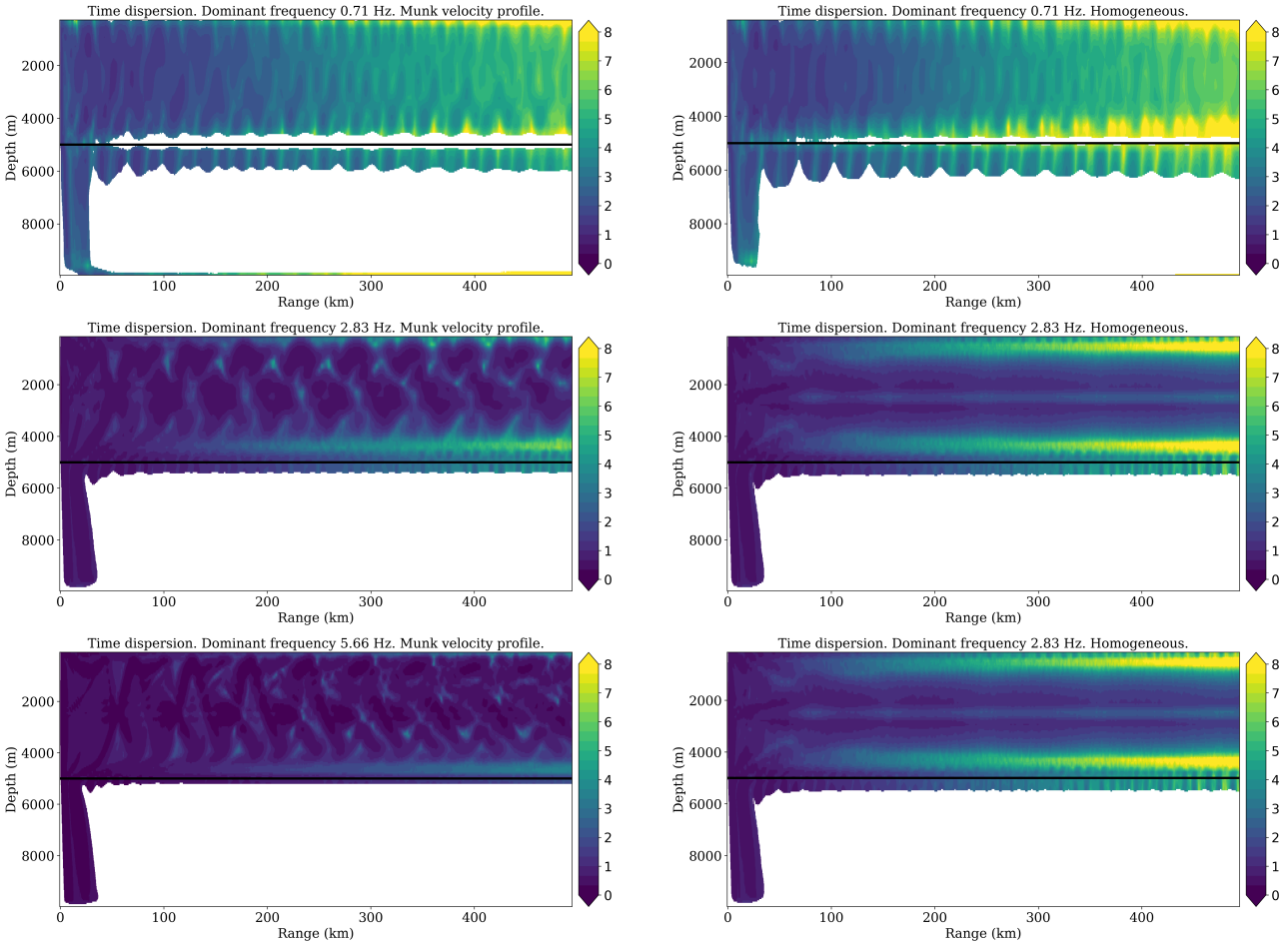

Figure 5.7 – Time dispersion maps for three different broadband sources. Munk profile in the water (left) and homogeneous water layer (right). Time dispersion values are shown only for transmission losses below 17 dB. The source is located at depth $Z_s = 2500$ m.

5.2.2.1 Energy distribution and signal dispersion in the non-attenuating case

Figure 5.6 illustrates the effect of the SOFAR channel and of the dominant frequency of the source on TLs. To compensate for the geometrical spreading, the TLs shown have been divided by range r. Namely, the figure shows for each position $\boldsymbol{x}$:

$$\langle TL \rangle (\boldsymbol{x}) = \frac{1}{r} TL(\boldsymbol{x}) \tag{5.11}$$

The transmission loss is set to 0 at a distance of 500 m from the source. The figure also shows ray tracing performed with the program Bellhop (Porter & Bucker [1987]; Porter [2011]) and superimposed on the figure corresponding to the source with a dominant frequency 5.66 Hz in the case of a Munk velocity profile.

Some remarks can be made. First, at long range, the patterns are blurred and the energy distribution gets more and more homogeneous. Furthermore, in the non homogeneous cases one can note that when frequency increases, the energy gets closer to the caustics predicted by ray tracing. This observation holds only in the case of broadband sources and not in the monochromatic case (see the two sub-figures at the bottom of Figure 5.6 and compare them with the ray tracing shown above in the same figure). When increasing the frequency, in the monochromatic case, the energy does not seem to get closer to the caustics predicted by ray tracing. An explanation of this phenomenon can be linked to the fact that ray theory involves the notion of travel time, which is intrinsically a multi-frequency

quantity. This case is a good illustration of the interest of computing broadband transmission losses and not only monochromatic ones.

Let us now compare the transmission loss maps in the case of a variable velocity profile in the water and in the case of a homogeneous fluid medium. Significant differences, in terms of energy distribution, are observed for frequencies 2.88 Hz and 5.66 Hz. In the homogeneous case the energy thus appears to quickly gather around the direct path, while in the case with a SOFAR channel we observe the patterns corresponding to caustics, which we have already described above.

In the low frequency case ($f_0 = 0.71$ Hz) however the transmission losses appear to be only slightly sensitive to the sound speed variations. This was to be expected, as the wavelengths in that case are comparable to the size of the waveguide. For all the frequencies considered, Figure 5.7 show that the presence of a sound speed channel favors signal dispersion. This effect is even more pronounced at high frequency and near the sea surface and the seabed (where the transmission losses are observed to be high as well). This accounts for the high number of reflections needed to reach these points (see Ewing & Worzel [1948] for example). Let us remind that we consider a non-attenuating sea bottom here.

In order to illustrate the effect of the SOFAR channel in the time domain, a comparison between two pressure signals recorded at range 480 km and depth -2722 m is shown in Figure 5.8. They have been recorded in the case of the source with dominant frequency 2.83 Hz and a non-attenuating seabed for the two different sound speed profiles in the water.

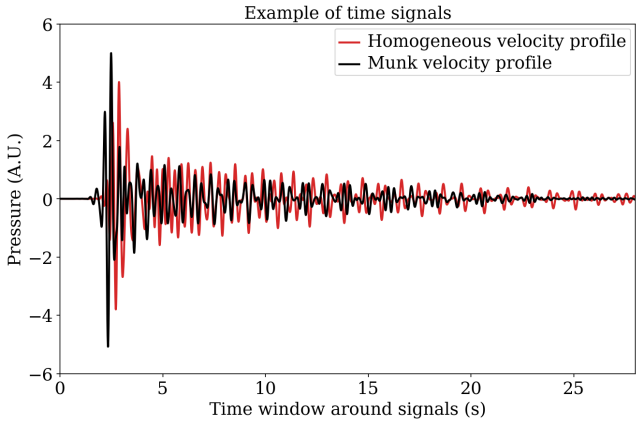

Figure 5.8 – Example of time signals recorded at range 480 km and depth -2722 m in the case of the source with dominant frequency 2.83 Hz and a non-attenuating seabed for the two different velocity profiles in the water.

Although the signals look very similar, we can notice that the signal recorded in the presence of a Munk sound speed profile is slightly more impulsive and therefore of shorter duration than the signal recorded in the case of a homogeneous water layer.

5.2.2.2 Efficiency of the SOFAR channel for attenuating and non-attenuating sea bottoms

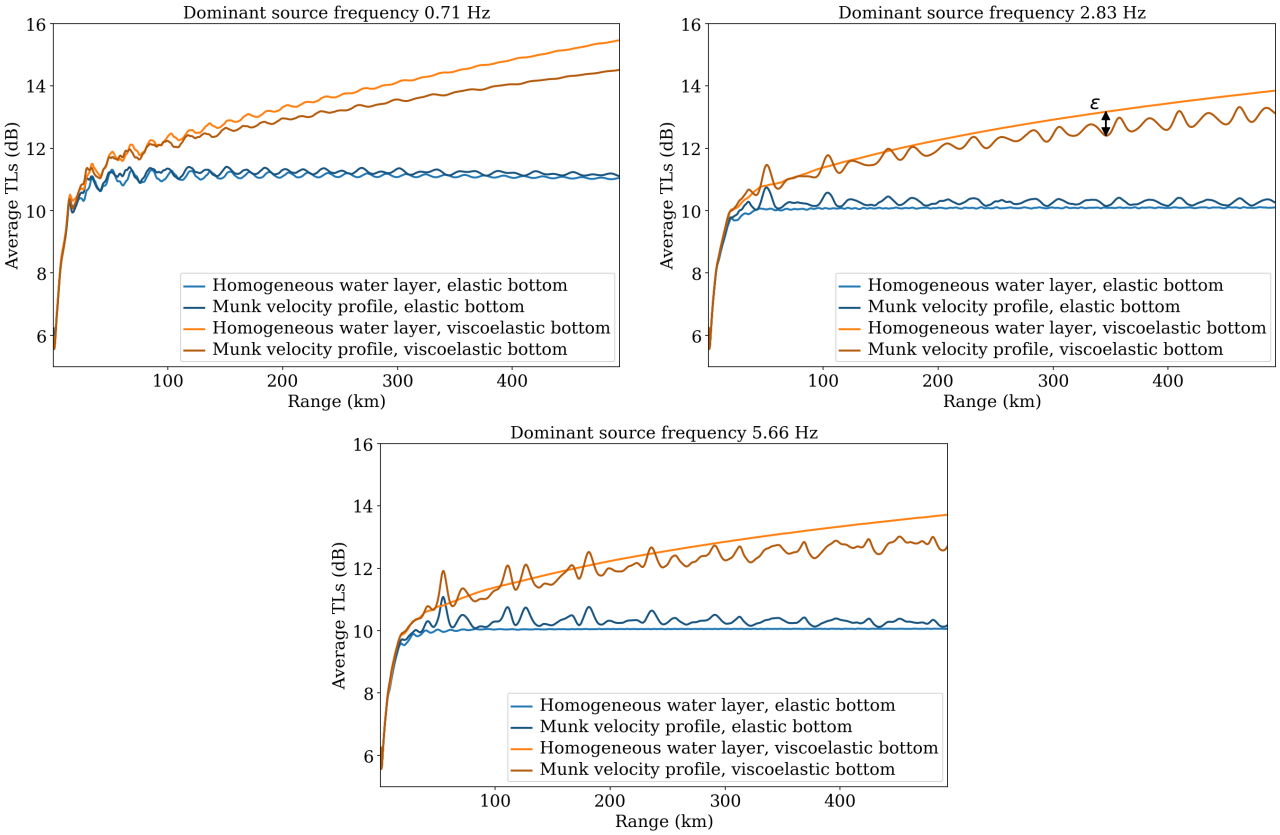

Figure 5.9 – Average transmission losses as a function of range as defined by equations (5.18) and (5.12) for the three different broadband sources considered. These quantities have been calculated in four different configurations described in the captions.

Figure 5.9 shows the average transmission losses for depths between $z_1 = -500$ m and $z_2 = -4500$ m as a function of the distance r to the axis for the three source frequencies considered and the two types of ocean model (homogeneous or Munk velocity profile). To compensate for the geometrical spreading, TLs have been divided by range r. Namely, the figures show

$$\langle TL \rangle (r) = \frac{1}{r\,(z_1 - z_2)} \int_{z_2}^{z_1} TL(r, z)\, dz\,. \tag{5.12}$$

These are the same kind of maps than those shown in Figure (5.6), but averaged over depth. These curves show that, in the non-attenuating case (blue curves) the presence of a sound speed channel does not have a visible effect on the averaged energy transmission at long distances. Total internal reflections are the governing physical phenomena in this case in which both the speeds of the compressional and shear waves in the bottom are higher than the speed of sound in the water. Thus, if the seabed is not attenuating the transmission of sound in the ocean only marginally depends on the sound speed profile. This observation does not depend on frequency.

The addition of attenuation in the seabed on the ocean floor changes the scenario. The orange curves in the sub-figures of Figure 5.9 show the evolution of the transmission losses with distance r from the source for the same setting as previously but with viscoelastic attenuation in the seabed ($\alpha_p = \alpha_s = 0.3$ dB.λ at 2.83 Hz). We can then see that the presence of a SOFAR channel favors energy transmission by limiting the number of interactions with the seabed. It is then interesting to

quantitatively study the gain in terms of transmission losses that can be attributed to the channel. Let us call it $\epsilon(r)$:

$$\epsilon(r) = \langle TL_{\text{homo}} \rangle (r) - \langle TL_{\text{Munk}} \rangle (r) \,, \tag{5.13}$$

where "homo" refers to the case of a homogeneous water layer and "Munk" to the case of a Munk-type sound speed channel. This quantity is represented in Figure 5.10, as a function of range, for the three dominant source frequencies and two types of seabed (elastic and viscoelastic).

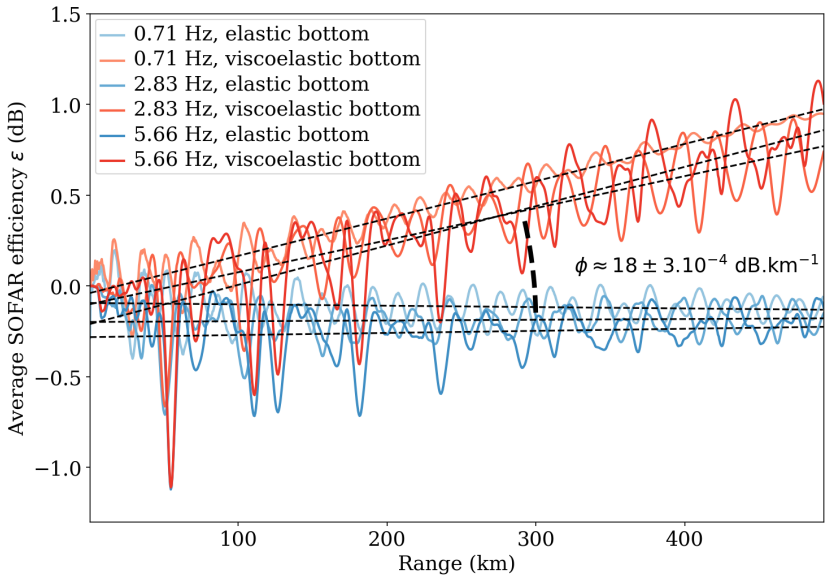

Figure 5.10 – Average SOFAR efficiency in dB as defined in equation (5.13). T-waves are shown as dashed gray curves, while explosions are shown as solid lines. Black dashed lines are the best linear fit for each curve. For each curve the angle ϕ with respect to the horizontal gives the gain in terms of depth averaged energy transmission induced by the SOFAR channel.

Seafloor attenuation is still equal to $\alpha_p = \alpha_s = 0.3$ dB.λ at the dominant frequency of each source. We can see that the gain induced by the SOFAR channel increases linearly with range. We can thus define a slope ϕ, shown in Figure 5.10, that accounts for the influence of the SOFAR channel on depth-averaged TLs, as

$$\phi = \left\langle \frac{d\left[\epsilon(r)\right]}{dr} \right\rangle . \tag{5.14}$$

Figure 5.10 shows that ϕ varies only very slightly in the frequency range considered. For the viscoelastic seabed studied ($\rho = 2200$ kg.m^{-3}, $V_p = 3700$ m.s^{-1}, $V_s = 1700$ m.s^{-1} and $\alpha_p = \alpha_s = 0.3$ dB.λ^{-1} at 2.83 Hz) this factor is $\phi = 18 \pm 3.10^{-4}$ dB.km^{-1}. This observation leads to several remarks. First, the gain induced by the channel, although noticeable, is remarkably low for the configuration considered. This value is comparable to the viscoacoustic attenuation of seawater, which is mostly ignored at the frequencies considered (Urick [1982]). Moreover, we could have expected a stronger dependence with frequency because each increase in frequency brings us closer to the high frequency approximation characteristics of ray tracing, which predicts a very strong influence of the channel. However, it should also be remembered that the amplitude of the reflection coefficient of a plane wave at an interface does not depend on frequency, which seems to explain this observation.

Let us thus mention that, as ϕ proves to depend little on source frequency, all the following simulations in this section will be made with a dominant frequency $f_0 = 2.83$ Hz only.

5.2.2.3 Analysis of the efficiency of the SOFAR channel in terms of energy channeling as a function of viscoelastic attenuation in the seabed

In Figure 5.11 let us now analyze effects of changing the value of the slope (ϕ in dB/km) defined by equation (5.14) as a function of the seabed viscoelastic attenuation for six different cases. This figure accounts for the influence of the SOFAR channel on depth-averaged TLs. To avoid overloading the figure, error bars are shown for only one curve; in the others the margins of error are similar. The attenuation values covered in the frequency band considered are consistent with the literature (see e.g. Hamilton [1980, 1985]; Chotiros [2017]).

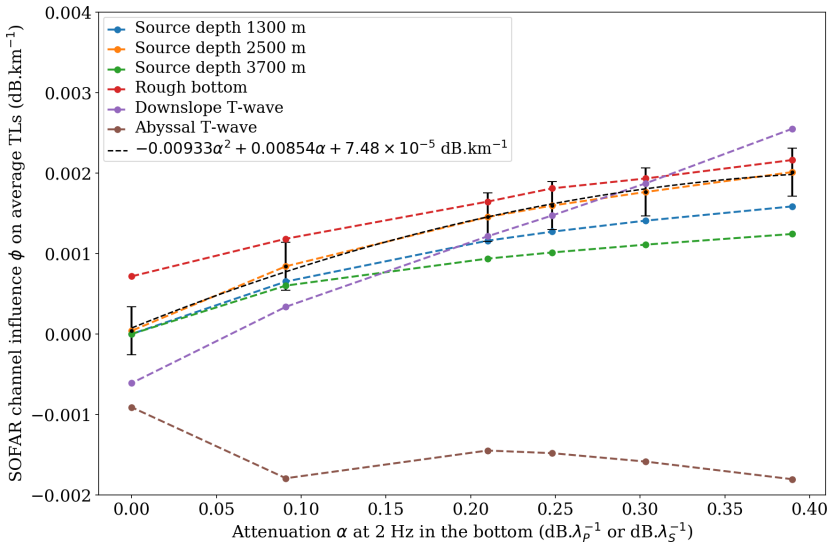

Figure 5.11 – Influence ϕ of the SOFAR channel on depth-averaged TLs, as defined in equation (5.14). Six different configurations are compared. A polynomial fit function is shown for the case with source depth 2500 m.

The curves labeled "Downslope T-wave" and "Abyssal T-wave" will be left aside for the moment. We first focus on the other ones, which correspond to explosions in the water layer. Three source depths are investigated. In addition, the curve labeled "Rough bottom" corresponds to a source depth of 2500 m to which a roughness has been added over the whole seafloor.

We can see that these curves are positive and increasing. Indeed, overall, the guided modes interact less with the bottom when the sound speed profile exhibits a minimum, which means that the more the ground is attenuating the more the structure of the sound speed profile is advantageous for transporting energy. In this context it is logical that the addition of a roughness on the bottom reinforces the gain induced by the channel by making the interactions with the ground all the more expensive. However, it may seem somewhat counterintuitive that the depth of the source corresponding to the minimum velocity in the water is not the optimal depth for the source in terms of average transmission losses over the depth of the water. However it is worth noting that the choice made in equation 5.12 to average transmission losses with depth is arbitrary. This choice was made because in most experiment nothing indicates, a priori, that the receiver being used is at an optimum position for energy reception (see the preferred zones in Figure 5.6). We can also study the influence of the SOFAR speed channel on the minimum transmission losses as a function of range. In that case minimum TLs over depth are computed for each range

$$TL^{\min}(r) = \min_{z \in [z_1, z_2]} \frac{TL(r,z)}{r} \,. \tag{5.15}$$

This allows for the calculation of the gain for each range induced by the SOFAR channel in terms of minimum possible transmission losses

$$\epsilon_{\min}(r) = TL^{\min}_{\text{homo}}(r) - TL^{\min}_{\text{Munk}}(r)\,, \tag{5.16}$$

where "homo" refers to the case of a homogeneous water layer and "Munk" to the case of a Munk-type sound speed channel. Finally, for each case studied, the average influence of the SOFAR channel on minimum possible TLs can be defined:

$$\phi_{\min} = \left\langle \frac{d\left[\epsilon_{\min}(r)\right]}{dr} \right\rangle . \tag{5.17}$$

This factor is shown in Figure 5.12 as a function of seabed attenuation in six different cases.

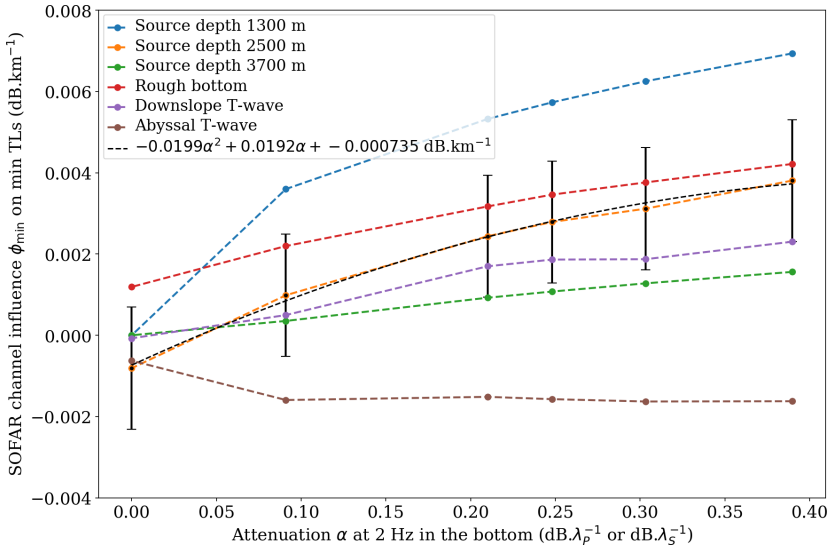

Figure 5.12 – Influence $\phi_{\min}$ of the SOFAR channel on minimum possible TLs as defined in equation (5.17). Six different configurations are compared. A polynomial fit function is shown for the case with source depth 2500 m. Note that the scale is different from that in Figure 5.11.

The observed values are higher than those shown in Figure 5.11, which were obtained by averaging over the water layer. In terms of minimum possible TLs, the presence or absence of the SOFAR channel can make a difference of up to 0.007 dB.km^{-1}, i.e. 7 dB over a 1000 km path, which is significant. The "channelizing" effect of the SOFAR channel now appears strongest when the depth of the source is at the depth of the minimum sound speed in the ocean. In this configuration the energy is channeled around the channel axis (see Figure 5.17, left) in accordance with ray tracing.

Analysis of the effect of the SOFAR channel on signal dispersion

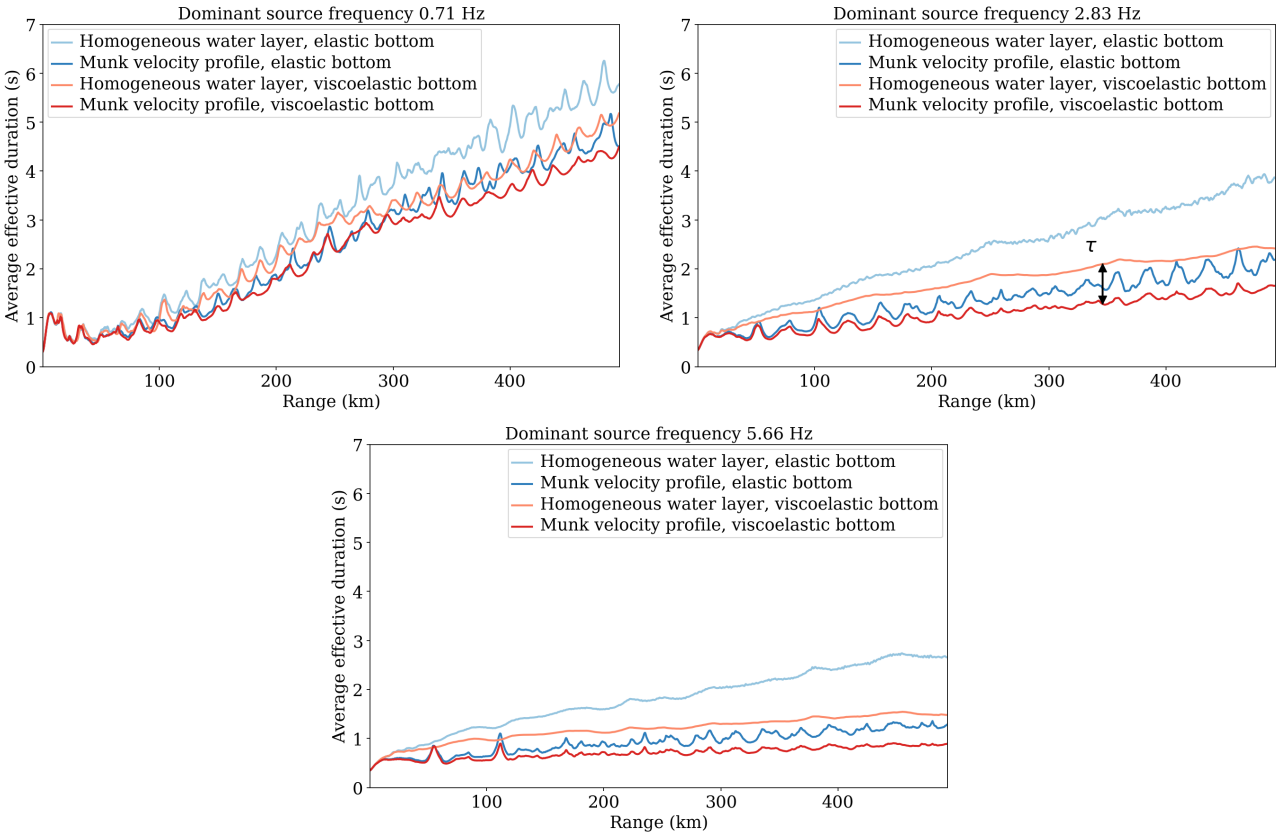

Figure 5.13 – Average effective durations as a function of range as defined by equations (5.18) and (5.12) for the three different broadband sources considered. These quantities have been calculated in four different configurations described in the captions.

Let us now discuss the dispersion of time signals. Figure 5.13 shows the depth-averaged time dispersion, defined in equation (5.6), between $z_1 = -500$ m et $z_2 = -4500$ m as a function of the distance r to the axis. Three source frequencies and two types of oceans (homogeneous or Munk velocity profile) are considered. Namely, the figures shows

$$\langle \mathcal{T} \rangle (r) = \frac{1}{(z_1 - z_2)} \int_{z_2}^{z_1} \mathcal{T}(r, z)\, dz\,. \tag{5.18}$$

This quantity is the same as that shown in Figure (5.7), but averaged over depth. As expected from Figure 5.7 these images confirm that, overall, the presence of a wave speed channel induces fewer time dispersion, even in the case of a non-attenuating elastic seabed. The time spreading appears to be more important in the case of low-frequency signals. This is illustrated in Figure 5.14, which shows the average decrease of time dispersion due to the SOFAR channel. It is defined by

$$\delta(r) = \langle \mathcal{T} \rangle_{\text{homo}} (r) - \langle \mathcal{T} \rangle_{\text{Munk}} (r)\,, \tag{5.19}$$

where “homo” refers to the case of a homogeneous water layer and “Munk” refers to the case of a Munk-type sound speed channel.

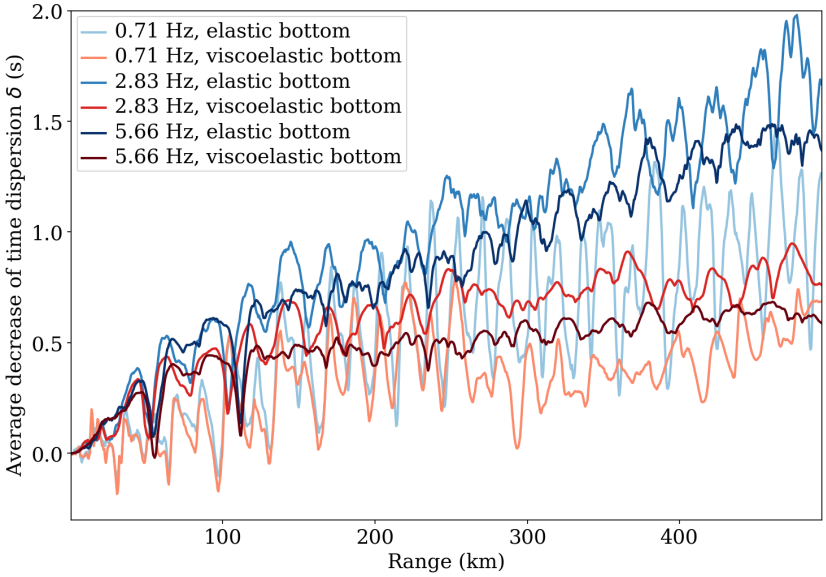

Figure 5.14 – Average decrease of time dispersion due to the SOFAR channel in seconds as defined in equation (5.19).

The decrease of time dispersion evaluated as a function of range varies between 0.5 s and 1.5 s over 500 km for the cases considered and is more important for non-attenuating seabeds. These values correspond to an increase in travel time of 0.15 s to 0.45 s every 100 s in the water (not always linear), which is significantly lower than the values given by Ewing & Worzel [1948], for example, who reported an increase of 1 s every 100 s but in almost perfect accordance with the calculations of Piserchia et al. [1998] (their Figure 9). These differences may be due to differences in the seabed seismic properties (De Groot-Hedlin [2004]), source depth (Piserchia et al. [1998]), or topography, and suggest that time dispersion is particularly sensitive to the characteristics of the configuration and may constitute an interesting parameter to consider in the framework of an inverse problem.

5.2.3 Source below the seabed

5.2.3.1 Configuration studied

In the case of T-waves, the source is not in the water layer but is a seismic event in the seabed. Let us thus perform the same kind of study as in the previous subsection but for a seismic source, set below the seabed. T-waves are excited from downslope conversion or from scattering on a rough seabed. In this subsection the source depth is $Z_s = 12$ km (7 km below the seabed). The seafloor can be either dipping by an angle of $\theta = 9°$ over a length $L = 30$ km or can exhibit a roughness. In this case we recall that it has a Gaussian height distribution function and a Gaussian autocovariance function, with RMS height of 20 m and correlation length of 80 m respectively. The configuration is described in Figure 5.4. Contrary to the previous subsection, the rough area does not cover the whole model but rather has a length of $L = 30$ km, and the seafloor is flat beyond this range. The transmission losses are set to 0 in the middle of the water layer at range $L = 30$ km. In the following, T-waves generated from downslope conversion will be called “downslope” T-waves, while T-waves generated from scattering by a rough seabed will be called “abyssal” T-waves.

5.2.3.2 Increase of TLs induced by the SOFAR channel for T-waves

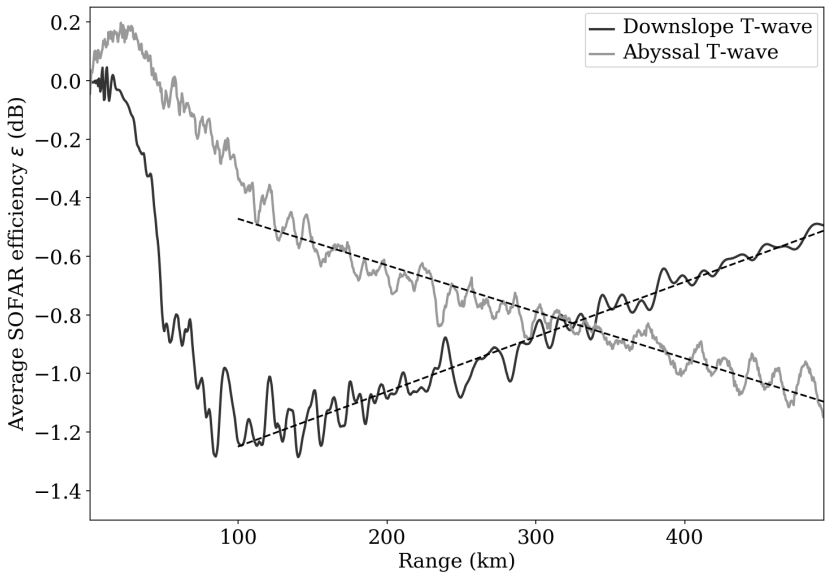

Figure 5.15 – Same as Figure 5.10 but for T-waves instead of explosions. Black dashed lines are the best linear fit for each curve after range 100 km.

For both types of T-waves (downslope or abyssal) the gain in depth-averaged transmission losses ϵ induced by the SOFAR channel (as defined in equation (5.13)), is shown as a function of range in Figure 5.15. It is noticeable that at the distances considered ϵ is negative, which means that the SOFAR channel has, on average, a "negative" effect on T-wave energy transmission. In other words, the presence of the channel induces, on average, more transmission losses than in the homogeneous case in this configuration. After a given range (100 km here), downslope-converted T-waves do take advantage of the SOFAR: ϵ increases with a slope comparable to those obtained with a source in the water layer. On the contrary, the absence of a SOFAR channel seems to always have a "positive" effect on the T-wave created by scattering on a rough seabed. Hence negative and decreasing $\epsilon(r)$ are observed in this case. This means that the homogeneous sound speed profile is more efficient than the variable sound speed profile to transmit energy at long range for this type of source. This observation can be explained by the different modal structures obtained in the downslope and abyssal cases. Abyssal T-waves are composed of higher-order modes whose depth function is more favorable in the case of a homogeneous water layer. It is also possible to give an explanation from the point of view of ray theory: since the rough seafloor is located below the critical depth, no ray generated there can end up channeled through the waveguide in this case, which may explain why the homogeneous case may be more efficient for energy transmission. It has to be reminded here that the differences in terms of energy transmission at 500 km between the homogeneous and SOFAR configurations remain quite low anyway.

Decrease in time dispersion induced by the SOFAR channel for T-waves

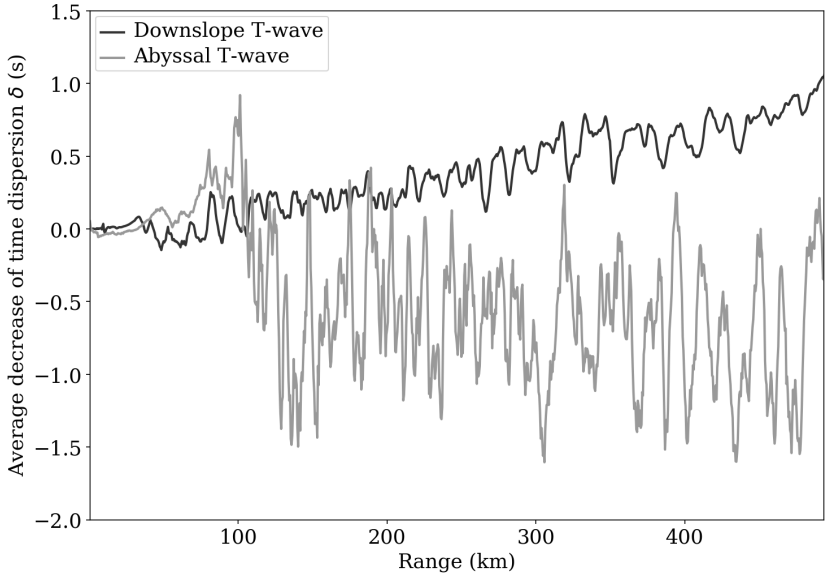

Figure 5.16 – Average decrease of time dispersion due to the SOFAR channel in seconds as defined in equation (5.19). Same as Figure 5.14 but for T-waves instead of explosions.

The average decrease δ in terms of time dispersion due to the SOFAR channel, defined in equation (5.19), is shown in Figure 5.16 for the abyssal and downslope converted T-waves. In the downslope case the increase observed with range is comparable to that obtained for an explosive source in the water layer. This means that on average the presence of the SOFAR channel induces less time dispersion on these T-waves. It is the opposite in the case of the abyssal T-wave. The presence of the channel appears to lead to an overall increase in time dispersion. However, in this case no particular trend is observed with increasing range.

Analysis of the efficiency of the SOFAR channel in terms of T-wave energy channeling as a function of viscoelastic attenuation

Figure 5.11 shows the mean slope ϕ of the curves presented in Figure 5.15 (see equation (5.14)) as a function of the viscoelastic attenuation of the seabed. In the case of T-waves, these slopes are calculated from range 100 km from which the evolution is linear (see the gray curves in Figure 5.15). Figure 5.11 confirms that after a given range (100 km here) downslope-converted T-waves take advantage of the SOFAR channel in proportions comparable to signals resulting from explosions in water, and that abyssal T-waves are of higher energy in the absence of a SOFAR channel, regardless of the seabed attenuation value. These observations do not change when considering $\phi_{\min}$ instead of ϕ, that is to say when considering the influence of the SOFAR speed channel on the *minimum* transmission losses as a function of range (Figure 5.12).

Transmission loss depth profiles

Examples of transmission loss profiles versus depth in the water layer are shown in Figure 5.17. They have been calculated at range $r = 480$ km for four different configurations and two different sound speed profiles in the water layer. In all cases the sources have a dominant frequency of 2.83 Hz and the seabed is attenuating ($\alpha_p = \alpha_s = 0.25$ dB.λ at 2.83 Hz). In the case of an explosion at the depth corresponding to the minimum sound speed in water (1300 m) the energy concentrates around that depth. When the source is far from that depth, such as the one shown for an explosion at 3700 m,

this is not the case anymore: the energy spreads in the whole water column. In the case of T-waves (sub-figures one the right-hand side) the observation is similar. Indeed, in that case, the source of the excitation is not a point any more but rather covers an extended area that is not limited to the minimum sound speed location in water.

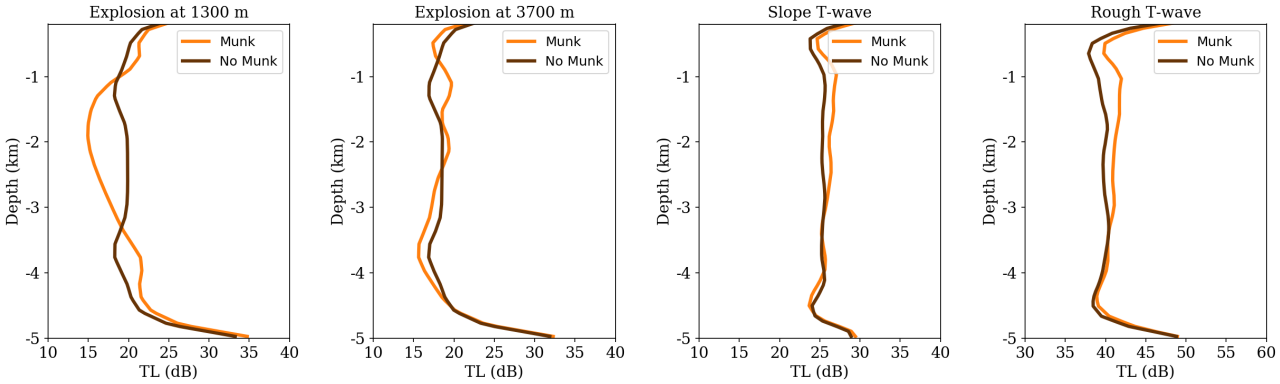

Figure 5.17 – Examples of TLs profiles at range $r = 480$ km. In all cases the sources used have a dominant frequency og 2.83 Hz and the seabed is attenuating ($\alpha_p = \alpha_s = 0.25$ dB.λ at 2.83 Hz). Two different velocity profiles in the water are considered (see Figure (5.4), right). Labels "No Munk" refer to the homogeneous water layer. Let us note that a different abscissa is used in the case of a T-wave generated by scattering on a rough seabed (right).

Time frequency structure of the signals, inverse time dispersion

Full waveform simulations in the time domain allow for a direct study of signals in the time-frequency plane. It is then interesting to compare in this way the signals obtained for different configurations as well as the effect of the speed channel on spectrograms. A comparison between six signals recorded at range 480 km and depth -2278 m is thus shown in Figure 5.18.

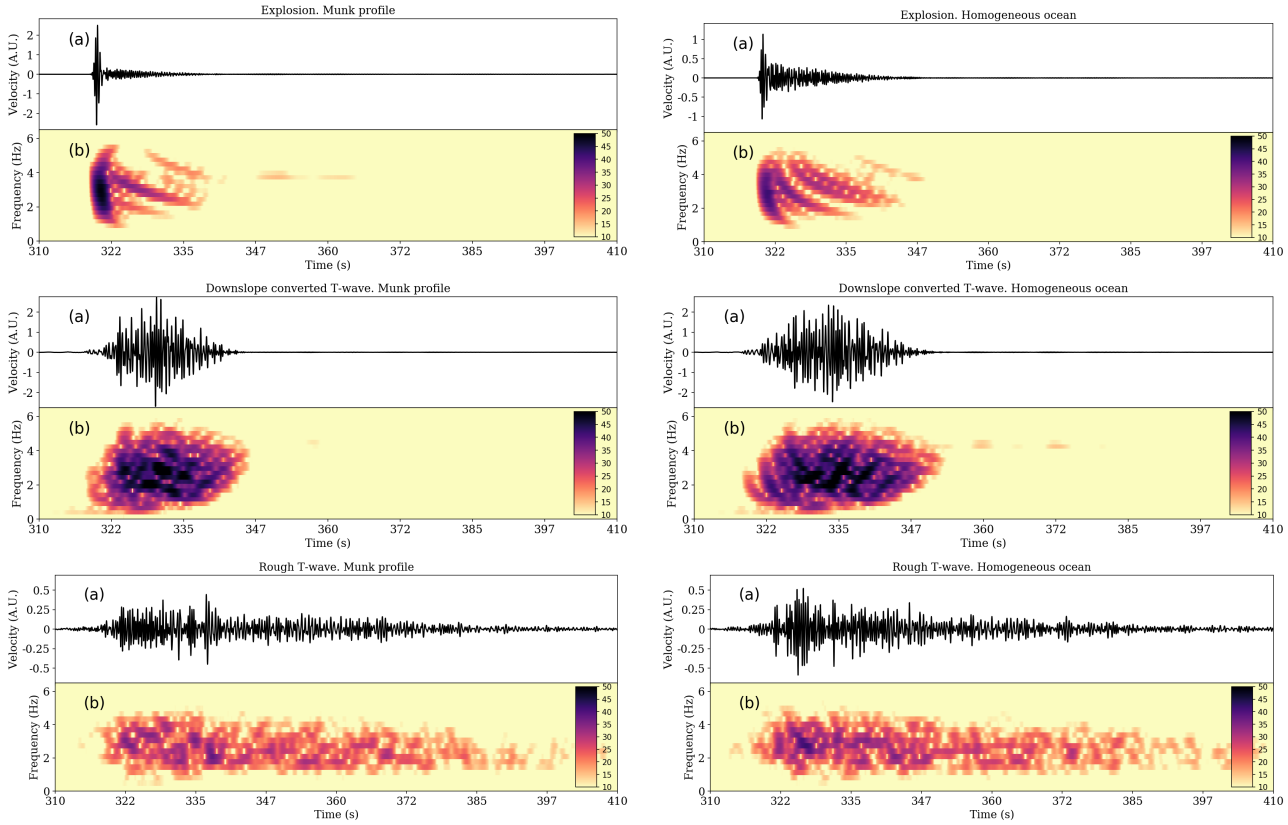

Figure 5.18 – Comparison of different acoustic signals in the time-frequency domain. Each signal has been recorded at range 480 km and depth -2278 m. The source has a dominant frequency of 2.83 Hz and the seabed is attenuating ($\alpha_p = \alpha_s = 0.39$ dB.λ at 2.83 Hz). **Left**: Munk profile in the water. **Right**: Homogeneous water. From top to bottom: explosion at depth 2500 m in an ocean with a variable velocity profile, downslope-generated T-wave ($Z_s = 12000$ m, slope described in the text), abyssal T-wave ($Z_s = 12000$ m, rough seabed described in the text). For all sub-figures: (a) Vertical particle velocity (arbitrary velocity unit) (b) Power Spectral Density (in dB) as a function of time and frequency.

For each case the source has a dominant frequency of 2.83 Hz and the seabed is attenuating ($\alpha_p = \alpha_s = 0.39$ dB.λ at 2.83 Hz). The two signals at the top of the figure were generated by an explosive source at depth $Z_s = 2500$ m for a flat ocean with and without a SOFAR channel, respectively. For comparison, the two signals in the middle of the figure are T-phases generated by downslope conversion at the slope described above for the two velocity profiles in the water studied. Finally, the two lower figures correspond to abyssal T-phases generated by scattering on a rough seabed. Let us first notice that the presence or absence of a SOFAR sound speed channel does not induce significant qualitative differences between the signals recorded at the position considered. Besides, important differences can be noted between the different configurations. In the case of an underwater explosion, the arrival is impulsive and followed by a tail composed of several dispersive modes (normal dispersion). As already mentioned, the signal generated in the presence of a variable sound speed profile is relatively shorter in duration than the one generated for a homogeneous ocean. The case of a downslope-generated T-wave is however significantly different. The wave packet has a more complex structure, and although the first arrivals exhibit normal dispersion the second part of the signals shows a characteristic inverse dispersion. Such structural differences between explosions and T-waves have been reported by Talandier & Okal [2016], who showed that these characteristics in the time-frequency plane constitute a robust means to differentiate the two phenomena. However, the authors found no explanation for these differences.

It is important to remember that the guided waves that can exist in the water layer are exactly the same regardless of their source. Only the modal content changes, i.e. which modes are excited. Thus,

arrivals with inverse dispersion are made of the same modes as those with normal dispersion. Let us propose a tentative explanation: we simplify the model by placing ourselves in the case of a perfect iso-velocity waveguide of thickness H and of sound speed c (see e.g. Jensen et al. [2011] p. 344-349). In that case a mode of order $m \in [\![1, \infty[\![$ can propagate if and only if the following relationship is verified:

$$Hf > \frac{c}{2}\left(m - \frac{1}{2}\right), \tag{5.20}$$

where f is the incident frequency. Let us then assume that the depth increases with range. A given mode m will therefore be generated at a larger or smaller distance depending on the frequency of the incident wave. The lower the frequency the lower it will be generated on the slope, the higher the frequency the higher it will be generated. Assuming that the wave illuminates the entire slope at the same time the mode considered will be simultaneously generated at high frequency at the top and at low frequency at the bottom. As the mode then travels at the same group speed it will never recover the delay. Hence for all modes the low frequencies will precede the high frequencies throughout the propagation, resulting in reverse dispersion.

The case of abyssal T-waves, generated by scattering on a rough seafloor, is also quite different. The signals obtained are even more complex and of much longer duration. They also exhibit significant frequency variations over time. Real T-waves are most likely a mixture of these two idealized cases. In the configuration chosen we can notice that the simulated amplitudes are clearly lower in the abyssal case than in the case of downslope conversion, in spite of the fact that the source was identical. This suggests that downslope conversion is largely predominant over abyssal conversion for this rather hard and steep seabed. The opposite scenario is typically expected for a gently sloping, sediment covered seafloor (De Groot-Hedlin & Orcutt [1999, 2001a]).

5.2.4 Conclusions

In this section we first studied acoustic energy transmission from an explosion in a waveguide. When increasing the frequency, the energy from the explosion appears to get closer to the caustics predicted by ray tracing but without impeding the propagation in shadow zones beyond them. Maximum differences of approximately 4-8 dB are predicted between neighboring caustics and shadow zones in the case of a source with a dominant frequency of $f_0 = 5.66$ Hz. However these observations hold only in the case of broadband sources and not in the monochromatic case, in which the energy does not seem to get closer to the caustics predicted by ray tracing when increasing the frequency. This feature illustrates the interest of computing broadband transmission losses in addition to monochromatic ones.

We then investigated numerically the influence of the SOFAR channel on energy transmission and time dispersion. In most cases, although the signals look very similar we noticed that the signal recorded in the presence of a Munk sound speed profile was slightly more impulsive and therefore of shorter duration than the signal recorded in the case of a homogeneous water layer. In general, time dispersion is seen to be particularly sensitive to the configuration studied and might constitute an interesting parameter to monitor in the context of an inverse problem. Besides, if the seabed is non-attenuating the SOFAR channel has no visible effect on depth-averaged energy transmission. When introducing viscoelasticity in the seabed, the presence of the SOFAR channel generates a noticeable gain. That gain was however remarkably low in the configurations that we considered, not exceeding 0.002 dB.km^{-1}. The frequency of the simulated waves had little influence on these conclusions. There is a good chance, however, that the reality is quite different. As the frequency increases, the guided waves will interact more with superficial layers which, in practice, will exhibit lower wave speeds, stronger attenuation and greater apparent roughness. However, it is interesting to note that the model, which seems a priori realistic, of a flat and homogeneous seabed ($\rho = 2200$ kg.m^{-3}, $V_p = 3700$ m.s^{-1}, $V_s = 1700$ m.s^{-1}) with attenuation of the order of one tenth of dB per wavelength sometimes

seems inadequate to describe the propagation of guided waves, even at the frequencies considered ($<$ 8 Hz). Indeed, this simplified model, makes the presence of the SOFAR channel incidental for the propagation of energy. However some studies (e.g. Ewing & Worzel [1948]) show that, on the contrary, it is sometimes difficult in practice to record a reflected signal over a few hundred kilometers. It is also true that other works (e.g. Stephen et al. [2009, 2013]) document reflected signals clearly recorded at several thousand kilometers. Our work suggests that the difference between these datasets is to be found in the surface layer structure of the seabed rather than in the ocean.

Downslope and abyssal T-waves were also simulated in this section. At the distances considered the SOFAR channel has, on average, a negative effect on T-wave energy transmission. After a given range however (100 km here), downslope-converted T-waves take advantage of the SOFAR channel in proportions comparable to signals resulting from explosions. On the contrary, abyssal T-waves simulated are more powerful in the absence of a SOFAR channel, regardless of the seabed attenuation value. Explosions and T-waves were also compared in the time-frequency plane. Such an analysis revealed in particular that downslope-generated T-waves and explosions exhibited structural differences, as reported by Talandier & Okal [2016] who showed that the dispersion characteristics constitute a robust means to differentiate the two phenomena. A simple explanation for this unusual dispersion has been suggested based on modal analysis.

This section allows for better understanding of some of the results presented in Lin et al. [2014] for example. The authors showed regional T-waves recorded (at 250 km) by an ocean-bottom seismometer. This observation was presented as surprising because the instrument was located “outside of the SOFAR channel”. In this section we showed that the SOFAR channel is not a necessary condition for T-waves generation, all the more so at regional distances. The authors then built a model based on ray tracing but without considering sea-bottom attenuation; however we showed that such an omission implies almost perfect energy conservation over long distance.

Note also that in the case of the abyssal T-wave we meshed a rough seabed. This was not a problem because the roughness was not too severe. However, in future work it would be interesting to avoid having to explicitly mesh the sea-bottom roughness. The work of Capdeville et al. [2015] has shown that in the case of elastic geophysical models it is possible to resort to homogenization ("upscaling") techniques to avoid having to create a very complex and very dense mesh honoring the finer structures of the model. How this could be extended to the case of a fluid-solid interface would thus be of interest.

5.2.5 Acknowledgments

We are grateful to Jean-Pierre Vilotte, Oleg A. Godin and Raphaël F. Garcia for fruitful discussion. This work was granted access to the French HPC resources of TGCC under allocation #gen7165 and of CINES under allocation #A0020407165, both made by GENCI, and of the Aix-Marseille Supercomputing Mesocenter under allocations #b025. We gratefully acknowledge the support of NVIDIA Corporation with the donation of hardware for this research through their Hardware Grant Request program.

Chapter 6

On geoacoustic Doppler spectroscopy and cargo ships

In this chapter, we present and validate a numerical method based on time-domain spectral elements for full-wave propagation problems with moving acoustic sources. We then apply it to geo-acoustic Doppler spectroscopy of marine sediments. We finally propose a new mechanism of T-wave generation together with an alternative explanation to the waves observed by Evers et al. [2014] both at sea and in the atmosphere following a 2004 earthquake in the Macquarie Ridge.

6.1 Sediment sounding with flying vehicles

This section seems not to be quite on tracks with the T-waves topic and indeed it is not really, but was initially. When Oleg Godin came to LMA as a visiting researcher, he suggested modeling earthquakes as moving sources in elastic media in order to explain the T-waves and infrasound waves described by Evers et al. [2014] and discussed in next section. Inconclusive results led us to abandon the initial project, but the tools had been validated and included in the official SPECFEM2D code. Thus, a new study using these tools appeared interesting to us after reading Buckingham [2003]; Buckingham & Giddens [2006]; Buckingham [2010]; Bevans & Buckingham [2017].

6.1.1 Introduction

It has been known for many years that the sound from large aircrafts is detectable beneath the ocean surface (Urick [1972]; Medwin et al. [1973]; Richardson et al. [2013]). However, to our knowledge, the idea of using the sound generated by an aircraft flying over the sea to study the seabed appears for the first time in Buckingham et al. [2002a,b]. The authors showed that the sound from the propeller was detected not only at a microphone in the air and at hydrophones below the sea surface but also at an instrument buried about 1 m deep in the sediment. This result allowed them to estimate the local sound velocity in the sediment, water and atmosphere from the Doppler shifts due to the motion of the aircraft. The theoretical advances that followed (Buckingham [2003]; Buckingham & Giddens [2006]) provided a deeper understanding of the physics behind the Doppler-shifted field in the channel and the sediments. This work opened the door to inversion of the Doppler-shifted modes associated with each harmonic in order to estimate the sound speed in the sediment as well as other geoacoustic parameters (shear speed, porosity, density and grain size), even using only receivers moored in the water. Conveniently for such inversion purposes, the sound of light aircrafts appears to contain low frequency harmonics (down to ∼80 Hz), the intensity of which varies only weakly throughout the angular range (Buckingham et al. [2006]). This unusual acoustic inversion technique is known as

geoacoustic Doppler spectroscopy (Buckingham [2010]).

More recently, Bevans & Buckingham [2017] presented an original technique using a low-flying light helicopter and an inversion procedure using the coherence function of the head-wave generated at the ocean-sediment interface. The sound produced by the rotors has a broad frequency bandwidth rich in low frequencies (down to about 13 Hz and up to 2.5 kHz), which gives it a greater potential as a low-frequency sound source than the propeller noise of an aircraft. In addition, the new inversion technique is more efficient than the one presented in Buckingham et al. [2002a,b]. It is based on a two-point measurement using a pair of hydrophones located in the water. Provided that the source is at a suitable range from the receivers, a head-wave generated at the ocean-sediment interface can be detected. Theoretically, one can define the horizontal coherence function for this wave whose real and imaginary parts are sinusoidal functions of frequency. Assuming that the distance between the hydrophones is known, these curves only depend on the sound speed in the sediments. By matching the zeros in the analytical expression for the horizontal coherence function and the corresponding zeros in the coherence data, one can then recover the sediment sound speed. Because it uses the entire frequency spectrum, this method seems more suitable for noisy environments. Moreover, it does not require the receivers to be buried in the sediments, which is more convenient from a practical point of view.

The sound speed values measured by Bevans & Buckingham [2017] near Scripps Pier in San Diego, California, USA, are of 1682.42 ± 16.20 m.s^{-1}. The objective of this chapter is to investigate the effect of variable sound velocity in the seabed on such experiments using numerical modeling based on our spectral-element method in the time domain. The configurations studied in this section are intrinsically 3-D. However, the frequencies considered currently do not allow for such simulations to be performed. In the case of moving sources, it is also not possible to resort to an axisymmetric implementation because the moving source breaks the symmetry of the problem (because it moves it does not remain on the symmetry axis). We will, therefore, adopt a 2-D Cartesian model, keeping in mind that this is a limiting assumption.

6.1.2 Spectral-element implementation of moving sources in the time domain

Let us consider a fluid medium Ω_f in the Cartesian 2-D case. In the following, $\boldsymbol{x} = (x, z)$ denotes the position vector and a dot over a symbol denotes time differentiation. The time-dependent pressure perturbation in the fluid is written $P(\boldsymbol{x}, t)$. A pressure point-source is considered at a position $\boldsymbol{x}_s(t)$ that depends on time. As shown in Chapter 3 the wave equation (3.1) in a spatially-heterogeneous fluid can be obtained for a scalar potential defined as $\ddot{\chi} = -P$ and can be written in its strong form as

$$\frac{1}{\kappa}\ddot{\chi} = \boldsymbol{\nabla} \cdot \left(\frac{\boldsymbol{\nabla}\chi}{\rho} \right) + \frac{1}{\kappa} S(t) \delta_{\boldsymbol{x}_s(t)} \,, \tag{6.1}$$

where $\rho(\boldsymbol{x})$ is the distribution of density, $\kappa(\boldsymbol{x})$ is the adiabatic bulk modulus of the fluid, and $S(t)$ is the source time function. We recall that this formulation is more convenient from a numerical point of view than directly using pressure because that allows for numerical fluid-solid coupling based on a non-iterative scheme (see Everstine [1981] and Chaljub & Valette [2004] in the context of spectral-element techniques). Let us note here that the approach would apply equally well to elastic or viscoelastic media.

In the spectral-element formulation, a weak form of equation (6.1) is obtained by dotting the wave equation (3.8) with a scalar test function $\boldsymbol{x} \mapsto w(\boldsymbol{x})$ and integrating by parts over the model volume:

$$\int_{\Omega_f} w \frac{1}{\kappa} \ddot{\chi} \, \mathrm{d}^2\boldsymbol{x} \;=\; -\int_{\Omega_f} \frac{1}{\rho} \boldsymbol{\nabla} w \cdot \boldsymbol{\nabla}\chi \, \mathrm{d}^2\boldsymbol{x} + \int_{\Gamma} \frac{1}{\rho} w \boldsymbol{n} \cdot \dot{\boldsymbol{u}} \, \mathrm{d}\Gamma + \frac{1}{\kappa(\boldsymbol{x}_s(t))} w(\boldsymbol{x}_s(t)) S(t) \,, \tag{6.2}$$

where Γ refers to the boundaries with normal $\boldsymbol{n}(\boldsymbol{x})$, and $\boldsymbol{u}(\boldsymbol{x}, t)$ refers to the displacement field. This equation must hold for any test function. The model Ω_f is subdivided into a number of non-

overlapping quadrangular elements Ω_e , $e = 1, \ldots, n_e$, such that $\Omega_f = \bigcup_{e=1}^{n_e} \Omega_e$. The integrals in the weak form (6.2) are then split into integrals over the elements, in turn expressed as integrals over 2-D and 1-D reference elements $\Lambda = [-1, 1] \times [-1, 1]$ and $[-1, 1]$ thanks to an invertible mapping between global coordinates (x, z) and reference local coordinates (ξ, η). In the classical spectral-element method, integrals along ξ and η are computed based upon Gauss-Lobatto-Legendre (GLL) quadrature. The integral of a function is expressed as a weighted sum of the values of the function at N specified collocation points called GLL points (containing -1 and 1). The N GLL points along ξ will be noted ξ_i, and those along η will be noted η_i, the basis functions being $\xi \mapsto \ell_i(\xi)$ or $\eta \mapsto \ell_i(\eta)$. Any function $f : (\xi, \eta) \mapsto f(\xi, \eta)$ on Λ can be decomposed based on its values at the GLL points,

$$f(\xi, \eta) \approx \sum_{i,j=0}^{N} f(\xi_i, \eta_j)\ell_i(\xi)\ell_j(\eta)\,. \tag{6.3}$$

In the case of a moving source the application point of the source changes over time, which in practice results in the following procedure: at each time step the element now carrying the source is located and its coordinates (ξ_s, η_s) in the reference element are computed. The contribution of the source at each GLL point (ξ_i, η_j) with $i, j \in [\![0, N]\!]$ is then computed based on (6.3) and is added to the local second time derivative of the potential $\ddot{\chi}(\xi_i, \eta_j)$.

6.1.3 Moving source in a perfect waveguide, validation of the implementation

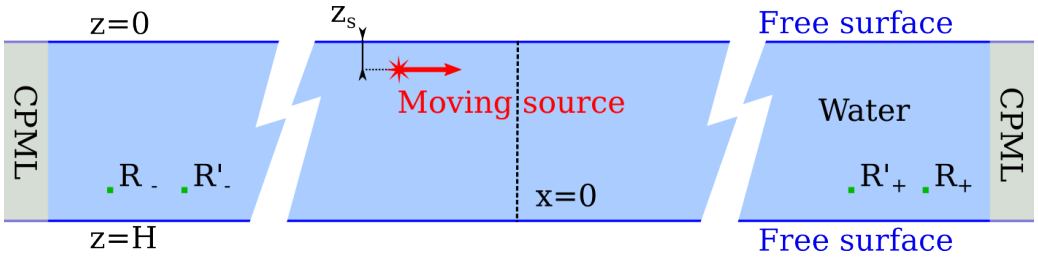

Figure 6.1 – The perfect waveguide setting. The field is recorded at the receiver position represented by green squares. The figure is not at scale.

In order to validate our implementation let us study the case of a moving source in a perfect fluid waveguide described in Figure (6.1). This problem has a simple analytical solution that we will first recall. Let us thus consider a homogeneous fluid layer of thickness H and sound velocity c containing a source at depth z_s emitting a pressure signal $S(t)$ while moving horizontally with speed $V = Mc$. The factor M is the Mach number of the source. The pressure field $P(\mathbf{x}, t) = P(x, z, t)$ verifies the following inhomogeneous wave equation:

$$\nabla^2 P(\mathbf{x}, t) - \frac{1}{c^2}\partial_t^2 P(\mathbf{x}, t) = S(t)\delta(x - Vt)\delta(z - z_s)\,. \tag{6.4}$$

In the Fourier domain this equation reads

$$\nabla^2 P(\mathbf{x}, \omega) + \frac{\omega^2}{c^2} P(\mathbf{x}, \omega) = \frac{\delta(z - z_s)}{2\pi V} S(\frac{x}{V}) e^{\mathbf{i}\omega \frac{x}{V}}\,. \tag{6.5}$$

Let us now suppose that the source has harmonic time dependence with pulsation ω_0, so that

$$S(t) = S_0 \cos(\omega_0 t) = \frac{S_0}{2}\left(\exp(-\mathbf{i}\omega_0 t) + \exp(\mathbf{i}\omega_0 t)\right). \tag{6.6}$$

Let us note here that only the contribution $\frac{S_0}{2}\exp(-\mathbf{i}\omega_0 t)$ eventually leads to physical results, and thus the details of the calculation will only be given for this source term. From now on the pressure

field created by this term will therefore be assimilated to the total pressure field and denoted P. One then gets the (inhomogeneous) equation

$$\nabla^2 P(\mathbf{x},\omega) + \frac{\omega^2}{c^2} P(\mathbf{x},\omega) = \frac{\delta(z)}{4\pi V} S_0 \exp\left(\mathbf{i}\left[\omega - \omega_0\right]\frac{x}{V}\right) . \tag{6.7}$$

Let us first consider the homogeneous equation. It may be written as:

$$\frac{\partial^2 P_0}{\partial x^2}(\mathbf{x},\omega) + \frac{\partial^2 P_0}{\partial z^2}(\mathbf{x},\omega) = \frac{\omega^2}{c^2} P_0(\mathbf{x},\omega) . \tag{6.8}$$

Separating the variables as $P_0(\boldsymbol{x},\omega) = X(x,\omega)Z(z,\omega)$ yields the two independent equations

$$\left\{ \begin{array}{rcl} \frac{\partial^2 Z}{\partial z^2} + k_d^2 Z & = & 0 \\ \frac{\partial^2 X}{\partial x^2} + \left[\left(\frac{\omega}{c}\right)^2 - k_d^2\right] X & = & 0 \end{array} \right. . \tag{6.9}$$

From the first equation, taking into account the pressure release conditions at $z = 0$ and $z = H$ one obtains $Z(z,\omega) = A(\omega)\sin(k_d z)$ with

$$k_d = \pm\frac{m\pi}{H} \quad m = 1, 2, 3, \text{ etc.} \tag{6.10}$$

This equation is important because it shows that only a discrete number of modes can propagate in the model considered. In the following we will note $k_{dm} = k_d$. For the second equation we set $k_{0m}^2 = \left(\frac{\omega}{c}\right)^2 - k_{dm}^2$, and considering only the waves traveling towards the positive x we get the solutions

$$X(x,\omega) = B(\omega)\exp(-\boldsymbol{i}k_{0m}x) . \tag{6.11}$$

The choice of considering only the waves traveling in the positive x-direction will be justified afterwards. Combining the different parts we get the solution of the homogeneous equation:

$$P_0(\mathbf{x},\omega) = C(\omega)\sin(k_d z)\exp(-\boldsymbol{i}k_{0m}x) . \tag{6.12}$$

This is the general form of any mode able to propagate in the waveguide. Each mode has a characteristic phase velocity $c_{pm} = \frac{\omega}{k_{0m}}$ that can be written

$$c_{pm}(\omega) = \frac{c}{\sqrt{1 - \left(\frac{m\pi c}{H\omega}\right)^2}} , \tag{6.13}$$

and a group velocity $c_{gm} = \frac{d\omega}{dk_{0m}} = \left[\frac{dk_{0m}}{d\omega}\right]^{-1}$ that in the case considered may be expressed

$$c_{gm} = \frac{c}{c_{pm}} . \tag{6.14}$$

It is important to emphasize that no other possible combination of velocities and frequencies than those allowed by equations (6.13) and (6.14) is possible in the waveguide considered, regardless of the source creating the vibrations. To find the relations between the source velocity, its frequency and the modes that are generated, one then has to look for particular solutions to equation (6.7). Supposing that

$$P(x,z,\omega) = g(z)\exp\left(\mathbf{i}\left[\omega - \omega_0\right]\frac{x}{V}\right) , \tag{6.15}$$

one obtains

$$\partial_z^2 g(z) + \left[\underbrace{\frac{\omega^2}{c^2} - \frac{(\omega-\omega_0)^2}{V^2}}_{k^{\star 2}}\right] g(z) = \frac{\delta(z-z_s)}{4\pi V} S_0 \tag{6.16}$$

which is a classical inhomogeneous Helmholtz equation. From this equation it can be verified that the derivatives of g must have a discontinuity at $z = z_s$, while g has to be continuous. Namely:

$$\left\{ \begin{array}{rcl} \partial_z g(z_s^+) - \partial_z g(z_s^-) & = & \dfrac{S_0}{4\pi V} \\ g(z_s^+) - g(z_s^-) & = & 0 \end{array} \right. , \tag{6.17}$$

considering the subsonic ($V < c$) case $k^{\star 2} \geq 0$, which entails $\dfrac{\omega_0}{1+M} \leq \omega \leq \dfrac{\omega_0}{1-M}$. The boundary conditions (6.17) yields

$$\left\{ \begin{array}{rcll} g(z) & = & \dfrac{S_0}{4\pi V} \dfrac{\sin\left(k^\star(z_s - H)\right) \sin\left(k^\star z\right)}{k^\star \sin\left(k^\star H\right)} & \text{if } z < z_s \\ g(z) & = & \dfrac{S_0}{4\pi V} \dfrac{\sin\left(k^\star z_s\right) \sin\left(k^\star(z - H)\right)}{k^\star \sin\left(k^\star H\right)} & \text{if } z > z_s \end{array} \right. , \tag{6.18}$$

which gives the pressure field in the Fourier domain

$$\left\{ \begin{array}{rcll} P(\boldsymbol{x}, \omega) & = & \dfrac{S_0}{4\pi V} \dfrac{\sin\left(k^\star(z_s - H)\right) \sin\left(k^\star z\right)}{k^\star \sin\left(k^\star H\right)} \exp \frac{\mathbf{i}(\omega - \omega_0)x}{V} & \text{if } z < z_s \\ P(\boldsymbol{x}, \omega) & = & \dfrac{S_0}{4\pi V} \dfrac{\sin\left(k^\star z_s\right) \sin\left(k^\star(z - H)\right)}{k^\star \sin\left(k^\star H\right)} \exp \frac{\mathbf{i}(\omega - \omega_0)x}{V} & \text{if } z > z_s \end{array} \right. . \tag{6.19}$$

Getting back to the time domain one obtains an equation of this kind

$$P(\boldsymbol{x}, \omega) = \frac{S_0}{4\pi V} \int_{-\infty}^{+\infty} \frac{A(\omega)}{I(\omega)} \exp \mathbf{i} \left[\frac{(\omega - \omega_0)}{V} x - \omega t \right] d\omega \quad \text{if } z > z_s \,, \tag{6.20}$$

which describes a continuous sum of phases traveling at (phase) speed

$$v_p = \frac{\omega V}{\omega - \omega_0} \,. \tag{6.21}$$

Among these phases, the residue theorem will only select the (propagative) modes corresponding to the poles of the integrand $I(\omega)$.

$$\mathrm{Res}\left(P(\boldsymbol{x}, \omega), \omega_i\right) = \lim_{\omega \to \omega_i} P(\boldsymbol{x}, \omega)(\omega - \omega_i) \tag{6.22}$$

The dispersion equation $\sin\left(k^\star H\right) = 0$ has an infinite number of solutions that can be written

$$k_n^{\star \pm} = \frac{\omega_0}{(M^2 - 1)\, c} \left[-1 \mp M \sqrt{1 - (1 - M^2) \left(\frac{\pi n c}{\omega_0 H} \right)^2} \right] . \tag{6.23}$$

Using frequencies instead of circular frequencies by noting $f_0 = \dfrac{\omega_0}{2\pi}$, $f_n^\pm = \dfrac{\omega_n}{2\pi} = \dfrac{c k_n^{\star \pm}}{2\pi}$ and $F_n = \sqrt{1 - M^2} \dfrac{nc}{2H}$, one can obtain

$$f_n^\pm = \frac{F}{(1 - M^2)} \left[1 \pm M \sqrt{1 - \frac{F_n^2}{f_0^2}} \right] . \tag{6.24}$$

The phase velocities of these modes are

$$v_{pn}^\pm = \frac{f_n^\pm V}{f_n^\pm - f_0} \,, \tag{6.25}$$

and their wavenumbers are

$$k_n^{\pm} = \frac{2\pi f_n^{\pm}}{v_{pn}^{\pm}} \,. \tag{6.26}$$

One can obtain their group velocities $c_{gn}^{\pm}$ by use of formula (6.14) using the phase velocity (6.25). Examples of dispersion curves calculated for $c = 1500$ m.s^{-1}, $H = 150$ m and sources moving at three different Mach numbers are shown in Figure 6.2.

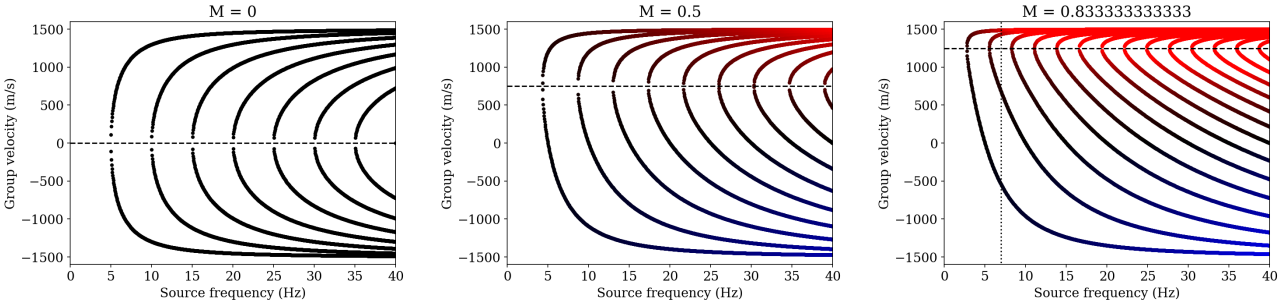

Figure 6.2 – Examples of dispersion curves calculated for $c = 1500$ m.s^{-1}, $H = 150$ m and sources moving at three different Mach number indicated at the top of each sub-figure. The dashed lines indicate the source speed. The color gives the frequency of the modes created with respect to the frequency of the source. Black: $f_n = f_0$, blue: $f_n - f_0 = -20Hz$ and smaller, red: $f_n - f_0 = 40Hz$ and higher. The vertical dotted line in the figure on the right-hand side indicated the source frequency chosen for the benchmark.

When the source is not moving (case shown in the left sub-figure) it creates modes having the same frequency as the source and traveling in both directions symmetrically. When a moving source is considered instead, the symmetry is broken. Typically, high-frequency modes are created in front of the source while low-frequency modes are created behind. In order to validate our implementation let us consider a monochromatic source at 7 Hz moving with Mach number $M = 0.833$. This case is indicated by a dotted line in Figure 6.2. As can be seen, the theory then predicts the excitation of one mode traveling in the opposite direction (negative group velocity) and of slightly lower frequency than the source, while three modes are expected in the direction of the source motion. Details of the modal content expected are summarized in Table 6.1. Let us now compare these theoretical results

n	f_n^+ in Hz	f_n^- in Hz	c_{gn}^+ in m.s^{-1}	c_{gn}^- in m.s^{-1}
1	40.449	5.3693	1488.5	-546.68
2	34.622	11.196	1436.1	674.63

Table 6.1 – Details of the modes generated in the case of a monochromatic source at 7 Hz moving with Mach number $M = 0.833$ in a water waveguide of thickness 150 m.

with those from our spectral-element technique for that setting. A fluid layer is set with compressional wave velocity $c = 1500$ m.s^{-1} and density $\rho = 1000$ kg.m^{-3}. As previously, we set $z = 0$ m at the fluid surface. The source moves horizontally at depth $z_s = -53.5$ m, with speed $V = Mc = 1250$ m.s^{-1}corresponding to a Mach number $M = 0.833$. It has a source time function defined by

$$s(t) = \begin{cases} \frac{A}{2}\left(1 - \cos\left(\Delta\pi t\right)\sin\left(2\pi f_0 t\right)\right) & \text{if } 0 < t < \frac{2}{\Delta} \\ 0 & \text{otherwise} \end{cases} \,, \tag{6.27}$$

where A is the maximum amplitude of the source, f_0 is the dominant frequency of the source signal, and Δ is its bandwidth. We set the dominant frequency at $f_0 = 7$ Hz. In order to generate almost monochromatic signals a small bandwidth $\Delta = 0.2$ Hz is chosen. The wavefield is computed up to a range of 17 km in both directions, the energy coming out of this box being absorbed by PMLs. The mesh is composed of $3200 \times 20 = 64,000$ spectral elements whose polynomial degree is $N = 4$.

The total number of unique GLL in the mesh is $(3200N + 1) \times (20N + 1) = 1,036,881$. This mesh can resolve frequencies up to approximately 60 Hz. We select a time step $\Delta t = 0.4$ ms and simulate a total of 262,144 time steps, i.e. $\sim$ 105 s. The pressure time series and spectrograms recorded at position $x, z = (-15500$ m, -135 m), which is in front of the source, and at position $x, z = (15500$ m, -135 m) which is behind the source, are shown in Figure 6.3 and are compared with the expected arrival times and frequencies of the modes. These two receivers are labeled R_+ and R_- respectively in Figure 6.1.

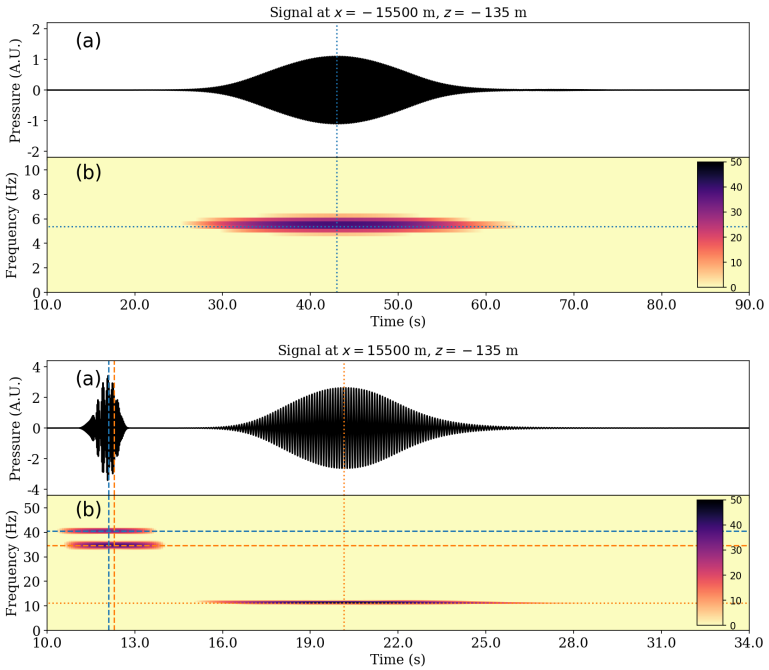

Figure 6.3 – Comparison of the theoretical frequencies and arrival times of the maximum amplitude of the modes (horizontal and vertical lines) with the signals simulated numerical based upon the spectral-element method. The dotted lines refer to the "−" modes (see equation (6.24)) while the dashed lines refer to the "+" modes. The blue lines are for first mode ($n = 1$) and the orange lines are for mode number $n = 2$. For both sub-figures: (a) Pressure seismogram (arbitrary pressure unit). Although arbitrary, the amplitude of the synthetic signals can be compared because the arbitrary scaling is the same in the linear wave equation. (b) Power Spectral Density (in dB) as a function of time and frequency.

The receiver position has been chosen so that all the modes predicted can be observed. The frequency of the mode simulated is in excellent agreement with the theoretical one. To estimate the theoretical arrival times for each mode, two additional receivers were located at horizontal distance 5000 m from the receiver mentioned above. They are labeled R'_+ and R'_- in Figure 6.1. At these positions each mode has been band-pass filtered and the arrival time of its maximum amplitude was used at a reference to predict its arrival time 5000 m further away, based on the group velocities calculated (see Table 6.1). The behavior of the modes in the time domain also appears to be in agreement with our calculations.

In order to check the validity of our implementation for a wider frequency range, we perform the same simulation using a broadband source instead of an almost monochromatic source. The dominant frequency is still $f_0 = 7$ Hz but a bandwidth $\Delta = 8.0$ Hz is now chosen. The pressure time series and spectrograms recorded at the receivers R_+ and R_-, which are respectively in front and behind the source, are shown in Figure 6.4 and are compared with the expected arrival times and frequencies of the modes.

Due to the still limited bandwidth, not all the modes are generated; however those that are generated fit the theoretical dispersion curves in the time-frequency plane very well. Note the presence of modes "traveling" at zero speed and making the time signal infinitely long. A very good match

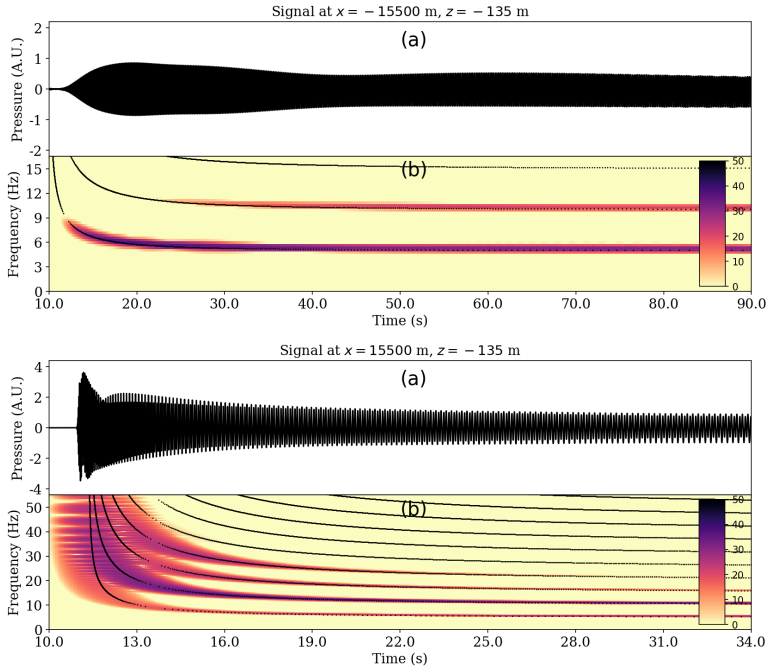

Figure 6.4 – Comparison of the theoretical frequencies and arrival times of the maximum amplitude of the modes (black dots) with the simulated signals. For both sub-figures: (a) Pressure seismogram (arbitrary pressure unit). Although arbitrary, the amplitude of the synthetic signals can be compared because the arbitrary scaling is the same in the linear wave equation. (b) Power Spectral Density (in dB) as a function of time and frequency.

is found between the spectral-element results and the analytical solution, both in terms of frequency and of group speed, thus validating our technique for this benchmark case.

6.1.4 Estimating the sound speed of a shallow-water marine sediment with Doppler spectroscopy. Influence of the shear wave velocity in the seabed

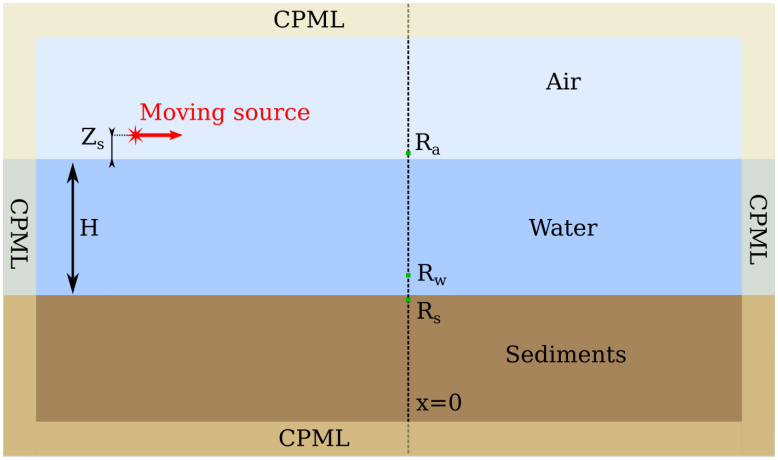

Figure 6.5 – Setting of the study. The field is recorded at the receiver positions indicated by green squares. The figure is not at scale.

Let us apply the technique presented above to a setting similar to the one studied by Buckingham et al. [2002a,b]. The model is composed of three layers: a sedimentary layer, a water layer and an air layer. It is shown in Figure 6.5. The water layer is $H = 20$ m thick and has density $\rho_w = 1000$

kg.m^{-3} and compressional wave speed $c_w = 1500$ m.s^{-1}. The air has density $\rho_a = 1.225$ kg.m^{-3} and compressional wave speed $c_a = 320$ m.s^{-1}. The sediment has density $\rho_s = 2000$ kg.m^{-3} and compressional wave speed $c_s = 1685$ m.s^{-1}. An acoustic source moves in the air $Z_s = 8$ m above the sea surface at a speed of $V = 60$ m.s^{-1}, which corresponds to a Mach number of $M = \frac{V}{c_a} \sim 0.188$. As suggested by Buckingham et al. [2002b] the pressure signal emitted is composed of a fundamental sinusoidal tone at 83.3 Hz with four harmonics at multiples of the fundamental tone and of decreasing amplitude. In order to ensure zero initial conditions the time series is multiplied by a Tukey window. The resulting source signal, shown in Figure 6.6 is supposed to model the noise produced by a light propeller-driven aircraft.

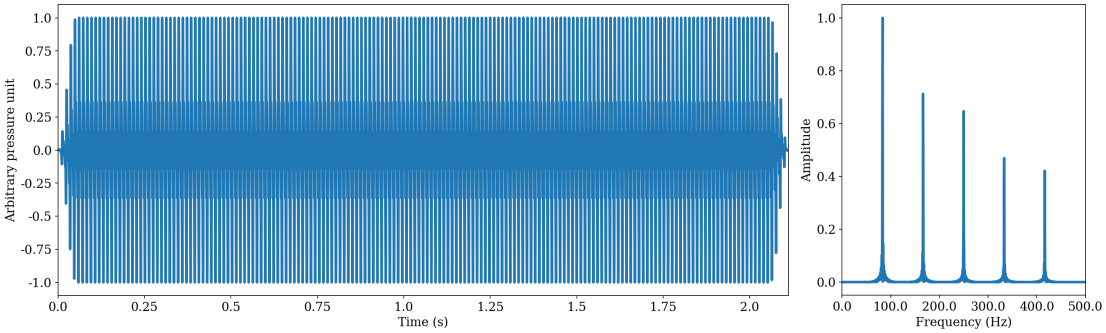

Figure 6.6 – Source used for the simulation. **Left**: Pressure with respect to time. **Right**: Power Spectral Density of the source signal.

The aircraft starts at position $x_0 = -60$ m and emits for approximately 2.11 s, during which it moves to $x = 66.6$ m, flying over the three receivers R_s, R_w and R_a shown in Figure 6.5, which are located at position $x = 0$ m at depths $z_a = 2$ m, $z_w = -19.5$ m and $z_s = -21.0$ m respectively. The spectral-element mesh is composed of ~ 2.0 million elements whose polynomial degree is $N = 4$. The total number of unique GLL in the mesh is approximately 32.6 millions. 99.99% of the acoustic elements have at least 8 grid points per pressure wavelength in the fluid at the minimum wavelength expected due to the Doppler shift. We select a time step $\Delta t = 3.25 \times 10^{-6}$ s based on the stability and accuracy conditions of the explicit, conditionally-stable time scheme, and simulate a total of 0.65 million time steps, i.e. ∼2.11 s. The energy coming out of the domain under study, shown in Figure 6.5, is absorbed by PML absorbing layers. Frequencies up to ∼800 Hz are resolved. The simulation performed took approximately one hour on 480 processor cores of a parallel supercomputer equipped with Intel ® Xeon® E5-2690 v3 processors. Figure 6.7 shows the seismograms simulated in the air, water and sediments, and a comparison with the expected Doppler shifts.

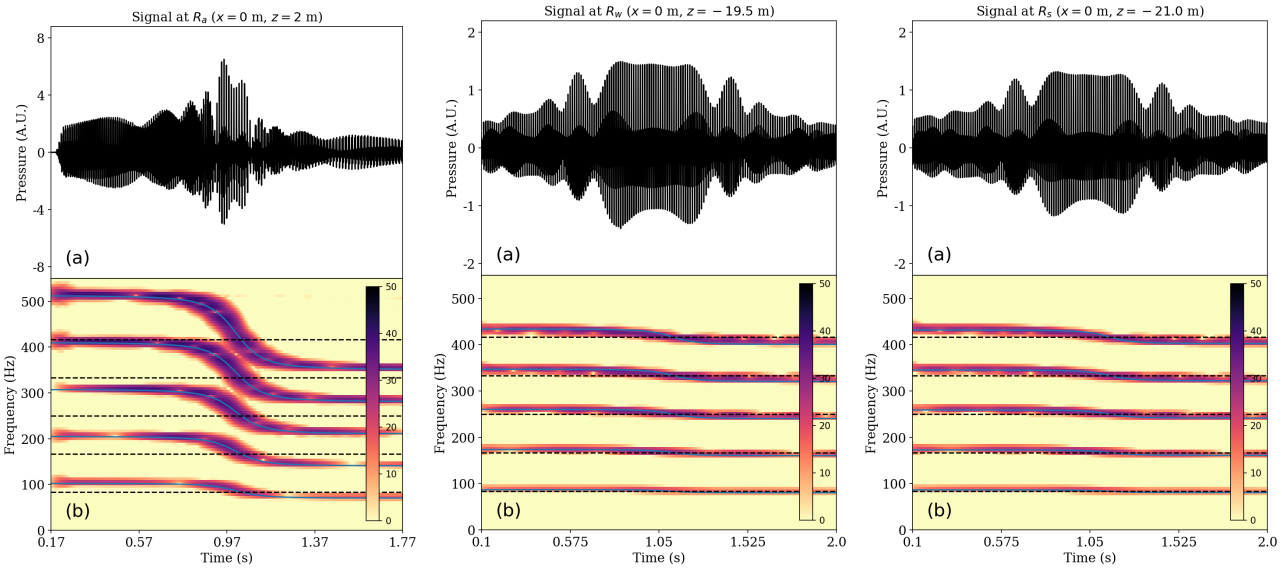

Figure 6.7 – Signal recorded at the three receivers R_a (left), R_w (middle) and R_s (right) shown in Figure 6.5. For each sub-figure: (a) Pressure seismogram (arbitrary pressure unit). Although arbitrary, the amplitude of the synthetic signals can be compared because the arbitrary scaling is the same in the linear wave equation. (b) Power Spectral Density (in dB) as a function of time and frequency. The black dashed lines refer to the frequencies of the harmonics emitted by the source. The blue curves represent the theoretical Doppler shifts expected, which are given by equation (6.28).

In the case studied, (described in Figure 6.5) geometrical ray theory predicts that a given harmonic of frequency f emitted by the source is received at a given receiver with the time dependent Doppler shifted frequency

$$f_D(t) = \frac{f}{1 - M_\star^2} \left[1 - \frac{M_\star V t}{\sqrt{(Vt)^2 + (1 - M_\star^2) Z_s^2}} \right] , \tag{6.28}$$

where $c_\star$ is the velocity of the medium containing the receiver considered, $M_\star = \frac{V}{c_\star}$ and $t = 0$ when the source is at $x = 0$ (see Buckingham et al. [2002b]). This expression was used as a reference (blue curves) in Figure 6.7. Although the relationship (6.28) is based on geometrical ray theory, we see that it predicts quite well the spectrograms simulated with our full-wave method. It is worth noting that Buckingham & Giddens [2006] derived an exact full-wave solution for this problem in order to improve Doppler spectroscopy inversion.

We have then tested the sensitivity of these results to the addition of a shear wave speed of 400 m.s^{-1} in the seabed. However this had no visible effect on the spectrograms obtained, which will therefore not be shown. This suggests that this information can not be recovered directly with this method but only indirectly from the measured P-wave velocity (as suggested by Buckingham [2010]). It can be explained by the fact that there is only a weak $P \to S$ conversion generated at the interface in this case.

We thus chose to resort to acoustic media and performed sensitivity analyses to assess the influence of a strong velocity gradient in the sediment. At the sea floor depth, the sound speed is still 1685 m.s^{-1} but it now increases linearly with depth by 50 m.s^{-1} every meter. The spectrograms obtained are shown in Figure 6.8.

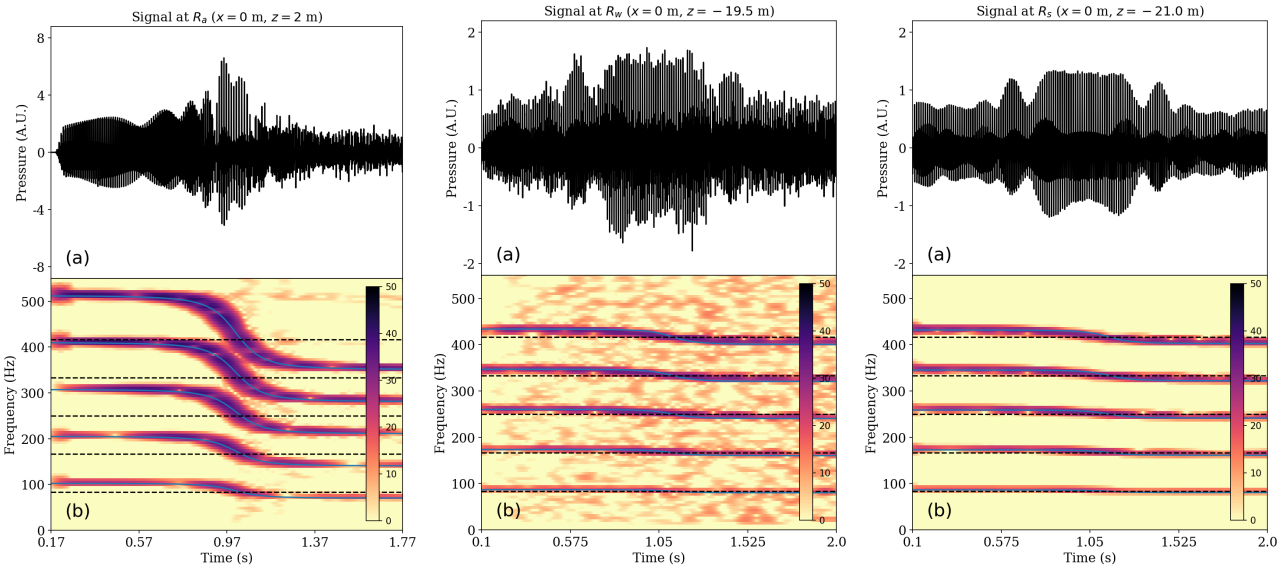

Figure 6.8 – Same than Figure 6.7 in the case of a significant gradient in the seabed.

In this case as well, the effect on the spectrograms is rather small, the Doppler shifted harmonics are the same or almost the same, which is expected from the relation (6.28). Some differences can nonetheless be noted, especially for the signal recorded in the water, which appears noisier.

6.1.5 Conclusions and perspectives

We have presented and validated a numerical method based on time-domain spectral elements for the solution of full-wave propagation problems with moving acoustic sources. Our calculations have included viscoelastic ocean bottoms and we have used PML absorbing layers to efficiently absorb the outgoing wavefield. The method has been applied to the calculation of the full wavefield produced by a light aircraft flying above the ocean. This configuration, presented by Buckingham et al. [2002b], allows for the estimation of the compressional wave velocity in the sediments. In addition, the effect of the introduction of a shear wave speed or of a strong sound speed gradient in the sediment has been investigated. The results obtained prove not to be very sensitive to these modifications. Nevertheless, the addition of a sound speed gradient in the sediment is seen to slightly affect the signal recorded in the water, which appears noisier in this case.

Regarding the assessment of marine sediment velocity, and aside from the head-wave method presented by Bevans & Buckingham [2017], it should be noted that it would probably be more efficient to use a horizontal array of about 20 meters immersed in water (64 hydrophones would be sufficient for the frequencies considered) and to use it to perform a F-K transform. Indeed, the dispersion curves obtained would not depend on the excitation source, which would then allow for iterative fitting with theoretical curves using a Bayesian algorithm for example. Even better, in order to avoid setting receivers in the water or in the sediment it would be interesting to study the field recorded at the level of the flying vehicle or a few tens of meters behind it in order to avoid direct arrivals as much as possible. Like aircrafts towing advertising banners over beaches, one could imagine a light plane or a helicopter towing a very sensitive microphone that would be used to map marine sediments in shallow water. The study of the field recorded by such an instrument should make it possible to perform a feasibility study of this kind of experiments. Of course, as the signal will have to cross the sea surface twice, extremely low signal-to-noise ratios are to be expected. Hopefully, the source signal would be known with precision and could be subtracted. Moreover, as shown by Bevans & Buckingham [2017] a light helicopter can produce low-frequency sound (first main rotor harmonic at 13 Hz in the case that they considered). This property can potentially allow one to take advantage of the abnormal

transparency of the water surface (Godin [2006, 2008a,b]) in the case of a low-altitude flight above shallow water. All the numerical tools are ready for a study of the feasibility of such a method in future work.

6.2 Generation of T-waves and of atmospheric infrasounds by diffraction from a cargo ship

In this section we propose a new mechanism of T-wave generation together with an alternative explanation to the waves observed by Evers et al. [2014] both at sea and in the atmosphere following a 2004 earthquake in the Macquarie Ridge.

To date in the literature there are five main documented modes of T-wave generation:

- Generation of T-waves in the form of Airy waves by a source situated close to the seabed.
- Downslope conversion by multiple reflections over a sloping sea bottom
- Generation by scattering or reflection on a rough seabed
- Generation by scattering or reflection on a rough sea surface
- Generation by scattering or reflection on the ice cap at the highest latitudes.

We propose a new possible generation mechanism of T-waves from the diffraction of acoustic waves by a cargo ship. The efficiency of this process is to be evaluated in comparison with downslope conversion. In the presence of such a diffraction point, acoustic waves can also be generated in the atmosphere. In order to also investigate this phenomenon, the atmosphere will be included in the following simulations. It should be noted that the study of infrasound in the atmosphere, caused by meteorites or large earthquakes for instance, is a large field of study in itself and is the subject of numerous publications (see e.g. Hedlin et al. [2010]; Astafyeva et al. [2011]; Brown et al. [2013]; Brissaud et al. [2016]; Gainville et al. [2017] and reference therein).

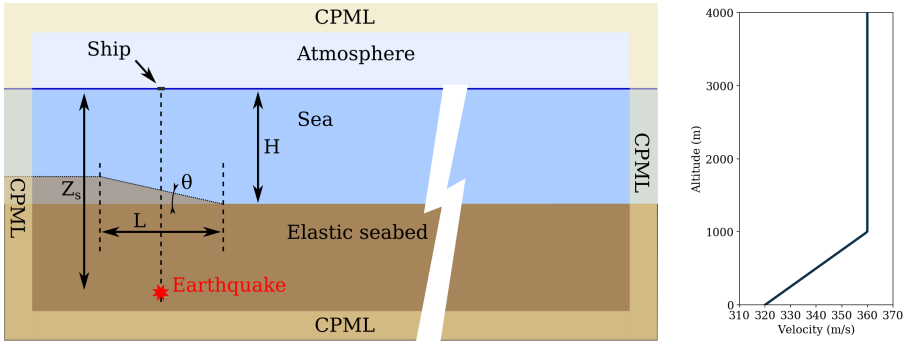

Figure 6.9 – **Left**: this picture summarizes the simulations performed in this section. The ocean depth is $H = 4000$ m. The seafloor can also be dipping above the earthquake by an angle of $\theta = 12°$ over a length $L = 6$ km. **Right**: Sound speed profile in the atmosphere used.

The number of container ships and other giant tankers has soared since the 1990s (Tournadre [2014]). There are now tens of thousands of them sailing the seas of the globe. The largest are up to 400 m long. At the time of the annual review 2017 on maritime transport of the United Nations Conference on Trade and Development UNCTAD [2017] (p. 32) the commercial world fleet counted 93,161 vessels with an average tonnage of 24,062 dead-weigth tons. This corresponds to ships measuring between 120 and 150 m, which is the size of a wavelength in water at 10 Hz and can therefore potentially diffract waves of comparable frequency and generate guided waves in the water and/or in

the atmosphere. For that reason, in the following we will study whether the presence of a boat could explain the waves observed by Evers et al. [2014] both at sea and in the atmosphere following a 2004 earthquake on the Macquarie Ridge (magnitude $M_w = 8.1$, one of the largest strike-slip events ever); Diffraction by a cargo ship could be an alternative explanation to the evanescent coupling proposed by the authors.

The configuration is presented in Figure 6.9. The model is composed of a semi-infinite homogeneous viscoelastic seabed ($\rho = 2200$ kg.m^{-3}, $V_p = 3500$ m.s^{-1}, $V_s = 2059$ m.s^{-1} and $\alpha_p = \alpha_s = 0.23$ dB.λ^{-1} at 3.0 Hz) covered with a homogeneous water layer of height $H = 4000$ m, density $\rho_w = 1000$ kg.m^{-3} and sound speed $c = 1500$ m.s^{-1}. The atmosphere is modeled as a fluid medium of density $\rho_a = 1.225$ kg.m^{-3}and of sound speed varying with altitude as described in Figure 6.9, right. For this study we will only consider altitudes below 4000 m, and thus we will neglect density variations in the atmosphere, which are only a second-order effect in such a case.A rectangular steel cargo boat ($\rho = 8000$ kg.m^{-3}, $V_p = 5800$ m.s^{-1} and $V_s = 3400$ m.s^{-1}) is placed on the sea surface. It has a length of 200 m, a height of 100 m and a draught of 30 m[1].

An earthquake is generated in the seabed at depth $Z_s = 8$ km at the vertical of the ship position. It is a vertical force with a Ricker source time function of dominant frequency $f_0 = 3$ Hz. Figure 6.10 shows some snapshots of the wavefield generated.

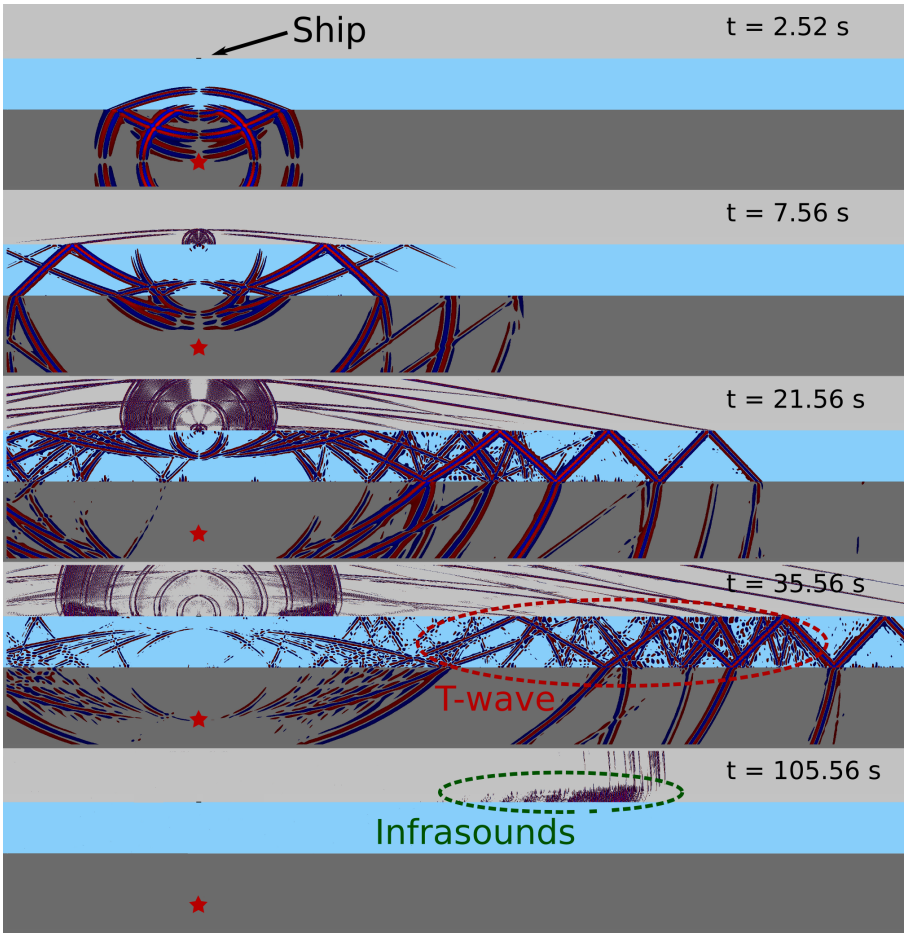

Figure 6.10 – Snapshots of the wavefield (displacement in the horizontal direction) for an earthquake with dominant frequency 3.0 Hz. The water depth is 4000 m, and the source is at the vertical of the ship, at a depth of 8 km. The maximum range shown in this figure is ∼52 km but in the simulations the field is calculated up to 100 km.

[1]Let us note that of course such a synthetic rectangular cargo would sink quickly! We designed it like that to drastically simplify mesh creation.

The presence of this diffraction point allows for the generation of a T-wave in the water layer. In addition, strong infrasounds are also observed, channeled in the first kilometer of the atmosphere.

Let us first study the waves generated in the water. The signals recorded in the water at 2000 m depth and 90 km range are presented in Figure 6.11 and are compared with the signals generated by the same source, without the cargo ship but with the slope of 12° described in Figure 6.9 and that generates a downslope-converted T-wave of comparable amplitude.

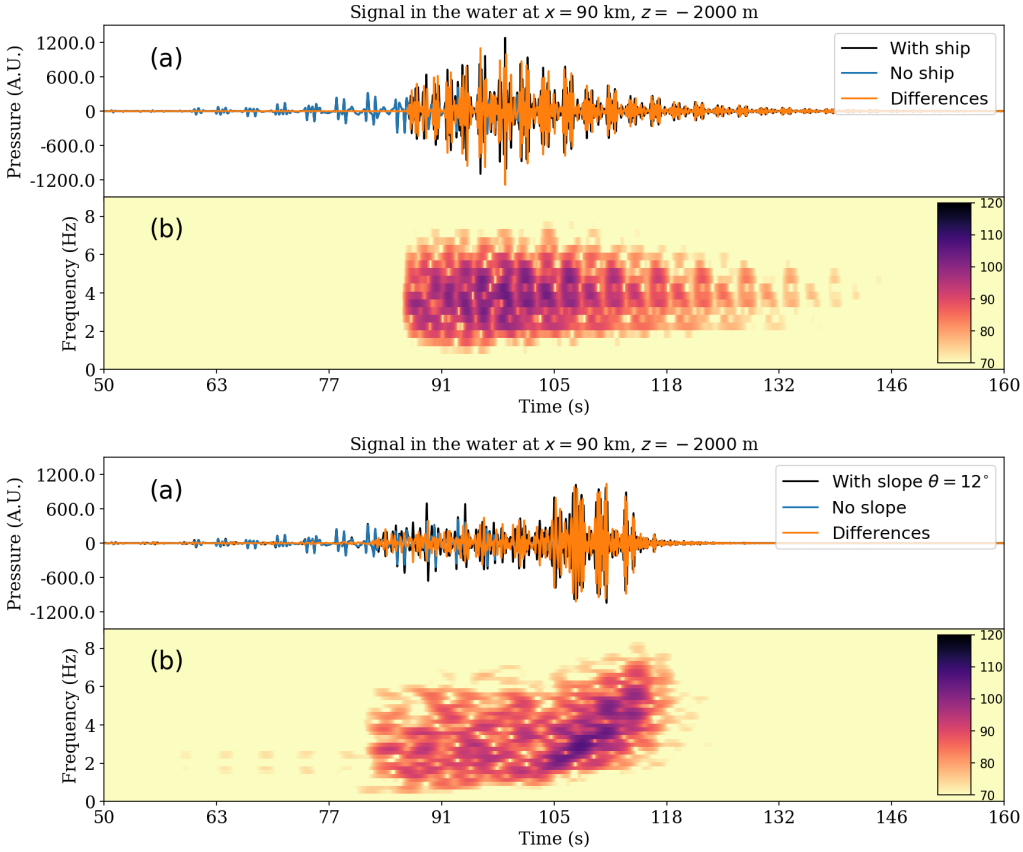

Figure 6.11 – Comparison in the time-frequency domain of a T-phase generated by diffraction on a ship (top) and a T-phase generated by downslope conversion (bottom). See Figure 6.9 for the settings of the simulations. Each signal has been recorded at range 90 km and depth -2000 m. For all sub-figures: (a) Pressure (arbitrary pressure unit). The orange curve is the difference between the black and the blue curves. (b) Power Spectral Density (in dB) of the orange curve as a function of time and frequency.

The T-phase is obtained by subtracting the signal obtained with a flat bottom and without the boat from the signals generated with the slope or the cargo ship. The onset of the T-phase generated by diffraction is globally more impulsive than the onset of the T-phase generated by downslope conversion. It exhibits oscillations in time created by the scattering of the successive reflections between the sea surface and the seabed. Evidence of weak normal dispersion is observed in the time-frequency plane. Moreover, two frequencies seem to be favored, around 2 and 3.4 Hz respectively. The reason for the existence of these privileged frequency bands is unknown at this point. On the contrary, in the case of the T-wave generated by downslope conversion we observe a significant inverse dispersion, which we already observed in Chapter 5 for a similar case (Figure 5.18 on page 143). We proposed an explanation for this phenomenon based on modal analysis. The amplitudes are comparable. We can thus conclude that in the configuration studied the waves created by diffraction by a cargo ship correspond in terms of amplitude to a T-wave generated by downslope conversion on a 6-km long slope of 12°. Although our modeling of a boat is rudimentary, this order of magnitude is interesting. Indeed, the presence of

a slope of this size on such a hard seabed and just above the hypocenter is not negligible in terms of T-waves (see Chapter 4). These results suggest that diffraction by ships can create strong T-waves with a structure reminiscent of an explosion. It is worth noting that there are thousands of such big ships travelling in the oceans at a given time. It is thus likely that this phenomenon has already been observed, particularly in ocean areas in which maritime traffic is dense.

Let us now look at the simulated acoustic field in the atmosphere. Figure 6.12 shows broadband Transmission Losses (TLs in dB), as defined in Chapter 5 in the first kilometer of the atmosphere.

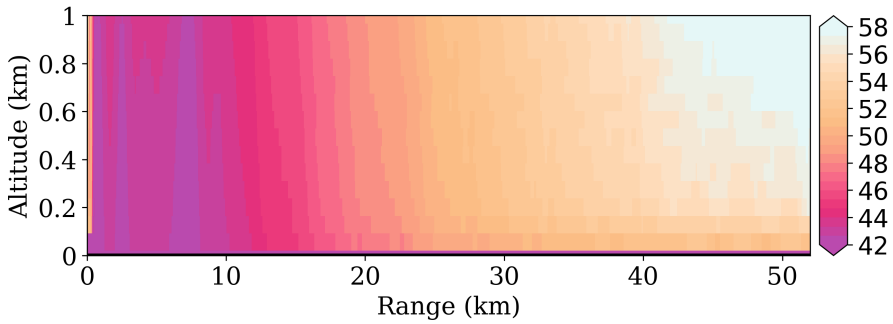

Figure 6.12 – Broadband transmission losses (in dB), as defined in Chapter 5 in the first kilometer of the atmosphere. The range is the horizontal distance to the center of the boat. The presence of the guided wave traveling horizontally in the atmosphere is clearly visible on the right between altitude 0 and 200 m. The transmission losses are set to zero 200 m above the source.

The presence of a guided wave, visible in the snapshots of Figure 6.10 and moving horizontally in the atmosphere is clearly visible. The transmission losses observed between the vicinity of the source (the TLs shown are set to zero 200 m above the source) and the waves guided in the atmosphere are significant (∼50 dB) but do not prevent any transmission, especially in the case of a large earthquake. Figure 6.13, taken from Evers et al. [2014], shows the spectrogram of the infrasounds recorded at the IMS eight-element microbarometer array IS05AU located in Tasmania near Australia (coordinates 42.5°S, 147.7°E altitude 315 m) following a 2004 earthquake on the Macquarie Ridge (M_w = 8.1, coordinates 49.96° S, 161.13° E, see Robinson [2011]) at 1321 km of the observation point.

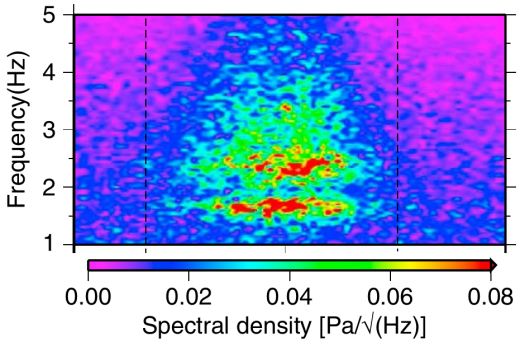

Figure 6.13 – Taken from Evers et al. [2014]. Spectrogram of the signal recorded at infrasound array IS05AU. It has been filtered with a second-order Butterworth band-pass filter with corner frequencies of 1 to 5 Hz. The total duration shown is 30 minutes.

The signal is emergent and exhibits two main favored frequency bands around 1.7 Hz and 2.3 Hz. The onset corresponds to a celerity (horizontal distance divided by traveltime) of 330 m/s, which may imply propagation in the troposhere from the epicenter (Evers et al. [2014]). Two signals simulated in the atmosphere at altitudes 100 m and 1050 m are shown in Figure 6.14 for comparison. It is not necessarily straightforward to compare them with the real signal. Even if propagation distances are

drastically different (50 km against 1300 km) and the atmospheric model is very basic, some qualitative observations can be made.

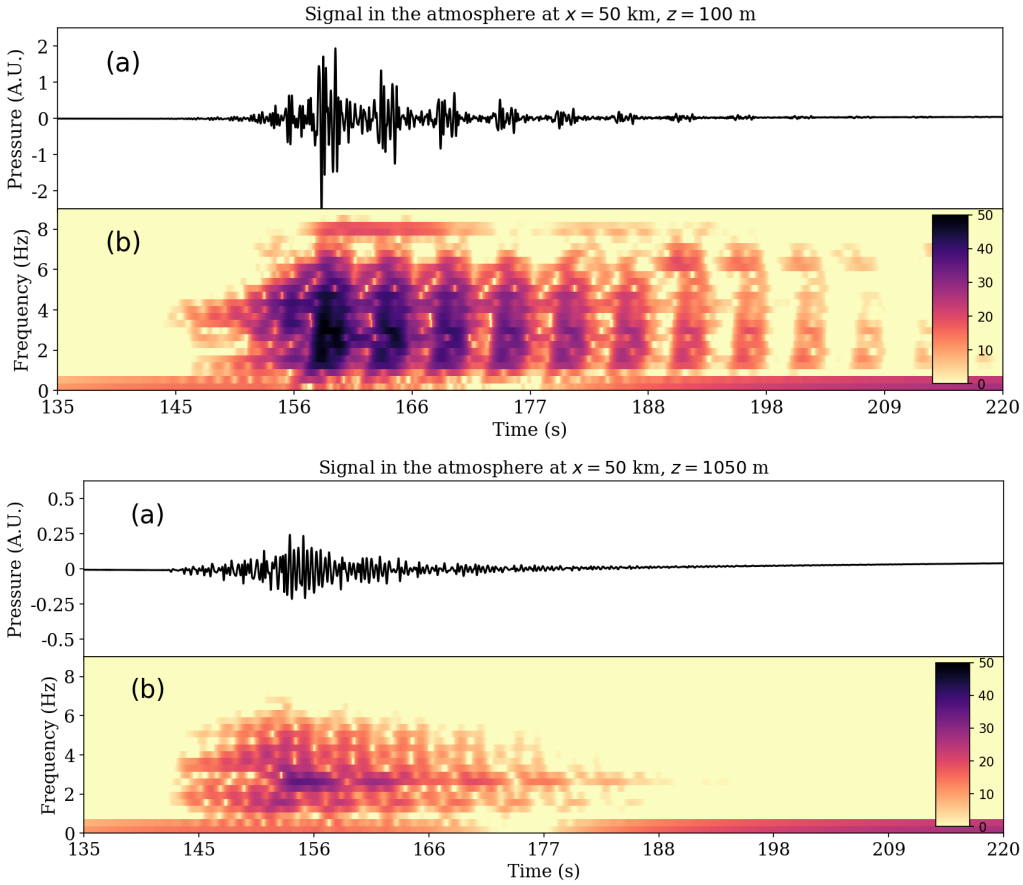

Figure 6.14 – Comparison in the time-frequency domain of the infrasounds generated in the atmosphere by diffraction on a large cargo ship at two different altitudes. See Figure 6.9 for the settings of the simulations. Each signal has been recorded at range 50 km. The top signal has been recorded at altitude 100 m and the bottom one at altitude 1050 m. For all sub-figures: (a) Pressure (arbitrary pressure unit) (b) Power Spectral Density (in dB) as a function of time and frequency.

The signal generated at 100 m altitude exhibits several periodic pulses (every ∼5.3 s) because of the successive reflections between the seafloor and the sea surface, which are diffracted by the boat. We can note that, at first glance, there is no evidence of such fluctuations in the signal shown by Evers et al. [2014] and reproduced in Figure 6.13. It is however important to note that the time scales are very different between Figures 6.13 and 6.14 (total duration of 30 min versus 1 min 25 s). If such fluctuations existed they would therefore be too high frequency to be seen in Figures 6.13. In any case, they must be particularly sensitive to bathymetry, which is quite rough near the real epicenter. At the onset the signal has energy in two frequency bands in particular, which corresponds rather well to the real signal although the favored frequencies observed are different. Compared to the signal generated at 100 m altitude, the signal generated at 1050 m is ten times smaller in amplitude, is of lower frequency, and also exhibits the two favored frequency bands. The successive pulses does not appear to reach this altitude.

6.2.1 Conclusions of this section

We have seen that diffraction by a cargo ship of 200 m length can create quite powerful T-waves with low dispersion. Although our modeling of a boat has been quite basic, our simulations suggest

that this T-wave generation mode must be particularly frequent in areas in which maritime traffic is important. This diffraction phenomenon could also explain some abyssal T-waves (see Chapter 1).

Taking the atmosphere into account in our simulations allowed us to show that diffraction by a cargo ship could also generate guided waves in the atmosphere. This mode of infrasound generation may constitute an alternative explanation to the evanescent coupling proposed by Evers et al. [2014] to explain the waves observed in the atmosphere following an earthquake in 2004 on the Macquarie Ridge. Unfortunately the AIS (Automatic Identification System), which is the automatic tracking system now used for ships, has only been made mandatory by the International Maritime Organization (IMO) since 2004. Furthermore, until 2009, the visibility of a vessel by AIS was conditioned to the presence of a receiver within a radius of about 20 nautical miles. Only ports and some coastal areas were therefore well covered. At high seas, ships remained totally invisible in real time.Nowadays the situation has changed because AIS satellites have been launched, significantly reducing the number of white areas (Eiden & Martinsen [2010]; Cheng [2014]). Any ship equipped with AIS can now easily be located, at any time and any place (Serry & Lévêque [2015]). It should therefore be easy now to get the traffic in a given area at a given time to infer the presence of a boat after an earthquake and confirm if the mechanism of T-wave generation that we propose can be observed in real situations.

Achievements and future prospects

On T-waves

The study of literature spanning nearly 90 years and of the data to which we have had access clearly confirms the interest that T-waves can have for the study of volcanic and seismic phenomena in marine environments for example. It also shows their great complexity and variability. Thus, the results obtained so far sometimes seem contradictory and in any case strongly dependent on observation conditions. For example, it is known that there is only a weak correlation between the magnitude of earthquakes and the amplitude of the T-waves that they can generate.

Through a number of numerical simulations, this thesis has allowed us to illustrate and understand some characteristics explaining the complexity of the phenomenon. As expected, the energy and duration of these waves are particularly sensitive to the environment. In particular, the slopes and characteristics of the seabed play a crucial role in both the solid - fluid and fluid - solid conversions. This can mislead localization algorithms in real situations.

Similarly, the depth and position of an earthquake relative to the slope are of great importance, with the existence of privileged areas for the generation of T-waves, which we have mapped. However, as Jamet et al. [2013] had already noted, the sound speed profile in the ocean appears to be only of second-order importance. We have tried to carefully analyze its impact, and in the configurations studied, the presence of a SOFAR channel slightly limits the time dispersion but only introduces a gain in terms of energy transmission of a few thousandths of dB per kilometer, which is comparable to the effect of viscoacoustic attenuation of seawater. At the distances and frequencies considered (frequency less than 20 Hz, distance less than 1000 km) we, therefore, believe that the influence of the SOFAR channel on the phenomenon has been overestimated in the literature, which has sometimes led to misinterpretation. Similarly, our study in the Ionian Sea suggests that T-waves are only slightly sensitive to the radiation pattern of the source. In the context of this study, it seems promising that despite the complexity of the problem we managed to simulate realistic T-waves in a configuration involving two fluid-solid conversions.

Moreover, in the case of the conversion of an acoustic wave on a slope, our simulations predict the generation of a strong Rayleigh wave, whose signal, recorded inland, is very sensitive to the slope and to the characteristics of the environment, but very little sensitive to the modal structure of the incident wave. Although coastal receivers generally have much lower signal-to-noise ratios than hydrophones in water (De Groot-Hedlin & Orcutt [2001b]), and although hard seabeds are probably rare in reality, this phenomenon may have interesting implications. Indeed, this surface wave probably carries a lot of information about the water layer, which could perhaps be recovered through an inverse problem. One

can imagine, for example, determining the appropriate coasts for this type of mechanism and installing seismic stations there. The Rayleigh waves created during the arrival of the T-waves could then be used to obtain information on oceanographic processes, for example. Our study presented in Appendix A suggests that the Pacific atolls, for example, might be adequate, which would undoubtedly deserve further analysis. In general, our simulations indicate that the temporal dispersion of the signals is particularly sensitive to the parameters of the media and could thus possibly constitute an interesting marker to take into account in the framework of an inverse problem.

Finally, we have shown that a medium-sized commercial vessel, as there are tens of thousands nowadays in the oceans of the globe, could create, by diffraction, T-waves of substantial amplitude (of the order of those created by downslope conversion on a slope of 12°) and low dispersion. This T-wave generation mechanism, to our knowledge undocumented, should be particularly frequent in areas in which maritime traffic is significant and could explain some abyssal T-waves that are still poorly understood. Taking the atmosphere into account in these simulations, we realized that diffraction by a commercial ship could also generate guided infrasound in the lower layers of the atmosphere. This mechanism of infrasound creation may constitute an alternative explanation to the evanescent coupling proposed by Evers et al. [2014] to explain the waves observed in Tasmania following an earthquake in 2004 on the Macquarie Ridge.

In this thesis, we have tried to highlight the range of possibilities offered by the type of numerical methods used. Apart from the topics already mentioned in this section, it might be interesting, for example, to look at the location of earthquakes from T-waves using simple models and inversion methods. For this reason, it would seem interesting in future work to couple a finite-element method, like the one we used, with a parabolic method in order to be able to tackle large-scale problems. We could then pave the way for processing a real database of earthquakes located by other methods. It should also be noted that the use of machine-learning algorithms also seems particularly suitable in this case. When the technology allows it, it will also be interesting to work in 3-D, especially in the case of conversion of acoustic waves on a coast.

On geoacoustic Doppler spectroscopy

We have only addressed this subject very briefly and we cannot really mention any real results at this stage. Nevertheless, we presented and validated numerical tools to calculate the acoustic field created by a moving source. The method was applied to a light aircraft flying over the ocean. This configuration, presented by Buckingham et al. [2002a], can be used to estimate the pressure wave speed in the sediments. The effect of a shear wave speed and of a sound speed gradient in the sediment has been discussed. It seems to us that, in this case, the numerical method that we have developed is a promising tool that can allow for dealing with more complex models with bathymetry and/or variations of the media properties.

On High-Performance Computing (HPC) for underwater acoustics

During this thesis we presented and validated a numerical method based on spectral elements in the time domain for fluid-solid axisymmetric problems. The model includes the backscattered field, which cannot be modelled, for example, based on the parabolic approximation. Our calculations took into account viscoelastic ocean bottoms, and we used PML absorbing layers to effectively absorb the outgoing field in the bounded geometric domains. In addition, we presented an efficient procedure for calculating transmission-loss and time-dispersion maps from such methods. This tool has allowed us to extend the notion of transmission losses to non-monochromatic signals as well as to elastic media. At the end of this thesis, it seems to us that this type of full-waveform modelling techniques, by their accuracy and flexibility, can significantly contribute to the field of underwater acoustics.

However, a number of challenges remain in the future to deal with large-scale 3-D cases. As we have experienced (see appendix B) the main drawback of the classical spectral-element method (in 3-D) is the generation of meshes consisting exclusively of hexahedra, which is often difficult in practice, especially in coastal and shallow water areas. Although this problem can be overcome by making the method discontinuous (Bernardi et al. [1994]; Kopriva et al. [2002]; Chaljub et al. [2003]; Legay et al. [2005]; Kopriva [2006]; Wilcox et al. [2010]; Acosta Minolia & Kopriva [2011]), working with tetrahedra (Wingate & Boyd [1996]; Taylor & Wingate [2000]; Komatitsch et al. [2001]; Mercerat et al. [2006]) or by using a discontinuous Galerkin method (Lesaint & Raviart [1974]; Käser & Dumbser [2008]; Wilcox et al. [2010]) this can only be done at the cost of significantly higher computation time, and often greater programming effort in the case of mixed meshes. In this respect, methods combining spectral elements and discontinuous Galerkin approaches in different parts of the model appear promising (see Brissaud et al. [2017]; Terrana et al. [2018]).

An even more promising short-term approach is methods that couple (semi-)analytical or fast approximation-based (i.e., not full wave) codes, such as parabolic solvers, with a full waveform 3-D solver only in regions of the model where this is needed (van Manen et al. [2007]; Tong et al. [2014]; Monteiller et al. [2013, 2015]; Masson & Romanowicz [2017a,b]; Broggini et al. [2017]). In the case of underwater acoustics, parabolic-SEM coupling would avoid the long-range propagation of inaccuracies usually observed near the source in parabolic equation solutions (De Groot-Hedlin [2008]), while taking advantage of the efficiency of this method in terms of computing time for long-range propagation. Furthermore, from a computer science point of view, we believe that the field can greatly benefit from the use of computing on GPU graphics accelerators (see e.g. Komatitsch et al. [2010]; Michéa & Komatitsch [2010]; Komatitsch [2011]; Gokhberg & Fichtner [2016]).

It is also important to note that for this type of approach, data processing can also constitute a challenge in itself in the case of large-scale problems. It is common in this case to have to work with terabytes of results. This problem, known as "big data", is also undergoing very rapid progress, particularly with the evolution of computer hardware (Gropp & Sterling [2015]).

Another aspect of future developments in HPC for underwater acoustics is related to inverse imaging problems. First of all, full waveform inversions, although quite widespread nowadays in oil-industry seismics and in seismology (e.g. Monteiller et al. [2015]) are still very rare in underwater acoustics and are, in practice, limited to the field of oil and gas exploration (see for example Bornstein et al. [2013]; Ratcliffe et al. [2014]; Borisov & Singh [2015]). With current sensor networks, both at sea and onshore, there is an abundance of data and it would eventually be worth conducting large-scale ocean tomography using such methods. Without going that far, it would already be very interesting to build full-waveform sensitivity kernels, for the amplitude or duration of T-waves for example (for sensitivity kernels see for example Tromp et al. [2005, 2008], or Skarsoulis & Cornuelle [2004]; Iturbe et al. [2009]; Aulanier et al. [2013]; Roux et al. [2013]; Dzieciuch & Cornuelle [2017] in the field of underwater acoustics).

Concerning inversions and the evolution of computing capacities it is likely that Bayesian methods will become more and more popular (Bottero et al. [2016b]; Dettmer et al. [2018]; Luu et al. [2018]). Indeed, these algorithms allow non-linear problems to be addressed, while quantifying the uncertainties associated with the final model, at the cost of a much higher number of calculations than the case of linearized approaches based on the gradient of a cost function for example. In combination with full-waveform methods, excellent results are to be expected, especially for poorly conditioned problems or for those that remain reasonable in terms of the number of degrees of freedom (typically less than a few hundred with current machines and technologies). In addition, Bayesian methods can adapt to the data sets and to the complexity of the problems studied in order to propose an optimum number of unknowns. Within the framework of our work, for example, the study of marine sediments by Doppler spectroscopy seems to be a case particularly suited to the use of these algorithms in underwater acoustics.

Of course, the current impressive and growth in the field of machine-learning methods, which manage to deal with increasingly complex problems, will probably create revolutions or at least very significant advances in the field of underwater acoustics as well. This area is just beginning to benefit from the phenomenal progress made in recent years (see for example Niu et al. [2017]) and further progress is to be expected. As an example, it seems certain that this type of algorithm can greatly improve the location of earthquakes based on T-waves.

Résultats et perspectives pour le futur

Ceci est une version en français de la conclusion précédente en anglais.

Sur le sujet des ondes T

L'étude de près de 90 ans de littérature ainsi que les données auxquelles nous avons eu accès montrent clairement l'intérêt que peuvent avoir les ondes T pour l'étude des phénomènes volcaniques et sismiques en milieu marin par exemple. Elle montrent également leur très grande complexité et variabilité. Ainsi les résultats obtenus jusqu'à maintenant par la communauté scientifique semblent parfois contradictoires, et en tout cas fortement dépendants des conditions d'observation. Il est par exemple connu qu'il n'y a qu'une faible corrélation entre la magnitude des séismes et l'amplitude des ondes T qu'ils peuvent générer.

Grâce à de nombreuses modélisations cette thèse nous a permis d'illustrer et de comprendre certaines caractéristiques expliquant la complexité du phénomène. Comme on pouvait s'y attendre, l'énergie et la durée de ces ondes est particulièrement sensible à l'environnement. Nous avons vu en particulier que les pentes et les caractéristiques du fond marin jouaient un rôle capital autant sur la conversion solide-fluide que fluide-solide. Ces particularités peuvent du reste tromper les algorithmes de localisation en situation réelle. De même, la profondeur et la position du tremblement de terre vis-à-vis de la pente s'avère être de grande importance, avec l'existence de zones privilégiées pour la génération des ondes T, que nous avons cartographiées. Cependant, comme l'avait déjà remarqué Jamet et al. [2013], le profil de vitesse dans l'océan s'avère n'être qu'un paramètre de deuxième ordre, dont nous avons évalué l'impact. Dans les configurations étudiées la présence du canal SOFAR limite légèrement la dispersion temporelle mais n'introduit un gain en termes de transmission énergétique que de l'ordre de quelques millièmes de dB par kilomètre, ce qui est comparable à l'effet de l'atténuation viscoacoustique de l'eau de mer. Aux distances et fréquences considérées (fréquence inférieure à 20 Hz, distance inférieures à 1000 km) nous pensons donc que l'influence du canal SOFAR sur le phénomène a été surestimée dans la littérature, ce qui a parfois mené à des interprétations biaisées. De même, notre étude dans la mer Ionienne suggère que les ondes T ne sont que faiblement sensibles au diagramme de rayonnement de la source. Au sujet de cette étude il faut noter qu'il est encourageant de constater que malgré la complexité du problème nous sommes parvenu à simuler des ondes T réalistes dans une configuration mettant en jeu deux conversions fluide-solide.

En outre, dans le cas de la conversion d'une onde acoustique sur une pente nos simulations prédisent la création d'une forte onde de Rayleigh, dont le signal, enregistré à l'intérieur des terres, est

très sensible à la pente et aux caractéristiques de l'environnement, mais très peu sensible à la structure modale de l'onde incidente. Bien que les récepteurs côtiers aient généralement des rapports signal sur bruit beaucoup plus faibles que les hydrophones dans l'eau (De Groot-Hedlin & Orcutt [2001b]), et bien que les fonds marins durs soient probablement rares dans la réalité, ce phénomène peut avoir des implications intéressantes. En effet, cette onde de surface porte probablement beaucoup d'informations sur la couche d'eau, qui pourraient peut-être être récupérées dans le cadre d'un problème inverse. On peut par exemple imaginer de déterminer les côtes favorables pour ce type de mécanisme et d'y installer des stations sismiques. Les ondes de Rayleigh créées à l'arrivée des ondes T pourraient alors être utilisées pour obtenir des informations sur les processus océanographiques par exemple. Notre étude présentée en annexe A suggère que les atolls du Pacifique pourraient convenir, ce qui mériterait sans doute une analyse plus poussée. En règle générale nos simulations indiquent que la dispersion temporelle des signaux est particulièrement sensible aux paramètres des milieux et pourrait donc éventuellement constituer un marqueur intéressant à prendre en compte dans le cadre d'un problème inverse.

Pour finir, nous avons montré qu'un bateau commercial de taille moyenne, comme il y en a aujourd'hui des dizaines de milliers sur les mers du globe, pouvait créer, par diffraction, des ondes T d'une d'amplitude conséquente (de l'ordre de celles créées par conversion "downslope" sur une pente de 12°) et de faible dispersion. Ce mode de génération d'onde T, encore non documenté, devrait être particulièrement fréquent dans les zones où le trafic maritime est important et pourrait expliquer certaines ondes T abyssales encore incomprises. En prenant l'atmosphère en compte dans ces simulations, nous nous sommes aperçu que la diffraction par un navire commercial pouvait également générer des infrasons guidés dans les couches basses de l'atmosphère. Ce mode de production d'infrasons peut constituer une explication alternative au couplage évanescent proposé par Evers et al. [2014] pour expliquer les ondes observées en Tasmanie à la suite d'un tremblement de terre en 2004 sur la dorsale Macquarie.

Au cours de cette thèse nous avons essayé de mettre en lumière l'éventail des possibilités offertes par le type de méthode numérique utilisée. Mis à part les sujets déjà évoqués dans cette partie, il pourrait par exemple être intéressant de se pencher sur la localisation des tremblements de terre à partir des ondes T en utilisant des modèles simples et des méthodes d'inversion. Pour cela il semblerait aujourd'hui judicieux de coupler une méthode type éléments finis comme celle que nous avons utilisée avec une méthode de type parabolique afin de pouvoir aborder des problèmes à plus grande échelle. Nous pourrions alors préparer le terrain pour traiter une base de données réelles comprenant des séismes localisés par d'autres méthodes. Notons par ailleurs que l'utilisation d'un algorithme d'apprentissage nous paraît également particulièrement adaptée dans ce cas. Quand la technologie le permettra il sera également bien entendu intéressant de travailler en 3-D, notamment pour le cas de la conversion d'une onde acoustique sur une côte.

Sur la spectroscopie Doppler géoacoustique

Nous n'avons abordé que très brièvement ce sujet et nous ne pouvons pas vraiment parler de véritables résultats à ce stade. Néanmoins nous avons présenté et validé des outils numériques pour calculer le champ acoustique crée par une source en mouvement. La méthode a été appliquée au cas d'un avion léger volant au-dessus de l'océan. Cette configuration, présentée par Buckingham et al. [2002a], permet d'estimer la vitesse des ondes de compression dans les sédiments. L'effet de l'ajout d'une vitesse d'onde de cisaillement et d'un gradient de vitesse du son dans les sédiments a été discuté. Il nous semble que dans ce cas encore, la méthode numérique que nous avons mise au point est particulièrement performante et peut permettre de traiter des cas complexes avec une bathymétrie et/ou des variations des propriétés des milieux.

Sur le calcul haute performance (HPC) pour l'acoustique sous-marine

Au cours de cette thèse nous avons présenté et validé une méthode numérique fondée sur des éléments spectraux dans le domaine temporel pour les problèmes axisymétriques de propagation linéaire couplée fluide-solide. Le modèle inclut le champ rétrodiffusé, qui ne peut pas être modélisé par exemple en utilisant l'approximation de l'équation parabolique. Nos calculs ont pris en compte des fonds océaniques viscoélastiques, et nous avons utilisé des couches absorbantes de type PML pour absorber efficacement le champ sortant en domaine géométrique borné. En outre, nous avons présenté une procédure efficace pour calculer des cartes de pertes de transmission et de dispersion temporelle à partir de ce type de méthodes. Cet outil nous a permis d'étendre la notion de pertes de transmission aux signaux non monochromatiques ainsi qu'aux milieux élastiques. À l'issue de cette thèse, il nous semble que ce type de techniques de modélisation de la forme d'onde complète, de par leur précision et leur flexibilité, ont le potentiel de constituer un apport significatif au domaine de l'acoustique sous-marine. Il reste cependant un certain nombre de défis à relever dans le futur pour pouvoir traiter des cas 3-D à grande échelle. Comme nous en avons fait l'expérience (voir annexe B) le principal point faible de la méthode des éléments spectraux classiques (en 3-D) est la génération de maillages constitués exclusivement d'hexaèdres, ce qui est souvent difficile en pratique, notamment dans les zones côtières et par petits fonds. Bien que l'on puisse s'affranchir de ce problème en rendant la méthode discontinue (Bernardi et al. [1994]; Kopriva et al. [2002]; Chaljub et al. [2003]; Legay et al. [2005]; Kopriva [2006]; Wilcox et al. [2010]; Acosta Minolia & Kopriva [2011]), en travaillant avec des tétraèdres (Wingate & Boyd [1996]; Taylor & Wingate [2000]; Komatitsch et al. [2001]; Mercerat et al. [2006]) ou en utilisant directement une méthode Galerkin discontinue (Lesaint & Raviart [1974]; Käser & Dumbser [2008]; Wilcox et al. [2010]) cela ne se fait qu'au prix d'un temps de calcul significativement plus élevé, et surtout d'une complexité de programmation souvent plus importante dans le cas de maillages mixtes. À cet égard, les méthodes combinant les éléments spectraux à l'approche Galerkin discontinue dans des parties distinctes du modèle semblent aujourd'hui prometteuses (voir Brissaud et al. [2017]; Terrana et al. [2018]).

Une approche encore plus prometteuse à court terme réside dans les méthodes couplant des codes rapides (semi-)analytiques ou approchés (comme les solvers paraboliques) avec des solvers 3-D en forme d'onde complètes seulement dans les régions du modèle où cela est nécessaire (van Manen et al. [2007]; Tong et al. [2014]; Monteiller et al. [2013, 2015]; Masson & Romanowicz [2017a,b]; Broggini et al. [2017]). Dans le cas de l'acoustique sous-marine, un couplage parabolique-SEM par exemple permettrait d'éviter la propagation à longue distance d'inexactitudes dans les solutions d'équations paraboliques habituellement observées près de la source (De Groot-Hedlin [2008]), tout en tirant parti de l'efficacité de cette méthode en termes de temps de calcul pour la propagation à longue distance. En outre, d'un point du vue informatique, nous pensons que le domaine aura beaucoup à gagner de l'utilisation des calculs sur accélérateurs graphiques GPU (voir e.g. Komatitsch et al. [2010]; Michéa & Komatitsch [2010]; Komatitsch [2011]; Gokhberg & Fichtner [2016]).

Il est également important de noter que pour ce type d'approche le traitement des données peut aussi constituer un défi en soi dans le cas des problèmes à grande échelle. Il est commun d'avoir à travailler avec des téraoctets de résultats. Ce problème, connu sous le nom de "big data", fait également des progrès très rapides notamment avec l'évolution du matériel informatique (Gropp & Sterling [2015]).

Un autre aspect des évolutions à venir en HPC pour l'acoustique sous-marine concerne les problèmes inverses d'imagerie. Les inversions en forme d'onde complète tout d'abord, bien qu'assez répandues de nos jours en sismique pétrolière et en sismologie (e.g. Monteiller et al. [2015]) sont encore très rares en acoustique sous-marine et sont, en pratique, limitées au domaine de l'exploration pétrolière (voir par exemple Bornstein et al. [2013]; Ratcliffe et al. [2014]; Borisov & Singh [2015]). Avec

les réseaux de capteurs actuels, autant en mer que sur terre, les données ne manquent pas et il serait bon à terme de pouvoir effectuer des tomographies océaniques à grande échelle en utilisant de telles méthodes. Sans aller aussi loin, il serait déjà fort intéressant de construire des noyaux de sensibilité en forme d'onde complète, pour l'amplitude ou la durée des ondes T par exemple (pour les noyaux de sensibilité voir par exemple Tromp et al. [2005, 2008], ou Skarsoulis & Cornuelle [2004]; Iturbe et al. [2009]; Aulanier et al. [2013]; Roux et al. [2013]; Dzieciuch & Cornuelle [2017] dans le domaine de l'acoustique sous-marine).

Concernant l'inversion et l'évolution des capacités de calcul il est probable que les méthodes Bayésiennes vont devenir de plus en plus populaires (Dosso & Dettmer [2011]; Bottero et al. [2016b]; Dettmer et al. [2018]; Luu et al. [2018]). En effet ces algorithmes permettent de traiter des problèmes non linéaires tout en quantifiant les incertitudes associées au modèle final, au prix d'un nombre de calculs très supérieur au cas des approches linéarisées de type gradient d'une fonction coût. En association avec les méthodes en forme d'onde complète d'excellents résultats sont à attendre, surtout pour les problèmes mal conditionnés ou pour ceux qui restent raisonnables en termes de nombre de degrés de liberté (typiquement inférieur à quelques centaines avec les machines et technologies actuelles). En outre les méthodes Bayésiennes peuvent s'adapter aux jeux de données et à la complexité des problèmes étudiés afin de proposer un nombre d'inconnues optimum. Dans le cadre de nos travaux l'étude des sédiments marins par spectroscopie Doppler par exemple nous paraît être un cas particulièrement adapté à l'utilisation de ces algorithmes.

Bien entendu, l'actuel essor impressionnant dans le domaine des méthodes d'apprentissage ("Machine learning"), qui parviennent à traiter des problèmes toujours plus complexes, créera probablement des révolutions ou tout au moins des avancées très significatives dans le domaine de l'acoustique sous-marine également. Ce domaine commence tout juste à bénéficier des progrès phénoménaux de ces dernières années (voir par exemple Niu et al. [2017]) et de nouvelles avancées sont à prévoir. Pour donner un exemple, il nous parait certain que ce type d'algorithmes peut permettre d'améliorer grandement la localisation des séismes par les ondes T.

Appendix A

Study of acoustic wave conversion at an atoll

This appendix is, in form and substance, very similar to section 4.1. It is dedicated to a real case study of a signal recorded on an atoll following an explosion at sea. This example makes it possible to study fluid-solid conversion without having to deal with the additional complexity of a first solid-fluid conversion as in the case of the generation of T-waves. Let us recall nevertheless that signals from explosions are known to last less time than T-phases (Milne [1959], Ben-Menahem & Toksöz [1963]) and that their structures clearly differ in the time-frequency plane (see Chapter 5).

This study has been placed in an appendix because there is still some doubt about the data being analyzed.

A.1 Introduction

French Polynesia in the Pacific Ocean and more particularly the Society and Tuamotu Archipelagos is characterized by numerous volcanic islands and seamounts rising above the ocean floor. In 1989 a marine seismic survey called MidPlate II was conducted in the region in order to study the deep crustal structure of these two very different geologic edifices (Grevemeyer et al. [2001], Patriat et al. [2002]). In addition to airgun shots, dynamite charges were detonated during the survey. The signals have also been recorded at the onshore stations of the Réseau Sismique Polynésien (RSP) and were kindly provided to us by Jacques Talandier, emeritus researcher at the Laboratoire de Géophysique (LDG) of the French Commissariat à l'Energie Atomique (CEA). In this appendix we show several simulations of one of the dynamite shots that was recorded at station VAH located near the shore on the Rangiroa atoll (see Figure A.1). At that time for this seismic station only the vertical component of the ground velocity was available. The explosive contained 86 kg of TNT (1.5 g.cm^{-3}) and was fired 25 km north-west of the Mehetia volcanic island (latitude: - 17.68, longitude: -148.2), at a distance of 278 km from the seismic station. The depth given is 215 m but these explosives being initially dedicated to the destruction of submarines there can be a certain margin of uncertainty. The setting considered is convenient because the direct wavefronts are almost perpendicular to the shore, which most likely limits 3-D effects and validates the use of an axisymmetric model. A 2-D geological background in the vertical plane containing the source and the receiver is shown in Figure A.2. The bathymetry is extracted from the SRTM30_PLUS model (see Becker et al. [2009]; Sandwell et al. [2014]), which has 0.5 arc-minute resolution (approximately 920 m in the area). In 1989 a marine seismic survey called MidPlate II was conducted in the region in order to study the deep crustal structure of the Society and Tuamotu Archipelagos (Grevemeyer et al. [2001],Patriat et al. [2002]). The subterranean interfaces were extrapolated from this survey (Patriat et al. [2002]), and we added the 400 m-thick oceanic sedimentary layer found by Talandier & Okal [1987b]. Let us note the particularly deep crustal

root (21 km) underlying the Tuamotu plateau. Realistic densities and compressional wave velocities (V_p) for each domain are shown in Table A.1, defined following Patriat et al. [2002]. The shear wave velocities shown (V_s) have been chosen in order to get a ratio $V_p/V_s \approx 1.7$. Due to the limited amount of information available in the area, viscoelastic attenuation values were chosen arbitrarily.

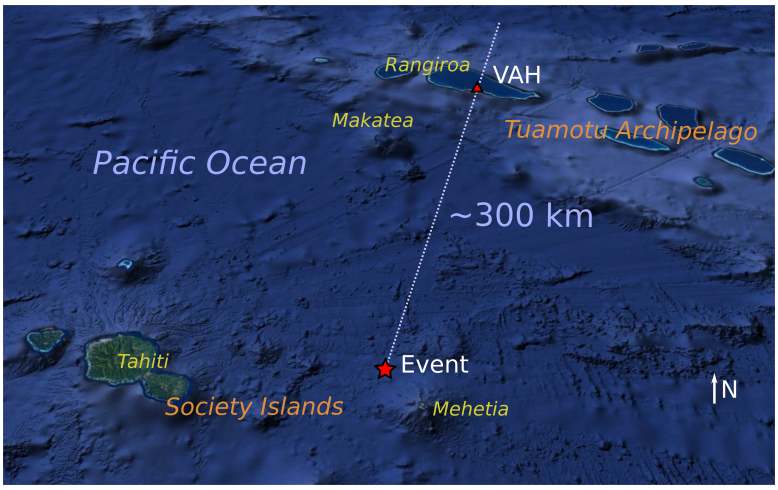

Figure A.1 – Setting of the experiment considered. The event is indicated by a red star. It is located at latitude: -17.68°, longitude: -148.2° and at an approximate depth of 215 m. Station VAH at which the wave field is recorded is shown as a small red triangle.

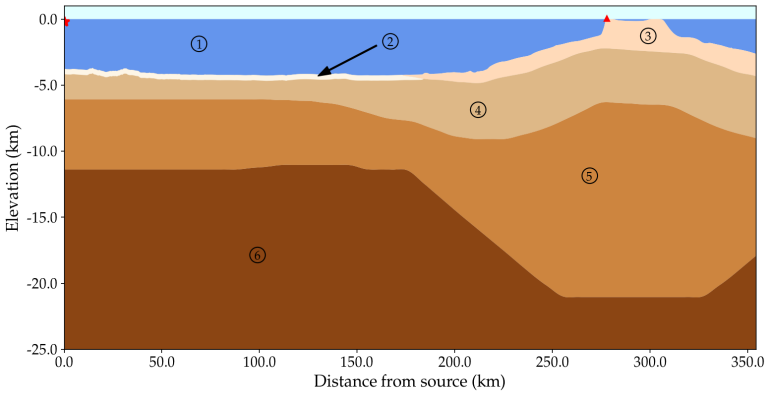

Figure A.2 – Setting of the 2.5-D experiment together with a realistic geological structure (extrapolated from Patriat et al. [2002], to which we added the sedimentary layer discovered by Talandier & Okal [1987b]. The source is on the axis an the left hand side at depth 215 m. The velocity profile in the water is depicted in Figure A.3. Station VAH at which the wave field is recorded is shown as a small red triangle. The seismic properties of each domain are shown in Table A.1.

A.2 Observations and simulations

The vertical velocity signal recorded at station VAH is shown at the top of Figure A.5 and exhibits an impulsive first arrival with a dominant frequency around 5-6 Hz. The depth and weight of the explosive, together with its type (TNT, 1.5 g.cm^{-3}) and a law for the detonation allow to calculate theoretically the pressure signal generated following Coles et al. [1946]; Jones & Miller [1948]. That signal is shown in blue in Figure A.4. Its frequency spectrum has a first peak around 10 Hz and has energy up to at least 50 Hz. Let us note that this frequency content seems to differ quite significantly from the signal recorded at station VAH; this point will be further discussed below. It is in any case

too high to consider an affordable numerical simulation based on spectral elements, even in 2-D. In order to study the phenomenon anyway, and as the recorded frequencies at VAH were not as high, we chose to filter the theoretical signal with a Savitzky–Golay filter. The filtered signal obtained, shown in Figure A.4, was used instead as a pressure source time function in our simulations.

The velocity profile used in the water column is shown in dark blue in Figure A.3, extracted from Levitus [1983]. A constant velocity profile of 1482.1 m.s^{-1}, corresponding to the minimum value of the variable velocity profile, was also used in our simulations in order to estimate the influence of a variation of sound velocity in the water for this case.

The spectral-element mesh is composed of $\sim$ 3.1 million elements whose polynomial degree is $N = 4$. The total number of unique GLL/GLJ points in the mesh is approximately 50 millions. Depending on the velocity profile used in the fluid the number of points per wavelength slightly varies. In the worst case, 99.9% of the acoustic elements have at least 5 grid points per pressure wavelength in the fluid, and 99.9% of the elements in the viscoelastic part have at least 6.5 points per shear wavelength. We select a time step $\Delta t = 0.23$ ms based on the stability and accuracy conditions of the explicit, conditionally-stable time scheme, and simulate a total of 1.75 million time steps, i.e. 402.5 s. The energy coming out of the domain under study, shown in Figure A.2, is absorbed by PML absorbing layers. Frequencies up to ~20 Hz are resolved. The displacement vector is recorded at station VAH. Each simulation performed took approximately 14 hours on 1120 processor cores of a parallel supercomputer equipped with Intel ® Xeon® E5-2690 v3 processors.

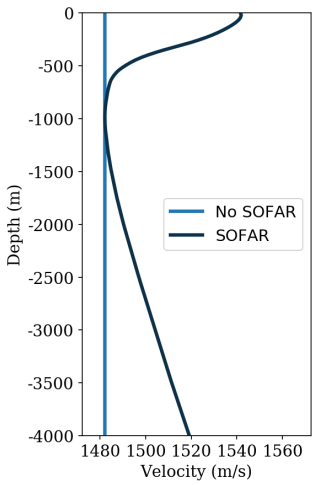

Figure A.3 – Sound speed profiles in the ocean used for the numerical simulation. The model labeled SOFAR has been chosen following Levitus [1983].

Figure A.5 shows a comparison between the real signal and two synthetic signals at station VAH, with and without a SOFAR channel. Let us first focus on the model with a SOFAR channel; the differences with the other model will be discussed afterward. The durations of the synthetic and real signals are similar. Despite this, the signals compare poorly. The synthetic signal is less impulsive, its amplitude decreases more slowly, and most of all its frequency content is clearly higher than the real one. It is, moreover, reasonable to assume that this frequency shift would have been even greater if the unfiltered theoretical source signal (blue curve in Figure A.4) had been used.

Two main scenarios (or a combination of them) can explain these differences: either the source model used does not correspond to the actual situation, or the numerical model is not realistic.

Let us start by examining the possible limitations of our numerical model. First of all, due to the lack of precision on the knowledge of bathymetry in the area, the seabed is likely to appear flatter than it is for the high frequencies that may benefit from a probable lack of scattering. However, this is unlikely to explain such differences. Indeed at these distances a significant part of the energy travels

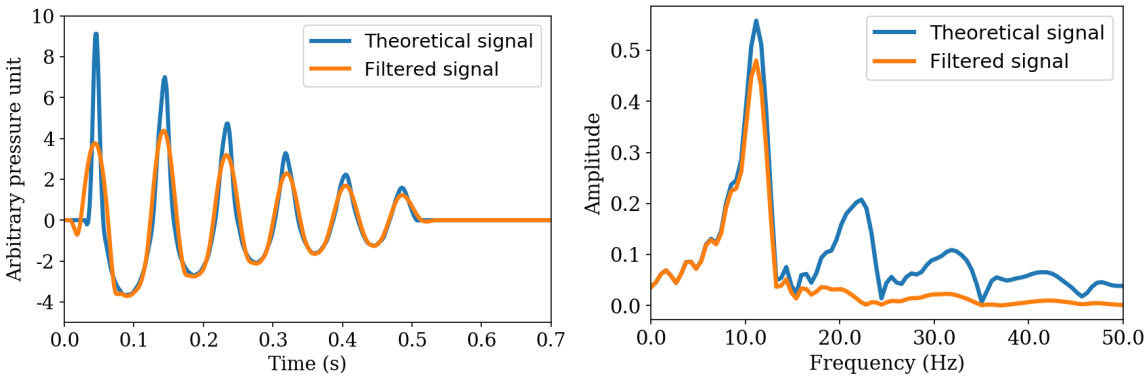

Figure A.4 – Comparison in the time (left) and frequency (Power Spectral Density, right) domains between the theoretical pressure signal generated from the source used (Coles et al. [1946]; Jones & Miller [1948]) and the pressure signal used in our simulations.

	Label used in Figure	Description
Ocean	1	$\rho = 1000$ kg.m^{-3}, the profile is shown in Figure A.3
Oceanic sediments	2	$\rho = 1700$ kg.m^{-3}, $V_p = 1900$ m.s^{-1}, $V_s = 1000$ m.s^{-1}, $\alpha_p = 0.3$ dB.λ_p^{-1} , $\alpha_s = 0.3$ dB.λ_s^{-1}
Atoll sediments (Lime-stone)	3	$\rho = 2390$ kg.m^{-3}, $V_p = 3300$ m.s^{-1}, $V_s = 1940$ m.s^{-1}, $\alpha_p = 0.25$ dB.λ_p^{-1} , $\alpha_s = 0.25$ dB.λ_s^{-1}
Upper crust (Basalts)	4	$\rho = 2560$ kg.m^{-3}, $V_p = 5200$ m.s^{-1}, $V_s = 3060$ m.s^{-1}, $\alpha_p = 0.21$ dB.λ_p^{-1} , $\alpha_s = 0.21$ dB.λ_s^{-1}
Lower crust (Gabbro)	5	$\rho = 2850$ kg.m^{-3}, $V_p = 6740$ m.s^{-1}, $V_s = 3965$ m.s^{-1}, $\alpha_p = 0.10$ dB.λ_p^{-1} , $\alpha_s = 0.10$ dB.λ_s^{-1}
Mantle	6	$\rho = 3340$ kg.m^{-3}, $V_p = 8200$ m.s^{-1}, $V_s = 4820$ m.s^{-1}, $\alpha_p = 0.05$ dB.λ_p^{-1} , $\alpha_s = 0.05$ dB.λ_s^{-1}

Table A.1 – Description of the media implemented. V_p is the compressional wave speed, V_s is the shear wave speed, and α_p and α_s are the corresponding attenuation coefficients at 10 Hz expressed in dB per wavelength.

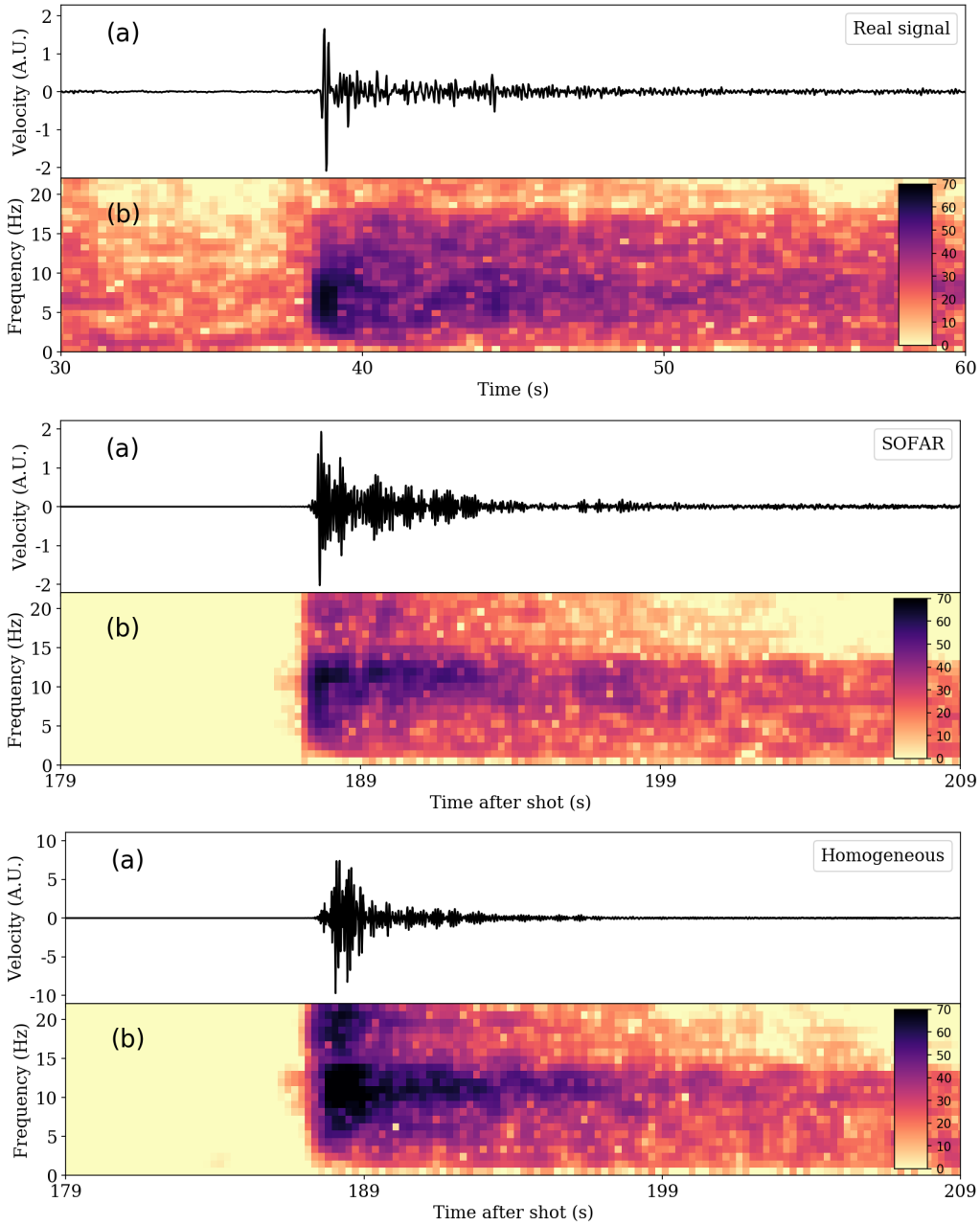

Figure A.5 – Comparison of the synthetic signals to the real one at station VAH. The top figure is the real signal (bandpass-filtered between 0.5 Hz and 25 Hz), and the middle and the bottom ones are the synthetic signals, respectively with and without a SOFAR channel. For the three pictures: (a) Seismogram of the vertical component of the velocity vector (arbitrary velocity unit). (b) Power Spectral Density (in dB) as a function of time and frequency. Note that the time of the shot is not known, consequently the time shown in the top figure is arbitrary. The amplitude of the synthetic signals can be compared.

without interaction with the seabed. High frequencies should therefore be found in the real signal. Likewise, this cannot explain the presence of low frequencies in the actual signal.

Another but similar bias in our model may concern the seismic properties of the seabed. Attenuation has been set to be constant over all frequencies, while in reality the seabed is typically more attenuating for high frequencies compared to low frequencies (see Hamilton [1980, 1985] or Chapter 6 of Chotiros [2017]). To give an order of magnitude we could have $\alpha_p = 0.1$ dB.λ_p^{-1} at 1 Hz but $\alpha_p = 0.6$ dB.λ_p^{-1} at 20 Hz for example. This phenomenon must obviously favor low frequencies but cannot explain alone the huge discrepancies observed. Besides, the explanation faces the same problem as mentioned above for roughness.

One could also mention the influence of gravity, which may be important for underwater explosions. This effect has been omitted from the governing equations (3.1) and (3.3). It has been shown however that gravitational effects can play a prominent role in the case of the propagation of low frequency acoustic waves that can be generated from underwater explosions. In these cases, some of the basic acoustic mode properties, such as amplitude and speed, can be modulated fundamentally (Kadri & Stiassnie [2012]; Kadri et al. [2017]). Employing acoustic-gravity wave theory, which accounts for both the slight compressibility of water and gravitational effects may be necessary in this case to properly describe the propagation of acoustic waves. It is difficult to assess the influence of such effects in our case.

We do not currently see other physical mechanisms capable of converting high frequencies to low frequencies in this way.

The differences, however, can also come from our source model, which may be inappropriate. For example from Swisdak Jr [1978] p. 68-70 one can compute the dominant frequency of oscillation F of the bubbles of burnt gases formed by a TNT charge detonated underwater ($\sim$ frequency of first peak in Figure (A.4), right) as a function of the charge weight W in kilograms and of the depth of the charge H in meters:

$$F = C\frac{(H + H_0)^{\frac{5}{6}}}{W^{\frac{1}{3}}}, \tag{A.1}$$

where $H_0 = 10$ m and $C = 0.474$ s^{-1}.m$^{-5/6}$.kg$^{1/3}$. In our case we can hardly imagine an error on the mass of the charge $W = 86$ kg used. The depth of detonation, however, may be inaccurate. Formula (A.1) gives $F = 9.95$ Hz for $H = 215$ m, $F = 8.65$ Hz for $H = 180$ m and $F = 5.48$ Hz for $H = 100$ m.

Let us then suppose that the charge exploded at depth 100 m. The signals obtained with and without a SOFAR channel are shown in Figure A.6, the particle motion at station VAH in the model including a SOFAR channel being shown in Figure A.7.

Note that the signal obtained for this new configuration and in particular its frequency content is much more realistic, which suggests that the depth of the source may indeed have been poorly evaluated. The first arrival is more impulsive and of shorter duration, which better fits the data. Finally, the amplitude ratio between this first arrival and the following ones is correct. The particle motion recorded at the VAH station on the atoll coast shows that this first arrival is mostly composed of surface waves, which was to be expected from the studies presented in Chapter 4.

Regarding the difference between the homogeneous and SOFAR models one can see that signals with and without a wave speed channel exhibit fairly large differences in amplitude and waveform for the cases studied. As mentioned in Chapter 4, this particular sensitivity may have interesting implications, for the study of marine currents for example. Hence this suggests that a difference of a few percents on the speed of sound in water may imply differences of about 200 % (or even 500 % in the high-frequency case) on the amplitude of the wave recorded at the coast. This phenomenon may also partly explain the unusual T-wave reported by Talandier & Okal [1979], which was recorded surprisingly small at Rarotonga compared to Tahiti after its propagation from the Tonga archipelago.

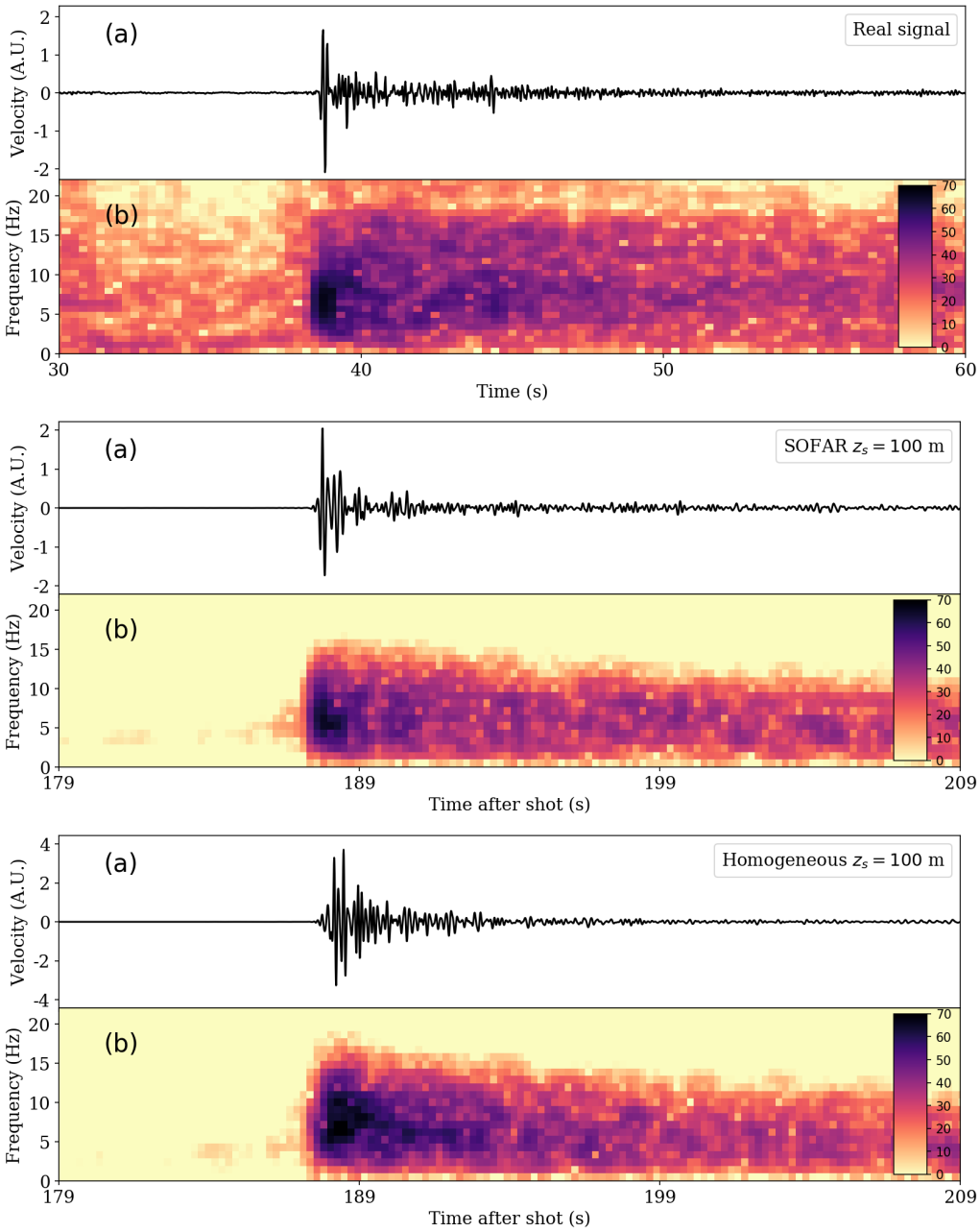

Figure A.6 – Comparison of the synthetic signals to the real one at station VAH for a shallower source. The top figure is the real signal (bandpass-filtered between 0.5 Hz and 25 Hz), and the middle and bottom signals are the synthetic ones with and without a SOFAR channel respectively. For the three pictures: (a) Seismogram of the vertical component of the velocity vector (arbitrary velocity unit). (b) Power Spectral Density (in dB) as a function of time and frequency. The time of the shot is not known, consequently the time shown in the top figure is arbitrary. The amplitude of the synthetic signals can be compared.

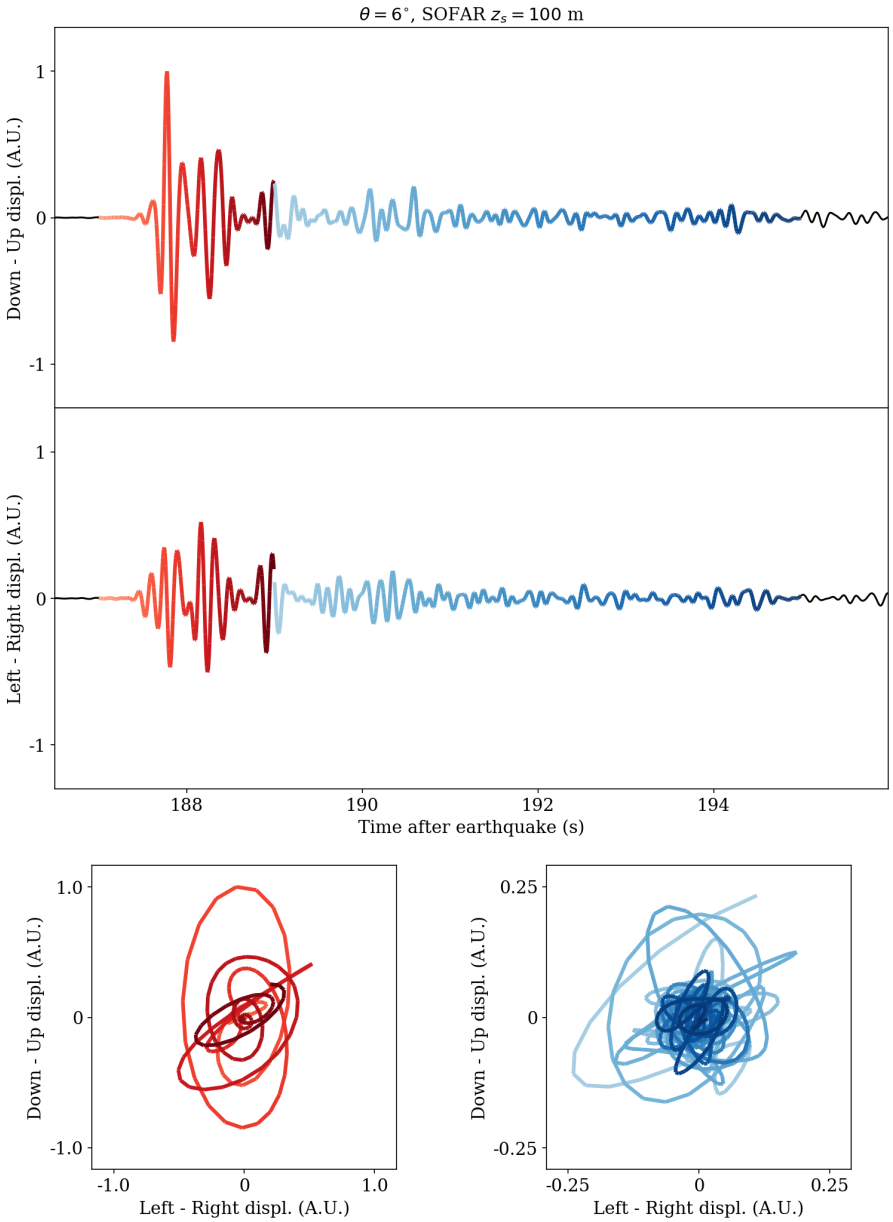

Figure A.7 – Sketch showing particle motion at station VAH in the case of a charge detonated at depth $z_s = 100$ m in a model including a SOFAR channel. The main arrivals exhibit retrograde particle motion characteristic of Rayleigh waves.

Figure A.8 shows the broadband transmission losses map as defined in Chapter 5 in the case of an explosive charge detonated at depth $z_s = 100$ m in a model including a SOFAR channel. This figure exhibits several interesting features. First of all it illustrates the penetration of energy in sediments and in the atoll. In particular, it can be seen that the energy is rapidly attenuated during propagation in the atoll. Furthermore we can see that the guided modes reach supercritical incidence for the P waves around the range 270 km after successive reflections between the sloping bottom and the surface. Their energy subsequently couples with the bottom, as was detailed in Chapters 4 and 5. Note also that this map takes into account the reflections on the atoll, which probably affect the patterns visible in the ocean in a way that is hard to forecast.

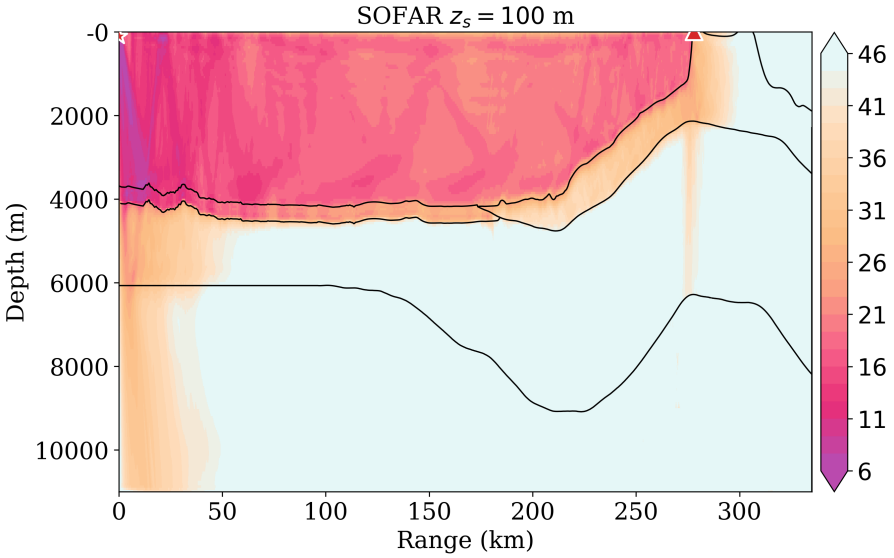

Figure A.8 – Broadband transmission losses, as defined in Chapter 5 in the case of an explosive charge detonated at depth $z_s = 100$ m in a model that includes a SOFAR channel.

A.3 Conclusions

This appendix has shown a real case study of a signal recorded on an atoll following an underwater explosion. Such an example has allowed us to study the interaction of a guided acoustic wave with a coast without having to deal with the additional complexity of a first solid-fluid conversion as in the case of the generation of T-waves. Contrary to the other numerical studies presented in this document, particular care has been taken in modeling the source (TNT, 1.5 g.cm^{-3}). However, our synthetic signals do not match the observations very closely, especially in the frequency domain. Such a poor fit can be explained either by a poor evaluation of the source depth, or by a bias in our model (bathymetry, viscoelastic attenuation, compressibility or gravity effects). It is difficult to determine the main factor, as it may also not be unique. The first hypothesis was tested by simulating a source at a depth of 100 m instead of 215 m. The results obtained were much more realistic in this case, which suggests that the explosion depth of 215 m given may indeed be inaccurate. It is unfortunate that no measurements were taken in the water offshore of the atoll for the same event or that the horizontal velocity components at the VAH station were not available. It would also be interesting to try a more recent explosive source model (e.g. Hunter & Geers [2004]).

Each simulation was performed for two different velocity profiles in the ocean to test the sensitivity of our data to variations in water properties. The simulated signals on the atoll coast are mostly composed of Rayleigh waves whose amplitude and waveform significantly depend on the properties of the water layer. As mentioned in Chapter 4 this effect may have interesting implications, for the study

of marine currents for example. Hence our calculations suggest that a difference of a few percents in the speed of sound in the water may imply differences of about 200 % (or even 500 % in the high-frequency case) in the amplitude of the wave recorded at the coast. This phenomenon may also partly explain the unusual T-wave reported by Talandier & Okal [1979], which was recorded surprisingly small at Rarotonga compared to Tahiti after its propagation from the Tonga archipelago.

Appendix B

3-D simulations. A meshing challenge.

At first, when studying T-waves in the Ionian Sea (Chapters 2 and 4), 2.5-D simulations were supposed to be preliminary results before going to more realistic 3-D configurations and comparing with INGV data. The CAD model of the Ionian sea and its surroundings has been constructed and is shown in Figure B.1.

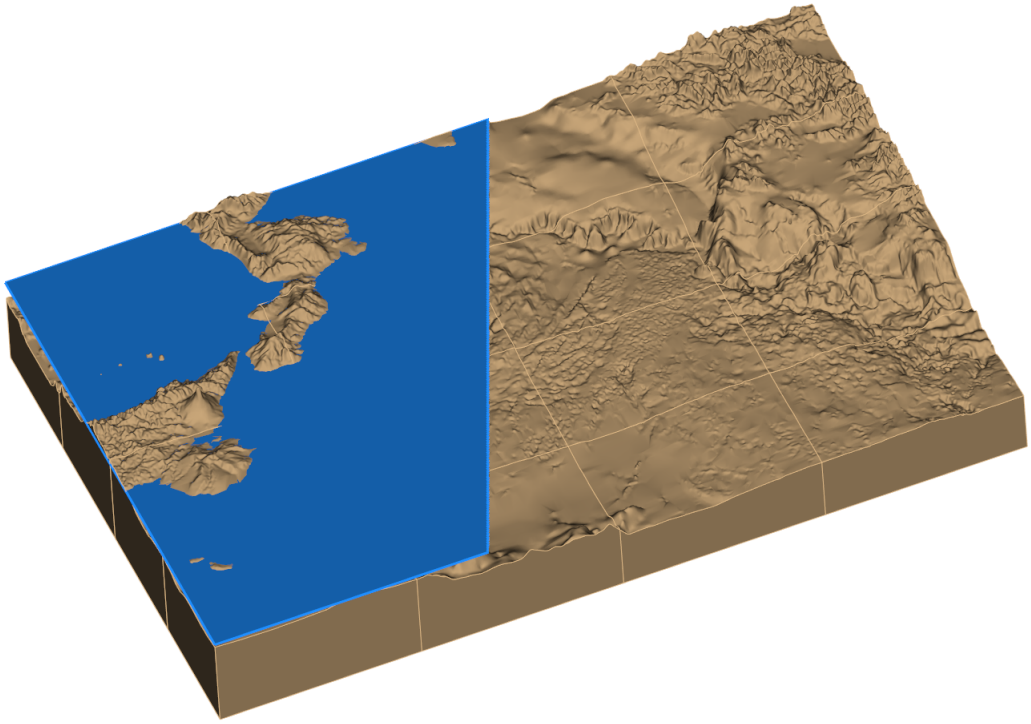

Figure B.1 – Our CAD model of the Ionian sea. The vertical scale has been exagerated 7 times.

The topography has been obtained from the US National Geophysical Data Center [2011]. However, next step involved building of a big 3-D unstructured hexahedral elements mesh of that model (∼200M elements). Due to technical issues, we did not manage to obtain a suitable mesh. While the construction of such a mesh using tetrahedral elements may be achieved by commercial or non-commercial softwares, creating a complex hexahedral mesh is still a challenging problem (Stupazzini et al. [2009]; Erickson [2014]), especially when of considerable size. We planed to mesh the computational domain thanks to the software CUBIT (available at cubit.sandia.gov) that incorporates a set of powerful and advanced meshing schemes specifically developed to handle the hexahedral unstructured

meshing problem. The real topography being irregular the main issue for us is the meshing of the water. Hence physical interfaces have to be meshed precisely. To develop a meshing strategy we have created toy models, an example of which is shown in Figure B.2, made up from a random smooth realistic topography.

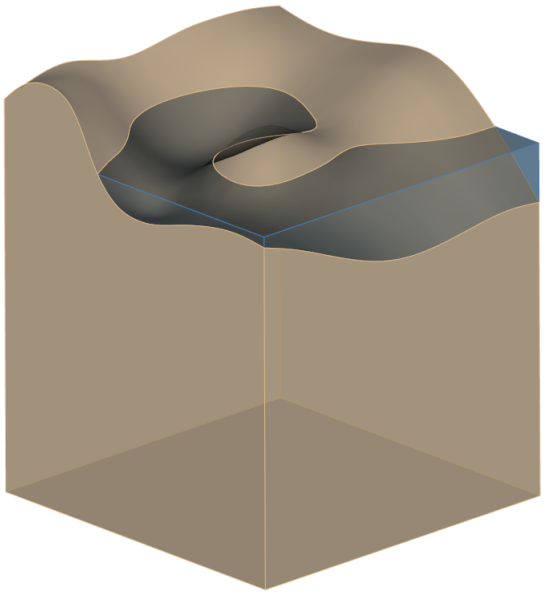

Figure B.2 – Example of 3-D toy model built consisting of an irregular water part (in blue) lying above a bedrock.

We manage to properly mesh some of them by first meshing with tetrahedral elements and then converting them into hexahedral elements (with a small loss in mesh quality). However this strategy failed when increasing the complexity of the seabed in order to get closer to a real model such as the one shown in Figure B.1. Hence each step take then a prohibitive computational time to run and requiring terabytes of memory. A possible work-around avoiding meshing difficulties would be to create a virtual free surface. It would suffice to mesh the elastic part first and then extrude the surface mesh of the sea bottom up to a distance above sea level and then set the acoustic potential at the integration points to zero if their vertical coordinate is greater than zero. Unfortunately, as shown in Figure B.3 (for 2-D mesh), this approach created too much diffractions at the reflection of acoustic waves on the virtual irregular sea surface.

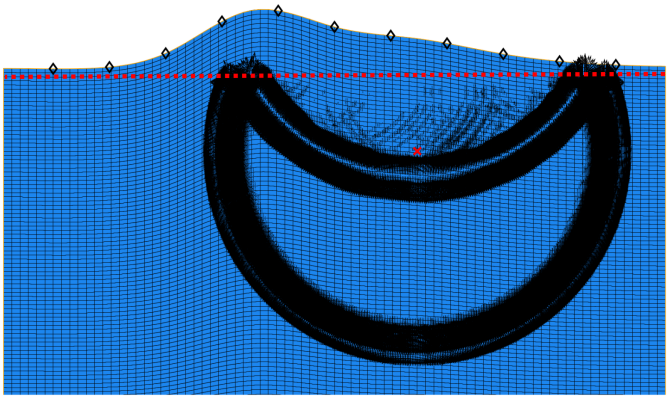

Figure B.3 – Displacement vector plot in an acoustic medium. The red dotted line spot the position of the actual free surface we want to simulate. This is an attempt with SPECFEM 2-D by setting the potential of each integration point in the water to zero if its vertical coordinate is above the virtual free surface. The source has been set at the red cross.

Another possibility is to try another software offering parallel meshing capabilities such as ANSYS

(www.ansys.com) or Bolt™ (www.csimsoft.com/boltoverview). Bolt™ has been tested and is promising for this purpose. It relies on the overlay-grid or mesh-first method starting from a Cartesian grid encompassing the geometry. As illustrated in Figure B.4, geometric features are then "sculpted" from this base and boundaries to create the final hex mesh.

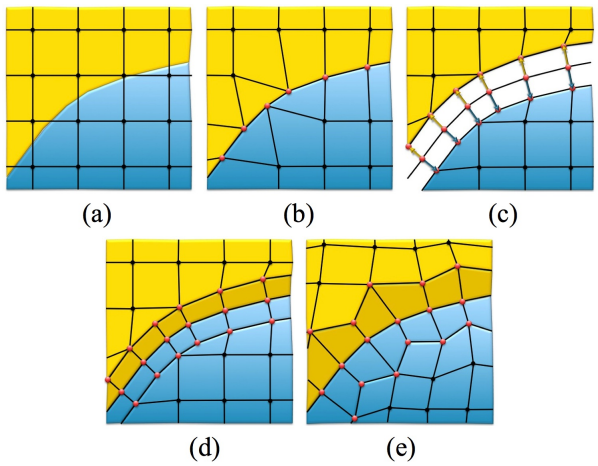

Figure B.4 – The procedure for generating a hex mesh using Bolt™ as described in the documentation. Beginning with a Cartesian grid as the base mesh, shown in (a), a geometric description is imposed. Nodes from the base grid that are near the boundaries are projected to the geometry, locally distorting the nearby hex cells (b). A pillow layer of hexes is then inserted at the surfaces by duplicating the interface nodes on either side of the boundaries and inserting hexes ((c) and (d)). While constraining node locations to remain on the interfaces, smoothing procedures can now be employed to improve mesh quality of nearby hexes (e).

However, although it proved able to mesh any complex water layer alone, Bolt™ is unfortunately not (yet?) able to mesh full realistic geological models, such as the one we are interested in.

Appendix C

Glossary

The reader will find here a brief definition for the terms in blue spread all over these pages. To construct these definitions we used the following sites extensively: dosits.org/glossary, earthquake.usgs.gov/learn/glossary, www.marineinsight.com and of course Wikipedia.

Acoustic pressure: local pressure deviation from the ambient (average or equilibrium) atmospheric pressure, caused by a sound wave (see also **Hydrostatic pressure**).

Adiabatic approximation: upon this approximation one neglects any exchange of energy between modes while they evolve (see **Modal decomposition**).

Adiabatic bulk modulus: see **Bulk modulus**.

Airgun: an airgun is designed to release compressed air, which forms bubbles. The formation of bubbles produces a loud sound that is used to explore the geologic structure of the ocean floor.

Anelastic attenuation: as a seismic wave propagates through a medium, the elastic energy associated with the wave is gradually absorbed by the medium, eventually ending up as heat energy. This is known as anelastic attenuation or absorption.

Anisotropic: having properties that differ according to the direction of measurement (see also **Isotropic**).

Arc minute: unit of angular measurement equals to 1/60 of one degree.

Autocovariance function: the autocovariance is a function that gives the **covariance** (cov) of a stochastic process with itself at pairs of time points. Let $X = (X_t)$ be a stochastic process. With the usual notation E; for the expectation operator, if the process has the mean function $\mu_t = E[X_t]$ then the autocovariance is given by $C_{XX}(t,s) = \text{cov}(X_t, X_s) = E[(X_t - \mu_t)(X_s - \mu_s)] = E[X_t X_s] - \mu_t \mu_s$ where t and s are two time periods or moments in time.

Axisymmetric 2-D: to construct a 2-D axisymmetric model, it is assumed that the problem under study has rotational symmetry (see also **Cartesian 2-D**).

Back-azimuth: the signal propagation direction in the horizontal plane. This information can be used to locate an acoustic source.

Bathymetry: refers to the topography of the seabed as well as the science associated with measuring the depths and relief of the ocean.

Beamforming: also called spatial filtering, it is a signal processing technique used in sensor arrays for directional signal transmission or reception. This is achieved by combining elements in an antenna array in such a way that signals at particular angles experience constructive interference while others experience destructive interference (see also **Large-aperture array**).

Body waves: refers to the P and S waves or reflections of either. Travel inside the material.

Body wave magnitude: measure of the magnitude of an earthquake based on the **body waves** it has produced. The precise definition of the term has often changed in history.

Broadband: composed of several frequencies, it is the opposite of monochromatic.

Bulk modulus: commonly noted K, it is a measure of the incompressibility of the material. Suppose that a material of initial volume V_0 is subjected to a pressure variation ΔP which induces a volume variation ΔV. The bulk modulus of this material is then $K = V_0 \frac{\Delta P}{\Delta V}$.

Bulk wave: this term is used to designate the waves that travel in the volume of a solid, said in opposition to the surface waves.

Cartesian 2-D: to construct a Cartesian 2-D it is assumed that the problem under study in infinite along a line. It is also called plane strain 2-D (see also **Axisymmetric 2-D**).

Caustic: in ray theory a caustic is a curve or surface to which each of the acoustic rays is tangent. Caustics are very energetic zones.

Conjugate depth: see **Critical depth.**

Correlation length: the correlation length of a rough surface is defined as the average distance between two points of the same height.

Critical angle: for an acoustic ray traveling from a slow medium to a fast medium, the critical angle is the smallest angle of incidence for which no refraction occurs. The angle of refraction would be 90°, but instead the ray is reflected at the interface between the two media. See also **Ray theory**, **Total internal reflection** and **Supercritical incidence**.

Critical depth: depth below which ray theory predicts that no ray can be channeled into the sound channel.

Cutoff depth (mode): depth of water necessary for the existence of a given guided mode.

Deep earthquakes: a deep (focus) earthquake in seismology is an earthquake with a hypocenter depth exceeding 300 km.

Diffraction: refers to a variety of phenomena occurring when a wave encounters an obstacle (or a slit) whose size is comparable to its wavelength. According to the Huygens-Fresnel principle, a diffracting point hit by a wavefront can be considered as a secondary source.

Dip-slip: dip-slip faults are inclined fractures where the blocks have mostly shifted vertically.

Dispersion: dispersion is the phenomenon in which the velocity of a wave depends on its frequency.

Doppler shift: change in frequency or wavelength of a wave in relation to observer who is moving relative to the wave source.

Eddies (ocean): temporary loops of swirling water that can travel long distances before dissipating.

Eigenray: ray connecting a given source and receiver.

El Niño: warm seasonal coastal current off Peru and Ecuador whose importance for the world climate is significant.

Envelope (of a curve): boundary of the region filled by the curve.

Epicenter: point on the earth's surface vertically above the **hypocenter**.

Finite-element (technique, method): the finite element method (FEM) is a numerical method for obtaining an analytical solution to partial differential equations associated with physical systems (e. g. the momentum equation (3.1) with boundary conditions). To solve the problem, it subdivides the physical domain under consideration into smaller parts called finite elements. The elementary equations that model these finite elements are then assembled into a larger algebraic system of equations that models the entire problem. The FEM then uses variational methods from the calculation of variations to approximate a solution.

FK transform: two-dimensional Fourier transform in time and space. F refers to the frequency (Fourier transform over time) and K to the wave number (Fourier transform in space, using a receiver array). See also **Fourier transform**.

Focus: see **Hypocenter.**

Forearc: region between the subduction zone and the volcanic chain (volcanic arc).

Forward simulation: synthetic data simulation knowing the model (see also **Inverse problems**).

Fourier transform: this mathematical method decomposes a temporal signal into its component frequencies in the same way that a musical chord can be described by the frequencies (or pitches) of the notes that it contains. The Fourier transform can also be defined with respect to a space variable. In this case, one no longer speaks of temporal frequency but of spatial frequency: the wave number.

Front: boundary between two distinct water masses moving in different directions

Full wave: taking into account the full waveform. We speak of full-wave method when the entire signal is modeled, i.e. when very few approximations are made from the basic equations.

Geometrical spreading: when a wave propagates from a source, the area covered by the wave becomes larger and larger. As the emitted energy is fixed it implies a decrease in the intensity of the wave as it propagates. This purely geometric effect is called geometrical spreading.

Grazing angle: angle with respect to an interface. We speak about wave at grazing incidence when the wave is propagating nearly parallel to the interface.

Group velocity: velocity with which the overall shape of the wave's amplitudes propagates through space. (see also **Phase velocity**).

Gyres: spiraling circulations thousands of miles in diameter and rimmed by large, permanent ocean currents.

Hankel functions: noted $H_\alpha^{(1)}(x)$ and $H_\alpha^{(2)}(x)$ the Hankel function are the linearly independent solutions of the Bessel equation: $x^2\frac{d^2y}{dx^2} + x\frac{dy}{dx} + (x^2 - \alpha^2)\ y = 0$ where α is a real or complex arbitrary number.

Helmholtz equation: it is the equation $\nabla^2 A + k^2 A = 0$ where ∇^2 is the Laplacian, k is the wavenumber and A is the amplitude. One can obtain a Helmholtz equation can be obtained by expressing the momentum equation (equation (3.1)) in the frequency domain (see **Fourier transform**).

Hooke's law: it is equation (3.20), or (3.22). Equation (3.21) in the linear, elastic, isotropic case. linking stress and strain tensors.

Hôpital's rule (De l'): for functions f and g which are differentiable on an open interval I except possibly at a point c contained in I, if $\lim_{x\to c} f(x) = \lim_{x\to c} g(x) = 0$ or $\pm\infty$, $g'(x) \neq 0$ for all x in I with $x \neq c$, and $\lim_{x\to c} \frac{f'(x)}{g'(x)}$ exists, then: $\lim_{x\to c} \frac{f(x)}{g(x)} = \lim_{x\to c} \frac{f'(x)}{g'(x)}$.

Hotspot earthquakes: earthquakes occurring inside volcanic edifices.

Hydrophone: an underwater microphone that will listen to, or pick up, acoustic signals. A hydrophone converts acoustic energy into electrical energy.

Hydrostatic pressure: pressure which exists in a fluid at rest and which is due to its own weight (see also **Acoustic pressure**).

Hypocenter: the hypocenter of an earthquake (also called focus) is the point on the fault plane where the rupture starts. The fault may rupture in one direction from the hypocenter, or in both directions. That is, the hypocenter may be at the edge of the rupture or within the rupture. The earthquake depth is usually taken as that of the hypocenter, even if the fault ruptures to the surface.

Impedance (acoustic): in the fluid case, the characteristic acoustic impedance of a medium of density ρ and sound velocity c is the quantity ρc.

Intermediate depth earthquakes: intermediate (focus) earthquake in seismology is an earthquake with a hypocenter at depth comprised between 70 and 300 km (see also **Shallow earthquakes** and **Deep earthquakes**).

Internal tides: they are generated as the surface tides move stratified water up and down sloping topography, which produces a wave in the ocean interior. So internal tides are internal waves at a tidal frequency.

Internal waves : internal waves are gravity waves that oscillate within a fluid medium, rather than on its surface. See Laurent et al. [2012]. Indeed gravity waves are generated in a fluid medium or at the interface between two media when the force of gravity or buoyancy tries to restore equilibrium. An example of such an interface is that between the atmosphere and the ocean, which gives rise to wind waves.

Inverse dispersion: special kind of dispersion with the lower frequencies traveling faster than higher ones (see also **Normal dispersion**).

Inverse problems: is the process of calculating from a set of observations the causal factors that produced them (for example inferring the seismic properties in the Earth knowing seismograms recorded at its surface). We also call this approach "inversion".

Inversion: see **Inverse problems**.

Isotropic: having properties that are identical in all directions (see also **Anisotropic**).

Large-aperture array: such an instrument is composed of a large number of small, fixed receiver elements coupled to appropriate systems which can be arranged in a regular or random pattern. It can be used, for example, to obtain information on the direction of the arrival of the "beam" (see also **Beamforming**).

Least squares method: form of mathematical regression analysis that finds the best fit for a data set. "Least squares" means that the overall solution minimises the sum of the squares of the constructed residuals by subtracting real and synthetic data.

Legendre polynomials: often written P_n with $n \in \mathbb{R}$ they are solutions to Legendre's differential equation: $\frac{\mathrm{d}}{\mathrm{d}x}\left[(1-x^2)\,\frac{\mathrm{d}P_n(x)}{\mathrm{d}x}\right] + n(n+1)P_n(x) = 0\,.$

Lg: wavegroup observed at larger regional distances and caused by superposition of multiple S-wave reverberations and S to P and/or P to S conversions inside the whole crust. The maximum energy travels with a group velocity around 3.5 km/s.

Love wave: in seismology, Love waves are surface seismic waves that cause horizontal shifting of the Earth during an earthquake (see Figure G.1). Love waves travel with a lower velocity than P- or S- waves, but faster than Rayleigh waves. These waves are observed only when there is a low velocity layer overlying a high velocity layer/ sub-layers (see also **Rayleigh wave**).

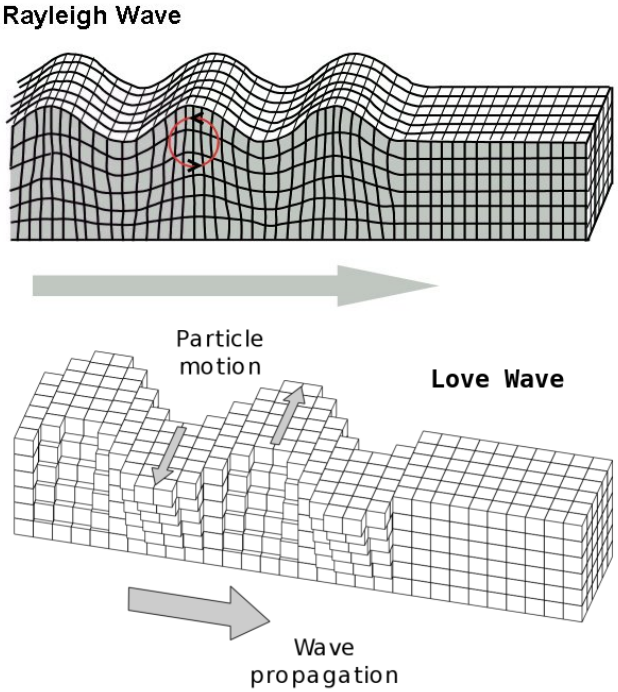

Figure G.1 – Comparison of Love and Rayleigh wave particle motions. Adapted from Wikipedia.

Magma dike intrusion: formation of a sheet of magmatic rock in a fracture of a pre-existing rock body. Magmatic dikes form when magma intrudes into a crack then crystallizes as a sheet intrusion, either cutting across layers of rock or through a contiguous mass of rock.

Matched-Field processing: signal processing technique that has a variety of applications in underwater acoustics and is based on the comparison between measured data and predictions made for these data that are calculated from an underwater sound propagation model (McGraw-Hill & Parker [2003]).

Megathrust: a sudden slip along a fault between a subducting and an overriding plate; results in a major earthquake

Mesoscale variability/noise: the mesoscale variability generally refers to ocean signals (eddies for example) with space scales of 50-500 km and time scales of 10-100 days.

Mid-ocean spreading ridge: the mid-ocean ridge is an extensive underwater mountain range that is formed because of the constantly altering tectonic plates and the heat that is emitted from the core of the earth. The mid-ocean ridge is a phenomenon that is responsible for dividing the oceans and since the heat that is emitted from the earth is continuous, it results in these mid-ocean ridges being altered and created continuously at the same time. See also **Seafloor spreading**.

Modal decomposition: decomposition of the acoustic field into a combination of a set of elementary functions called normal modes whose contributions depend in particular on the conditions that are considered at the borders of the domain. We speak of a modal basis. Some modes are propagative and others are evanescent.

Mode coupling: exchange of energy between modes while they evolve (see **Modal decomposition** and **Adiabatic approximation**).

Moment centroid (of an earthquake): center of energy release, usually near the center of the rupture area. The earthquake depth is usually taken as that of the **hypocenter**, even if the fault ruptures to the surface.

Momentum equation: it is equation (3.1) or equation (3.3).

Munk profile: classical idealized ocean sound-speed depth profile described by Munk [1974]. It is represented as a dark blue line in Figure 4.11, right.

Nx2D simulation: reconstruction of a 3-D field by running a number N of axisymmetric 2-D simulations in range and depth.

Non-isotropic: see **Anisotropic**.

Normal dispersion: special kind of dispersion with the higher frequencies traveling faster than lower ones (see also **Inverse dispersion**).

Normal-fault: a normal fault is a dip-slip fault in which one side drops down relatively to the other side (see **Dip-slip** and **Reverse fault**).

Normal mode: see **Modal decomposition**.

Ocean Bottom Seismometer (OBS): instrument that is designed to record the earth motion under oceans (or lakes) from man-made and natural sources.

Offset (of a Gaussian distribution): offset of the Gaussian function from zero.

Onset time (of phase): time interval between the appearance of the phase envelope above the ambient noise and its first peak (see also **Rise time**).

Parabolic approximation: see the box on page 47.

Pg wave: at short distances between an event and a receiving station, the Pg wave refers to the upgoing P-wave from the source. At larger distances the so called Pg phase includes arrivals resulting from multiple P-wave reverberations within the entire crust that propagate at a group velocity around 5.8 km.s^{-1}.

Phase velocity: velocity at which a phase of the wave (for example, a crest) travels (see also **Group velocity**).

Pn wave: compressional wave refracted on the boundary between the upper Earth mantle and the crust.

Power Spectral Density: describes the distribution of power into frequency components composing a time series. According to Fourier analysis, any physical signal can be decomposed into a number of discrete frequencies, or a spectrum of frequencies over a continuous range. The statistical average of a signal as analyzed in terms of its frequency content, is called its spectrum.

Prograde particle motion: circular movement, clockwise, caused by the passage of a wave. In this definition it is assumed that the wave is seen traveling from left to right (see also **Retrograde particle motion**).

Propagative mode: mode that actually propagate in the medium (see **Modal decomposition**)

Quadrature: in numerical analysis, a quadrature rule is an approximation of the definite integral of a function, usually stated as a weighted sum of function values at specified points within the domain of integration.

Quality factor: quantifies the effects of anelastic attenuation on the seismic wavelet caused by fluid movement and grain boundary friction. Noted Q it is usually defined by the equation $\frac{A(x)}{A_0} = \exp\left[\frac{-\omega x}{2cQ}\right]$ where ω is the angular frequency, c is the medium velocity and $\frac{A(x)}{A_0}$ is the amplitude decay of the wave over distance x.

Radiation: emission or transmission of energy in the form of waves or particles through space or through a material medium.

Radiation condition (Sommerfeld): this condition has been defined as "the energy which is radiated from the sources must scatter to infinity; no energy may be radiated from infinity into the field".

Radiation pattern: refers to the directional (angular) dependence of the strength of the waves from a source.

Range: the magnitude of a horizontal distance to a source.

Ray theory: can be derived from the wave equation (equation (3.1) or equation (3.3)) when some simplifying assumptions are introduced. It is essentially a high-frequency approximation allowing to consider the propagation of sound on the basis of the concept of rays considered as lines along which the acoustic energy is transported.

Rayleigh–Kirchhoff approximation: see e.g. Ogilvy & Merklinger [1991].

Rayleigh wave: type of surface wave that travels near the surface of solids (see Figure G.1). Rayleigh waves include both longitudinal and transverse motions that decrease exponentially in amplitude as distance from the surface increases (see also **Love wave**).

Refraction: refraction refers to the deflection of a wave at the interface between two media of different velocities.

Retrograde particle motion: circular movement, anti-clockwise, caused by the passage of a wave. In this definition it is assumed that the wave is seen traveling from left to right (see also **Prograde particle motion**).

Reverse fault: a reverse fault is a dip-slip fault in which one of the rocky block is pushed up relatively to the other side (see **Normal fault** and **Dip-slip**)

Richter scale: magnitude scale developed in 1935 by Charles F. Richter as a mathematical device to compare the size of earthquakes. The magnitude of an earthquake is determined from the logarithm of the amplitude of waves recorded by seismographs. Note that most seismological authorities now use other scales.

Ricker wavelet: second derivative of a Gaussian wavelet. Also called Mexican hat because of its shape.

Ridge: see **Mid-ocean spreading ridge**.

Rise time (of phase): Time between the emergence of the phase and its peak amplitude (see also **Onset time** and Figure B on page 13).

RMS (Root-mean-square): square root of the mean square (the arithmetic mean of the squares of a set of numbers).

Salinity: is the saltiness or amount of salt dissolved in a body of water.

Scaling (efficiency): this measure indicates how efficient a program is as the number of parallel processing elements increases.

Scattering: general physical process where the waves are forced to deviate from a straight trajectory by one or more paths due to localized non-uniformities in the medium through which they pass.

Seafloor spreading: seafloor spreading is a process that occurs at mid-ocean ridges, where new oceanic crust is formed through volcanic activity and then gradually moves away from the ridge. Seafloor spreading helps explain continental drift in the theory of plate tectonics.

Seismic moment: usually noted M_0 it is a measure of the strength of an earthquake incorporating the length of the fractured region.

Seismograph: see **Seismometer**.

Seismometer: also called seismograph, it is an instrument that measures motion of the ground, caused by, for example, an earthquake, a volcanic eruption, or the use of explosives.

Seismogram: graph output by a seismograph. It is a record of the ground motion at a measuring station as a function of time. Seismograms typically record motions in three Cartesian axes (x, y, and z), with the z axis perpendicular to the Earth's surface and the x- and y- axes parallel to the surface.

Sg wave: at short distances between an event and a receiving station, the Sg wave refers to the upgoing S-wave from the source.

SH waves: an S wave polarized in the horizontal plane (see Also **SV waves**)

Shelf (continental): underwater landmass which extends from a continent, resulting in an area of relatively shallow water known as a shelf sea. Much of the shelves were exposed during glacial periods and interglacial periods.

Signal-to-noise ratio: measure that compares the level of a desired signal to the level of background noise.

Shallow earthquakes: shallow (focus) earthquake in seismology is an earthquake with a hypocenter at depth comprised between 0 and 70 km (see also **Intermediate earthquakes** and **Deep earthquakes**).

Slab: a slab is the portion of a tectonic plate that is being subducted.

Snell's law: formula used to describe the relationship between the angles of incidence and refraction, when waves pass through a boundary between two different isotropic media. See equation 4.1 on page 98.

Sonar: originally an acronym for SOund Navigation And Ranging. Sonar is a technique that uses sound propagation (usually underwater, as in submarine navigation) to navigate, communicate with or detect objects on or under the surface of the water, such as other vessels.

Source image method: this method is based on the decomposition of the total sound field into a sum of contributions from a series of image sources. Each image source corresponds to the waves emitted by the real source and that has undergone a number of interactions with the boundaries of the studied domain.

Spectrogram: visual representation of the spectrum of frequencies of sound or other signal as they vary with time. See also **Power Spectral Density**.

Spectrum: see **Power Spectral Density**.

STA/LTA (ratio): ratio of a short term average amplitude (STA) to a long term average (LTA) of a signal. This ratio is used as a basic method for automatic event detection.

Stochastic: term applied to processes that have random characteristics.

Stoneley-Scholte interface waves: surface wave (interface wave) propagating at an interface between a fluid and an elastic solid medium

Strain: small changes in length and volume associated with deformation of the earth by tectonic stresses or by the passage of seismic waves.

Stress: force per unit area acting on a plane within a body. Six values are required to characterize completely the stress at a point: three normal components and three shear components.

Strike-slip: strike-slip faults are inclined fractures where the blocks have mostly shifted horizontally.

Strong-motion seismometer: also called accelerograph, this instrument can measure ground acceleration. Strong-motion seismometers are not as sensitive to ground motions as classical seismometers but they stay on scale during the strongest seismic shaking.

Supercritical incidence: an acoustic ray traveling from a slow medium to a fast medium is at supercritical incidence when its incidence angle (angle with respect to the normal at the interface) is above the critical angle. The ray is then reflected at the interface between the two media. See also **Critical angle**, **Ray theory** and **Total internal reflection**.

Surface waves: a surface wave is a seismic seismic wave that is trapped near the surface of the earth.

SV waves: an S wave polarized in the vertical plane (see also **SH waves**)

Teleseismic: teleseismic is pertaining to earthquakes at distances greater than 1,000 km from the measurement site.

Total internal reflection: phenomenon which occurs when a propagated wave strikes a medium boundary at an angle larger than a particular critical angle with respect to the normal to the surface. The wave cannot pass through and is entirely reflected. See also **Critical angle**, **Ray theory** and **Supercritical incidence**.

Transducer: instrument that converts electrical signals into ultrasound and conversely.

Transfer function: mathematical function giving the corresponding output value for each possible value of the input to the system considered.

Transmission Loss: accumulated decrease in intensity of a waveform energy as a wave propagates outwards from a source, or as it propagates through a certain area or through a certain type of structure.

Triplet station: station comprising three hydrophones which allows back-azimuth determination to be carried out. See Graeber & Piserchia [2004].

Triplication: folding of a wavefront. See e.g. Thomsen & Dellinger [2003].

Troposhere: lowest layer of Earth's atmosphere, and is also where nearly all weather conditions take place. It contains approximately 75% of the atmosphere's mass and 99% of the total mass of water vapor and aerosols. The average depths of the troposphere are 18 km in the tropics, 17 km in the mid latitudes, and 6 km in the polar regions in winter.

Tsunami earthquakes: earthquakes anomalously efficient in its tsunami generation than expected from their conventional seismic waves.

Tsunamigenic earthquakes: earthquakes that generated a detectable tsunami.

Virtual source method: based on modeling a boundary or an interface by a collection of sources with unknown complex amplitudes. The functions representing the sources must satisfy the wave equation and the radiation condition in the far field. See e.g. Abawi & Porter [2007].

Wadati-Benioff zone: dipping tabular zone beneath a subduction zone.

Wavefront: locus of points characterized by propagation of positions of identical phase (crests or troughs for example).

Wave-number-integration: see chapter 4 of Jensen et al. [2011].

Wedge apex: wedge summit.

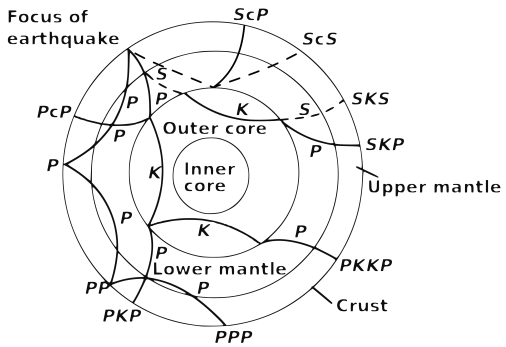

Figure G.2 – The nomenclature should be clear after having look at this image. Cross section of the whole Earth, showing the complexity of paths of earthquake waves. The paths curve because the different rock types found at different depths change the speed at which the waves travel. Solid lines marked P are compressional waves; dashed lines marked S are shear waves. S waves do not travel through the core but may be converted to compressional waves (marked K) on entering the core (PKP, SKS). Waves may be reflected at the surface (PP, PPP, SS). Adapted from the United States Geological Survey website.

Bibliography

Abawi, A. T., 2002. An energy-conserving one-way coupled mode propagation model, *Journal of the Acoustical Society of America*, **111**(1), 160–167.

Abawi, A. T. & Porter, M. B., 2007. Propagation in an elastic wedge using the virtual source technique, *Journal of the Acoustical Society of America*, **121**(3), 1374–1382.

Abdolali, A., Cecioni, C., Bellotti, G., & Kirby, J. T., 2015. Hydro-acoustic and tsunami waves generated by the 2012 Haida Gwaii earthquake: Modeling and in situ measurements, *Journal of Geophysical Research: Oceans*, **120**(2), 958–971, doi: 10.1002/2014JC010385.

Abe, K., 1973. Tsunami and mechanism of great earthquakes, *Physics of the Earth and Planetary Interiors*, **7**(2), 143–153, doi: 10.1016/0031-9201(73)90004-6.

Accaino, F., Catalano, R., Di Marzo, L., Giustiniani, M., Tinivella, U., Nicolich, R., Sulli, A., Valenti, V., & Manetti, P., 2011. A crustal seismic profile across Sicily, *Tectonophysics*, **508**(1), 52–61.

Achenbach, J. D., 1973. *Wave Propagation in Elastic Solids*, North-Holland, Amsterdam, The Netherlands.

Acosta Minolia, C. A. & Kopriva, D. A., 2011. Discontinuous Galerkin spectral element approximations on moving meshes, *J. Comput. Phys.*, **230**(5), 1876–1902, doi: 10.1016/j.jcp.2010.11.038.

Adams, R. D., 1979. T-phase recordings at Rarotonga from underground nuclear explosions, *Geophysical Journal of the Royal Astronomical Society*, **58**(2), 361–369, doi: 10.1111/j.1365-246X.1979.tb01030.x.

Ainslie, M. A. & McColm, J. G., 1998. A simplified formula for viscous and chemical absorption in sea water, *Journal of the Acoustical Society of America*, **103**(3), 1671–1672.

Aki, K. & Richards, P. G., 1980. *Quantitative seismology, theory and methods*, W. H. Freeman, San Francisco, USA, 700 pages.

Alterman, Z. & Karal Jr, F., 1968. Propagation of elastic waves in layered media by finite difference methods, *Bulletin of the Seismological Society of America*, **58**(1), 367–398.

Araki, E., Stephen, R. A., Shinohara, M., Kanazawa, T., & Suyehiro, K., 2004. T-phase observed at deep seafloor boreholes, in *AGU Fall Meeting Abstracts*.

Arnold, J. M. & Felsen, L. B., 1983. Rays and local modes in a wedge-shaped ocean, *Journal of the Acoustical Society of America*, **73**(4), 1105–1119.

Arnold, J. M. & Felsen, L. B., 1984. Intrinsic modes in a nonseparable ocean waveguide, *Journal of the Acoustical Society of America*, **76**(3), 850–860.

Astafyeva, E., Lognonné, P., & Rolland, L., 2011. First ionospheric images of the seismic fault slip on the example of the tohoku-oki earthquake, *Geophysical Research Letters*, **38**(22).

ATOC Consortium, 1998. Ocean climate change: Comparison of acoustic tomography, satellite altimetry, and modeling, *Science*, **281**(5381), 1327–1332, doi: 10.1126/science.281.5381.1327.

Aubrat, J., 1963. Ondes T réfléchies dans la mer des antilles (Reflected T-waves in the Caribbean Sea), *Annales de Géophysique*, **19**, 386.

Aubrat, J., 1965. *Ondes T dans la mer des Antilles (T-waves in the Caribbean Sea)*, ORSTOM, Paris, France, 191 pages.

Aulanier, F., Nicolas, B., Mars, J. I., Roux, P., & Brossier, R., 2013. Shallow-water acoustic tomography from angle measurements instead of travel-time measurements, *Journal of the Acoustical Society of America*, **134**(4), EL373–EL379.

Baggeroer, A. B., Scheer, E. K., NPAL Group (and Colosi, J., Cornuelle, B., Dushaw, B., Dzieciuch, M., Howe, B., Mercer, J., Munk, W., Spindel, R., & Worcester, P., 2005. Statistics and vertical directionality of low-frequency ambient noise at the North Pacific Acoustics Laboratory site, *Journal of the Acoustical Society of America*, **117**(3), 1643–1665.

Balanche, A., Guennou, C., Goslin, J., & Mazoyer, C., 2009. Generation of hydroacoustic signals by oceanic subseafloor earthquakes: a mechanical model, *Geophysical Journal International*, **177**(2), 476–480.

Båth, M., 1954. A study of T phases recorded at the Kiruna seismograph station, *Tellus*, **6**(1), 63–72.

Båth, M. & Shahidi, M., 1971. T-phases from Atlantic earthquakes, *Pure and Applied Geophysics*, **92**(1), 74–114, doi: 10.1007/BF00874995.

Bathe, K.-J., 2006. *Finite element procedures*, Klaus-Jurgen Bathe.

Bécache, E., Joly, P., & Tsogka, C., 2000. An analysis of new mixed finite elements for the approximation of wave propagation problems, *SIAM Journal on Numerical Analysis*, **37**(4), 1053–1084.

Becker, J. J., Sandwell, D. T., Smith, W. H. F., Braud, J., Binder, B., Depner, J., Fabre, D., Factor, J., Ingalls, S., Kim, S.-H., Ladner, R., Marks, K., Nelson, S., Pharaoh, A., Trimmer, R., Rosenberg, J. V., Wallace, G., & Weatherall, P., 2009. Global bathymetry and elevation data at 30 arc seconds resolution: SRTM30_PLUS, *Marine Geodesy*, **32**(4), 355–371, doi: 10.1080/01490410903297766.

Ben-Menahem, A. & Toksöz, M. N., 1963. Source-mechanism from spectra of long-period seismic surface waves., *Bulletin of the Seismological Society of America*, **53**(5), 905–919.

Bérenger, J. P., 1994. A Perfectly Matched Layer for the absorption of electromagnetic waves, *J. Comput. Phys.*, **114**(2), 185–200.

Bernardi, C., Maday, Y., & Patera, A. T., 1994. A new nonconforming approach to domain decomposition: the Mortar element method, in *Nonlinear partial differential equations and their applications*, Séminaires du Collège de France, pp. 13–51, Pitman, Paris.

Bernardi, C., Dauge, M., Maday, Y., & Azaïez, M., 1999. *Spectral methods for axisymmetric domains*, Series in applied mathematics, Gauthier-Villars, Paris, France, 358 pages.

Bevans, D. A. & Buckingham, M. J., 2017. Estimating the sound speed of a shallow-water marine sediment from the head wave excited by a low-flying helicopter, *Journal of the Acoustical Society of America*, **142**(4), 2273–2287, doi: 10.1121/1.5007953.

Biot, M. A., 1952. The interaction of Rayleigh and Stoneley waves in the ocean bottom, *Bulletin of the Seismological Society of America*, **42**(1), 81–93.

Blackman, D. K., Nishimura, C. E., & Orcutt, J. A., 2000. Seismoacoustic recordings of a spreading episode on the Mohns Ridge, *Journal of Geophysical Research: Solid Earth*, **105**(B5), 10961–10973.

Boatwright, J. & Choy, G. L., 1986. Teleseismic estimates of the energy radiated by shallow earthquakes, *J. Geophys. Res.*, **91**(B2), 2095–2112, doi: 10.1029/JB091iB02p02095.

Bohnenstiehl, D. R., 2007. Comment on "the directionality of acoustic T-phase signals from small magnitude submarine earthquakes" [j. acoust. soc. am. 119, 3669-3675 (2006)], *Journal of the Acoustical Society of America*, **121**(3), 1293–1296, doi: 10.1121/1.2435982.

Bohnenstiehl, D. R. & Tolstoy, M., 2003. Comparison of teleseismically and hydroacoustically derived earthquake locations along the north-central Mid-Atlantic ridge and equatorial East Pacific rise, *Seismological Research Letters*, **74**(6), 791–802.

Bohnenstiehl, D. R., Dziak, R. P., Matsumoto, H., & Lau, T.-K. A., 2013. Underwater acoustic records from the March 2009 eruption of Hunga Ha'apai-Hunga Tonga volcano in the Kingdom of Tonga, *Journal of Volcanology and Geothermal Research*, **249**, 12–24, doi: 10.1016/j.jvolgeores.2012.08.014.

Boore, D. M., 1972. Finite difference methods for seismic wave propagation in heterogeneous materials, in *Methods in Computational Physics: Advances in Research and Applications*, vol. 11, pp. 1–37, Elsevier.

Borisov, D. & Singh, S. C., 2015. Three-dimensional elastic full waveform inversion in a marine environment using multicomponent ocean-bottom cables: a synthetic study, *Geophysical Journal International*, **201**(3), 1215–1234.

Bornstein, G., Biescas, B., Sallarès, V., & Mojica, J., 2013. Direct temperature and salinity acoustic full waveform inversion, *Geophysical Research Letters*, **40**(16), 4344–4348.

Bottero, A., Cristini, P., Komatitsch, D., & Asch, M., 2016a. An axisymmetric time-domain spectral-element method for full-wave simulations: Application to ocean acoustics, *Journal of the Acoustical Society of America*, **140**(5), 3520–3530, doi: 10.1121/1.4965964.

Bottero, A., Gesret, A., Romary, T., Noble, M., & Maisons, C., 2016b. Stochastic seismic tomography by interacting markov chains, *Geophysical Journal International*, **207**(1), 374–392.

Brekhovskikh, L. M., 1949. On the propagation of sound in the underwater sound channel, *Dokl. Akad. Nauk. SSSR*, **69**, 157–160.

Brekhovskikh, L. M. & Godin, O. A., 1990. *Acoustics of layered media I*, vol. 5 of **Springer Series on Wave phenomena**, Springer-Verlag, Berlin, Germany, 240 pages.

Brekhovskikh, L. M. & Godin, O. A., 1999. *Wave Propagation in a Range Dependent Waveguide*, pp. 243–360, Springer Berlin Heidelberg, Berlin, Heidelberg.

Brekhovskikh, L. M. & Godin, O. A., 2013. *Acoustics of layered media II: point sources and bounded beams*, vol. 10, Springer Science & Business Media.

Brekhovskikh, L. M. & Lysanov, Y. P., 1982. *Fundamentals of Ocean Acoustics*, Springer Series in Electrophysics, New York.

Brissaud, Q., Martin, R., Garcia, R. F., & Komatitsch, D., 2016. Finite-difference numerical modelling of gravitoacoustic wave propagation in a windy and attenuating atmosphere, *Geophysical Journal International*, **206**(1), 308–327.

Brissaud, Q., Martin, R., Garcia, R. F., & Komatitsch, D., 2017. Hybrid galerkin numerical modelling of elastodynamics and compressible navier-stokes couplings: applications to seismo-gravito acoustic waves, *Geophysical Journal International*, **210**(2), 1047–1069.

Broggini, F., Vasmel, M., Robertsson, J. O. A., & van Manen, D.-J., 2017. Immersive boundary conditions: Theory, implementation, and examples, *Geophysics*, **82**(3), T97–T110, doi: 10.1190/geo2016-0458.1.

Brown, P., Assink, J., Astiz, L., Blaauw, R., Boslough, M., Borovička, J., Brachet, N., Brown, D., Campbell-Brown, M., Ceranna, L., et al., 2013. A 500-kiloton airburst over chelyabinsk and an enhanced hazard from small impactors, *Nature*, **503**(7475), 238.

Buckingham, M. J., 1987. Theory of three-dimensional acoustic propagation in a wedgelike ocean with a penetrable bottom, *Journal of the Acoustical Society of America*, **82**(1), 198–210, doi: 10.1121/1.395546.

Buckingham, M. J., 1992. *Ocean-acoustic propagation models*, EUR-OP.

Buckingham, M. J., 2003. On the sound field from a moving source in a viscous medium, *Journal of the Acoustical Society of America*, **114**(6), 3112–3118.

Buckingham, M. J., 2010. Geo-acoustic doppler spectroscopy: A novel acoustic technique for surveying the seabed, *AIP Conference Proceedings*, **1272**(1), 212–218, doi: 10.1063/1.3493064.

Buckingham, M. J. & Giddens, E. M., 2006. Theory of sound propagation from a moving source in a three-layer Pekeris waveguide, *Journal of the Acoustical Society of America*, **120**(4), 1825–1841.

Buckingham, M. J., Giddens, E. M., Pompa, J. B., Simonet, F., & Hahn, T. R., 2002a. Sound from a light aircraft for underwater acoustics experiments?, *Acta Acustica united with Acustica*, **88**(5), 752–755.

Buckingham, M. J., Giddens, E. M., Simonet, F., & Hahn, T. R., 2002b. Propeller noise from a light aircraft for low-frequency measurements of the speed of sound in a marine sediment, *Journal of Computational Acoustics*, **10**(04), 445–464.

Buckingham, M. J., Giddens, E. M., & Simonet, F., 2006. Inversion of the propeller harmonics from a light aircraft for the geoacoustic properties of marine sediments, in *Acoustic Sensing Techniques for the Shallow Water Environment*, pp. 257–263, Springer.

Buehler, J. S. & Shearer, P. M., 2015. T phase observations in global seismogram stacks, *Geophysical Research Letters*, **42**(16), 6607–6613, doi: 10.1002/2015gl064721.

Burton, P. W., Xu, Y., Qin, C., Tselentis, G.-A., & Sokos, E., 2004. A catalogue of seismicity in Greece and the adjacent areas for the twentieth century, *Tectonophysics*, **390**(1), 117–127.

Butler, R., 2006. Observations of polarized seismoacoustic T waves at and beneath the seafloor in the abyssal Pacific ocean, *Journal of the Acoustical Society of America*, **120**(6), 3599–3606.

Butler, R. & Lomnitz, C., 2002. Coupled seismoacoustic modes on the seafloor, *Geophysical Research Letters*, **29**(10).

Byerly, P. & Herrick, C., 1954. T phases from hawaiian earthquakes, *Bulletin of the Seismological Society of America*, **44**(2A), 113–121.

Byerly, P. & Wilson, J. T., 1936. Northern California earthquakes, April 1, 1934, to December 31, 1935, *Bulletin of the Seismological Society of America*, **26**(3), 207–213.

Calò, M., Dorbath, C., Luzio, D., Rotolo, S. G., & D'Anna, G., 2012. Seismic velocity structures of southern Italy from tomographic imaging of the Ionian slab and petrological inferences, *Geophysical Journal International*, **191**(2), 751–764, doi: 10.1111/j.1365-246X.2012.05647.x.

Cansi, Y. & Bethoux, N., 1985. T waves with long inland paths: Synthetic seismograms, *Journal of Geophysical Research: Solid Earth*, **90**(B7), 5459–5465, doi: 10.1029/JB090iB07p05459.

Capdeville, Y., Zhao, M., & Cupillard, P., 2015. Fast Fourier homogenization for elastic wave propagation in complex media, *Wave Motion*, **54**, 170–186, doi: 10.1016/j.wavemoti.2014.12.006.

Caplan-Auerbach, J. & Duennebier, F., 2001. Seismic and acoustic signals detected at Lo'ihi seamount by the Hawai'i Undersea Geo-Observatory, *Geochemistry, Geophysics, Geosystems*, **2**(5), n/a–n/a, doi: 10.1029/2000GC000113.

Caplan-Auerbach, J., Fox, C. G., & Duennebier, F. K., 2001. Hydroacoustic detection of submarine landslides on Kilauea volcano, *Geophysical Research Letters*, **28**(9), 1811–1813.

Caplan-Auerbach, J., Dziak, R. P., Bohnenstiehl, D. R., Chadwick, W. W., & Lau, T. K., 2014. Hydroacoustic investigation of submarine landslides at West Mata volcano, Lau Basin, *Geophysical Research Letters*, **41**(16), 5927–5934.

Carlson, A., Kalinowski, A. J., & Patel, J., 1976. Solutions of a general class of fluid structure problems by the finite element method, in *Naval Underwater Systems Center TR-5361*.

Carmona, E., Almendros, J., Alguacil, G., Soto, J. I., Luzón, F., & Ibáñez, J. M., 2015. Identification of T-waves in the Alboran sea, *Pure and Applied Geophysics*, **172**, 3179–3188, doi: 10.1007/s00024-014-1018-1.

Chaljub, E. & Valette, B., 2004. Spectral element modelling of three-dimensional wave propagation in a self-gravitating Earth with an arbitrarily stratified outer core, *Geophys. J. Int.*, **158**, 131–141.

Chaljub, E., Capdeville, Y., & Vilotte, J. P., 2003. Solving elastodynamics in a fluid-solid heterogeneous sphere: a parallel spectral-element approximation on non-conforming grids, *J. Comput. Phys.*, **187**(2), 457–491.

Chapman, N. R. & Marrett, R., 2006. The directionality of acoustic T-phase signals from small magnitude submarine earthquakes, *Journal of the Acoustical Society of America*, **119**(6), 3669–3675, doi: 10.1121/1.2195073.

Chapman, N. R. & Marrett, R., 2007. Reply to "comment on 'the directionality of acoustic T-phase signals from small magnitude submarine earthquakes' [j. acoust. soc. am. 119, 3669-3675 (2006)]", *Journal of the Acoustical Society of America*, **121**(3), 1297–1298, doi: 10.1121/1.2435984.

Chave, A. D., Duennebier, F. K., & Butler, R., 2000. Putting H2O in the ocean, *Oceanus*, **42**(1), 6.

Chen, C.-W., Huang, C.-F., Lin, C.-W., & Kuo, B.-Y., 2017. Hydroacoustic ray theory-based modeling of T wave propagation in the deep ocean basin offshore eastern Taiwan, *Geophysical Research Letters*, **44**(10), 4799–4805, doi: 10.1002/2017GL073516, 2017GL073516.

Chen, P.-F., Chen, K.-X., & Cheng, H.-Y., 2015. Frequent excitations of T waves by earthquakes in the South Mariana Arc, *Journal of Asian Earth Sciences*, **98**, 50–60.

Cheng, Y., 2014. Satellite-based AIS and its comparison with LRIT, *TransNav: International Journal on Marine Navigation and Safety of Sea Transportation*, **8**.

Chiu, C.-S., 1994. Downslope modal energy conversion, *Journal of the Acoustical Society of America*, **95**(3), 1654–1657, doi: 10.1121/1.408552.

Chotiros, N. P., 2017. *Acoustics of the Seabed as a Poroelastic Medium*, Springer.

Chung, E. T. & Engquist, B., 2006. Optimal discontinuous Galerkin methods for wave propagation, *SIAM Journal on Numerical Analysis*, **44**(5), 2131–2158.

Chunmei, Y., Liangang, L., Fangli, Q., & Wenyu, L., 2016. Three-dimensional analytical solution and numerical solution in a penetrable wedge-shaped waveguide, in *2016 IEEE/OES China Ocean Acoustics (COA)*, pp. 1–6, doi: 10.1109/COA.2016.7535827.

Clayton, J. D. & Rencis, J. J., 2000. Numerical integration in the axisymmetric finite element formulation, *Advances in Engineering Software*, **31**, 137–141.

Cohen, G., 2002. *Higher-order numerical methods for transient wave equations*, Springer-Verlag, Berlin, Germany, 349 pages.

Cohen, G. & Fauqueux, S., 2000. Mixed finite elements with mass-lumping for the transient wave equation, *Journal of Computational Acoustics*, **8**(01), 171–188.

Coles, J., Christian, E., Slifko, J., Niffenegger, C., & Rogers, M., 1946. Shockwave parameters from spherical TNT charges detonated underwater, *Underwater Explosives Laboratory, Woods Hole, MA*.

Collins, M. D. & Siegmann, W. L., 2017. Treatment of variable topography with the seismoacoustic parabolic equation, *IEEE Journal of Oceanic Engineering*, **42**(2), 488–493, doi: 10.1109/JOE.2016.2571818.

Collins, M. P., 1936. Bulletin number 5, *Harvard University Seismograph Station*, **5**, 23.

Colosi, J. A. & Flatté, S. M., 1996. Mode coupling by internal waves for multimegameter acoustic propagation in the ocean, *Journal of the Acoustical Society of America*, **100**(6), 3607–3620.

Cook, R. W. & Stevens, J. L., 1998. TP phase observations at the PIDC, *Transactions of the American Geophysical Union*, **79**, F558.

Cooke, R. J. S., 1967. Observations of the seismic T phase at Macquarie Island, *New Zealand Journal of Geology and Geophysics*, **10**(5), 1212–1225, doi: 10.1080/00288306.1967.10420212.

Coppens, A. B. & Sanders, J. V., 1980. Propagation of sound from a fluid wedge into a fast fluid bottom, in *Bottom-Interacting Ocean Acoustics*, pp. 439–450, eds Kuperman, W. A. & Jensen, F. B., Springer, Boston, MA, USA.

Coulomb, J. & Molard, P., 1949. Ondes séismiques au fond de la mer des Antilles (Seismic waves at the bottom of Caribbean sea), *Ann. Géophys.*, **5**, 212–214.

Coulomb, J. & Molard, P., 1952. Propagation des ondes séismiques T dans la mer des Antilles (Seismic waves in the Caribbean sea), *Ann. Géophys.*, **8**, 264–266.

Cowen, J. P., Baker, E. T., & Embley, R. W., 2004. Detection of and response to mid-ocean ridge magmatic events: Implications for the subsurface biosphere, *The Subseafloor Biosphere at Mid-Ocean Ridges*, pp. 227–243.

Cristini, P. & Komatitsch, D., 2012. Some illustrative examples of the use of a spectral-element method in ocean acoustics, *Journal of the Acoustical Society of America*, **131**(3), EL229–EL235, doi: 10.1121/1.3682459.

Dahlen, F. A. & Tromp, J., 1998. *Theoretical Global Seismology*, Princeton University Press, Princeton, New-Jersey, USA, 944 pages.

De Groot-Hedlin, C., 2004. Criteria for discretization of seafloor bathymetry when using a stairstep approximation: Application to computation of T-phase seismograms, *Journal of the Acoustical Society of America*, **115**(3), 1103–1113, doi: 10.1121/1.1643361.

De Groot-Hedlin, C., 2005. Estimation of the rupture length and velocity of the Great Sumatra earthquake of dec 26, 2004 using hydroacoustic signals, *Geophysical Research Letters*, **32**(11), n/a–n/a, doi: 10.1029/2005GL022695, L11303.

De Groot-Hedlin, C., 2008. A finite difference solution to the Helmholtz equation in a radially symmetric waveguide: application to near-source scattering in ocean acoustics, *Journal of Computational Acoustics*, **16**(03), 447–464, doi: 10.1142/S0218396X08003683.

De Groot-Hedlin, C. & Orcutt, J. A., 1999. Synthesis of earthquake-generated T-waves, *Geophysical Research Letters*, **26**(9), 1227–1230, doi: 10.1029/1999GL900205.

De Groot-Hedlin, C. & Orcutt, J. A., 2000. Detection of T-phases at island seismic stations: Dependence on seafloor slope, seismic velocity and roughness, Tech. rep., Scripps Institution Of Oceanography La Jolla CA.

De Groot-Hedlin, C. & Orcutt, J. A., 2001a. Excitation of T-phases by seafloor scattering, *Journal of the Acoustical Society of America*, **109**(5), 1944–1954.

De Groot-Hedlin, C. & Orcutt, J. A., 2001b. T-phase observations in northern California: Acoustic to seismic coupling at a weakly elastic boundary, *Pure and Applied Geophysics*, **158**(3), 513–530, doi: 10.1007/PL00001193.

De Groot-Hedlin, C. & Orcutt, J. A., 2001c. *Monitoring the Comprehensive Nuclear-Test-Ban-Treaty: Hydroacoustics*, Springer.

De Groot-Hedlin, C., Blackman, D., & Orcutt, J., 2004. The use of hydroacoustic phases for the detection of oceanic events: Observations and numerical modeling, Tech. rep., Scripps Institution Of Oceanography La Jolla CA.

Deane, G. B. & Buckingham, M. J., 1993. An analysis of the three-dimensional sound field in a penetrable wedge with a stratified fluid or elastic basement, *Journal of the Acoustical Society of America*, **93**(3), 1319–1328, doi: 10.1121/1.405417.

Delaney, J. R., Kelley, D. S., Lilley, M. D., Butterfield, D. A., Baross, J. A., Wilcock, W. S. D., Embley, R. W., & Summit, M., 1998. The quantum event of oceanic crustal accretion: Impacts of diking at mid-ocean ridges, *Science*, **281**(5374), 222–230.

DeSanto, J. A., 1979. *Ocean Acoustics*, vol. 8 of **Topics in Current Physics**, Springer Berlin Heidelberg, Berlin, Heidelberg, Germany, 285 pages.

Desaubies, Y., Chiu, C.-S., & Miller, J. H., 1986. Acoustic mode propagation in a range-dependent ocean, *Journal of the Acoustical Society of America*, **80**(4), 1148–1160.

Dettmer, J., Dosso, S. E., & Holland, C. W., 2018. High performance computing methods for nonlinear bayesian uncertainty quantification, *Journal of the Acoustical Society of America*, **143**(3), 1925–1925, doi: 10.1121/1.5036286.

Deville, M. O., Fischer, P. F., & Mund, E. H., 2002. *High-Order Methods for Incompressible Fluid Flow*, Cambridge University Press, Cambridge, United Kingdom, 528 pages.

Dietz, R. S. & Sheehy, M. J., 1954. Transpacific detection of Myojin volcanic explosions by underwater sound, *GSA Bulletin*, **65**(10), 941, doi: 10.1130/0016-7606(1954)65[941:TDOMVE]2.0.CO;2.

Dormy, E. & Tarantola, A., 1995. Numerical simulation of elastic wave propagation using a finite volume method, *Journal of Geophysical Research: Solid Earth*, **100**(B2), 2123–2133.

Dosso, S. E. & Dettmer, J., 2011. Bayesian matched-field geoacoustic inversion, *Inverse Problems*, **27**(5), 055009.

D'Spain, G. L., Berger, L. P., Kuperman, W. A., Stevens, J. L., & Baker, G. E., 2001. Normal mode composition of earthquake T phases, *Pure and Applied Geophysics*, **158**(3), 475–512, doi: 10.1007/PL00001192.

Duennebier, F. K., 1968. Spectral variation of the T phase, Tech. rep., Hawaii Univ. Honolulu Inst. Of Geophysics.

Duennebier, F. K. & Johnson, R. H., 1967. T-phase sources and earthquake epicenters in the Pacific basin, Tech. rep., Hawaii Institute Of Geophysics University of Hawaii Honolulu.

Dumbser, M., Käser, M., & De La Puente, J., 2007. Arbitrary high-order finite volume schemes for seismic wave propagation on unstructured meshes in 2D and 3D, *Geophys. J. Int.*, **171**(2), 665–694.

Dunn, R. A., 2015. Ocean acoustic reverberation tomography, *Journal of the Acoustical Society of America*, **138**(6), 3458–3469.

Dushaw, B. D., Howe, B. M., Cornuelle, B. D., Worcester, P. F., & Luther, D. S., 1995. Barotropic and baroclinic tides in the central north Pacific ocean determined from long-range reciprocal acoustic transmissions, *Journal of Physical Oceanography*, **25**(4), 631–647.

Dushaw, B. D., Sagen, H., & Beszczynska-Möller, A., 2016. On the effects of small-scale variability on acoustic propagation in Fram Strait: The tomography forward problem, *Journal of the Acoustical Society of America*, **140**(2), 1286–1299, doi: 10.1121/1.4961207.

Dziak, R. P., 2001. Empirical relationship of T-wave energy and fault parameters of northeast Pacific ocean earthquakes, *Geophysical Research Letters*, **28**(13), 2537–2540, doi: 10.1029/2001GL012939.

Dziak, R. P. & Fox, C. G., 1999. The january 1998 earthquake swarm at Axial Volcano, Juan de Fuca Ridge: Hydroacoustic evidence of seafloor volcanic activity, *Geophysical Research Letters*, **26**(23), 3429–3432.

Dziak, R. P., Bohnenstiehl, D. R., Matsumoto, H., Fox, C. G., Smith, D. K., Tolstoy, M., Lau, T. K., Haxel, J. H., & Fowler, M. J., 2004a. P-and T-wave detection thresholds, Pn velocity estimate, and detection of lower mantle and core P-waves on ocean sound-channel hydrophones at the Mid-Atlantic Ridge, *Bulletin of the Seismological Society of America*, **94**(2), 665–677.

Dziak, R. P., Smith, D. K., Bohnenstiehl, D. R., Fox, C. G., Desbruyeres, D., Matsumoto, H., Tolstoy, M., & Fornari, D. J., 2004b. Evidence of a recent magma dike intrusion at the slow spreading Lucky Strike segment, Mid-Atlantic Ridge, *Journal of Geophysical Research: Solid Earth*, **109**(B12).

Dziak, R. P., Hammond, S. R., & Fox, C. G., 2011. A 20-year hydroacoustic time series of seismic and volcanic events in the northeast Pacific ocean, *Oceanography*, **24**.

Dziak, R. P., Bohnenstiehl, D. R., & Smith, D. K., 2012. Hydroacoustic monitoring of oceanic spreading centers: Past, present, and future, *Oceanography*, **25**(1), 116–127.

Dzieciuch, M. & Cornuelle, B., 2017. Calculating a sensitivity kernel for the final cutoff of received energy in a broadband channel impulse response, *The Journal of the Acoustical Society of America*, **142**(4), 2718–2718.

Eaton, J. P., Richter, D. H., & Ault, W. U., 1961. The tsunami of may 23, 1960, on the Island of Hawaii, *Bulletin of the Seismological Society of America*, **51**(2), 135–157.

Eiden, G. & Martinsen, T., 2010. Vessel density mapping, Tech. rep., Luxspace Sarl.

Erickson, J., 2014. Efficiently Hex-meshing things with topology, *Discrete Comput. Geom.*, **52**(3), 427–449.

Evans, R. B., 1983. A coupled mode solution for acoustic propagation in a waveguide with stepwise depth variations of a penetrable bottom, *Journal of the Acoustical Society of America*, **74**(1), 188–195, doi: 10.1121/1.389707.

Evernden, J. F., 1970. T-phase data on Kamchatka/Kurils earthquakes, *Bulletin of the Seismological Society of America*, **60**(4), 1061–1076.

Evers, L. G. & Snellen, M., 2015. Passive probing of the sound fixing and ranging channel with hydro-acoustic observations from ridge earthquakes, *Journal of the Acoustical Society of America*, **137**(4), 2124–2136.

Evers, L. G., Brown, D., Heaney, K. D., Assink, J. D., Smets, P. S. M., & Snellen, M., 2014. Evanescent wave coupling in a geophysical system: Airborne acoustic signals from the Mw 8.1 Macquarie ridge earthquake, *Geophysical Research Letters*, **41**(5), 1644–1650.

Everstine, G. C., 1981. A symmetric potential formulation for fluid-structure interaction, *ASME J. Sound Vib.*, **79**(1), 157–160.

Ewing, M. & Press, F., 1953. Mechanisms of T wave propagation, *Annales Géophysique*, **9**(3), 248.

Ewing, M. & Worzel, J. L., 1948. Long-range sound transmission, *Geological Society of America Memoirs*, **27**, 1–32.

Ewing, M., Woolard, G. P., Vine, A. C., & Worzel, J. L., 1946. Recent results in submarine geophysics, *GSA Bulletin*, **57**(10), 909.

Ewing, M., Tolstoy, I., & Press, F., 1950. Proposed use of the T phase in tsunami warning systems, *Bulletin of the Seismological Society of America*, **40**(1), 53–58.

Ewing, M., Press, F., & Worzel, J. L., 1952. Further study of the T phase, *Bull. seism. Soc. Am.*, **42**, 37–51.

Favier, N., Chevrot, S., & Komatitsch, D., 2004. Near-field influences on shear wave splitting and traveltime sensitivity kernels, *Geophys. J. Int.*, **156**(3), 467–482, doi: 10.1111/j.1365-246X.2004.02178.x.

Fichtner, A., 2010. *Full Seismic Waveform Modelling and Inversion*, Advances in Geophysical and Environmental Mechanics and Mathematics, Springer-Verlag, Berlin, Germany, 343 pages.

Finetti, I. R., 2005. *CROP project: deep seismic exploration of the central Mediterranean and Italy*, vol. 1, Elsevier.

Fix, G. J. & Marin, S. P., 1978. Variational methods for underwater acoustic problems, *Journal of Computational Physics*, **28**(2), 253–270, doi: 10.1016/0021-9991(78)90037-2.

Foreman, T. L., 1983. Ray modeling methods for range dependent ocean environments, Tech. rep., Texas University at Austin Applied Research Laboratory.

Fournier, A., Bunge, H.-P., Hollerbach, R., & Vilotte, J.-P., 2004. Application of the spectral-element method to the axisymmetric Navier-Stokes equation, *Geophys. J. Int.*, **156**(3), 682–700.

Fox, C. G. & Dziak, R. P., 1998. Hydroacoustic detection of volcanic activity on the Gorda ridge, February-March 1996, *Deep Sea Research Part II: Topical Studies in Oceanography*, **45**(12), 2513–2530, doi: 10.1016/S0967-0645(98)00081-2.

Fox, C. G. & Dziak, R. P., 1999. Internal deformation of the Gorda Plate observed by hydroacoustic monitoring, *Journal of Geophysical Research: Solid Earth*, **104**(B8), 17603–17615.

Fox, C. G., Dziak, R. P., Matsumoto, H., & Schreiner, A. E., 1994. Potential for monitoring low-level seismicity on the Juan de Fuca Ridge using military hydrophone arrays, *Marine Technology Society Journal*, **27**(4), 22–30.

Fox, C. G., Radford, W. E., Dziak, R. P., Lau, T.-K., Matsumoto, H., & Schreiner, A. E., 1995. Acoustic detection of a seafloor spreading episode on the juan de fuca ridge using military hydrophone arrays, *Geophysical Research Letters*, **22**(2), 131–134.

Fox, C. G., Matsumoto, H., & Lau, T.-K. A., 2001. Monitoring Pacific Ocean seismicity from an autonomous hydrophone array, *Journal of Geophysical Research: Solid Earth*, **106**(B3), 4183–4206.

Francois, R. E. & Garrison, G. R., 1982. Sound absorption based on ocean measurements. part ii: Boric acid contribution and equation for total absorption, *Journal of the Acoustical Society of America*, **72**(6), 1879–1890.

Frank, S. D., Collis, J. M., & Odom, R., 2012. Modeling oceanic T-phases and interface waves with a seismic source and parabolic equation solutions, in *Proceedings of Meetings on Acoustics ECUA'2012*, vol. 17(1), p. 070010, ASA.

Frank, S. D., Collis, J. M., & Odom, R. I., 2015. Elastic parabolic equation solutions for oceanic T-wave generation and propagation from deep seismic sources, *Journal of the Acoustical Society of America*, **137**(6), 3534–3543.

Freeman, S. E., D'Spain, G. L., Lynch, S. D., Stephen, R. A., Heaney, K. D., Murray, J. J., Baggeroer, A. B., Worcester, P. F., Dzieciuch, M. A., & Mercer, J. A., 2013. Estimating the horizontal and vertical direction-of-arrival of water-borne seismic signals in the northern Philippine sea, *Journal of the Acoustical Society of America*, **134**(4), 3282–3298.

Frosch, R. A., 1964. Underwater sound: Deep-ocean propagation, *Science*, **146**(3646), 889–894.

Gainville, O., Henneton, M., & Coulouvrat, F., 2017. A re-analysis of carancas meteorite seismic and infrasound data based on sonic boom hypothesis, *Geophysical Journal International*, **209**(3), 1913–1923, doi: 10.1093/gji/ggx122.

Galanopoulos, A. G. & Drakopoulos, J. C., 1974. A T phase recorded on an accelerogram, *Bulletin of the Seismological Society of America*, **64**(3-1), 717–719.

Gavrilov, A. N. & Mikhalevsky, P. N., 2001. Mode-coupling effects in acoustic thermometry of the Arctic ocean, in *Inverse Problems in Underwater Acoustics*, pp. 105–126, eds Taroudakis, M. I. & Makrakis, G. N., Springer, New York, USA.

Geller, R. J., 1976. Scaling relations for earthquake source parameters and magnitudes, *Bulletin of the Seismological Society of America*, **66**(5), 1501–1523.

Gerritsma, M. I. & Phillips, T. N., 2000. Spectral element methods for axisymmetric Stokes problems, *J. Comput. Phys.*, **164**(1), 81–103, doi: 10.1006/jcph.2000.6574.

Ghalib, H. A. A., Barazangi, M., & Isacks, B. L., 1983. Excitation of T phases from shallow and intermediate-depth earthquakes in the southern Vanuatu (New Hebrides) arc, *Bulletin of the Seismological Society of America*, **73**(6A), 1921–1928.

Godin, O. A., 2006. Anomalous transparency of water-air interface for low-frequency sound, *Physical review letters*, **97**(16), 164301.

Godin, O. A., 2007. Surface-to-volume wave conversion in shallow water with a gently sloping bottom, *Acoustical Physics*, **53**(6), 714–720, doi: 10.1134/S1063771007060097.

Godin, O. A., 2008a. Low-frequency sound transmission through a gas-liquid interface, *The Journal of the Acoustical Society of America*, **123**(4), 1866–1879.

Godin, O. A., 2008b. Sound transmission through water–air interfaces: New insights into an old problem, *Contemporary Physics*, **49**(2), 105–123.

Goh, J. T. & Schmidt, H., 1996. A hybrid coupled wave-number integration approach to range-dependent seismoacoustic modeling, *Journal of the Acoustical Society of America*, **100**(3), 1409–1420, doi: 10.1121/1.415988.

Goh, J. T., Schmidt, H., Gerstoft, P., & Seone, W., 1997. Benchmarks for validating range-dependent seismo-acoustic propagation codes, *IEEE journal of oceanic engineering*, **22**(2), 226–236.

Gokhberg, A. & Fichtner, A., 2016. Full-waveform inversion on heterogeneous hpc systems, *Computers & Geosciences*, **89**, 260–268.

Graeber, F. M. & Piserchia, P.-F., 2004. Zones of T-wave excitation in the NE Indian ocean mapped using variations in backazimuth over time obtained from multi-channel correlation of IMS hydrophone triplet data, *Geophysical Journal International*, **158**(1), 239–256.

Green, R., 1962. Tasmanian records or earthquake T-phases from New Zealand, *New Zealand Journal of Geology and Geophysics*, **5**(2), 322–330.

Grevemeyer, I., Weigel, W., Schüssler, S., & Avedik, F., 2001. Crustal and upper mantle seismic structure and lithospheric flexure along the Society Island hotspot chain, *Geophysical Journal International*, **147**(1), 123–140, doi: 10.1046/j.0956-540x.2001.01521.x.

Gropp, W. & Sterling, T., 2015. Tracking the trajectory to exascale and beyond, HPC Wire (www.hpcwire.com).

Grote, M. J., Schneebeli, A., & Schötzau, D., 2006. Discontinuous Galerkin finite element method for the wave equation, *SIAM Journal on Numerical Analysis*, **44**(6), 2408–2431.

Guilbert, J., Vergoz, J., Schissele, E., Roueff, A., & Cansi, Y., 2005. Use of hydroacoustic and seismic arrays to observe rupture propagation and source extent of the Mw = 9.0 Sumatra earthquake, *Geophysical Research Letters*, **32**(15), doi: 10.1029/2005GL022966.

Gutenberg, B. & Richter, C. F., 1954. *Seismicity of the Earth*, Princeton University Press, Princeton, N.J., 310 pages.

Hamada, N., 1985. T waves recorded by ocean bottom seismographs off the south coast of Tokai area central Honshu Japan, *Journal of Physics of the Earth*, **33**(5), 391–410, doi: 10.4294/jpe1952.33.391.

Hamilton, E. L., 1980. Geoacoustic modeling of the sea floor, *Journal of the Acoustical Society of America*, **68**(5), 1313–1340, doi: 10.1121/1.385100.

Hamilton, E. L., 1985. Sound velocity as a function of depth in marine sediments, *Journal of the Acoustical Society of America*, **78**(4), 1348–1355, doi: 10.1121/1.392905.

Hamilton, G., 1977. Time variations of sound speed over long paths in the ocean, in *International workshop on low-frequency propagation and noise*, vol. 1, pp. 7–30.

Hammond, S. R. & Walker, D. A., 1991. Ridge event detection: T-phase signals from the Juan de Fuca spreading center, *Marine Geophysical Researches*, **13**(4), 331–348, doi: 10.1007/BF00366282.

Hanson, J. A. & Bowman, J. R., 2006. Methods for monitoring hydroacoustic events using direct and reflected T waves in the Indian ocean, *Journal of Geophysical Research: Solid Earth (1978-2012)*, **111**(B2), doi: 10.1029/2004JB003609.

Hanson, J. A. & Given, H. K., 1998. Accurate azimuth estimates from a large aperture hydrophone array using T-phase waveforms, *Geophysical research letters*, **25**(3), 365–368.

Hanson, J. A., Given, H. K., & Berger, J., 1996. Earthquake activity near Ascension Island, South Atlantic Ocean, as seen by a combined seismic/hydrophone array, *Geothermics*, **25**(4-5), 507513–511519.

Hanson, J. A., Reasoner, C. L., & Bowman, J. R., 2006. Hydroacoustic propagation loss from reflection and transmission over shallow bathymetry in the Indian ocean, *28th Seismic Research Review: Ground-Based Nuclear Explosion Monitoring Technologies*.

Heaney, K. D. & Campbell, R. L., 2016. Three-dimensional parabolic equation modeling of mesoscale eddy deflection, *Journal of the Acoustical Society of America*, **139**(2), 918–926, doi: 10.1121/1.4942112.

Heaney, K. D., Campbell, R. L., & Snellen, M., 2013. Long range acoustic measurements of an undersea volcano, *Journal of the Acoustical Society of America*, **134**(4), 3299–3306.

Heaney, K. D., Prior, M., & Campbell, R. L., 2017. Bathymetric diffraction of basin-scale hydroacoustic signals, *Journal of the Acoustical Society of America*, **141**(2), 878–885, doi: 10.1121/1.4976052.

Hedlin, M. A., Drob, D., Walker, K., & de Groot-Hedlin, C., 2010. A study of acoustic propagation from a large bolide in the atmosphere with a dense seismic network, *Journal of Geophysical Research: Solid Earth*, **115**(B11).

Hegewisch, K. C. & Tomsovic, S., 2011. A random matrix approach to long range acoustic propagation in the ocean, *Journal of the Acoustical Society of America*, **129**(4), 2600–2600.

Hildebrand, J. A., 2005. Impacts of anthropogenic sound, *Marine mammal research: conservation beyond crisis*, pp. 101–124.

Hildebrand, J. A., 2009. Anthropogenic and natural sources of ambient noise in the ocean, *Marine Ecology Progress Series*, **395**, 5–20.

Hildebrand, J. A., Fox, C. G., & Dziak, R. P., 1996. A multipath model for t-wave generation by seafloor earthquakes, *Journal of the Acoustical Society of America*, **100**(4), 2639–2639, doi: 10.1121/1.417777.

Hiyoshi, Y., Walker, D. A., & McCreery, C. S., 1992. T-phase data and regional tsunamigenesis in Japan, *Bulletin of the Seismological Society of America*, **82**(5), 2213–2223.

Holbrook, W. S., Páramo, P., Pearse, S., & Schmitt, R. W., 2003. Thermohaline fine structure in an oceanographic front from seismic reflection profiling, *Science*, **301**(5634), 821–824.

Hrennikoff, A., 1941. Solution of problems in elasticity by the Frame Work method, *J. Appl. Mech.*, **8**(4), 169–175.

Hughes, T. J. R., 1987. *The finite element method, linear static and dynamic finite element analysis*, Prentice-Hall International, Englewood Cliffs, New Jersey, USA, 704 pages.

Hunter, K. S. & Geers, T. L., 2004. Pressure and velocity fields produced by an underwater explosion, *Journal of the Acoustical Society of America*, **115**(4), 1483–1496, doi: 10.1121/1.1648680.

INGV, 2017. Istituto nazionale di geofisica e vulcanologia, `istituto.ingv.it/the-institute`, last accessed on November 20, 2017.

Isakson, M. J., 2018. Finite element modeling for ocean acoustics applications using high performance computing, *Journal of the Acoustical Society of America*, **143**(3), 1926–1926, doi: 10.1121/1.5036289.

Isakson, M. J. & Chotiros, N. P., 2011. Finite-element modeling of reverberation and transmission loss in shallow water waveguides with rough boundaries, *Journal of the Acoustical Society of America*, **129**, 1273–1279.

Isakson, M. J. & Chotiros, N. P., 2015. Finite-element modeling of acoustic scattering from fluid and elastic rough interfaces, *IEEE J. Ocean Eng.*, **40**(2), 475–484.

Ito, A., Sugioka, H., Suetsugu, D., Shiobara, H., Kanazawa, T., & Fukao, Y., 2012. Detection of small earthquakes along the Pacific-Antarctic ridge from T-waves recorded by abyssal ocean-bottom observatories, *Marine Geophysical Research*, **33**(3), 229–238, doi: 10.1007/s11001-012-9158-0.

Iturbe, I., Roux, P., Virieux, J., & Nicolas, B., 2009. Travel-time sensitivity kernels versus diffraction patterns obtained through double beam-forming in shallow water, *Journal of the Acoustical Society of America*, **126**, 713–720.

Jaggar, A. T., 1930. How the seismograph works, *The Volcano Letter*, **268**, 1–4.

Jamet, G., Guennou, C., Guillon, L., Mazoyer, C., & Royer, J.-Y., 2013. T-wave generation and propagation: A comparison between data and spectral element modeling, *Journal of the Acoustical Society of America*, **134**(4), 3376–3385.

Jenkins, E. W., Rivière, B., & Wheeler, M. F., 2002. A priori error estimates for mixed finite element approximations of the acoustic wave equation, *SIAM Journal on Numerical Analysis*, **40**(5), 1698–1715.

Jensen, F. B. & Ferla, C. M., 1990. Numerical solutions of range-dependent benchmark problems in ocean acoustics, *Journal of the Acoustical Society of America*, **87**(4), 1499–1510, doi: 10.1121/1.399448.

Jensen, F. B. & Kuperman, W. A., 1980. Sound propagation in a wedge-shaped ocean with a penetrable bottom, *Journal of the Acoustical Society of America*, **67**(5), 1564–1566.

Jensen, F. B. & Zampolli, M., 2010. Finite-element modeling in ocean acoustics: Where are we heading?, *AIP Conference Proceedings*, **1272**(1), 11–22, doi: 10.1063/1.3493052.

Jensen, F. B., Nielsen, P. L., Zampolli, M., Collins, M. D., & Siegmann, W. L., 2007. Benchmark scenarios for range-dependent seismo-acoustic models, in *Proceedings of the 8th International Conference on Theoretical and Computational Acoustics (ICTCA)*, pp. 407–414, Heraklion, Crete, Greece.

Jensen, F. B., Kuperman, W., Porter, M., & Schmidt, H., 2011. *Computational Ocean Acoustics*, Springer-Verlag, Berlin, Germany, 2nd edition., 794 pages.

Johnson, R. H., 1964. Earthquakes located by T phases during the Vela Uniform Aleutian Islands experiment, 1964, Tech. rep., Hawaii Univ. Honolulu Inst. Of Geophysics.

Johnson, R. H., 1966. Routine location of T-phase sources in the Pacific, *Bulletin of the Seismological Society of America*, **56**(1), 109–118.

Johnson, R. H., 1970. Estimating earthquake rupture length from T waves, *Tsunamis in the Pacific Ocean, by Adams, WA*, pp. 253–259.

Johnson, R. H. & Norris, R. A., 1968a. T-phase radiators in the western Aleutians, *Bulletin of the Seismological Society of America*, **58**(1), 1–10.

Johnson, R. H. & Norris, R. A., 1968b. Geographic variation of Sofar speed and axis depth in the Pacific Ocean, *Journal of Geophysical Research*, **73**(14), 4695–4700, doi: 10.1029/JB073i014p04695.

Johnson, R. H. & Northrop, J., 1966. A comparison of earthquake magnitude with T-phase strength, *Bulletin of the Seismological Society of America*, **56**(1), 119–124.

Johnson, R. H., Northrop, J., & Eppley, R., 1963. Sources of Pacific T phases, *Journal of Geophysical Research*, **68**(14), 4251–4260, doi: 10.1029/JZ068i014p04251.

Johnson, R. H., Norris, R. A., & Duennebier, F. K., 1967. Abyssally generated T phases, Tech. rep., Hawaii Institute Of Geophysics University of Hawaii Honolulu.

Johnson, R. H., Norris, R. A., Duennebier, F. K., & Northrop, J., 1971. T-phase data on Kamchatka/Kurils earthquakes: A reply, *Bulletin of the Seismological Society of America*, **61**(3), 791–794.

Jones, H. & Miller, A., 1948. The detonation of solid explosives: the equilibrium conditions in the detonation wave-front and the adiabatic expansion of the products of detonation, *Proc. R. Soc. Lond. A*, **194**(1039), 480–507.

Kadri, U. & Stiassnie, M., 2012. Acoustic-gravity waves interacting with the shelf break, *Journal of Geophysical Research: Oceans*, **117**(C3).

Kadri, U., Crivelli, D., Parsons, W., Colbourne, B., & Ryan, A., 2017. Rewinding the waves: tracking underwater signals to their source, *Scientific reports*, **7**(1), 13949.

Kalinowski, A. J., 1979. A survey of finite element-related techniques as applied to acoustic propagation in the ocean. part 1: Finite element method and related techniques, *Shock Vibration Digest*, **11**.

Kampanis, N. A. & Dougalis, V. A., 1999. A finite element code for the numerical solution of the Helmholtz equation in axially symmetric waveguides with interfaces, *J. Comput. Acoust.*, **7**(2), 83–110, doi: 10.1142/S0218396X99000084.

Kanamori, H., 1972. Mechanism of tsunami earthquakes, *Physics of the Earth and Planetary Interiors*, **6**(5), 346–359, doi: 10.1016/0031-9201(72)90058-1.

Käser, M. & Dumbser, M., 2006. An arbitrary high-order discontinuous Galerkin method for elastic waves on unstructured meshes - i. the two-dimensional isotropic case with external source terms, *Geophys. J. Int.*, **166**(2), 855–877.

Käser, M. & Dumbser, M., 2008. A highly accurate discontinuous Galerkin method for complex interfaces between solids and moving fluids, *Geophysics*, **73**(3), T23–T35, doi: 10.1190/1.2870081.

Keenan, R. E. & Merriam, L. R. L., 1991. Arctic abyssal T phases: Coupling seismic energy to the ocean sound channel via under-ice scattering, *Journal of the Acoustical Society of America*, **89**(3), 1128–1133, doi: 10.1121/1.400648.

Keller, J. B. & Karal Jr., F. C., 1960. Surface wave excitation and propagation, *Journal of Applied Physics*, **31**(6), 1039–1046.

Kelly, K. R., Ward, R. W., Treitel, S., & Alford, R. M., 1976. Synthetic seismograms: A finite-difference approach, *Geophysics*, **41**(1), 2–27.

Kokinou, E., Kamberis, E., Vafidis, A., Monopolis, D., Ananiadis, G., & Zelilidis, A., 2005. Deep seismic reflection data from offshore western Greece: a new crustal model for the Ionian Sea, *Journal of Petroleum Geology*, **28**(2), 185–202.

Komatitsch, D., 2011. Fluid-solid coupling on a cluster of GPU graphics cards for seismic wave propagation, *C. R. Acad. Sci., Ser. IIb Mec.*, **339**, 125–135, doi: 10.1016/j.crme.2010.11.007.

Komatitsch, D., 2018. Specfem3d_cartesian user manual, version 3.0, Tech. rep., Computational Infrastructure for Geodynamics, `geodynamics.org/cig/software/specfem3d/specfem3d-manual.pdf`, Last accessed on June 8, 2018.

Komatitsch, D. & Tromp, J., 1999. Introduction to the spectral-element method for 3-D seismic wave propagation, *Geophys. J. Int.*, **139**(3), 806–822, doi: 10.1046/j.1365-246x.1999.00967.x.

Komatitsch, D. & Vilotte, J. P., 1998. The spectral-element method: an efficient tool to simulate the seismic response of 2D and 3D geological structures, *Bull. seism. Soc. Am.*, **88**(2), 368–392.

Komatitsch, D., Barnes, C., & Tromp, J., 2000. Simulation of anisotropic wave propagation based upon a spectral element method, *Geophysics*, **65**(4), 1251–1260, doi: 10.1190/1.1444816.

Komatitsch, D., Martin, R., Tromp, J., Taylor, M. A., & Wingate, B. A., 2001. Wave propagation in 2-D elastic media using a spectral element method with triangles and quadrangles, *J. Comput. Acoust.*, **9**(2), 703–718, doi: 10.1142/S0218396X01000796.

Komatitsch, D., Ritsema, J., & Tromp, J., 2002. The spectral-element method, Beowulf computing, and global seismology, *Science*, **298**(5599), 1737–1742, doi: 10.1126/science.1076024.

Komatitsch, D., Erlebacher, G., Göddeke, D., & Michéa, D., 2010. High-order finite-element seismic wave propagation modeling with MPI on a large GPU cluster, *J. Comput. Phys.*, **229**(20), 7692–7714, doi: 10.1016/j.jcp.2010.06.024.

Komatitsch, D., Xie, Z., Bozdağ, E., Sales de Andrade, E., Peter, D., Liu, Q., & Tromp, J., 2016. Anelastic sensitivity kernels with parsimonious storage for adjoint tomography and full waveform inversion, *Geophys. J. Int.*, **206**(3), 1467–1478, doi: 10.1093/gji/ggw224.

Kopriva, D. A., 2006. Metric identities and the discontinuous spectral element method on curvilinear meshes, *Journal of Scientific Computing*, **26**(3), 301–327, doi: 10.1007/s10915-005-9070-8.

Kopriva, D. A., Woodruff, S. L., & Hussaini, M. Y., 2002. Computation of electromagnetic scattering with a non-conforming discontinuous spectral element method, *Int. J. Numer. Methods Eng.*, **53**(1), 105–122, doi: 10.1002/nme.394.

Kosuga, M., 2011. Localization of T-wave energy on land revealed by a dense seismic network in japan, *Geophysical Journal International*, **187**(1), 338–354.

Koyanagi, S., Aki, K., Biswas, N., & Mayeda, K., 1995. Inferred attenuation from site effect-corrected T phases recorded on the island of Hawaii, *Pure and Applied Geophysics*, **144**(1), 1–17.

Kozdon, J. E. & Dunham, E. M., 2014. Constraining shallow slip and tsunami excitation in megathrust ruptures using seismic and ocean acoustic waves recorded on ocean-bottom sensor networks, *Earth and Planetary Science Letters*, **396**, 56–65.

Kucukcoban, S. & Kallivokas, L. F., 2010. A mixed perfectly-matched-layer for transient wave simulations in axisymmetric elastic media, *Computer Modeling in Engineering and Sciences*, **64**(2), 109–145.

Landau, L. D. & Lifshitz, E. M., 1959. *Fluid mechanics*, Pergamon Press, New-York, USA, 536 pages.

Laurent, L. S., Alford, M. H., & Paluszkiewicz, T., 2012. An introduction to the special issue on internal waves, *Oceanography*, **2**(25), 15–19, doi: 10.5670/oceanog.2012.37.

Lee, D., Pierce, A. D., & Shang, E.-C., 2000. Parabolic Equation development in the twentieth century, *Journal of Computational Acoustics*, **08**(04), 527–637, doi: 10.1142/S0218396X00000388.

Leet, L. D., 1951. Discussion of "proposed use of the T phase in tsunami warning systems", *Bulletin of the Seismological Society of America*, **41**(2), 165–167.

Leet, L. D., Linehan, S. J. D., & Berger, P. R., 1951. Investigation of the T phase, *Bull. seism. Soc. Am.*, **41**, 123–141.

Legay, A., Wang, H. W., & Belytschko, T., 2005. Strong and weak arbitrary discontinuities in spectral finite elements, *Int. J. Numer. Methods Eng.*, **64**(8), 991–1008, doi: 10.1002/nme.1388.

Leonard, M., 2004. T-phase perception: The August 2003, Mw 7.1, New Zealand earthquake felt in Sydney 1,800 km away, *Seismological Research Letters*, **75**(4), 475–480.

Lesaint, P. & Raviart, P. A., 1974. On a finite-element method for solving the neutron transport equation (Proc. Symposium, Mathematical Research Center), in *Mathematical aspects of finite elements in partial differential equations*, vol. 33, pp. 89–123, Academic Press, New York, USA.

Levander, A. R., 1988. Fourth-order finite-difference P-SV seismograms, *Geophysics*, **53**(11), 1425–1436.

Levitus, S., 1983. Climatological atlas of the world ocean, *Eos, Transactions American Geophysical Union*, **64**(49), 962–963.

Lichte, H., 1919. Über den einflußhorizontaler temperaturschichtung des seewassers auf die reichweite von unterwasserschallsignalen (on the influence of horizontal temperature stratification of seawater on the range of underwater sound signals.), *Physikalische Zeitschrift*, **17**, 385–389.

Lin, C.-H., 2001. T-waves excited by S-waves and oscillated within the ocean above the southeastern taiwan forearc, *Geophysical Research Letters*, **28**(17), 3297–3300, doi: 10.1029/2001GL013152.

Lin, C. W., Chuang, L. Y. L., Huang, C. F., Chen, C. W., & Kuo, B. Y., 2014. T-wave observations on ocean-bottom seismometers offshore eastern Taiwan, in *Oceans 2014, Taipei*, pp. 1–5, doi: 10.1109/OCEANS-TAIPEI.2014.6964430.

Linehan, S. J. D., 1940. Earthquakes in the West Indian region, *Transactions American Geophysical Union*, **21**, 229–232.

Luu, K., Noble, M., Gesret, A., Belayouni, N., & Roux, P.-F., 2018. A parallel competitive particle swarm optimization for non-linear first arrival traveltime tomography and uncertainty quantification, *Computers & Geosciences*, **113**, 81–93, doi: https://doi.org/10.1016/j.cageo.2018.01.016.

Lysmer, J., Drake, L. A., & Bolt, B., 1972. A finite element method for seismology, *Methods in Computational Physics*, **11**, 181–216.

Mackenzie, K. V., 1981. Nine-term equation for sound speed in the oceans, *Journal of the Acoustical Society of America*, **70**(3), 807–812.

Magnoni, F., Casarotti, E., Michelini, A., Piersanti, A., Komatitsch, D., Peter, D., & Tromp, J., 2014. Spectral-element simulations of seismic waves generated by the 2009 l'Aquila earthquake, *Bull. seism. Soc. Am.*, **104**(1), 73–94.

Martin, R., Komatitsch, D., & Gedney, S. D., 2008. A variational formulation of a stabilized unsplit convolutional perfectly matched layer for the isotropic or anisotropic seismic wave equation, *Comput. Model. Eng. Sci.*, **37**(3), 274–304.

Masson, Y. & Romanowicz, B., 2017a. Fast computation of synthetic seismograms within a medium containing remote localized perturbations: a numerical solution to the scattering problem, *Geophysical Journal International*, **208**(2), 674–692, doi: 10.1093/gji/ggw412.

Masson, Y. & Romanowicz, B., 2017b. Box tomography: localized imaging of remote targets buried in an unknown medium, a step forward for understanding key structures in the deep earth, *Geophysical Journal International*, **211**(1), 141–163, doi: 10.1093/gji/ggx141.

Matzen, R., 2011. An efficient finite-element time-domain formulation for the elastic second-order wave equation: A non-split complex frequency-shifted convolutional PML, *Int. J. Numer. Methods Eng.*, **88**(10), 951–973, doi: 10.1002/nme.3205.

McDonald, B. E., 1996. Bathymetric and volumetric contributions to ocean acoustic mode coupling, *Journal of the Acoustical Society of America*, **100**(1), 219–224.

McGraw-Hill, P. S. & Parker, S., 2003. *McGraw-Hill Dictionary of scientific and technical terms*, McGraw-Hill.

McHenry, D., 1943. A lattice analogy for the solution of plane stress problems, *J. Inst. Civil Eng.*, **21**, 59–82.

McLaughlin, K. L., 1997. T-phase observations at San Nicolas Island, California, *Seism. Res. Lett*, **68**, 296.

Medwin, H., Helbig, R. A., & Hagy, J. D., 1973. Spectral characteristics of sound transmission through the rough sea surface, *Journal of the Acoustical Society of America*, **54**(1), 99–109, doi: 10.1121/1.1913582.

Mercerat, E. D., Vilotte, J. P., & Sánchez-Sesma, F. J., 2006. Triangular spectral-element simulation of two-dimensional elastic wave propagation using unstructured triangular grids, *Geophys. J. Int.*, **166**(2), 679–698.

Metz, D., Watts, A. B., Grevemeyer, I., Rodgers, M., & Paulatto, M., 2016. Ultra-long-range hydroacoustic observations of submarine volcanic activity at Monowai, Kermadec Arc, *Geophysical Research Letters*, **43**(4), 1529–1536, doi: 10.1002/2015GL067259.

Michéa, D. & Komatitsch, D., 2010. Accelerating a 3D finite-difference wave propagation code using GPU graphics cards, *Geophys. J. Int.*, **182**(1), 389–402, doi: 10.1111/j.1365-246X.2010.04616.x.

Milne, A. R., 1959. Comparison of spectra of an earthquake T-phase with similar signals from nuclear explosions, *Bulletin of the Seismological Society of America*, **49**(4), 317–329.

Monteiller, V., Chevrot, S., Komatitsch, D., & Fuji, N., 2013. A hybrid method to compute short period synthetic seismograms of teleseismic body waves in a 3-D regional model, *Geophys. J. Int.*, **192**(1), 230–247, doi: 10.1093/gji/ggs006.

Monteiller, V., Chevrot, S., Komatitsch, D., & Wang, Y., 2015. Three-dimensional full waveform inversion of short-period teleseismic wavefields based upon the SEM-DSM hybrid method, *Geophys. J. Int.*, **202**(2), 811–827, doi: 10.1093/gji/ggv189.

Munk, W., 2006. Ocean acoustic tomography, in *Physical Oceanography*, pp. 119–138, Springer.

Munk, W. H., 1974. Sound channel in an exponentially stratified ocean, with application to SOFAR, *Journal of the Acoustical Society of America*, **55**(2), 220–226.

Munk, W. H. & Forbes, A. M. G., 1989. Global ocean warming: An acoustic measure?, *Journal of Physical Oceanography*, **19**(11), 1765–1778, doi: 10.1175/1520-0485(1989)019<1765:GOWAAM>2.0.CO;2.

Munk, W. H., Spindel, R. C., Baggeroer, A., & Birdsall, T. G., 1994. The Heard island feasibility test, *Journal of the Acoustical Society of America*, **96**(4), 2330–2342.

Nagel, W. E., Kröner, D. H., & Resch, M. M., 2018. *High Performance Computing in Science and Engineering'17: Transactions of the High Performance Computing Center, Stuttgart (HLRS) 2017*, Springer.

National Geophysical Data Center, N., 2011. ETOPO1, global 1 arc-minute ocean depth and land elevation from the US National Geophysical Data Center (NGDC), NESDIS, NOAA, U.S. Department of Commerce.

Nguyen, H. & Nguyen, D. K., 1961. Sur les ondes T des séismes des Philippines enregistrées à Nha Trang (On T-waves generated by Philippine earthquakes recorded at Nha Trang), in *Annales de la Faculté des Sciences de Saigon*, vol. 1961, pp. 343–368.

Nissen-Meyer, T., Fournier, A., & Dahlen, F. A., 2007. A two-dimensional spectral-element method for computing spherical-earth seismograms - I. Moment-tensor source, *Geophys. J. Int.*, **168**(3), 1067–1092, doi: 10.1111/j.1365-246X.2006.03121.x.

Nissen-Meyer, T., Fournier, A., & Dahlen, F. A., 2008. A 2-D spectral-element method for computing spherical-earth seismograms - II. Waves in solid-fluid media, *Geophys. J. Int.*, **174**, 873–888, doi: 10.1111/j.1365-246X.2008.03813.x.

Nissen-Meyer, T., van Driel, M., Stähler, S. C., Hosseini, K., Hempel, S., Auer, L., Colombi, A., & Fournier, A., 2014. AxiSEM: Broadband 3-D seismic wavefields in axisymmetric media, *Solid Earth*, **5**(1), 425–445, doi: 10.5194/se-5-425-2014.

Niu, H., Reeves, E., & Gerstoft, P., 2017. Source localization in an ocean waveguide using supervised machine learning, *Journal of the Acoustical Society of America*, **142**(3), 1176–1188, doi: 10.1121/1.5000165.

Norris, R. A. & Johnson, R. H., 1969. Submarine volcanic eruptions recently located in the pacific by SOFAR hydrophones, *Journal of Geophysical Research*, **74**(2), 650–664.

Northrop, J., 1962. Evidence of dispersion in earthquake T phases, *Journal of Geophysical Research*, **67**(7), 2823–2830, doi: 10.1029/JZ067i007p02823.

Northrop, J., 1970. Accuracy of earthquake epicenters on the Gorda ridge, *Bulletin of the Seismological Society of America*, **60**(1), 265–267.

Northrop, J., 1974. T phases from the hawaiian earthquake of april 26, 1973, *Journal of Geophysical Research*, **79**(35), 5478–5481.

Obara, K. & Maeda, T., 2009. Reverse propagation of T-waves from the Emperor seamount chain, *Geophysical Research Letters*, **36**(8).

Odom, R. I. & Soukup, D. J., 2002. T-wave sources, slopes, rough bottoms and continuum, *Journal of the Acoustical Society of America*, **111**(5), 2387–2387, doi: 10.1121/1.4778113.

Odom, R. I. & Soukup, D. J., 2004. Modal scattering and T-waves: Sediment amplification and source effects, *Journal of the Acoustical Society of America*, **115**(5), 2445–2445.

Officer, C. B., 1958. *Introduction to the theory of sound transmission*, McGraw-Hill New York.

Ogasawara, H., Nakamura, T., Hachiya, H., Fujimori, H., & Mizutani, K., 2006. Fluctuation of long-distance sound propagation in the central pacific, *Japanese journal of applied physics*, **45**(5S), 4842.

Ogasawara, H., Nakamura, T., Fujimori, H., Hachiya, H., & Mizutani, K., 2008. Analysis of tidal effect on reciprocal sound propagation in central Pacific ocean, *Japanese Journal of Applied Physics*, **47**(5S), 4349.

Ogilvy, J. A. & Merklinger, H. M., 1991. Theory of wave scattering from random rough surfaces.

Okal, E. A., 1992. Use of the mantle magnitude Mm for the reassessment of the moment of historical earthquakes. II: Intermediate and deep events, *Pure and applied geophysics*, **139**(1), 59–85.

Okal, E. A., 1999. The probable source of the 1998 Papua New Guinea tsunami as expressed in oceanic T waves, *Eos, Trans. Amer. Geophys. Un*, **80**(46), F750.

Okal, E. A., 2001a. T-phase stations for the international monitoring system of the comprehensive nuclear-test ban treaty: A global perspective, *Seismological Research Letters*, **72**, 186–196.

Okal, E. A., 2001b. "Detached" deep earthquakes: Are they really?, *Physics of the Earth and Planetary Interiors*, **127**(1), 109–143.

Okal, E. A., 2003. T waves from the 1998 Papua New Guinea earthquake and its aftershocks: Timing the tsunamigenic slump, *Pure and Applied Geophysics*, **160**(10), 1843–1863, doi: 10.1007/s00024-003-2409-x.

Okal, E. A., 2007. The generation of T waves by earthquakes, *Adv. Geophys.*, **49**, 1–65.

Okal, E. A., 2011a. Encyclopedia of solid earth geophysics, in *Earth Sciences Series*, chap. T waves, pp. 1421–1423, ed. Gupta, H., Springer-Verlag.

Okal, E. A., 2011b. Tsunamigenic earthquakes: Past and present milestones, *Pure and Applied Geophysics*, **168**(6), 969–995, doi: 10.1007/s00024-010-0215-9.

Okal, E. A., 2013. From 3-Hz P waves to 0S2: No evidence of a slow component to the source of the 2011 Tohoku earthquake, *Pure and Applied Geophysics*, **170**(6-8), 963–973.

Okal, E. A. & Talandier, J., 1986. T-wave duration, magnitudes and seismic moment of an earthquake-application to tsunami warning, *Journal of Physics of the Earth*, **34**(1), 19–42.

Okal, E. A. & Talandier, J., 1997. T waves from the great 1994 Bolivian deep earthquake in relation to channeling of S wave energy up the slab, *Journal of Geophysical Research: Solid Earth*, **102**(B12), 27421–27437, doi: 10.1029/97JB02718.

Okal, E. A., Alasset, P.-J., Hyvernaud, O., & Schindele, F., 2003. The deficient T waves of tsunami earthquakes, *Geophysical Journal International*, **152**(2), 416–432, doi: 10.1046/j.1365-246X.2003.01853.x.

Okal, E. A., Bernard, E., & Robinson, A., 2009. Excitation of tsunamis by earthquakes, *The sea*, **15**, 137–177.

Outing, D. A., Siegmann, W. L., Collins, M. D., & Westwood, E. K., 2006. Generalization of the rotated parabolic equation to variable slopes, *Journal of the Acoustical Society of America*, **120**, 3534.

Pan, J. & Dziewonski, A. M., 2005. Comparison of mid-oceanic earthquake epicentral differences of travel time, centroid locations, and those determined by autonomous underwater hydrophone arrays, *Journal of Geophysical Research: Solid Earth*, **110**(B7).

Park, M. & Odom, R. I., 1999. The effect of stochastic rough interfaces on coupled-mode elastic waves, *Geophysical Journal International*, **136**(1), 123–143.

Park, M., Odom, R. I., & Soukup, D. J., 2001. Modal scattering: A key to understanding oceanic T-waves, *Geophysical Research Letters*, **28**(17), 3401–3404, doi: 10.1029/2001GL013472.

Patera, A. T., 1984. A spectral element method for fluid dynamics: laminar flow in a channel expansion, *J. Comput. Phys.*, **54**, 468–488.

Patriat, M., Klingelhoefer, F., Aslanian, D., Contrucci, I., Gutscher, M.-A., Talandier, J., Avedik, F., Francheteau, J., & Weigel, W., 2002. Deep crustal structure of the Tuamotu plateau and Tahiti (French Polynesia) based on seismic refraction data, *Geophysical research letters*, **29**(14).

Pavlis, G., 2004. Seismic event location: Fundamentals and potential problems in event locations utilizing T-phases, in *Proceedings, Seismo-Acoustic Applications in Marine Geology and Geophysics Workshop, Woods Hole Oceanographic Institution*.

Pekeris, C. L., 1948. Theory of explosion of sound in shallow water, *Geol. Soc. Am. Mem.*, **27**, 1–117.

Peter, D., Komatitsch, D., Luo, Y., Martin, R., Le Goff, N., Casarotti, E., Le Loher, P., Magnoni, F., Liu, Q., Blitz, C., Nissen-Meyer, T., Basini, P., & Tromp, J., 2011. Forward and adjoint simulations of seismic wave propagation on fully unstructured hexahedral meshes, *Geophys. J. Int.*, **186**(2), 721–739, doi: 10.1111/j.1365-246X.2011.05044.x.

Pierce, A. D., 1982. Guided mode disappearance during upslope propagation in variable depth shallow water overlying a fluid bottom, *Journal of the Acoustical Society of America*, **72**(2), 523–531, doi: 10.1121/1.388033.

Pierce, A. D., 1983. Augmented adiabatic mode theory for upslope propagation from a point source in variable-depth shallow water overlying a fluid bottom, *Journal of the Acoustical Society of America*, **74**(6), 1837–1847.

Pilant, W. L., 1979. *Elastic waves in the Earth*, vol. 11 of "Developments in Solid Earth Geophysics" Series, Elsevier Scientific Publishing Company, Amsterdam, The Netherlands, 506 pages.

Pinton, G. F. & Trahey, G. E., 2008. A comparison of time-domain solutions for the full-wave equation and the parabolic wave equation for a diagnostic ultrasound transducer, *IEEE Transactions on Ultrasonics, Ferroelectrics, and Frequency Control*, **55**(3), 730–733.

Piserchia, P.-F., Virieux, J., Rodrigues, D., Gaffet, S., & Talandier, J., 1998. Hybrid numerical modelling of T-wave propagation:application to the Midplate experiment, *Geophysical Journal International*, **133**(3), 789–800, doi: 10.1046/j.1365-246X.1998.00546.x.

Porter, M. B., 2011. The bellhop manual and user's guide: Preliminary draft, *Heat, Light, and Sound Research, Inc., La Jolla, CA, USA, Tech. Rep.*

Porter, M. B. & Bucker, H. P., 1987. Gaussian beam tracing for computing ocean acoustic fields, *Journal of the Acoustical Society of America*, **82**(4), 1349–1359, doi: 10.1121/1.395269.

Porter, M. B. & Reiss, E. L., 1984. A numerical method for ocean-acoustic normal modes, *Journal of the Acoustical Society of America*, **76**(1), 244–252.

Porter, M. B. & Reiss, E. L., 1985. A numerical method for bottom interacting ocean acoustic normal modes, *Journal of the Acoustical Society of America*, **77**(5), 1760–1767.

Porter, R. P., 1973. Dispersion of axial SOFAR propagation in the western Mediterranean, *Journal of the Acoustical Society of America*, **53**(1), 181–191, doi: 10.1121/1.1913317.

Press, F. & Ewing, M., 1950. Propagation of explosive sound in a liquid layer overlying a semi-infinite elastic solid, *Geophysics*, **15**(3), 426–446.

Press, F., Ewing, M., & Tolstoy, I., 1950. The Airy phase of shallow-focus submarine earthquakes, *Bulletin of the Seismological Society of America*, **40**(2), 111–148.

Prestininzi, P., Abdolali, A., Montessori, A., Kirby, J., & Rocca, M. L., 2016. Lattice Boltzmann approach for hydro-acoustic waves generated by tsunamigenic sea bottom displacement, *Ocean Modelling*, **107**, 14–20, doi: 10.1016/j.ocemod.2016.09.012.

Ratcliffe, A., Conroy, G., Vinje, V., & Bertrand, A., 2014. Full waveform inversion-a north sea obc case study-reloaded, in *76th EAGE Conference and Exhibition 2014*.

Rathje, E. M., Abrahamson, N. A., & Bray, J. D., 1998. Simplified frequency content estimates of earthquake ground motions, *Journal of Geotechnical and Geoenvironmental Engineering*, **124**(2), 150–159, doi: 10.1061/(ASCE)1090-0241(1998)124:2(150).

Ravet, J., 1940. Remarques sur quelques enregistrements d'ondes à très courte période au cours de tremblements de terre éloignés à l'observatoire du Faiere, Papeete, Tahiti (Remarks on some very short-period recordings at Faiere observatory, Papeete, Tahiti, during remote earthquakes), *Sixth Pacific Congress*, **1**, 127–130.

Richardson, W. J., Greene Jr., C. R., Malme, C. I., & Thomson, D. H., 2013. *Marine mammals and noise*, Academic press.

Rivière, B. & Wheeler, M. F., 2003. Discontinuous finite element methods for acoustic and elastic wave problems, *Contemporary Mathematics*, **329**, 271–282.

Robinson, D., 2011. A rare great earthquake on an oceanic fossil fracture zone, *Geophysical Journal International*, **186**(3), 1121–1134.

Rodgers, A. & Harben, P., 2000. T-phase observations from the May 1999 Ascension Island experiment, Tech. rep., Lawrence Livermore National Lab CA.

Roux, P., Marandet, C., Nicolas, B., & Kuperman, W. A., 2013. Experimental measurement of the acoustic sensitivity kernel, *Journal of the Acoustical Society of America*, **134**(1), EL38–EL44.

Rozenberg, L., 1949. About a new phenomenon in hydroacoustics, *Dokl. Akad. Nauk. SSSR*, **69**, 175–176.

Salon, S., Crise, A., Picco, P., Marinis, E. D., & Gasparini, O., 2002. Sound speed in the Mediterranean Sea: an analysis from a climatological data set, *Annales Geophysicae*, **21**, 833–846.

Salzberg, D., 2008. A hydro-acoustic solution to the local tsunami warning problem, in *AGU Fall Meeting Abstracts*.

Sandwell, D. T., Müller, R. D., Smith, W. H., Garcia, E., & Francis, R., 2014. New global marine gravity model from cryosat-2 and jason-1 reveals buried tectonic structure, *Science*, **346**(6205), 65–67.

Sato, Y., 1978. *Theory of Elastic Waves*, Iwanami, 329 pages. (in Japanese).

Schmidt, H., 1995. Marching wave-number-integration approach to range-dependent, two-way seismoacoustic propagation modeling, *Journal of the Acoustical Society of America*, **97**(5), 3316–3316.

Schmidt, H. & Jensen, F. B., 1985. A full wave solution for propagation in multilayered viscoelastic media with application to Gaussian beam reflection at fluid-solid interfaces, *Journal of the Acoustical Society of America*, **77**, 813–825.

Schmidt, H., Seong, W., & Goh, J. T., 1995. Spectral super-element approach to range-dependent ocean acoustic modeling, *Journal of the Acoustical Society of America*, **98**(1), 465–472.

Schmidt, H., Baggeroer, A. B., & Sperry, B. J., 2004. Wave-theory modeling of oceanic T-phase coupling at continental margins and seamounts, *Journal of the Acoustical Society of America*, **115**(5), 2444–2444, doi: 10.1121/1.4782145.

Scholte, J. G., 1947. The range of existence of Rayleigh and Stoneley waves, *Geophysical Supplements to the Monthly Notices of the Royal Astronomical Society*, **5**(5), 120–126.

Schreiner, A. E., Fox, C. G., & Dziak, R. P., 1995. Spectra and magnitudes of T-waves from the 1993 earthquake swarm on the Juan de Fuca Ridge, *Geophysical Research Letters*, **22**(2), 139–142, doi: 10.1029/94GL01912.

Scully-Power, P. & Stevenson, R. E., 1985. New advances towards ocean, acoustics and space integration, in *Adaptive Methods in Underwater Acoustics*, pp. 711–729, ed. Urban, H. G., Springer Netherlands, Dordrecht.

Seriani, G. & Priolo, E., 1994. A spectral element method for acoustic wave simulation in heterogeneous media, *Finite Elements in Analysis and Design*, **16**, 337–348.

Serry, A. & Lévêque, L., 2015. Le système d'identification automatique (AIS), *Netcom [on line]*, doi: 10.4000/netcom.1943, `journals.openedition.org/netcom/1943`, Last accessed on March 26, 2018.

Sgroi, T., Beranzoli, L., Di Grazia, G., Ursino, A., & Favali, P., 2007. New observations of local seismicity by the SN-1 seafloor observatory in the Ionian Sea, off-shore Eastern Sicily (Italy), *Geophysical Journal International*, **169**(2), 490–501.

Shapira, A., 1981. T phases from underwater explosions off the coast of Israel, *Bulletin of the Seismological Society of America*, **71**(4), 1049–1059.

Shearer, P., 2009. *Introduction to Seismology*, Cambridge University Press.

Shen, Y., 2002. Seismicity at the southern East Pacific Rise from recordings of an ocean bottom seismometer array, *Journal of Geophysical Research: Solid Earth*, **107**(B12).

Shimamura, H. & Asada, T., 1975. T waves from deep earthquakes generated exactly at the bottom of deep-sea trenches, *Earth and Planetary Science Letters*, **27**(2), 137–142.

Shurbet, D. H., 1955. Bermuda T phases with large continental paths, *Bulletin of the Seismological Society of America*, **45**(1), 23–35.

Shurbet, D. H. & Ewing, M., 1957. T phases at Bermuda and transformation of elastic waves, *Bulletin of the Seismological Society of America*, **47**(3), 251–262.

Skarsoulis, E. K. & Cornuelle, B. D., 2004. Travel-time sensitivity kernels in ocean acoustic tomography, *The Journal of the Acoustical Society of America*, **116**(1), 227–238.

Slack, P. D., Fox, C. G., & Dziak, R. P., 1999. P wave detection thresholds, Pn velocity estimates, and T wave location uncertainty from oceanic hydrophones, *Journal of Geophysical Research: Solid Earth*, **104**(B6), 13061–13072, doi: 10.1029/1999JB900112.

Snellen, M., Evers, L., & Simons, D., 2011. Modeling the long-range acoustic propagation for the May 2010 Sarigan volcano eruption, in *Proceedings of the Underwater Acoustic Measurements Conference, Kos, Greece*, pp. 1361–1368.

Solarino, S. & Eva, C., 2007. T waves in western Mediterranean sea after the May 21, 2003 Algerian earthquake, *Annals of Geophysics*, **50**(5).

Solovyev, S. L., Voronin, R. S., & Voronina, S. I., 1968. Seismic and hydroacoustic data on T-waves (literature review), tsunami problem, *Publ. House Nauka, Moscow*, **141**, 142–173.

Sperry, B., Goh, J. T., Baggeroer, A., & Schmidt, H., 1996. Possible mechanisms for T-phase generation, *Journal of the Acoustical Society of America*, **100**(4), 2641–2641, doi: 10.1121/1.417785.

Sperry, B., Schmidt, H., & Baggeroer, A., 1999. Propagation modeling of T-phase time series via RDOASES, *Journal of the Acoustical Society of America*, **105**(2), 1038–1039, doi: 10.1121/1.424955.

Spiesberger, J., 2007. Comparison of two and three spatial dimensional solutions of the wave equation at ocean-basin scales in the presence of internal waves, *Journal of the Acoustical Society of America*, **121**(5), 3076–3076, doi: 10.1121/1.4781904.

Spiesberger, J. L., 2010. Comparaison of two and three spatial dimensional solutions of a parabolic approximation of the wave equation at ocean-basin scales in the presence of internal waves: 100-150 Hz, *Journal of Computational Acoustics*, **18**(02), 117–129, doi: 10.1142/S0218396X10004115.

Spudich, P. & Orcutt, J., 1980. Petrology and porosity of an oceanic crustal site: Results from wave form modeling of seismic refraction data, *Journal of Geophysical Research: Solid Earth*, **85**(B3), 1409–1433.

Stephen, R. A., Bolmer, S. T., Dzieciuch, M. A., Worcester, P. F., Andrew, R. K., Buck, L. J., Mercer, J. A., Colosi, J. A., & Howe, B. M., 2009. Deep seafloor arrivals: An unexplained set of arrivals in long-range ocean acoustic propagation, *Journal of the Acoustical Society of America*, **126**(2), 599–606.

Stephen, R. A., Thompson Bolmer, S., Udovydchenkov, I. A., Worcester, P. F., Dzieciuch, M. A., Andrew, R. K., Mercer, J. A., Colosi, J. A., & Howe, B. M., 2013. Deep seafloor arrivals in long range ocean acoustic propagation, *Journal of the Acoustical Society of America*, **134**(4), 3307–3317.

Stevens, J. L., Baker, G. E., Xu, H., D'Spain, G., & Berger, L. P., 2000. Finite difference modeling of T-phase propagation from ocean to land, Tech. rep., Maxwell Technology Inc San Diego Ca Systems Div.

Stevens, J. L., Baker, G. E., Cook, R. W., D'Spain, G. L., Berger, L. P., & Day, S. M., 2001. Empirical and numerical modeling of T-phase propagation from ocean to land, *Pure and Applied Geophysics*, **158**(3), 531–565.

Stoneley, R., 1924. Elastic waves at the surface of separation of two solids, *Proc. R. Soc. London Ser. A.*, **106**, 416–428.

Strang, G. & Fix, G. J., 1973. *An analysis of the finite element method*, vol. 212, Prentice-Hall, Englewood Cliffs, New Jersey, USA.

Strohmaier, E., Dongarra, J., Simon, H., & Meuer, M., 2017. The Top500 list of the 500 most powerful commercially-available computer systems, `www.top500.org`, last accessed on November 22, 2017.

Stupazzini, M., Paolucci, R., & Igel, H., 2009. Near-fault earthquake ground-motion simulation in the Grenoble valley by a high-performance spectral element code, *Bull. Seismol. Soc. Am.*, **99**(1), 286–301.

Sturm, F. & Bonnel, J., 2016. Time-frequency features of 3-D sound propagation in wedge-shaped oceanic waveguides, *IEEE Journal of Oceanic Engineering*, **41**(3), 731–739.

Sugioka, H., Fukao, Y., & Hibiya, T., 2005. Submarine volcanic activity, ocean-acoustic waves and internal ocean tides, *Geophysical research letters*, **32**(24).

Sukhovich, A., Irisson, J.-O., Perrot, J., & Nolet, G., 2014. Automatic recognition of T and teleseismic P waves by statistical analysis of their spectra: An application to continuous records of moored hydrophones, *Journal of Geophysical Research: Solid Earth*, **119**(8), 6469–6485.

Swisdak Jr, M. M., 1978. Explosion effects and properties. part II. explosion effects in water, Tech. rep., Naval Surface Weapons Center White Oak Lab Silver Spring MD.

Takenaka, H., Tanaka, H., Okamoto, T., & Kennett, B. L. N., 2003. Quasi-cylindrical 2.5D wave modeling for large-scale seismic surveys, *Geophys. Res. Lett.*, **30**(21), 2086, doi: 10.1029/2003GL018068.

Talandier, J. & Kuster, G. T., 1976. Seismicity and submarine volcanic activity in french polynesia, *Journal of Geophysical Research*, **81**(5), 936–948, doi: 10.1029/JB081i005p00936.

Talandier, J. & Okal, E., 2001. Identification criteria for sources of T waves recorded in French Polynesia, *pure and applied geophysics*, **158**(3), 567–603, doi: 10.1007/PL00001195.

Talandier, J. & Okal, E. A., 1979. Human perception of T waves: The June 22, 1977 Tonga earthquake felt on Tahiti, *Bulletin of the Seismological Society of America*, **69**(5), 1475–1486.

Talandier, J. & Okal, E. A., 1987a. Seismic detection of underwater volcanism: The example of French Polynesia, *Pure and Applied Geophysics*, **125**(6), 919–950.

Talandier, J. & Okal, E. A., 1987b. Crustal structure in the Society and Tuamotu islands, French Polynesia, *Geophysical Journal International*, **88**(3), 499–528.

Talandier, J. & Okal, E. A., 1998. On the mechanism of conversion of seismic waves to and from T waves in the vicinity of island shores, *Bull. seism. Soc. Am.*, **88**(2), 621–632.

Talandier, J. & Okal, E. A., 2016. A new source discriminant based on frequency dispersion for hydroacoustic phases recorded by T-phase stations, *Geophysical Journal International*, **206**(3), 1784–1794, doi: 10.1093/gji/ggw249.

Tappert, F. D., 1974. Parabolic equation method in underwater acoustics, *Journal of the Acoustical Society of America*, **55**(S1), S34–S34, doi: 10.1121/1.1919661.

Tappert, F. D., 1977. The parabolic approximation method, in *Wave propagation in underwater acoustics*, pp. 224–287, Springer.

Tappin, D. R., Watts, P., & Grilli, S. T., 2008. The Papua New Guinea tsunami of 17 july 1998: anatomy of a catastrophic event, *Natural Hazards and Earth System Science*, **8**(2), 243–266.

Taylor, M. A. & Wingate, B. A., 2000. A generalized diagonal mass matrix spectral element method for non-quadrilateral elements, *Appl. Num. Math.*, **33**, 259–265.

Terrana, S., Vilotte, J. P., & Guillot, L., 2018. A spectral hybridizable discontinuous galerkin method for elastic-acoustic wave propagation, *Geophysical Journal International*, **213**(1), 574–602, doi: 10.1093/gji/ggx557.

Thomsen, L. & Dellinger, J., 2003. On shear-wave triplication in transversely isotropic media, *Journal of Applied Geophysics*, **54**(3-4), 289–296.

Tolstoy, I. & Ewing, M., 1950. The T phases of shallow-focus earthquakes, *Bull. seism. Soc. Am.*, **40**, 25–51.

Tolstoy, M. & Bohnenstiehl, D. R., 2005. Hydroacoustic constraints on the rupture duration, length, and speed of the great Sumatra-Andaman earthquake, *Seismological Research Letters*, **76**(4), 419–425.

Tolstoy, M. & Bohnenstiehl, D. R., 2006. Hydroacoustic contributions to understanding the December 26th 2004 great Sumatra-Andaman earthquake, *Surveys in Geophysics*, **27**(6), 633–646, doi: 10.1007/s10712-006-9003-6.

Tong, P., Komatitsch, D., Tseng, T.-L., Hung, S.-H., Chen, C.-W., Basini, P., & Liu, Q., 2014. A 3-D spectral-element and frequency-wave number hybrid method for high-resolution seismic array imaging, *Geophys. Res. Lett.*, **41**(20), 7025–7034, doi: 10.1002/2014GL061644.

Tournadre, J., 2014. Anthropogenic pressure on the open ocean: The growth of ship traffic revealed by altimeter data analysis, *Geophysical Research Letters*, **41**(22), 7924–7932, doi: 10.1002/2014GL061786.

Toyokuni, G., Takenaka, H., & Kanao, M., 2012. Quasi-axisymmetric finite-difference method for realistic modeling of regional and global seismic wavefield, review and application, in *Seismic Waves, Research and Analysis*, chap. 5, pp. 85–112, ed. Kanao, M., InTech, Rijeka, Croatia, doi: 10.5772/32422.

Tromp, J., Tape, C., & Liu, Q., 2005. Seismic tomography, adjoint methods, time reversal and banana-doughnut kernels, *Geophysical Journal International*, **160**(1), 195–216, doi: 10.1111/j.1365-246X.2004.02453.x.

Tromp, J., Komatitsch, D., & Liu, Q., 2008. Spectral-element and adjoint methods in seismology, *Communications in Computational Physics*, **3**(1), 1–32.

Tromp, J., Komatitsch, D., Hjörleifsdóttir, V., Liu, Q., Zhu, H., Peter, D., Bozdağ, E., McRitchie, D., Friberg, P., Trabant, C., & Hutko, A., 2010. Near real-time simulations of global CMT earthquakes, *Geophys. J. Int.*, **183**(1), 381–389, doi: 10.1111/j.1365-246X.2010.04734.x.

Turner, M. J., Clough, R. W., Martin, H. C., & Topp, L. J., 1956. Stiffness and deflection analysis of complex structures, *Journal of Aeronautical Sciences*, **23**(9), 805–823.

UNCTAD, 2017. Review of maritime transport 2017, United Nations Conference on Trade and Development, doi: 10.18356/a9b345e7-en.

Urick, R. J., 1972. Noise signature of an aircraft in level flight over a hydrophone in the sea, *Journal of the Acoustical Society of America*, **52**(3B), 993–999.

Urick, R. J., 1982. *Sound propagation in the sea*, Peninsula Publishing Los Altos, CA.

van Manen, D.-J., Robertsson, J. O. A., & Curtis, A., 2007. Exact wave field simulation for finite-volume scattering problems, *Journal of the Acoustical Society of America*, **122**(4), EL115–EL121, doi: 10.1121/1.2771371.

Virieux, J., 1986. P-SV wave propagation in heterogeneous media: Velocity-stress finite-difference method, *Geophysics*, **51**(4), 889–901, doi: 10.1190/1.1442147.

Wadati, K. & Inouye, W., 1953. On the T phase of seismic waves observed in Japan, *Proc. Japan Acad.*, **29**, 47–54.

Walker, D. A., 2001. *Volcanoes, El Niños, and the Bellybutton of the Universe*, Xlibris.

Walker, D. A. & Bernard, E. N., 1993. Comparison of T-phase spectra and tsunami amplitudes for tsunamigenic and other earthquakes, *Journal of Geophysical Research: Oceans*, **98**(C7), 12557–12565, doi: 10.1029/93JC00675.

Walker, D. A., McCreery, C. S., & Hiyoshi, Y., 1992. T-phase spectra, seismic moments, and tsunamigenesis, *Bulletin of the Seismological Society of America*, **82**(3), 1275–1305.

Walker, K. T., Ishii, M., & Shearer, P. M., 2005. Rupture details of the 28 March 2005 Sumatra Mw 8.6 earthquake imaged with teleseismic P waves, *Geophysical Research Letters*, **32**(24), n/a–n/a, doi: 10.1029/2005GL024395, L24303.

Wang, Y., Chevrot, S., Monteiller, V., Komatitsch, D., Mouthereau, F., Manatschal, G., Sylvander, M., Diaz, J., Ruiz, M., Grimaud, F., Benahmed, S., Pauchet, H., & Martin, R., 2016. The deep roots of the western Pyrenees revealed by full waveform inversion of teleseismic P waves, *Geology*, **44**(6), 475–478, doi: 10.1130/G37812.1.

Ward, S. N., 1980. Relationships of tsunami generation and an earthquake source, *Journal of Physics of the Earth*, **28**(5), 441–474.

Wilcock, W. S. D., Purdy, G. M., Solomon, S. C., DuBois, D. L., & Toomey, D. R., 1992. Microearthquakes on and near the East Pacific Rise, 9-10 N, *Geophysical research letters*, **19**(21), 2131–2134.

Wilcock, W. S. D., Stafford, K. M., Andrew, R. K., & Odom, R. I., 2014. Sounds in the ocean at 1-100 Hz, *Annual review of marine science*, **6**, 117–140.

Wilcox, L. C., Stadler, G., Burstedde, C., & Ghattas, O., 2010. A high-order discontinuous Galerkin method for wave propagation through coupled elastic-acoustic media, *J. Comput. Phys.*, **229**(24), 9373–9396, doi: 10.1016/j.jcp.2010.09.008.

Williams, C. M., Stephen, R. A., & Smith, D. K., 2006. Hydroacoustic events located at the intersection of the Atlantis (30°N) and Kane (23°40'N) transform faults with the Mid-Atlantic ridge, *Geochemistry, Geophysics, Geosystems*, **7**(6), 1–28, doi: 10.1029/2005GC001127.

Wingate, B. A. & Boyd, J. P., 1996. Spectral element methods on triangles for geophysical fluid dynamics problems, in *Proceedings of the Third International Conference on Spectral and High-order Methods*, pp. 305–314, Houston J. Mathematics, Houston, Texas.

Xie, Z., Komatitsch, D., Martin, R., & Matzen, R., 2014. Improved forward wave propagation and adjoint-based sensitivity kernel calculations using a numerically stable finite-element PML, *Geophys. J. Int.*, **198**(3), 1714–1747, doi: 10.1093/gji/ggu219.

Xie, Z., Matzen, R., Cristini, P., Komatitsch, D., & Martin, R., 2016. A perfectly matched layer for fluid-solid problems: Application to ocean-acoustics simulations with solid ocean bottoms, *Journal of the Acoustical Society of America*, **140**(1), 165–175, doi: 10.1121/1.4954736.

Xu, C.-X., Tang, J., Piao, S.-C., Liu, J.-Q., & Zhang, S.-Z., 2016. Developments of parabolic equation method in the period of 2000-2016, *Chinese Physics B.*, **25**(12), 124315.

Xu, R., Liu, B., & Dong, Y., 2013. Scalable hierarchical parallel algorithm for the solution of super large-scale sparse linear equations, *Journal of Applied Mechanics*, **80**(2), 020901.

Yang, Y. & Forsyth, D. W., 2003. Improving epicentral and magnitude estimation of earthquakes from T phases by considering the excitation function, *Bulletin of the Seismological Society of America*, **93**(5), 2106–2122, doi: 10.1785/0120020215.

Yun, S. & Lee, W. S., 2013. Hydroacoustic observation on the 2011 Tohoku earthquake, *Geophysics and Geophysical Exploration*, **16**(4), 234–239.

Zampolli, M., Tesei, A., Jensen, F. B., Malm, N., & Blottman III, J. B., 2007. A computationally efficient finite-element model with perfectly matched layers applied to scattering from axially symmetric objects, *Journal of the Acoustical Society of America*, **122**(3), 1472–1485.

Zienkiewicz, O. C. & Taylor, R. L., 1977. *The finite element method*, vol. 3, McGraw-Hill.